SQT

NASA

Technical Memorandum 80650

ATMOSPHERIC AND OCEANOGRAPHIC RESEARCH REVIEW—1979

Laboratory for Atmospheric Sciences Modeling and Simulation Facility

JANUARY 1980

National Aeronautics and Space Administration

Goddard Space Flight Center
Greenbelt, Maryland 20771

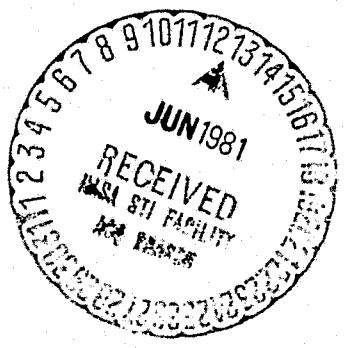

TM80650

ATMOSPHERIC AND OCEANOGRAPHIC RESEARCH REVIEW - 1979

LABORATORY FOR ATMOSPHERIC SCIENCES
MODELING AND SIMULATION FACILITY

JANUARY 1980

NASA GODDARD SPACE FLIGHT CENTER
GREENBELT, MARYLAND

TABLE OF CONTENTS

TABLE OF CONTENTS (Continued)

III. CLIMATE

TABLE OF CONTENTS (Continued)

IV. OCEAN/AIR INTERACTIONS

V. SUMMER LECTURE SERIES

TABLE OF CONTENTS (Continued)

I. INTRODUCTION

I. INTRODUCTION

The Modeling and Simulation Facility of the Laboratory for Atmospheric Sciences (GLAS) is engaged in general circulation modeling studies related to global atmospheric and oceanographic research. Research activities at the Goddard Modeling and Simulation Facility (GMSF) are organized in three areas: GARP/Global Weather, Climate, and Ocean/Air Interactions.

During the period of this review, GARP/Global Weather research was directed primarily toward the development of techniques for the utilization and analysis of the First GARP Global Experiment (FGGE) data sets. This involved acquisition and data file management efforts, development of improved techniques for the analysis of FGGE data, observing systems research, forecast model development, and diagnostic studies. Observing system studies were concerned with the development of a GLAS TIROS N sounding retrieval system and preparation for the joint NOAA/NASA Advanced Moisture and Temperature Sounder simulation study.

Climate research focused on the continued development of the GLAS general circulation model for short-range climate predictions, studies of the sensitivity of climate to boundary conditions, and predictability studies to determine which features of the global climate system can be computed deterministically or statistically. Ocean/air interaction studies concentrated on the development of models for the prediction of upper ocean currents, temperatures, sea state, mixed-layer depths, and upwelling zones, and on studies of the interactions of the atmospheric and oceanic circulation systems on time scales of a month or more.

This research review presents a synopsis of extended abstracts in the GARP/Global Weather, Climate and Ocean/Air Interaction studies conducted at the Modeling and Simulation Facility during the calendar year 1979.

A major event during the summer 1979 was the second annual visiting lecture series jointly sponsored by the Modeling and Simulation Facility and University of Maryland. The program included many distinguished university scientists and was extremely popular here at GLAS, even drawing a considerable attendance from the greater Washington, DC metropolitan area. Abstracts of the summer lectures are presented in section V.

A list of recent publications by the staff scientists and visiting scientists is presented in section VI.

II. GARP / GLOBAL WEATHER

TEMPERATURE SOUNDING FROM TIROS-N

(J. Susskind)

TIROS-N, the current operational meteorological satellite, contains three passive temperature sounding instruments, HIRS2, a 20-channel infrared radiometer, MSU, a 4-channel microwave radiometer, and SSU, a 3-channel pressure modulated infrared radiometer sounding the upper stratosphere. NOAA/NESS operationally produces global atmospheric temeprature soundings by analysis of observations from these three instruments using statistical regression methods. GLAS has developed a fundamentally different approach to analysis of satellite temeprature sounding data, which relies more heavily on the ability to account for the atmospheric physics giving rise to the observations rather than the statistical relationships of atmospheric properties to satellite observations. The method is believed to be superior to that in use operationally under partially cloudy conditions, especially over oceans.

The iterative scheme and cloud filtering methods used in the inversion process are closely related to those of Chahine (1970, 1974). Intrinsic in the use of the Chahine iterative retrieval scheme is the ability to accurately solve the forward problem, that is, given a guess set of atmospheric and surface parameters, accurately compute the corresponding observations as seen by the satellite instruments. The method involves iterative modification of the atmospheric parameters, starting from an initial guess, until sufficient agreement between computed and observed radiances is reached.

The Radiative Transfer Equation

Given atmospheric and surface conditions, the clear column radiances R_i observed by a sounding channel i can be expressed as

$$R_i = \varepsilon_i B_i[T_s]\, \tau_i(P_s) + (1 - \varepsilon_i)\, R_i{\downarrow}\, \tau_i(P_s) + \rho_i\, H_i\, \tau_{is}(P_s) + \int_{\ln P_s}^{\ln \bar{P}} B_i[T(P)]\, \frac{d\tau_i}{d \ln P}\, d \ln P \quad , \tag{1}$$

where ε_i is the surface emissivity averaged over sounding channel i, $B_i[T]$ is the mean Planck black-body function, averaged over channel i, of the temperature T, $\tau_i(P)$ is the mean atmospheric transmittance from pressure P to the top of the atmosphere and evaluated at θ, the zenith angle of the observation, $R_i{\downarrow}$ is an effective atmospheric emission downward flux, $\rho_i H_i \tau_{is}$ is the reflected solar radiation in the direction of the satellite, and the subscript s refers to surface. The integral, taken from the surface to the satellite pressure P, represents the upwelling atmospheric emitted radiation, which is a mean value of the black-body function of atmospheric temperature weighted by the channel-weighting function $d\tau_i/d \ln P$. Table 1 shows the channels, centers, and peak of the weighting function, and other relevant information, for the channels on MSU and HIRS. The current analysis does not employ the SSU observations.

Table 1. HIRS2 and MSU channels frequencies and peaks of the weighting functions or other relevant information.

Channel	$\nu(cm^{-1})$	Peak of $d\tau/d \ln P(mb)$	Peak of $B\ d\tau/d \ln P(mb)$
H1	668.40	30	20
H2	679.20	60	50
H3	691.10	100	100
H4	703.60	280	360
H5	716.10	475	575
H6	732.40	725	875
H7	748.30	Surface	Surface
H8	897.70	Window, sensitive to water vapor	
H9	1027.90	Window, sensitive to O_3	
H10	1217.10	Lower tropospheric water vapor	
H11	1363.70	Middle tropospheric water vapor	
H12	1484.40	Upper tropospheric water vapor	
H13	2190.40	Surface	Surface
H14	2212.60	650	Surface
H15	2240.10	340	675
H16	2276.30	170	425
H17	2310.70	15	2
H18	2512.00	Window, sensitive to solar radiation	
H19	2671.80	Window, sensitive to solar radiation	
	ν (GHz)		
M1	50.30	Window, sensitive to surface emissivity	
M2	53.74	500	
M3	54.96	300	
M4	57.95	70	

The transmittance functions of the HIRS channels are taken to be a product of dry transmittance functions, parameterized as a function of temperature profile and zenith angle (Mo and Susskind, 1978), and effective water vapor transmittances of the form $\tau_i(P, \theta) = \hat{\tau}^{-a_i W(P/P_s)^{n_i}}$, where W is is the column density of water vapor and a_i and n_i are channel-dependent constants (Halem and Susskind, 1977). The infrared emissivity ε_i is taken as .85 or .95 for land and water, respectively, at wavelengths greater than 10μm, and .95 or .98 for wavelengths less than 5μm (channels between 5 and 10μm were not used in the analysis). The effective downward flux, $R_i\downarrow$, is calculated according to Kornfield and Susskind (1977). The solar radiation term will be discussed later.

The microwave transmittances are taken to be products of O_2 transmittances, calculated as a function of temperature profile and zenith angle according to Rosenkrantz (1975), and water vapor transmittance having the same form as the infrared effective water vapor transmittances. Water vapor retrievals using the humidity sounding channels on HIRS2 are not done at this time, and W, the water vapor column density is estimated at the 24-h lagged analysis value, as is the surface pressure P_s. The microwave emissivity is calculated from the 50.3 GHz channels, as part of the iterative scheme, according to

$$\varepsilon = \frac{R_i - \int T d\tau - R_i\downarrow \tau_i(P_s)}{[T_s - R_i\downarrow]\, \tau_i(P_s)} \quad , \tag{2}$$

where R_i is the 50.3 GHz observed brightness temperature, T_s is the iterative surface temperature, and T(P) is the iterative atmospheric temperature profile used in the calculation of the upward and downward microwave fluxes emitted by the atmosphere. The transmittance functions are, of course, corrected for temperature, water vapor, and zenith angle as described earlier, but possible effects of liquid water attenuation on the 50.3 GHz channel are not accounted for. The emissivity determined from the 50.3 GHz channel observation is used, together with the iterative temperature profile, to calculate brightness temperatures for the other MSU channels.

Accounting for Effects of Clouds on the Infrared Observations

The infrared radiance observed in an otherwise homogeneous field of view, containing partial homogeneous cloud cover α, is given, by a reasonable approximation, as

$$R_i = \alpha R_{i,CLD} + (1 - \alpha)\, R_{i,CLR} \quad , \tag{3}$$

where $R_{i,CLD}$ and $R_{i,CLR}$ are the radiances which would have been observed if the field of view were completed cloudy or clear, respectively. Computation of clear column radiances $R_{i,CLR}$ can be done routinely as in Eq. (1), but computation of $R_{i,CLD}$ requires accurate knowledge of the optical as well as meteorological properties of the cloud. It is more advantageous to be able

to account for the effects of clouds indirectly than to have to model their radiative transfer properties. A method for doing this is employed, as proposed by Chahine (1974), using observations in adjacent fields of view using the assumption that both fields of view are identical (up to an accountable effect of zenith angle). An estimate of the clear column radiance, $R_{i,CLR}$, can be reconstructed from the observations according to

$$\hat{R}_{i,CLR} = R_{i,1} + \eta[R_{i,1} - R_{i,2}] \quad , \tag{4}$$

where $R_{i,j}$ is the observation for channel i in field of view j and η is given by $\alpha_1/(\alpha_2 - \alpha_1)$, with $\alpha_2 > \alpha_1$. Since α is dependent only on fractional cloud cover, η is independent of channel and spectral region. Given η, clear column radiances can be reconstructed from the observations using Eq. (4) and the effects of clouds are, in principle, accounted for.

These reconstructed clear column radiances are then used in the iterative temperature scheme. It is seen from Eq. (4) that large values of η will tend to amplify noise in the observations and are therefore undesirable. As shown by Chahine (1974) and Halem et al. (1978), η can be determined as part of an iterative scheme according to

$$\eta^{(N)} = \frac{R_7^{(N)} - R_{7,1}}{R_{7,1} - R_{7,2}} \quad , \tag{5}$$

where $R_7^{(N)}$ is the computed clear column radiance for the 15μm surface channel, using the N^{th} iterative temperature profile. The scheme will converge provided only 4.3 μm infrared channels are used for temperature sounding in the lower troposphere. The rate of convergence increases with the difference between the surface temperature and the cloud top temperature. Under some high noise, low contrast conditions, divergent solutions can occur in the sense that an overestimate of $\eta^{(N)}$ will cause an overestimate of the reconstructed 4.3 μm clear column radiances which, in turn, will yield an increased lower tropospheric temperature, producing an increased value of $R_7^{(N+1)}$, leading to an increased $\eta^{(N+1)}$, etc.

This situation is greatly alleviated by incorporation of a lower tropospheric microwave observation in the determination of η. The error in $\eta^{(N)}$ is a result of either an error in $R_7^{(N)}$, due to a wrong temperature profile or computational uncertainties such as the effect of water vapor on the transmittance functions of channel 7, observational errors in $R_{7,1}$, or errors in the assumption of only one degree of nonhomogeneity in the combined fields of view. The error in $R_7^{(N)}$ due to a wrong temperature profile can be well accounted for by adjusting the computed brightness temperature for channel 7 by the difference in the observed and computed microwave brightness temperatures for channel M2 according to

$$T_7 - T_7^{(N)} = T_{M2} - T_{M2}^{(N)} \quad , \tag{6}$$

where T_{M2} and $T_{M2}^{(N)}$ are the observed and calculated microwave brightness temperatures, $T_7^{(N)}$ is the calculated clear column brightness temperature for channel 7, and T_7 is the corrected clear column brightness temperature for channel 7. The corrected clear column radiance for channel 7, to be used in Eq. (5), is then given by

$$R_7^{(N)} = B_7\left[T_7^{(N)} + T_{2,M} - T_{2,M}^{(N)}\right] \tag{7}$$

This procedure not only speeds up convergence under all conditions but also stabilizes the solution in the sense that an increase in the iterative temperature profile in the lower troposphere will not, to a first approximation, cause an increase in η.

Determination of Surface Temperature

Given $\eta^{(N)}$, the clear column radiances for the three window channels 8, 18, and 19 are reconstructed according to Eq. (4). All three channels are relative atmospheric windows and are sensitive primarily to be surface (ground) temperature. The two 3.7μm channels have the advantage of being more sensitive to surface temperature and less sensitive to uncertainties in surface emissivity and atmospheric water vapor than the 11μm window channel. They have the disadvantage of being affected by solar radiation during the day, which must be accounted for before accurate surface temperatures can be calculated. At night, surface temperatures are taken to be the average of the surface temperature as determined from channels 18 and 19, where

$$T_{s,i}^{(N)} = B_i^{-1}\left[\frac{R_i^{(N)} - (1-\varepsilon_i)\,R_i^{(N)\downarrow}\,\tau_i^{(N)}(P_s) - \int_{\tau_2^{(N)}(P_s)}^{1} B_i(T^N)\,d\tau}{\varepsilon_i\,\tau_i^{(N)}P_s}\right]. \tag{8}$$

In general, $T_{s,18}$ and $T_{s,19}$ agree with each other to 1° but differ by a larger amount from the surface temperature as determined from the 11 μm window channel 8, especially when the water vapor column density along the path of observation is greater than 3 gm/cm^2.

During the day, the effects of solar radiation on the 3.7μm channels must be accounted for in obtaining accurate surface temperature retrievals from these channels. This can be done directly by subtracting $\rho_i H_i \tau_{is}(P_s)$ from $R_i^{(N)}$ and substituting the result into Eq. (8). $H_i\tau_{is}(P_s)$, the mean solar radiation across the channel, transversing the path from the sun to the earth and back to the satellite, can be well estimated as $2.16\pi \times 10^{-5}\, B_i\,[5600K]\cos\theta_H \tau_i(P_s, \theta_H + \theta)$ where θ_H is the solar zenith angle and the transmittance is computed at an effective zenith angle given by the sum of the solar and the satellite zenith angles.

The danger in such a procedure is the uncertainty in ρ_i. If the surface is Lambertian and the emissivity is known, ρ_i, the directional reflectance, is equal to $(1 - \varepsilon_i)/\pi$. Significant errors of up to a factor of 2 can be

made in the above estimation of ρ_i, which may produce errors of up to 10K in retrieved surface temperature. These errors arise from uncertainties in ε_i and the non-Lambertian character of the surface. However, the same uncertainties in ε_i do not appreciably effect the calculated thermal radiation.

An error in ρ_i will produce different errors in the surface temperature as retrieved from the two 3.7μm channels because dT/dB in channel 19 is twice as great as in channel 18. Consequently, agreement to within 1° of $T_{s,18}$ and $T_{s,19}$, obtained by subtracting $(1 - \varepsilon_i)/\pi H_i \tau_i(P_s)$ from $R_i(N)$ in Eq. (8), is taken as evidence of an accurate estimate value of ρ_i, and the average of $T_{s,18}$ and $T_{s,19}$ is taken as the surface temperature. If this agreement is not obtained, $T_{s,8}$, obtained from the 11μm window channel, is taken as the ground temperature, provided the water vapor column density along the observing path is less than 3 gm/cm^2.

As a final alternative, an attempt to solve simultaneously for T_s and ρ_i is made by linearizing Eq. (1) about $T_{s,8}$, which is expected to be a reasonable approximation of T_s, according to

$$R_i = \varepsilon B_i[T_{s,8}]\, \tau_i(P_s) + \varepsilon \left(\frac{dB_i}{dT}\right)_{T_{s,8}} (T_s - T_{s,8}) \qquad (9)$$

$$+ \rho H_i \tau_{i,s}(P_s) + (1 - \varepsilon)\, R_i\!\uparrow \tau_i(P_s) + \int B_i\, d\tau$$

Eq. (9) gives two linear equations, one for channel 18 and one for channel 19, for the two unknowns, T_s and ρ, and can be solved in a straightforward manner.

Iterative Procedure

Given an initial or N^{th} guess temperature profile $T^N(P)$, and surface temperature T_s^N, clear column radiances can be calculated from Eqs. (1) and (2) and algorithms to calculate transmittance functions and downward fuxes. Eqs. (4), (5), and (7) are then used to reconstruct clear column radiances $\hat{R}_i(N)$ for the infrared channels. T_s^{N+1} is obtained from Eqs. (8) or (9). $T^{N+1}(P)$ is obtained in a relaxation manner analogous to that of Chahine. Chahine assigns a pressure P_i to each temperature sounding channel i, given approximately by the peak of the weighting function for channel i, representing that portion of the atmosphere in which local changes of temperature will have the largest effect on the observed radiance for that channel. Chahine uses the iterative equation,

$$\frac{B_i[T^{N+1}(P_i)]}{B_i[T^N(P_i)]} = \frac{\hat{R}_i^{(N)}}{R_i^{(N)}} \qquad (10)$$

to determine a new estimate of temperature at each of the pressures P_i. Temperature at other pressures can be obtained by a variety of interpolation schemes or other constraints on the solution. Given $T^{N+1}(P)$ and T_s^{N+1}, the entire iterative procedure can then be repeated.

A more convenient form of the iterative equation for temperature can be written in terms of clear column brightness temperatures T_j for each channel, that is, the temperature of a black body with radiance R_j. The analogous equation to Eq. (10) becomes

$$T^{N+1}(P_i) = T^N(P_i) + \hat{T}_i^{(N)} - T_i^{(N)} \quad , \tag{11}$$

Eq. (11) reflects the very good approximation that, given a temperature profile and brightness temperature, if the entire profile and surface temperatures were changed slightly by ΔT, the brightness temperature will also change by ΔT regardless of the frequency region or nature of the weighting function.

The iterative scheme based on either Eq. (10) or, equivalently, Eq. (11) sometimes produces divergent solutions if noise in adjacent channels is large and of opposite sign. It was found that stability was increased, with only slight loss in speed of convergence, if the temperature at pressure P_i was modified according to a weighted difference of observed and calculated brightness temperatures for all channels according to

$$T^{N+1}(P_i) = T^N(P_i) + \sum_j W_{ij} \left(\hat{T}_j^{(N)} - T_j^{(N)} \right) / \sum_j W_{ij} \quad , \tag{12}$$

where W_{ij} is the relative change in brightness temperature for channel j produced by a change in temperature at pressure P_i.

From Eq. (1), to a good approximation,

$$\frac{dR_j}{dT(P_i)} = \left(\frac{dB_j}{dT} \right)_{T(P_i)} \left(\frac{dT_j}{d \ln P} \right)_{P_i} \quad . \tag{13}$$

W_{ij}, the relative change in brightness temperature for channel j produced by a change in temperature at P_i, is then given by

$$\begin{aligned} W_{ij} &= \frac{dT_j}{dT(P_i)} = \left(\frac{dT}{dB} \right)_{T_j} \frac{dR_j}{dT(P_i)} \\ &= \left(\frac{dT}{dB} \right)_{T_j} \left(\frac{dB}{dT} \right)_{T(P_i)} \left(\frac{dT_j}{d \ln P} \right)_{P_i} \end{aligned} \quad . \tag{14}$$

Using appropriate approximate forms for the black-body function at microwave and infrared wavelengths, one gets

$$W_{ij} = \left[\frac{T_j}{T(P_i)} \right]^2 \exp \left[1.439 \nu_{ij} \left(\frac{1}{T_j} - \frac{1}{T(P_i)} \right) \right] \left(\frac{dT_j}{d \ln P} \right)_{P_i} \tag{15a}$$

for infrared channels and

$$W_{ij} = \left(\frac{d\tau_j}{d \ln P} \right)_{P_i} \qquad (15b)$$

for microwave channels.

Fig. 1 shows the weighting functions as defined in Eq. (15) for the six TIROS-N channels used in the analysis of the data, for U.S. standard atmosphere under nadir viewing. The observations are most sensitive to atmospheric temperature changes below 500 mb and between 150 mb and 50 mb, with relative weakness in between. The six characteristic pressures used in the analysis are also shown in the figure.

Gridding of Satellite Data

In order to facilitate analysis of global data on a twice-daily basis, the HIRS data are gridded (averaged) prior to analysis so that one sounding is performed every 250 x 250 km. The 250 x 250 km area is first divided into four equal quadrants. In each quadrant, the HIRS spots (20 km x 20km at nadir) are divided into equal groups, representing the two fields of view, according to the brightness temperature of channel 8, the 11 μm window, with field of view 1 containing those spots with the largest radiances for this channel. The radiances for all spots in a field are averaged together for each channel to give the radiances for each field of view to be used in the analysis of the data. Each field of view is assigned a zenith angle weighted according to the cosine of the zenith angles of the individual spots. The microwave brightness temperatures and zenith angle of the MSU spot (110km x 110 km at nadir) most overlapping the quadrant, are assigned to each field of view. Using this gridding scheme, approximately 17000 retrievals are performed daily. The computing time for this is roughly 1 h CPU time on the Amdahl V/460.

Results

Global retrievals were run for the period 4 January-5 February 1979 using a 24-h lagged analysis initial guess. A shape-preserving interpolation scheme (Chahine, 1970), in which $T^{(N+1)}(P) - T^{N}(P)$ was taken to be linear in log P, was used in analysis of the data. In all of the cases, a sounding was rejected if, after five iterations, the RMS difference of computed and reconstructed brightness temperatures for the six temperature sounding channels was greater than 1° or the computed and observed brightness temperature for channel M2 differed by more than 1.5°. Approximately 30 percent of all soundings were rejected by these criteria, and of these, half which were rejected were considered clear. This indicates that only in approximately 15 percent of the cases was it too cloudy to perform retrievals using the infrared tropospheric channels. In contrast, the operational retrievals produced by NESS perform infrared tropospheric retrievals only 50 percent of the time. In the remainder of the cases, retrievals are performed using the HIRS stratospheric channels together with the MSU channels. These have been shown to be considerably less accurate compared with radiosondes.

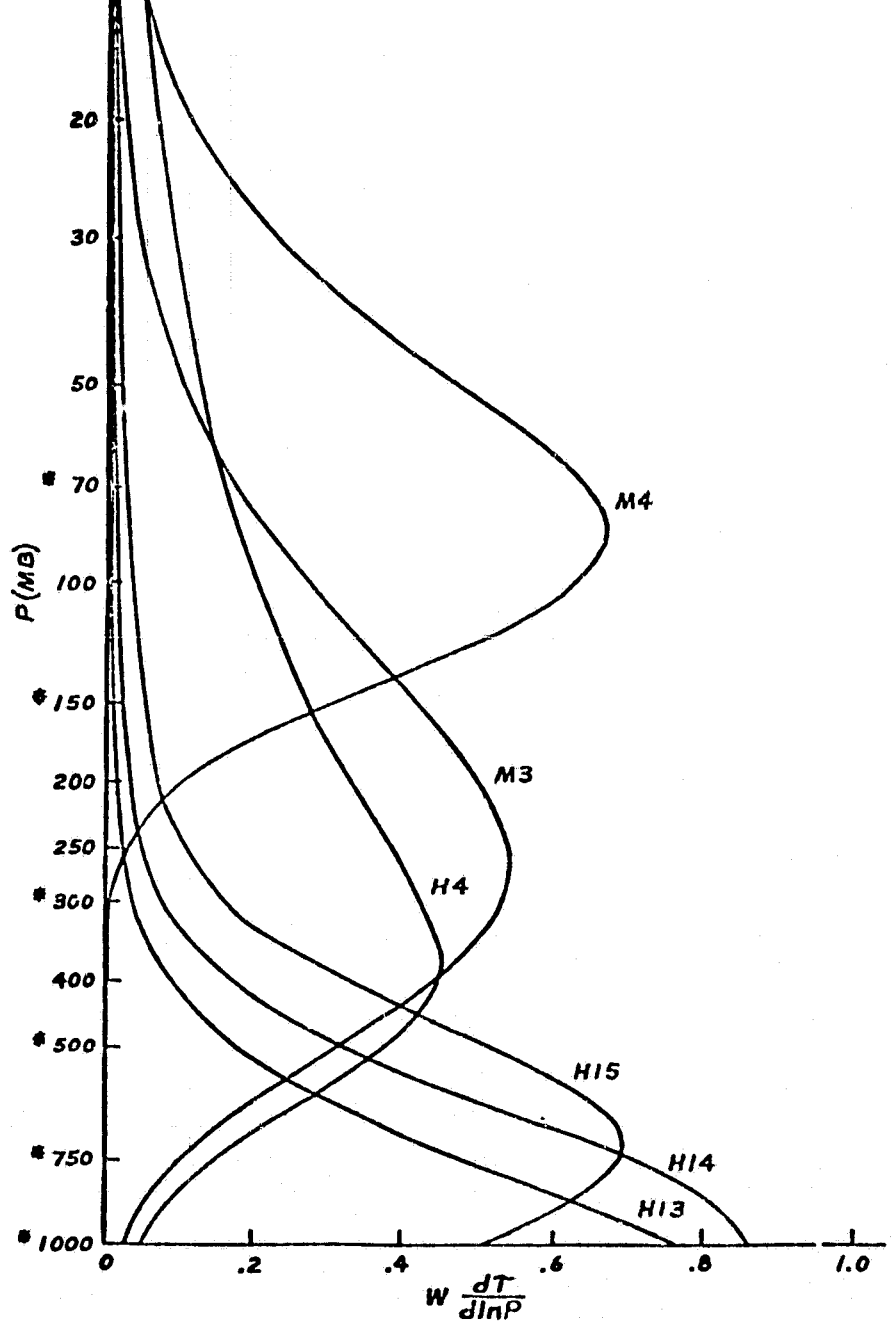

Fig. 1. Weighting functions for the six channels used to determine atmospheric temperature profile. * represents a pressure where iterative temperature adjustments are made.

Fig. 2 shows the RMS errors of layer mean temperatures from both the GLAS and operational retrievals, as compared to oceanic radiosondes colocated to within 110 km in space and 6 h in time. In the first graph, errors of all retrievals from each set, colocated with radiosondes are compared with each other. In the second graph, comparison is made only between those retrievals performed by NOAA under partially cloudy conditions and successful GLAS retrievals colocated to the same radiosondes. The GLAS retrievals are clearly significantly better in the troposphere under these conditions, in which the combination of the cloud problem and poor statistical representation of oceanic radiosondes in the regression data base used by NESS significantly degrade the operational results.

Fig. 3 shows a comparison of the 1000-500 mb thickness fields off western Europe at 0300 GMT 4 January 1979, derived on the McIDAS from the GLAS soundings and the NESS enhanced soundings (see Atlas et al., 1980). The general agreement between the fields is good, especially in the region over western Europe validated by radiosonde reports. The differences and their sources are being evaluated, particularly in regions where the enhanced soundings were microwave only, such as over England.

References

Atlas, R., G. Cole, R. Rosenberg, S. Palm, and A. Pursch, 1980: Enhancement of TIROS-N sounding and cloud motion wind data for the FGGE Special Effort. NASA Tech. Memo. (herein), Atmos. and Oceano. Res. Rev.-1979, NASA Goddard Space Flight Center, Greenbelt, Maryland.

Chahine, M. T., 1970: Inverse problems in radiative transfer: determination of atmospheric parameters. J. Atmos. Sci., 27, 960-967.

_____, 1974: Remote sounding of cloudy atmospheres, I. The single cloud layer. J. Atmos. Sci., 31, 233-243.

Kornfield, J., and J. Susskind, 1977: On the effect of surface emissivity on temperature retrievals. Mon. Wea. Rev., 105, 1605-1608.

Halem, M., and J. Susskind, 1977: GISS VTPR Processing Manual. NASA Rep. X-130-77-53, Appendix A, NASA Goddard Institute for Space Studies, New York, NY.

_____, M. Ghil, R. Atlas, J. Susskind, and W. J. Quirk, 1978: The GISS Sounding Temperature Impact Test. NASA Tech. Memo. 78063, NASA Goddard Space Flight Center, Greenbelt, Maryland, 2-38 to 2-43.

Mo, T., and J. Susskind, 1978: Rapid algorithm for calculation of temperature dependence of HIRS transmittance functions. NASA Tech. Memo. 80253, Atmos. and Oceano. Res. Rev.-1978, NASA Goddard Space Flight Center, Greenbelt, Maryland 20771, 81-87.

Rosencrantz, P. W., 1975: Shape of the 5mm oxygen band in the atmosphere. IEEE Trans. on Antennas and Propa., 23, 498-506.

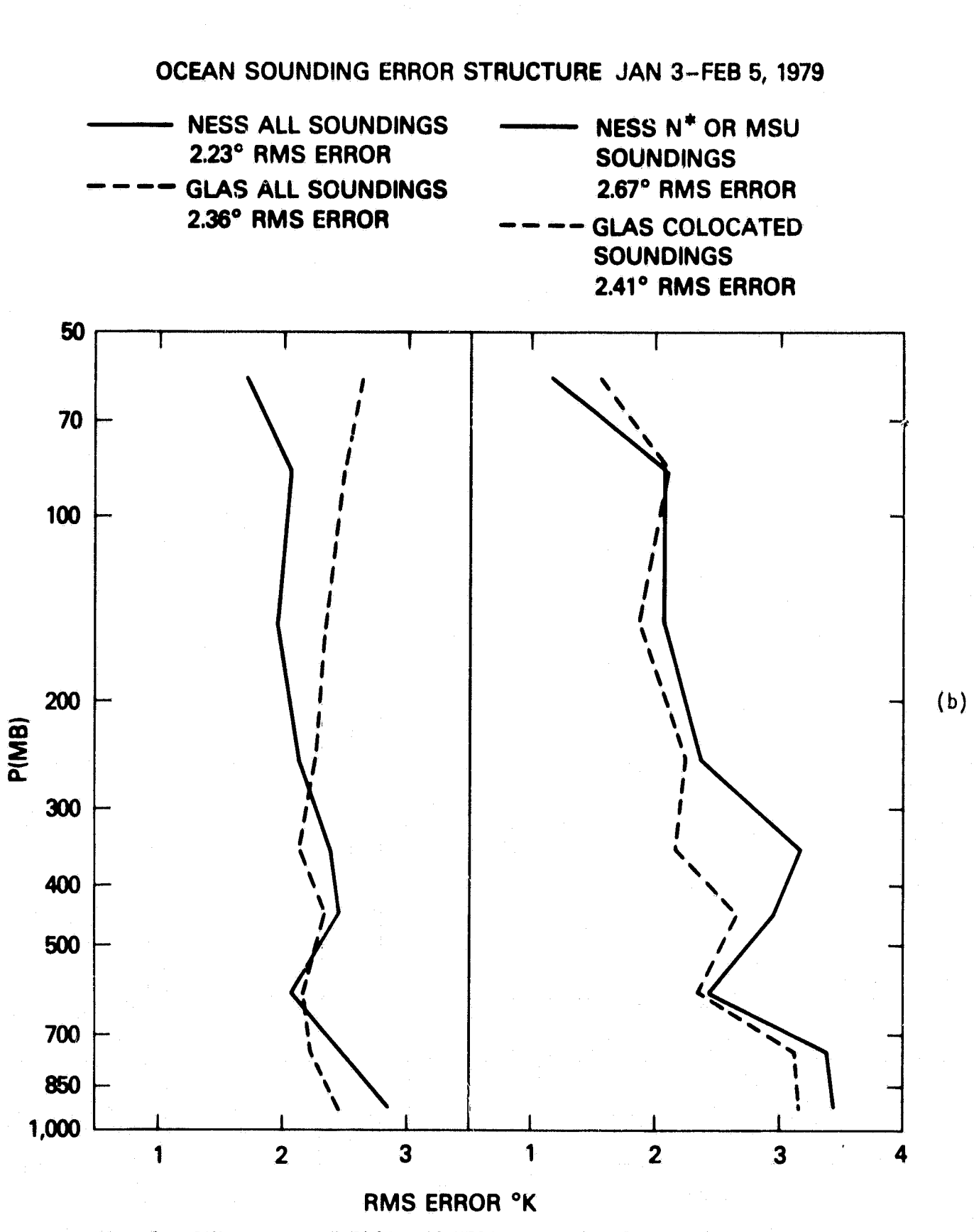

Fig. 2. RMS errors of GLAS and NESS operational soundings over oceans as compared to radiosondes colocated to 110 km. a) shows all NESS soundings colocated to radiosondes and all GLAS soundings colocated to radiosondes; b) shows statistics for all NESS retrievals under partially cloudy conditions colocated to both radiosondes and GLAS retrievals as well as statistics for the colocated GLAS retrievals.

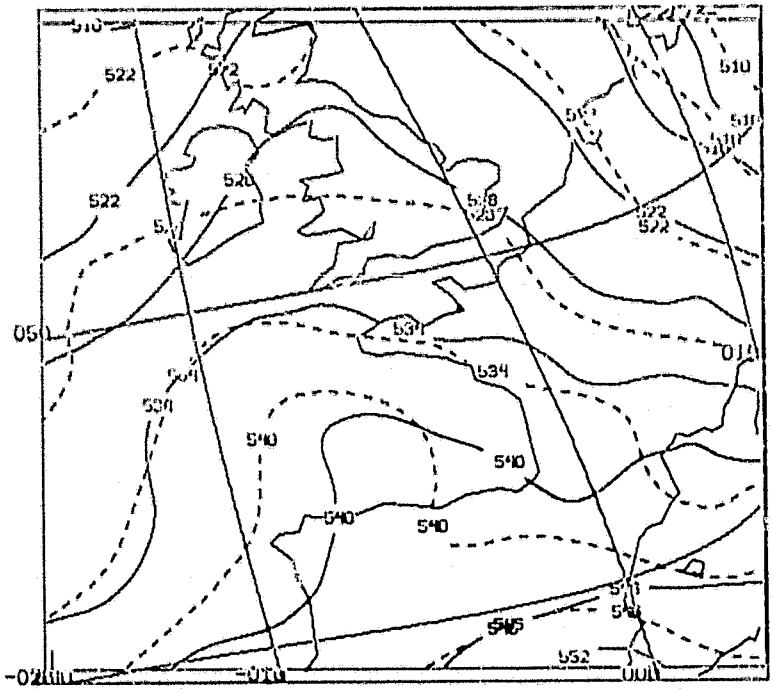

Fig. 3. 1000-500 mb thickness analyses based on enhanced TIROS-N retrievals (solid lines, see Atlas et al., 1980) and GLAS TIROS-N retrievals (dashed lines). The GLAS retrievals were unedited while the enhanced retrievals were subjectively edited by man-computer interaction.

ENHANCEMENT OF TIROS-N SOUNDING AND CLOUD MOTION WIND DATA FOR THE FGGE SPECIAL EFFORT

(R. Atlas, G. Cole, R. Rosenberg, S. Palm, and A. Pursch)

A "Special Effort" to produce high quality edited and enhanced global data sets is being conducted for the two special observing periods of the First GARP Global Experiment (FGGE), Greaves et al. (1979). The Special Effort is a joint project between NASA, NOAA, and the University of Wisconsin. Man-computer Interactive Data Access System (McIDAS) terminals, developed by the Space Science Engineering Center (SSEC) of the University of Wisconsin, are being utilized by experienced meteorologists at the National Meteorological Center (NMC) for data evaluation and quality assessment, and at the Goddard Laboratory for Atmospheric Sciences (GLAS) for satellite data enhancement. Interactive procedures for sounding and cloud motion wind enhancement were originally developed by the National Environmental Satellite Service and SSEC, and are described by Smith et al. (1978) and Menzel et al. (1978). More than 60 cases have been selected for enhancement, on the basis of meteorological interest, by an ad hoc international committee of participating scientists. These cases include situations of blocking, cutoff low development, cyclogenesis, and tropical circulations.

The sounding data enhancement is aimed at supplementing the operational satellite sounding data set with higher resolution soundings in meteorologically active regions, and with new soundings where data voids or soundings of questionable quality exist. The cloud motion wind enhancement is aimed at the rederivation of cloud heights in suspect areas using radiance information from polar orbiting satellites. After the enhancement process is completed, a final editing and quality assessment of the enhanced data is performed. The data will be archived as Level IIb and will be utilized in Level IIIb analyses.

The sounding enhancement process at GLAS is performed as follows: Once an area has been selected, the McIDAS operator begins by displaying all available conventional and special FGGE data for that area, the Level III analysis, and visible, infrared, and microwave images from Television Infrared Observational Satellite (TIROS)-N. At this stage, the operator notes where data deficiencies exist and, from the TIROS-N images, determines the extent of cloudiness and where the most intense atmospheric thermal gradients are located. High resolution temperature retrievals are then generated for the area. This is followed by a comprehensive manual editing of the retrievals to remove small-scale discontinuities due to cloud-induced noise while retaining significant meteorological structures.

Sounding data enhancement operations began on 3 December 1979. The first case selected for enhancement was a strong cyclone centered southeast of England at 0400 GMT 4 January 1979. The 1000 mb analysis for the enhanced region, from conventional data at 0000 GMT 4 January 1979, is shown in Fig. 1. Fig. . resents the 1000-500 mb thickness analysis utilizing the 29 radiosonde reports at were available for this region (with no satellite soundings) as

solid lines and the 1000-500 mb thickness analysis utilizing 141 enhanced satellite soundings (with no radiosonde data) as dashed lines. Good agreement between the pure SAT and pure NOSAT thickness analyses can be seen over western Europe, while poorer agreement is evident over England where only microwave retrievals could be generated, and over oceanic areas where virtually no radiosonde data was available and the NOSAT analysis is questionable.

References

Greaves, J. R., G. DiMego, W. L. Smith, and V. E. Suomi, 1979: A special effort to provide improved sounding and cloud motion wind data for FGGE. Bull. Amer. Meteor. Soc., 60, 124-127.

Menzel, W. P., W. L. Smith, and H. M. Woolf, 1978: A man interactive technique for specifying cloud heights from sounding radiance data. Proc. of the Third AMS Conf. on Atmos. Rad., Davis, California, 28-30 June.

Smith, W. L., C. M. Hayden, H. M. Woolf, H. B. Howell, and F. W. Nagle, 1978: Interactive processing of TIROS-N sounding data. Proc. of the AMS Conf. on Wea. Forecasting and Analysis and Aviation Meteor., Silver Spring, Maryland, 16-19 October.

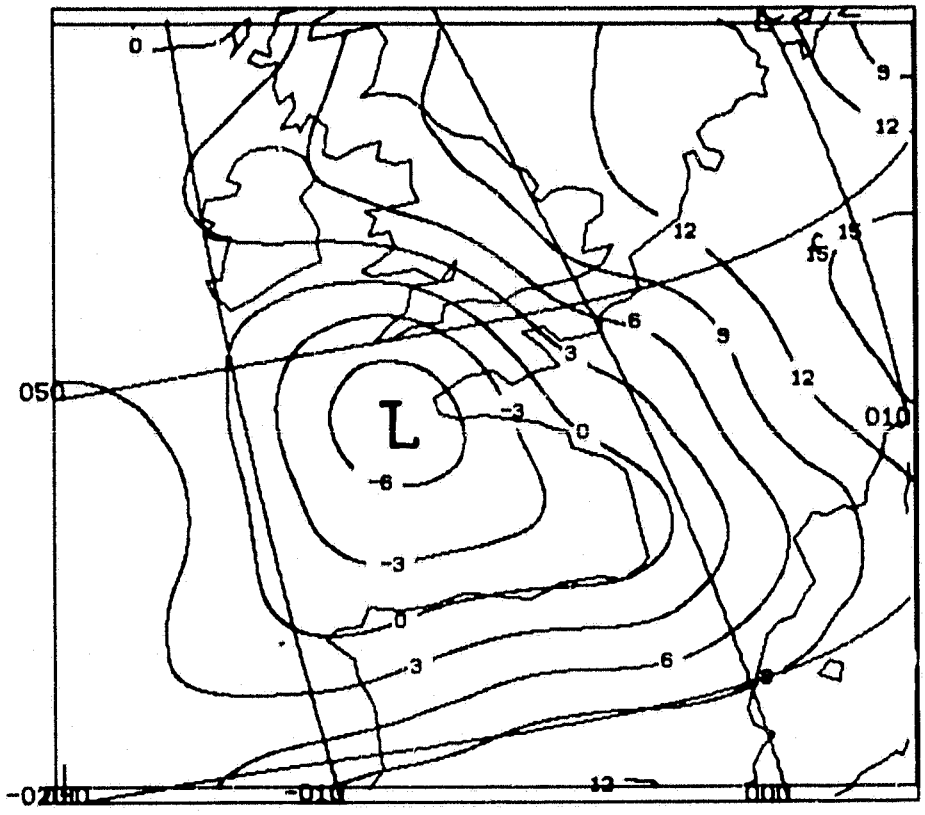

Fig. 1. 1000 mb analysis of conventional data for enhanced region.

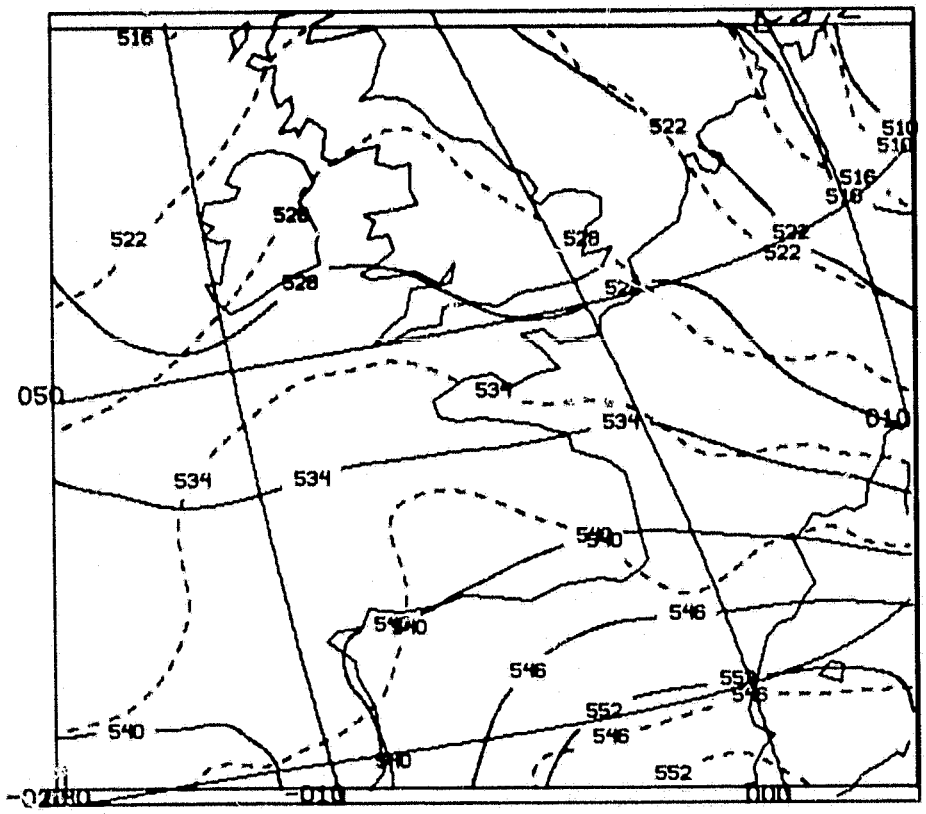

Fig. 2. 1000-500 mb thickness analyses based on radiosonde data (solid lines) and enhanced TIROS-N retrievals (dashed lines).

THE COMBINED INFLUENCE OF SATELLITE TEMPERATURE SOUNDING DATA AND INCREASED HORIZONTAL RESOLUTION ON GLAS MODEL FORECASTS

(R. Atlas, M. Halem, and M. Ghil)

Since the introduction of satellite-derived temperature soundings into the operational data base in 1972, a number of experiments have been conducted (Atkins and Jones, 1975; Desmarais et al., 1978; Druyan et al., 1978, Ghil et al., 1979a,b) to assess their influence on numerical weather forecasting. Objective measures of forecast accuracy have served as the primary tool for evaluating the predictive impact of the satellite temperature sounding data, along with some subjective evaluations by weather forecasters. The objective measures have generally shown either negligible or small beneficial impacts when averaged over many cases and continental regions. Even when specific forecasts show substantial objective impacts, subsequent subjective evaluations have shown the improvements to be of marginal value for forecasters. A principal reason may have been the fact that these statistical improvements occur in the 48-to-72 h forecast range when the model forecast accuracies have themselves deteriorated.

Thus, the question arises whether satellite sounding data might have greater influence, beneficial or otherwise, if numerical weather prediction (NWP) models had greater forecast skill. Recent studies by Robert (1976), Williamson (1978), and Quirk and Atlas (1977) have shown that forecast accuracy is generally improved with increased model resolution. The study here will report on comparisons of temperature sounding data impacts for the GLAS model with two different grid resolutions: a coarse 4° lat. x 5° long. grid and a finer 2.5° lat. x 3° long. grid.

The influence of satellite temperature sounding data and increased horizontal resolution on GLAS model forecasts was evaluated by means of objective measures of forecast accuracy and subjective comparisons of prognostic charts for eleven different forecasts from the February 1976 Data Systems Test (DST) period. Table 1 (adapted from Ghil et al., 1979b) summarizes the effects of satellite data and model resolution for the same quantities and regions of verification, previously presented by Ghil et al. (1979a).

Table 1. Objective assessments of forecast impact.

Experiment	- Control	Impact (%) S_1	Impact (%) RMS	Statistical significance (average/standard error) S_1	Statistical significance (average/standard error) RMS
SAT coarse	NOSAT coarse	4.46	12.41	1.85	2.59
NOSAT fine	NOSAT coarse	5.86	7.30	1.62	1.35
SAT fine	NOSAT fine	4.49	7.98	1.40	1.71
SAT fine	NOSAT coarse	10.01	14.47	2.67	2.47

In the table, the results of the SAT experiment with the fine model were compared with those of the coarse NOSAT experiment and with those of the fine NOSAT experiment. The fine NOSAT experiment appears as a control and in a comparison versus the coarse NOSAT. It can be seen that the effects of increased resolution and satellite data both act in the direction of improving the forecast accuracy. The two effects appear to be nearly additive, as indicated by a comparison of the results in the last three rows of the table. In addition, the SAT experiment, with the fine model, consistently gave impacts that are significantly higher than those of the corresponding experiment with the coarse model, when measured against the common standard of the coarse NOSAT experiment (viz., the second and the last row of the table).

Tables 2 and 3 present the consensus of three experienced forecasters in their subjective assessment of the prognostic charts. During the evaluation, the forecasters had no knowledge of which prognostic charts were made from SAT or NOSAT initial conditions. Following Atkins and Jones (1975), each forecast was classified according to the following scale:

A - SAT signficantly better than NOSAT,

B - SAT better than NOSAT,

C - SAT and NOSAT of equal quality,

D - SAT worse than NOSAT,

E - SAT significantly worse than NOSAT.

Each forecaster performed his evaluation independently. This was followed by a discussion of the prognostic differences, after which the ratings were averaged to arrive at the consensus.

The results of the comparisons for the sea level pressure and 500 mb height fields generated from the GLAS 4° lat. x 5° long. model and verified over North America are presented in Table 1 (reproduced from Ghil et al., 1979a). From this table it can be seen that at sea level none of the prognostic charts have been classified as A or E and that an almost equal number of B and D marks have been assigned. Although no significant impact has occurred at this atmospheric level, a tendency for more beneficial impacts at 48, 60, and 72 h is evident. At 500 mb, two 72-h prognostic charts have been classified as A and there were no E marks. In addition, more than three times as many B than D marks have been assigned. Impacts at this level are most consistently beneficial at 60 and 72 h.

Table 2 presents the results of the synoptic evaluation of sounding data impact using the GLAS 2.5° x 3° model. This table shows that a more substantial beneficial impact from satellite sounding data has resulted from the use of the higher resolution model. No significant negative impacts have occurred while five sea level pressure and four 500 mb prognostic charts have been significantly improved. Once again the effect of satellite data is largest during the latter half of the forecast period.

Table 2. Results of a subjective assessment of SAT and NOSAT forecasts using the GLAS 4° x 5° model.

Category	12 h	24 h	36 h	48 h	60 h	72 h	Total
			Sea level pressure				
A	0	0	0	0	0	0	0
B	0	1	1	4	3	4	13
C	8	8	7	5	5	5	39
D	3	2	3	2	2	2	14
E	0	0	0	0	0	0	0
			500 mb geopotential height				
A	0	0	0	0	0	2	2
B	2	2	2	3	4	4	17
C	8	9	9	5	7	4	42
D	1	0	0	3	0	1	5
E	0	0	0	0	0	0	0

Table 3. Results of a subjective assessment of SAT and NOSAT forecasts using the GLAS 2.5° x 3° model.

Category	12 h	24 h	36 h	48 h	60 h	72 h	Total
			Sea level pressure				
A	0	0	0	1	2	2	5
B	0	2	2	2	1	3	10
C	11	8	7	7	5	5	43
D	0	1	2	1	3	1	8
E	0	0	0	0	0	0	0
			500 mb geopotential height				
A	0	0	0	1	1	2	4
B	0	1	3	2	3	2	11
C	11	9	7	7	6	7	47
D	0	1	1	1	1	0	4
E	0	0	0	0	0	0	0

Two cases of significant forecast impact, the forecasts from 19 and 11 February 1976, were selected for a more detailed subjective analysis. The 72-h sea level pressure prognoses from these cases are presented here as illustrations of the combined influence of satellite data and increased resolution.

72-h Forecast from 0000 GMT 19 February 1976

This was a case in which a significant improvement to the predicted displacement of an intense winter storm occurred in the latter part of the forecast period. The initial conditions for this forecast showed a moderately intense low pressure system, associated with an upper level short wave trough, located off the northwest coast of the U.S. As the system moved inland, a new low developed along an already existing stationary front and became the dominant feature by 1200 GMT on 19 February. During the next 24 h, the low moved southeastward and intensified, after which time it recurved and then accelerated toward the northeast. This cyclone was accompanied by heavy snow, blizzard, or near-blizzard conditions in Colorado, Kansas, Nebraska, Iowa, Michigan, and Wisconsin, and tornadoes or severe thunderstorms in Kansas, Oklahoma, Texas, Arkansas, Missouri, Illinois, Louisiana, and Mississippi. Most of the severe weather occurred toward the end of the forecast period after the recurvature of the cyclone to the northeast.

Figs. 1a and 1b depict the 72-h SAT and NOSAT sea level pressure prognoses for the 4° x 5° model, while the corresponding SAT and NOSAT prognoses for the 2.5° x 3° model are shown in Figs. 1c and 1d. The verifying analysis is shown in Fig. 1e. Comparison of these charts reveals little difference between the two 4° x 5° model forecasts, however, a very significant improvement in the predicted displacement of the surface low has resulted from the inclusion of satellite data in the 2.5° x 3° model. The high resolution SAT prediction indicated recurvature of the low to the northeast while the other predictions did not. As a result, there was a more than 1000 km reduction in the vector error of the predicted position.

Since most of the severe weather occurred in conjunction with the recurvature of the low, it is clear that significantly improved local weather forecasts could have resulted from the use of the high resolution SAT prognoses in this situation. To investigate this point further, the high resolution SAT and NOSAT predictions of local convective instability, and also the destabilization by differential equivalent potential temperature advection, were compared. It was found that there was a 51 percent reduction in the RMS errors of convective instability and a 22 percent reduction in RMS errors of differential advection, in the prediction which included satellite-sounding data.

72-h Forecast from 0000 GMT 11 February 1976

In this case, a weak cyclone formed along a stationary front in southwest Canada, moved southeastward while intensifying during the first 40 h of the period, and then recurved to the east northeast.

Figs. 2a and 2b depict the 72-h SAT and NOSAT sea level pressure prognoses for the 4° x 5° model, while the corresponding SAT and NOSAT prognoses for the 2.5° x 3° model are presented in Figs. 2c and 2d. Fig. 2e shows the

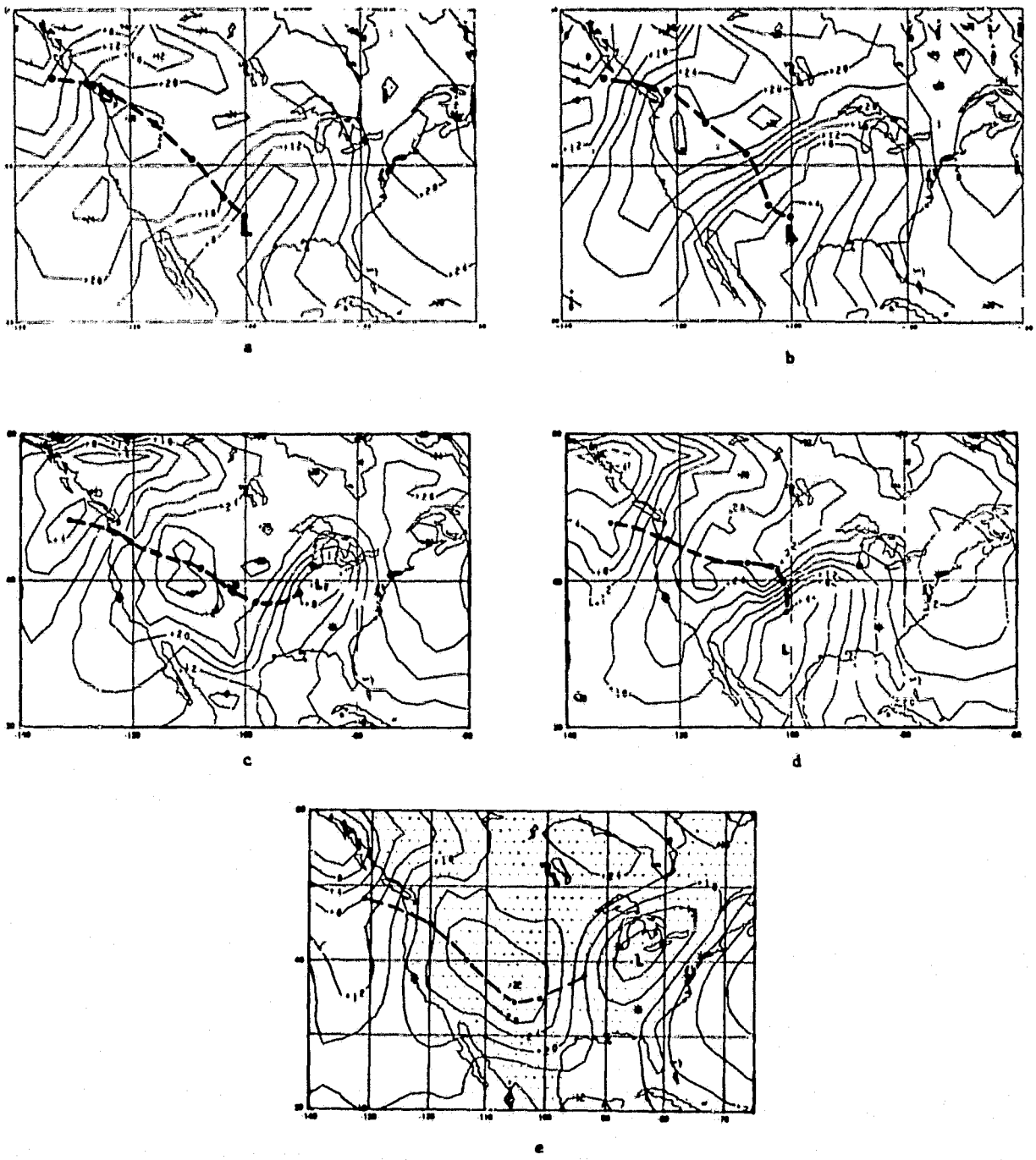

Fig. 1. The sea level pressure fields on 0000 GMT 22 February 1976:

a. the 72-h forecast from the 4° x 5° GLAS model with SAT initial conditions,
b. the corresponding NOSAT forecast using the 4° x 5° model,
c. the corresponding SAT forecast using the 2.5° x 3° GLAS model;
d. the corresponding NOSAT forecast using the 2.5° x 3° GLAS model,
e. the verifying NMC analysis. Dots represent past positions of the cyclone center at 12-h intervals beginning 0000 GMT 19 February 1976.

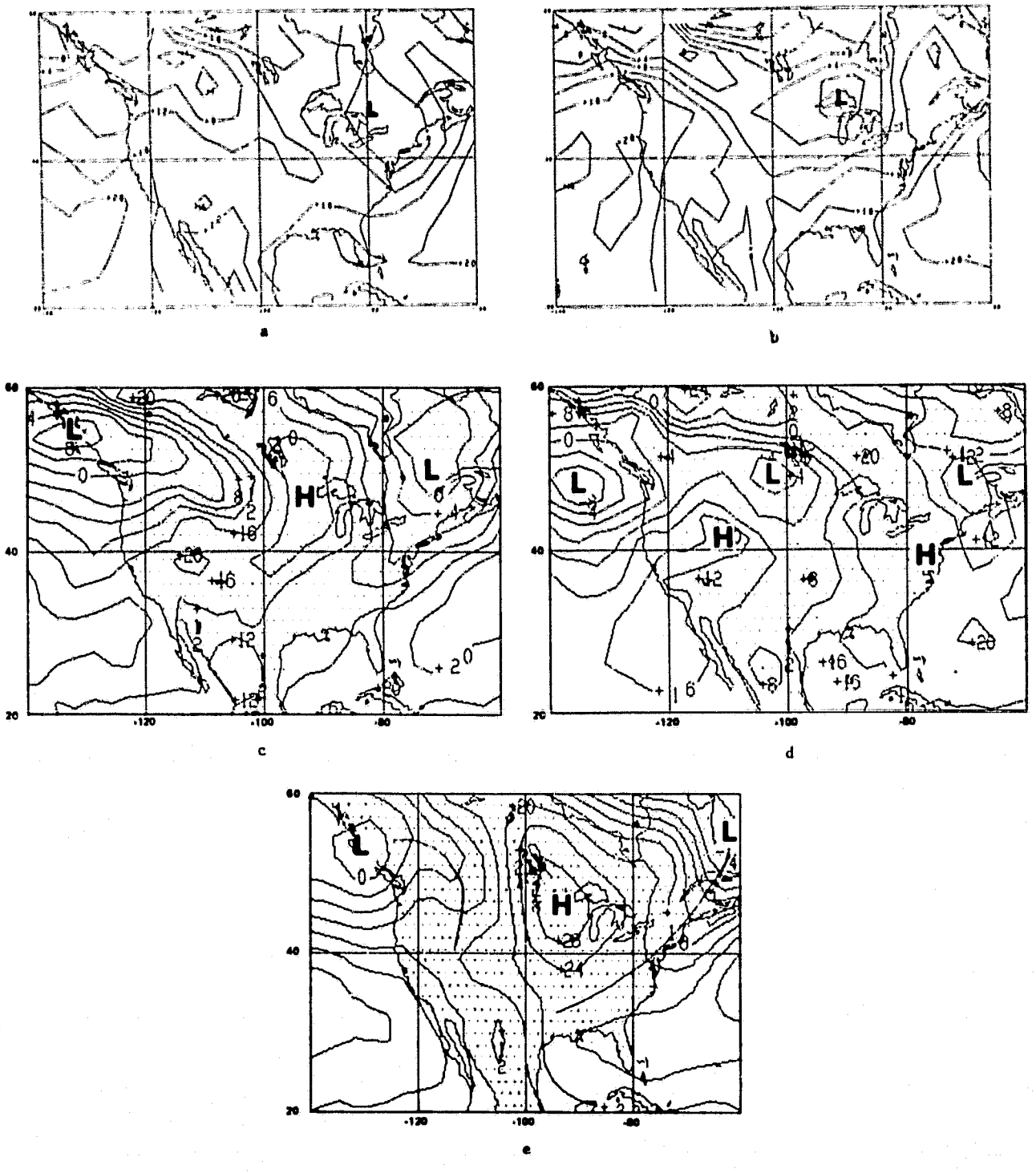

Fig. 2. The sea level pressure fields on 0000 GMT 14 February 1976:

a. the 72-h forecast from the 4° x 5° model with SAT initial conditions,
b. the corresponding NOSAT forecast using the 4° x 5° GLAS model;
c. the corresponding SAT forecast using the 2.5° x 3° GLAS model;
d. the corresponding NOSAT forecast using the 2.5° x 3° GLAS model;
e. the verifying NMC analysis.

verifying analysis. Comparison of these figures reveals that an improvement in the predicted displacement of the surface low has resulted from the inclusion of satellite data in the 4° x 5° model, but a much larger improvement has occurred in the 2.5° x 3° model. The high resolution SAT prognosis (Fig. 2c) is substantially better than the NOSAT (Fig. 2d) in its prediction of the cyclonic circulation over southeastern Canada and the northeastern U.S., as well as the anticyclone near the Great Lakes and the pressure trough which extends southeastward from southwest Canada.

References

Atkins, M. J., and M. V. Jones, 1975: An experiment to determine the value of satellite infrared spectrometer (SIRS) data in numerical forecasting. Meteor. Mag., 104, 125-142.

Desmarais, A., S. Tracton, R. McPherson, and R. Van Haaren, 1978: The NMC report on the Data Systems Test. NOAA-ST 78-218, National Meteorological Center, NOAA/NWS, 331 pp.

Druyan, L. M., T. Ben-Amram, Z. Alperson, and G. Ohring, 1978: The impact of VTPR data on numerical forecasts of the Israel Meteorological Service. Mon. Wea. Rev., 106, 859-869.

Ghil, M., M. Halem, and R. Atlas, 1979a: Time-continuous assimilation of remote-sounding data and its effect on weather forecasting. Mon. Wea. Rev., 107, 140-171.

_____, _____, and _____, 1979b: Effects of sounding temperature assimilation on weather forecasting: model dependence studies. Remote Sounding of the Atmos. from Space, H. J. Bolle, ed., Permagon Press, Oxford and New York, 21-25.

Quirk, W. J., and R. Atlas, 1977: The effect of increased horizontal resolution on synoptic forecasts with the GISS model of the global atmosphere. Conf. Papers, Third Conf. on Numerical Weather Prediction, 92-99.

Robert, A., 1976: Sensitivity experiments for the development of NWP models. Proc. of the (Eleventh) Stanstead Seminar, Publ. in Meteorology No. 114, McGill University, Montreal, Canada, 68-81.

Somerville, R. C. J., P. H. Stone, M. Halem, J. E. Hansen, J. S. Hogan, L. M. Druyan, G. Russell, A. S. Lacis, W. J. Quirk, and J. Tenenbaum, 1974: The GISS model of the global atmosphere. J. Atmos. Sci., 31, 84-117.

Stone, P. H., S. Chow, and W. J. Quirk, 1977: The July climate and a comparison of the January and July climates simulated by the GISS general circulation model. Mon. Wea. Rev., 105, 170-194.

Williamson, D. L., 1978: The relative importance of resolution, accuracy, and diffusion in short-range forecasts with the NCAR global circulation model. Mon. Wea. Rev., 106, 69-88.

A CASE STUDY OF THE GROWTH OF PROGNOSTIC DIFFERENCES BETWEEN GLAS MODEL FORECASTS FROM SAT AND NOSAT INITIAL CONDITIONS

(R. Atlas, R. Rosenberg, and S. Palm)

The high resolution GLAS model forecasts from 0000 GMT 19 February 1976, presented by Atlas et al. (1980), represent a case in which a significant beneficial impact resulted from the assimilation of satellite sounding data. Comparison of the 72-h forecasts from SAT and NOSAT initial conditions (Figs. 1c and 1d of Atlas et al., 1980) revealed that the predicted displacement of an intense surface low was similar for the first 36 to 48 h of the forecast, but then diverged rapidly. A study has been conducted to determine: (1) why the surface lows in the two forecasts suddenly diverge and move differently during the latter half of the forecast and (2) if differences in the upper level forcing for the cyclone at the time the two forecasts diverge can be traced to specific initial state differences between the SAT and NOSAT systems.

The initial sea level pressure and 1000-500 mb thickness, and 300 mb height and vorticity analyses, for the SAT and NOSAT forecasts from 19 February are displayed in Figs. 1 and 2. Comparison of these figures reveals no substantial difference in the initial representation of the surface low located at 46N, 132W, off the northwest coast of the U.S., although a modification of the 1000-500 mb thickness pattern has occurred. This results in an enhanced variation of thermal vorticity and thermal advection across the low center in the SAT case. At 300 mb, the assimilation of satellite sounding data has resulted in an intensification of the upper level vorticity maximum associated with the surface low and an elimination of the vorticity trough extending southward from this maximum. The satellite data has increased the northerly component of the wind and the cyclonic shear of the westerly component of the wind from 40N to 47N to the immediate west of the upper level trough. It also increased the anticyclonic shear of the westerly wind below 40N (wind component charts not shown). This results in a northward shift of the upper level vorticity advection areas in this region, such that there is stronger positive vorticity advection and positive vorticity tendencies to the east of the 300 mb vorticity maximum, and stronger negative vorticity advection and negative vorticity tendencies to the west of the maximum in the SAT case. This modification of the vorticity advection by satellite sounding data was found to be in agreement with satellite cloud imagery (see Hales, 1979, for discussion of technique). Additional modifications to the initial state by the assimilation of satellite data have been considered in this study but will not be described here.

Figs. 3-10 display the evolution of the sea level pressure, 1000-500 mb thickness, and 300 mb height and vorticity patterns at 12-h intervals for the first 48 h of both the SAT and NOSAT predictions. During the first 12 h of the forecast, both SAT and NOSAT move the surface low inland to 46N, 123W (Fig. 3). The SAT surface low has intensified while the NOSAT low has filled slightly. However, the SAT thickness gradient has weakened relative to the NOSAT, and there is now a larger variation of thermal vorticity and

stronger thermal vorticity advection across the low in the NOSAT case. At 300 mb, a small difference in the movement of the height trough and vorticity maximum has occurred (Fig. 4). The NOSAT vorticity maximum is located at 44N, 128W, while the SAT vorticity maximum has moved about 2.5° longitude further downstream. A comparison of the vorticity advection patterns and tendencies at 2-h intervals throughout this period indicated that the initial tendency for greater movement in the SAT system has been maintained.

During the next 24 h of the forecast, this trend continues and slightly larger differences between the SAT and NOSAT systems begin to develop. At 0000 GMT 20 February (Figs. 5 and 6), the NOSAT system has forecast the surface low to deepen slightly and move to 41.3N, 108W, and the 300 mb vorticity maximum to move to 42N, 123W. SAT forecasts a less organized surface low with three centers evident at this time but has maintained a somewhat stronger pressure gradient than the NOSAT to the west and southwest of the southernmost low center. SAT forecasts the 300 mb vorticity maximum to move to 41N, 117W, 5° longitude further downstream than the NOSAT maximum. However, in both forecasts, the strongest positive vorticity advection is to the southwest of the surface low position. By 1200 GMT 20 February, the NOSAT surface low is located at 41.2N, 105W, while SAT forecasts two low centers: one at 41.2N, 102W; the other at 36.2N, 102W (Fig. 7). Substantial differences in the low level thermal advection patterns are also evident at this time. In the NOSAT case, weak cold advection exists directly behind the surface low, with the strongest cold advection located further southwest beneath and slightly to the west of the upper level trough. This contributes to the deepening and slow rate of movement of the upper level trough in the NOSAT prediction. SAT predicts substantially stronger cold advection directly behind the surface low.

The relationship of low level thermal advection to the movement of surface lows is well known (Sutcliffe, 1947; Petterssen, 1954). Warm advection contributes to falling pressure and the generation of cyclonic vorticity in advance of cyclones while cold advection contributes to rising pressure and the destruction of cyclonic vorticity to the rear of cyclones. Thus, the gradient of thickness advection across a cyclone center is an important indicator of the rate of movement of that cyclone. In this case, the differences in the gradient of thickness advection that are established after 36 h are primarily associated with the differing rates of movement of the upper level vorticity maximum. Because of the different movements of the vorticity maximum relative to the surface low, there was an intensification of the pressure gradient to the southwest of the low center in the SAT forecast, while a broad area of surface pressure falls associated with the positive vorticity advection aloft weakened the pressure gradient to the immediate southwest of the surface low in the NOSAT forecast.

This effect amplified during the next 12 h in such a way that by 0000 GMT 21 February the gradient of thickness advection across the low center is nearly twice as strong in the SAT forecast as in the NOSAT. At this time, the surface low is located at 36.5N, 102W, in the NOSAT and 36N, 99W, in the SAT (Fig. 9). The 300 mb vorticity maximum is located at 36.2N, 111W, in the NOSAT and 38N, 102W, in the SAT (Fig. 10). The differing phase relationships between the upper level vorticity maximum and the surface low coupled with

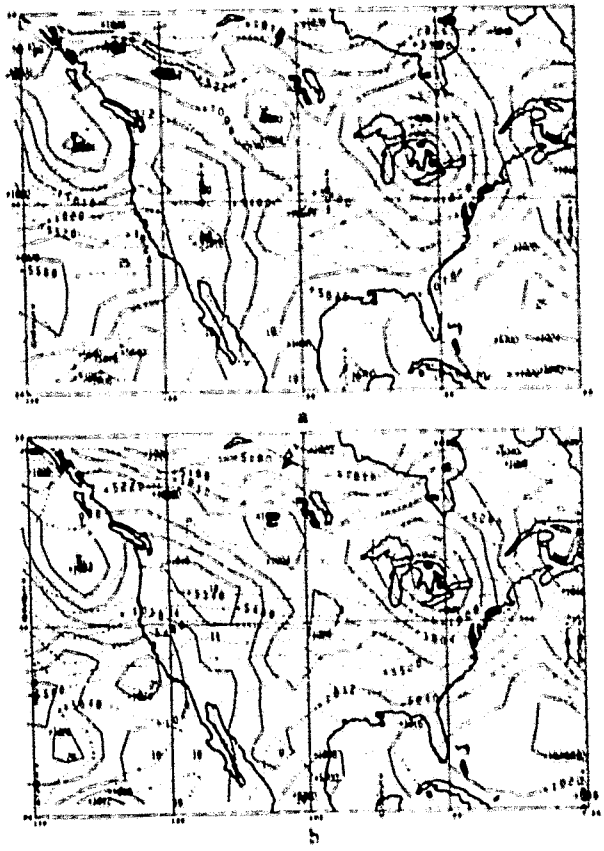

Fig. 1. SAT (a) and NOSAT (b) sea level pressure (solid lines) and 1000-500 mb thickness (dashed lines) for 0000 GMT 19 February 1976.

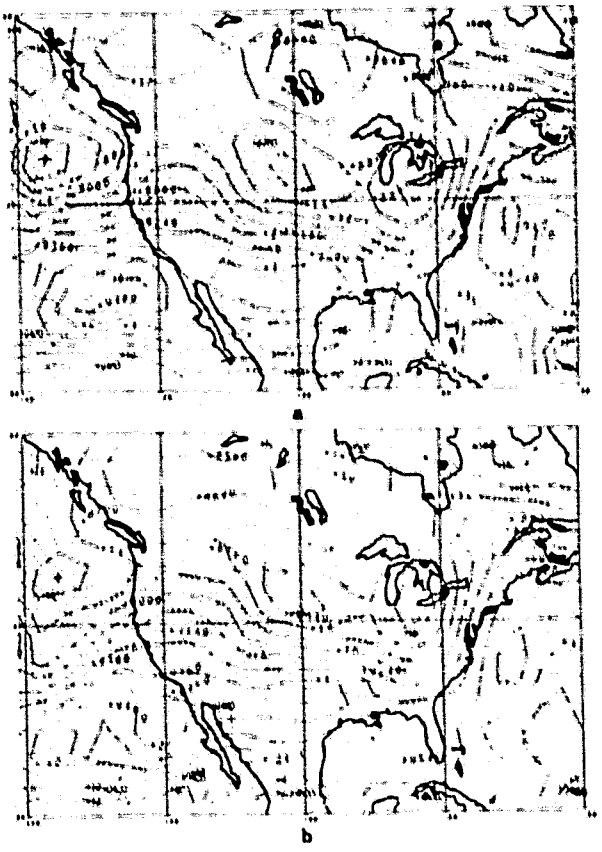

Fig. 2. SAT (a) and NOSAT (b) 300 mb absolute vorticity (solid lines) and 300 mb geopotential height (dashed lines) for 0000 GMT 19 February 1976.

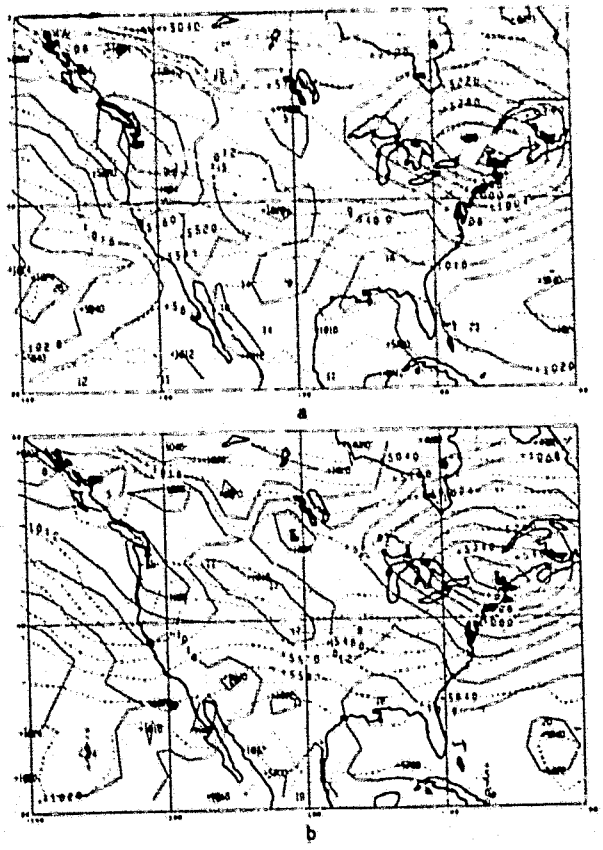

Fig. 3. As in Fig. 1 except for 1200 GMT 19 February 1976.

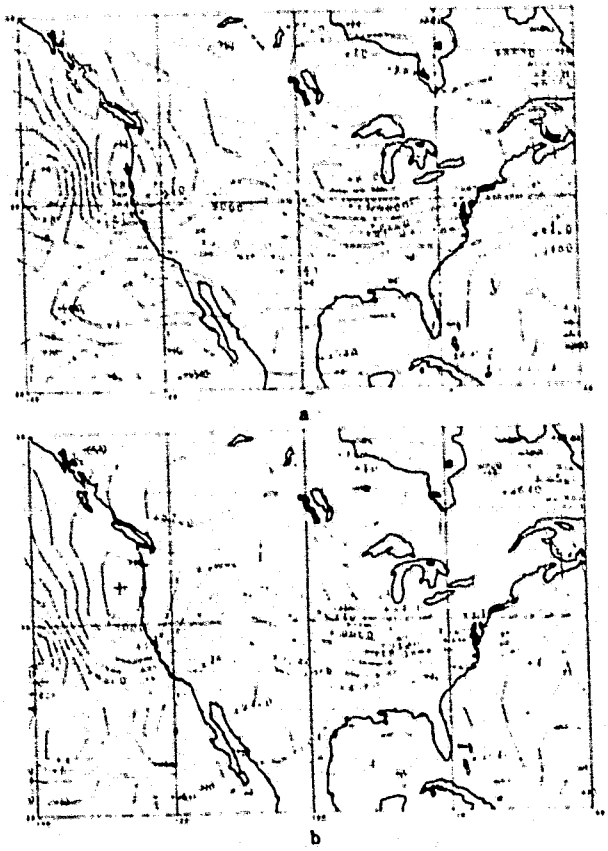

Fig. 4. As in Fig. 2 except for 1200 GMT 19 February 1976

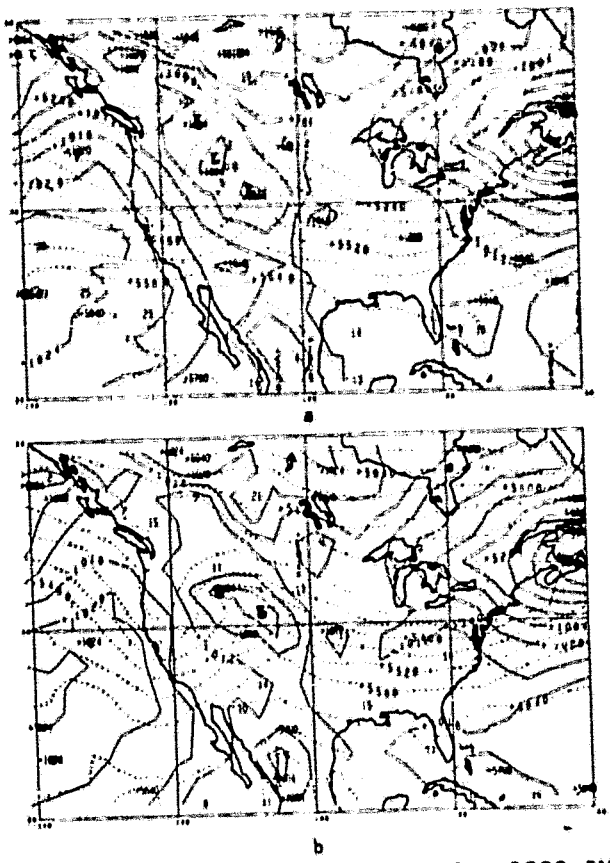

Fig. 5. As in Fig. 1 except for 0000 GMT 20 February 1976.

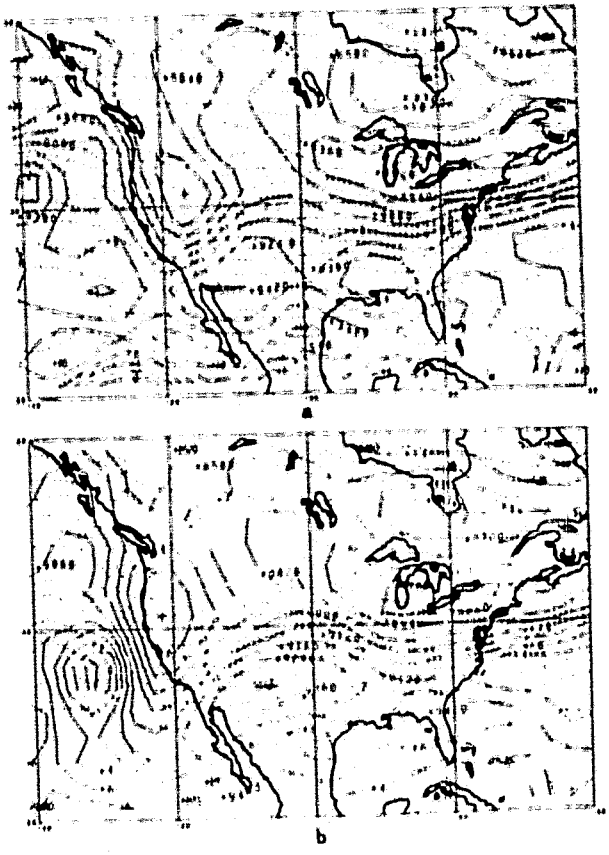

Fig. 6. As in Fig. 2 except for 0000 GMT 20 February 1976.

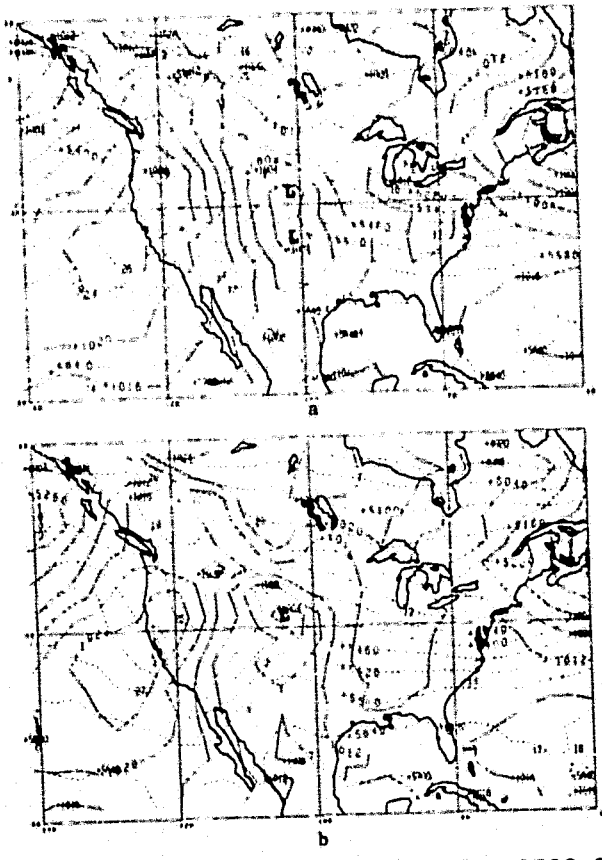

Fig. 7. As in Fig. 1 except for 1200 GMT 20 February 1976.

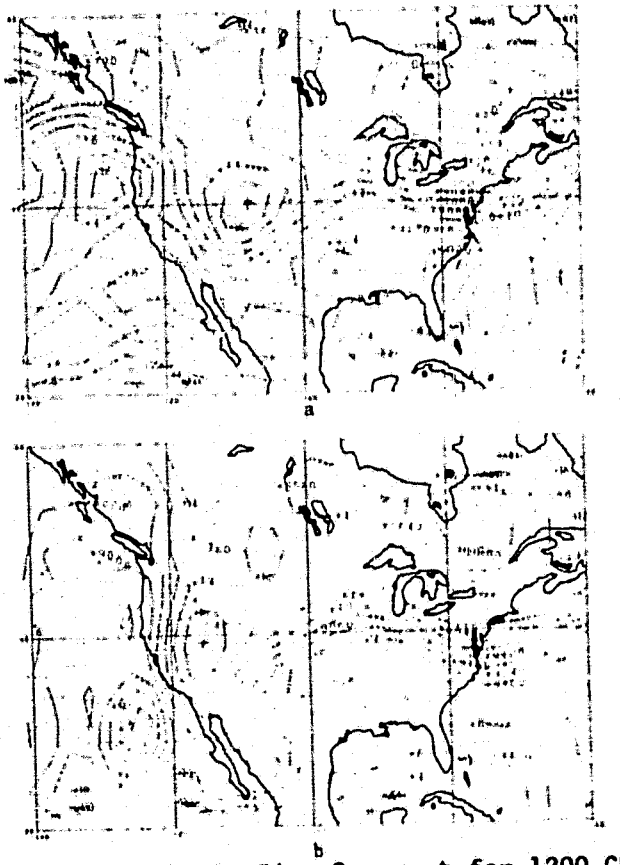

Fig. 8. As in Fig. 2 except for 1200 GMT 20 February 1976.

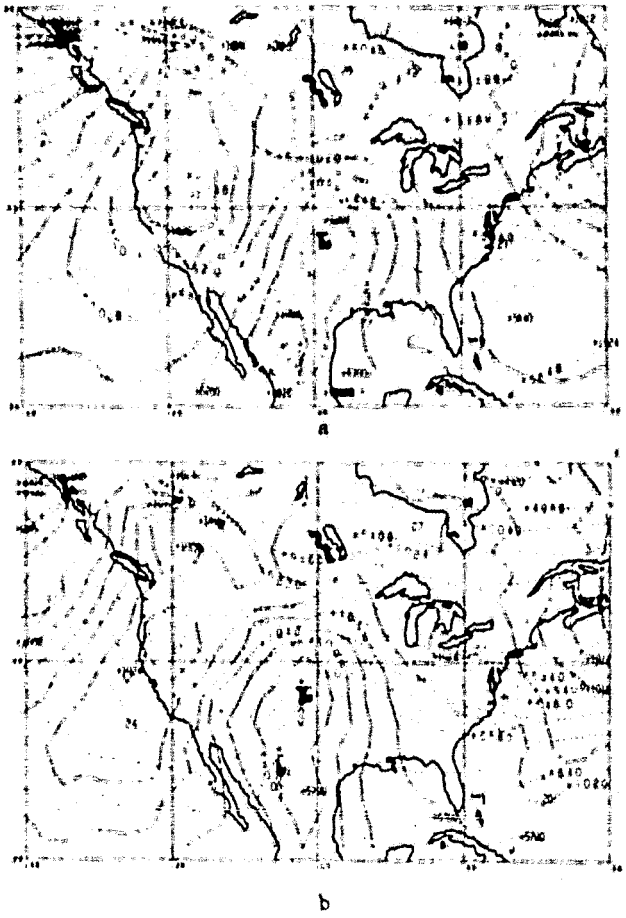

Fig. 9. As in Fig. 1 except for 0000 GMT 21 February 1976.

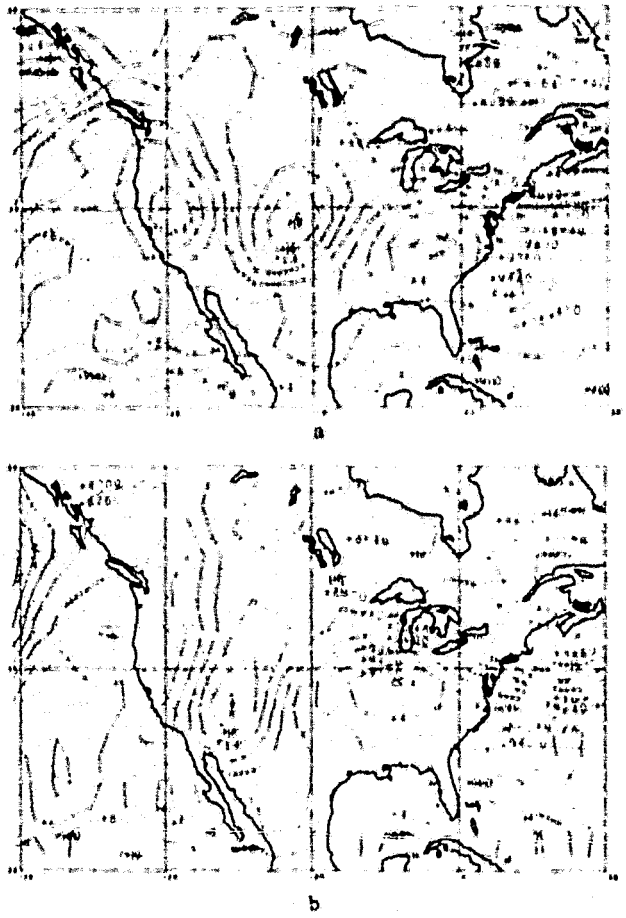

Fig. 10. As in Fig. 2 except for 0000 GMT 21 February 1976.

the differing thickness advection patterns result in the diverging paths of the surface low throughout the remainder of the forecast. In the SAT case, there is strong positive vorticity advection and warm advection to the east and northeast of the surface low and weaker vorticity advection coupled with strong cold advection to the immediate west and southwest of the surface low. This results in a strong isallobaric gradient across the low center such that recurvature to the east northeast occurs. In the NOSAT case, weak positive vorticity advection is coupled with warm advection to the northeast of the surface low while strong positive vorticity advection is coupled with weak cold advection to the immediate west and southwest of the surface low. As a result, the NOSAT surface low becomes "locked in" and does not progress eastward after this time.

References

Atlas, R., M. Halem, and M. Ghil, 1980: The combined influence of satellite temperature sounding data and increased horizontal resolution on GLAS model forecasts. NASA Tech. Memo. (herein), Atmos. and Oceano. Res. Rev.-1979, NASA Goddard Space Flight Center, Greenbelt, Maryland.

Hales, J. E., 1979: A subjective assessment of model initial conditions using satellite imagery. Bull. Amer. Meteor. Soc., 60, 206-211.

Petterssen, S., 1954: A general survey of the factors influencing development at sea level. J. Meteor., 12, 36-42.

Sutcliffe, R. E., 1947: A contribution to the problem of development. Quart. J. R. Meteor. Soc., 73, 370-383.

SYNOPTIC EVALUATION OF GLAS AND NMC HIGH RESOLUTION FORECASTS FROM 19 AND 11 FEBRUARY 1976

(R. Atlas)

The synoptic evaluation of the impact of satellite temperature sounding data on eleven high (~280 km) resolution GLAS model forecasts (Atlas, et al., 1980) revealed no examples of significant negative impacts and two cases in which major improvements to sea level pressure forecasts occurred: the 72-h forecasts from 0000 GMT 19 and 11 February 1976. In this paper, the GLAS SAT predictions for both of these cases are compared with the corresponding NOSAT forecasts from the National Meteorological Center (NMC) 7-level model. This model, which has a horizontal resolution of 190.5 km, has shown considerable improvement over the coarser mesh 6-level model and has been adopted by NMC as their operational forecasting model. Comparison of the GLAS SAT forecasts with the NMC high resolution NOSAT forecasts should provide additional evidence concerning the meteorological significance of the GLAS sounding data impact results.

Forecasts from 0000 GMT 19 February 1976

Figs. 1-6 depict the NMC 7-level NOSAT and GLAS SAT 72-h sea level pressure (solid lines) and 1000-500 mb thickness (dashed lines) forecasts and corresponding verification at 12-h intervals. Comparison of the two forecasts reveals that the GLAS SAT prediction of the cyclone's 72-h evolution is signficantly better than the NMC NOSAT prediction. At 12 h (Fig. 1), the error of the cyclone's position is reduced by 51 percent and the cyclone's central pressure error is reduced by 66 percent. At 24 h (Fig. 2), no cyclone is evident in the NMC prognosis. At 36 h (Fig. 3), the differences between the two sea level pressure forecasts are smaller. However, a more intense cyclonic circulation is predicted by the GLAS SAT, and the greater amplitude of the associated thickness pattern in the SAT forecast is also in better agreement with the analysis. At 48 h (Fig. 4), just prior to the outbreak of severe thunderstorms and tornadoes, major differences between the GLAS SAT and NMC NOSAT prognosis are evident. The structure, intensity, and position of the SAT cyclone is substantially better than in the NMC NOSAT. The position error has been reduced by 84 percent; the reduction of central pressure error is 45 percent. This trend continues to 60 h (Fig. 5), where the position error is reduced by 88 percent and the central pressure error by 46 percent. At 72 h (Fig. 6), there is a 34 percent reduction in position error and 75 percent reduction in central pressure error.

To investigate the effect of these differences further, the Computerized Severe Storm Model (CSSM), developed by Atlas (1978), has been applied to both the GLAS SAT and NMC NOSAT predictions. The CSSM consists of an objective procedure for computing and combining specific measures of instability and destabilization to yield a prediction of high-moderate, low, or neglible potential for severe local storm development. The SAT prediction of high potential accounted for 70 percent of the severe thunderstorm and tornado occurrences while the NMC NOSAT CSSM did not predict any areas of

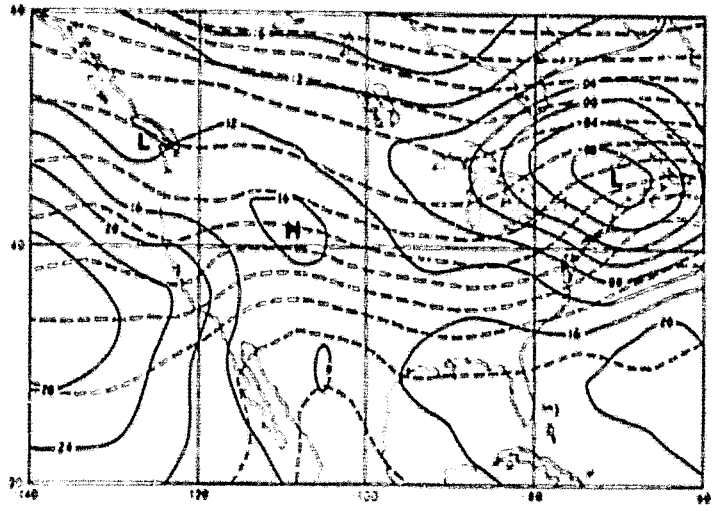

a. 12-h NMC 7L NOSAT forecast

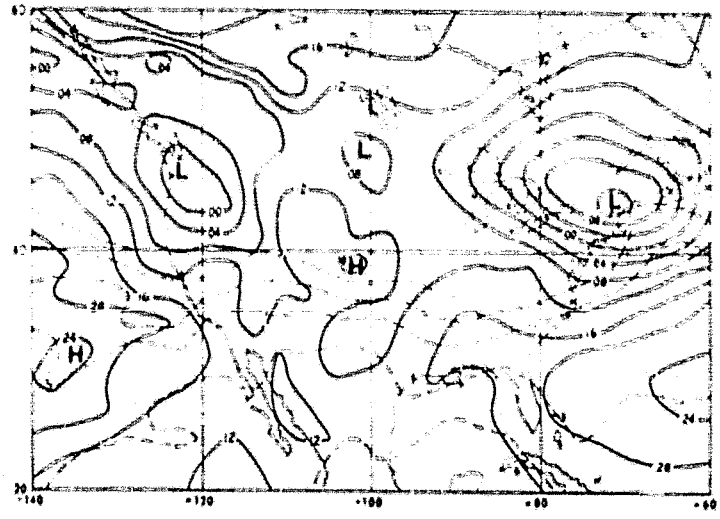

b. 12-h GLAS SAT forecast

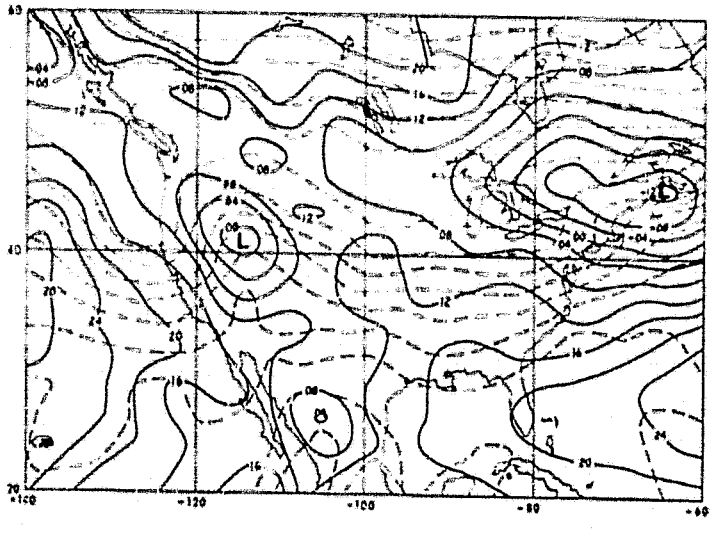

c. Analysis

Fig. 1. Sea level pressure/1000-500 mb thickness maps for 1200 GMT 19 February 1976.

high potential. The differences between the two CSSM forecasts were due primarily to a substantially improved prediction of differential equivalent potential temperature advection and convective instability in the SAT system.

Finally, differences between the GLAS SAT and NMC NOSAT initial states have been examined by means of horizontal maps and vertical cross sections of a variety of primary variables and derived quantities. Fig. 7 presents cross sections of absolute vorticity in relation to the initial position of the surface low. In the NMC NOSAT initial state, the upper level vorticity maximum is located directly above the surface low, whereas in the GLAS SAT there is a substantial slope of the vorticity maximum with height. The surface low in the SAT analysis is baroclinically unstable and intensifies as it moves inland during the first 12 h of the forecast, whereas the same low fills in the NMC prediction for the same period.

Forecasts from 0000 GMT 11 February 1976

Fig. 8 depicts the NMC 7-level NOSAT and GLAS SAT 72-h sea level pressure (solid lines) and 1000-500 mb thickness (dashed lines) forecasts and corresponding verification. The 24- and 48-h predictions (not shown) are contained in Atlas (1979).

At 24 h, there has been a 66 percent reduction of position error and an 87 percent reduction of central pressure error of the cyclone located in southwest Canada. Similarly, at 48 h, there has been a 76 percent reduction of position error and a 25 percent reduction of central pressure error of this cyclone, now centered near the Great Lakes. The position and orientation of the pressure trough extending southwestward from this cyclone, and the position of the anticyclone located off the east coast of the U.S. are better forecast by the GLAS SAT. In addition, a spurious cyclone, forecast by the NMC NOSAT to be over southwest Canada and the northwestern U.S., does not appear in the GLAS SAT. At 72 h, the GLAS SAT is significantly better than the NMC NOSAT in its prediction of the cyclonic circulation over southeastern Canada and the northeastern U.S., the anticyclone over the Midwest, the pressure trough extending southeastward from southwest Canada, and the shallow pressure troughing off the west coast of the U.S. The NMC NOSAT is slightly better in its prediction of the cyclone located off the northwest coast of the U.S. and also has a 26 percent smaller position error of the cyclone now located in eastern Canada. However, the central pressure error of this cyclone has been reduced by 53 percent in the GLAS SAT.

Two cases where NMC's operational model in 1976 had serious difficulties in foreasting for the U.S. have been examined. The GLAS model, when utilizing initial conditions which included satellite sounding data, was able to significantly improve upon the current operational model's predictions. Satellite temperature soundings appear to have potential to correct gross analysis errors which infrequently occur in the operational NMC system in data sparse regions.

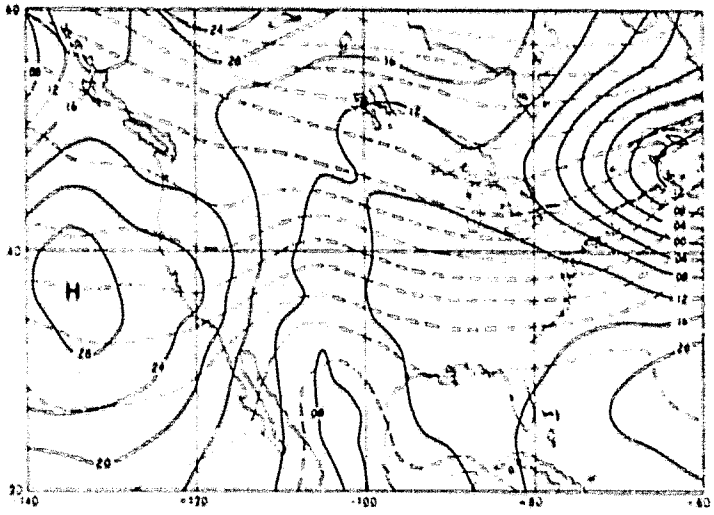

a. 24-h NMC 7L NOSAT forecast

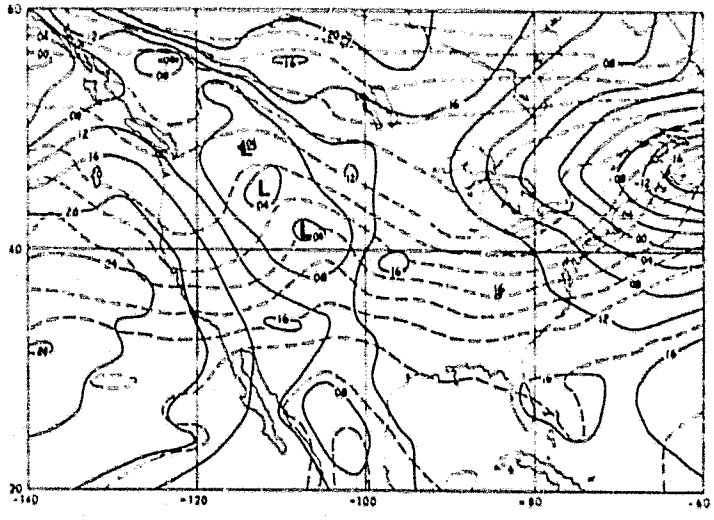

b. 24-h GLAS SAT forecast

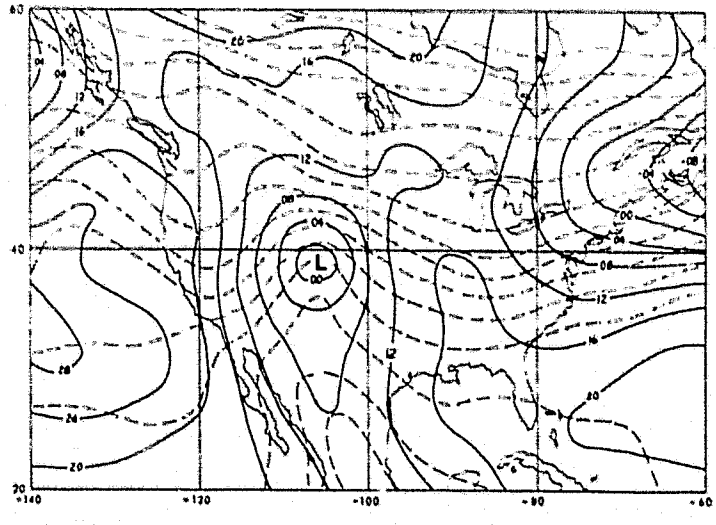

c. Analysis

Fig. 2. As in Fig. 1 except for 0000 GMT 20 February 1976.

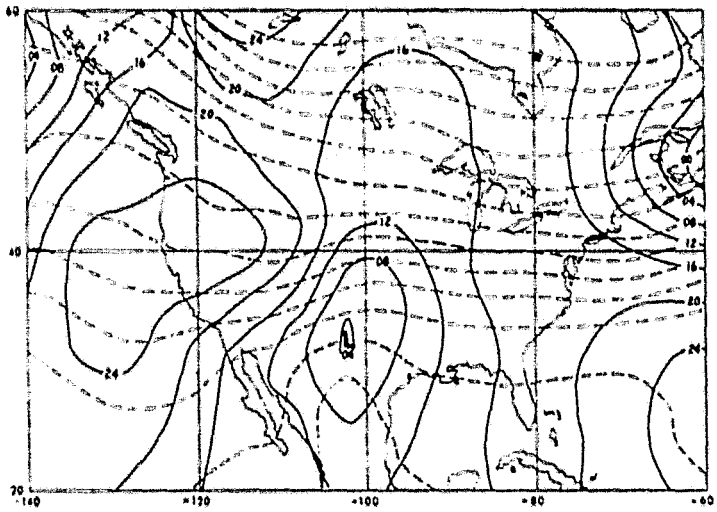

a. 36-h NMC 7L NOSAT forecast

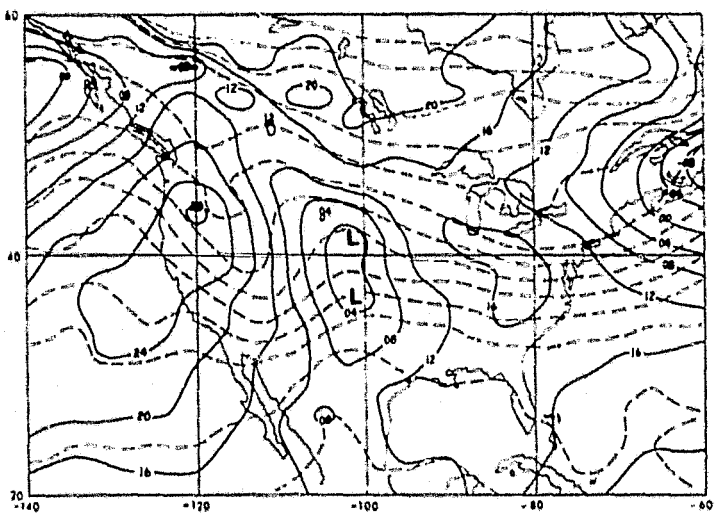

b. 36-h GLAS SAT forecast

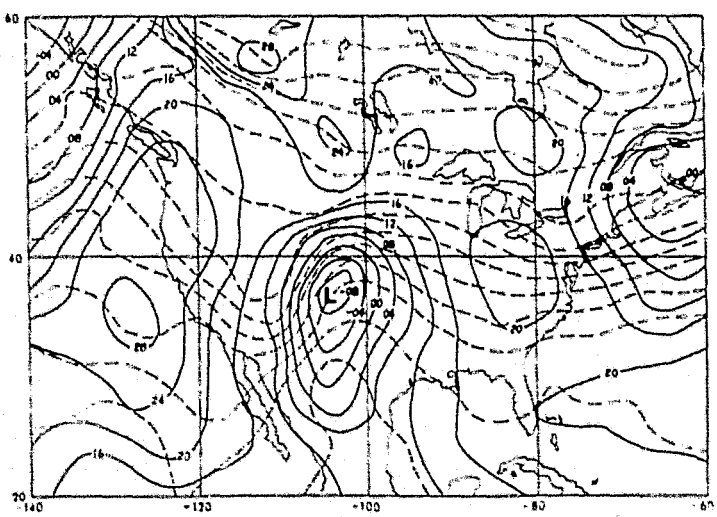

c. Analysis

Fig. 3. As in Fig. 1 except for 1200 GMT 20 February 1976

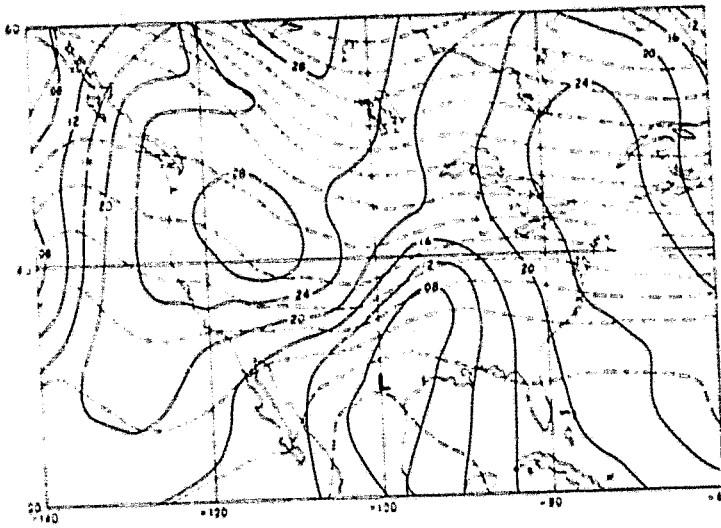

a. 48-h NMC 7L NOSAT forecast

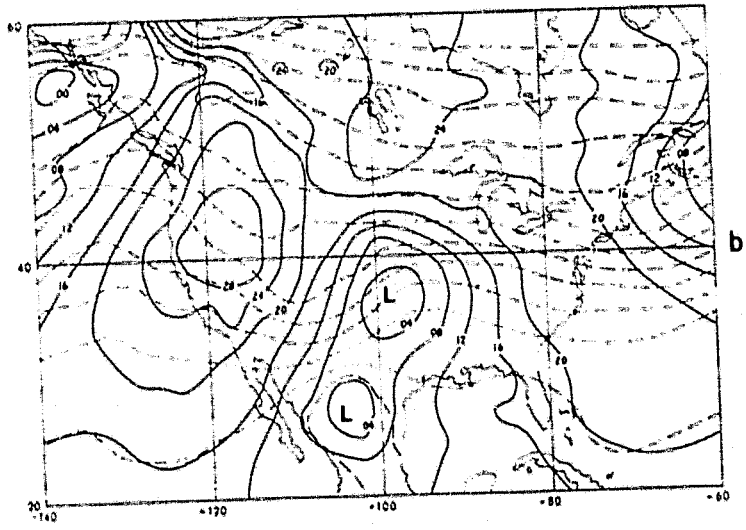

b. 48-h GLAS SAT forecast

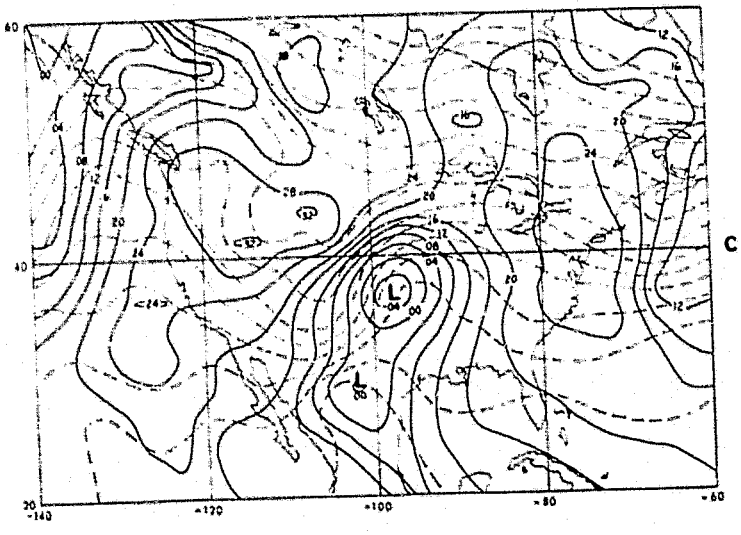

c. Analysis

Fig. 4. As in Fig. 1 except for 0000 GMT 21 February 1976.

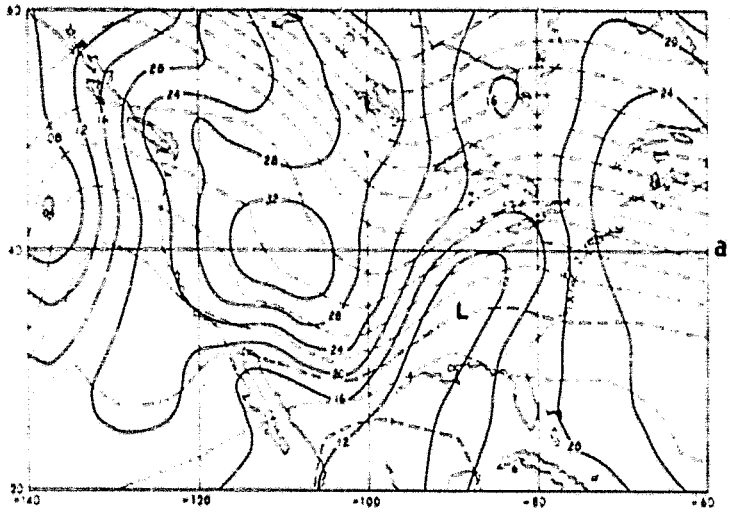

a. 60-h NMC 7L NOSAT forecast

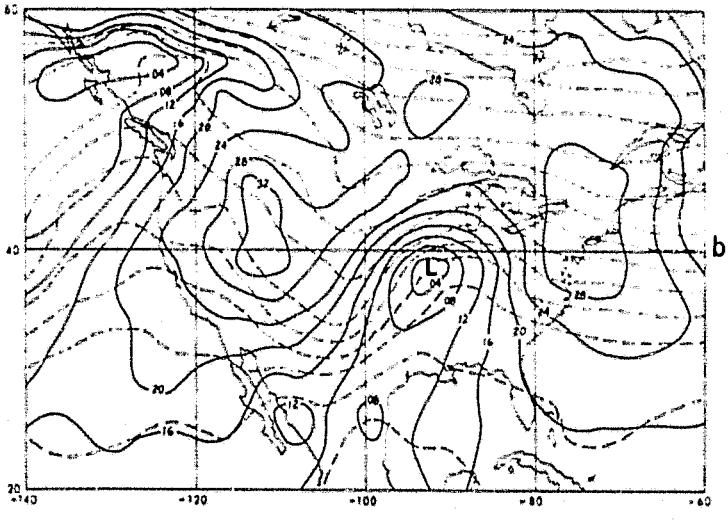

b. 60-h GLAS SAT forecast

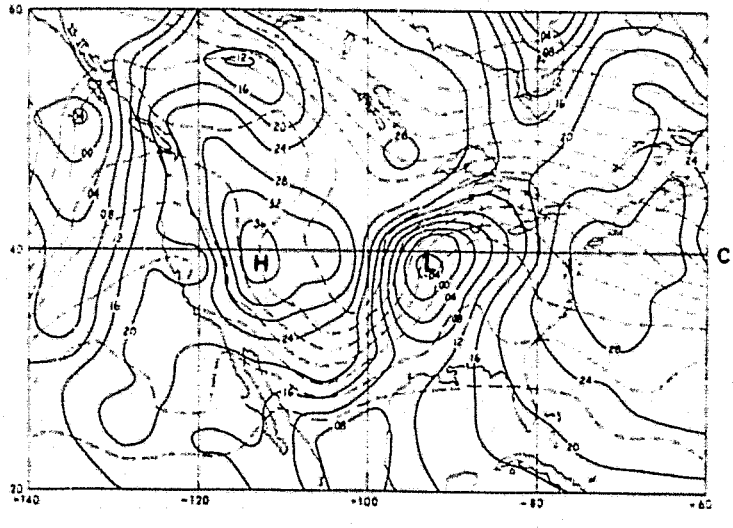

c. Analysis

Fig. 5. As in Fig. 1 except for 1200 GMT 21 February 1976.

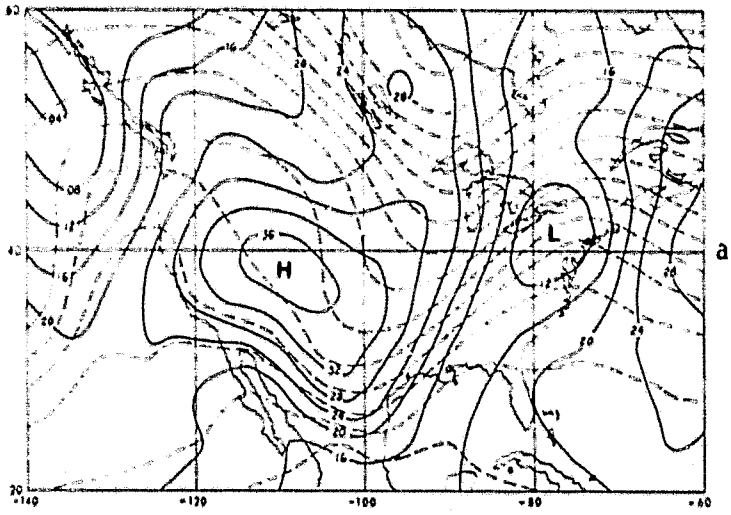

a. 72-h NMC 7L NOSAT forecast

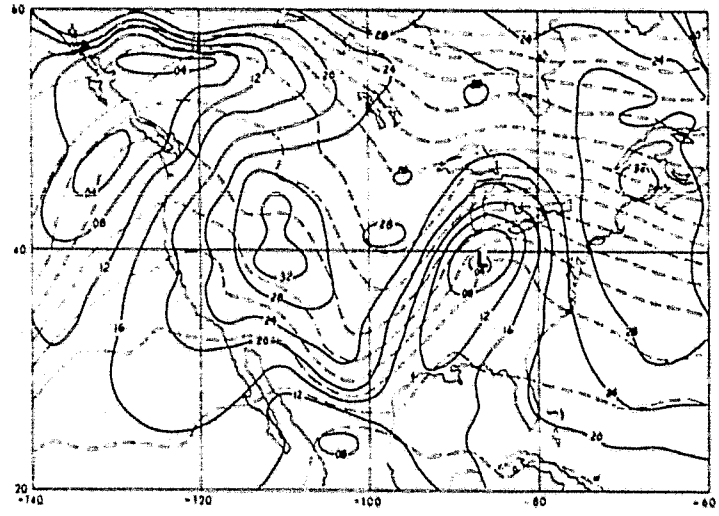

b. 72-h GLAS SAT forecast

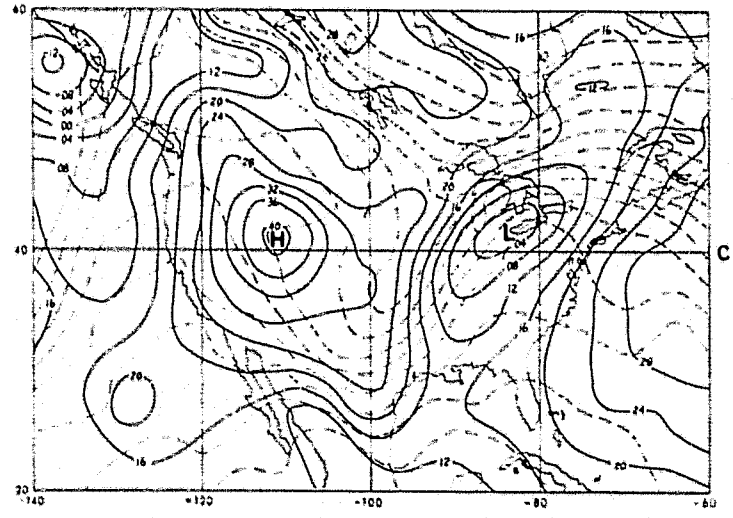

c. Analysis

Fig. 6. As in Fig. 1 except for 0000 GMT 22 February 1976.

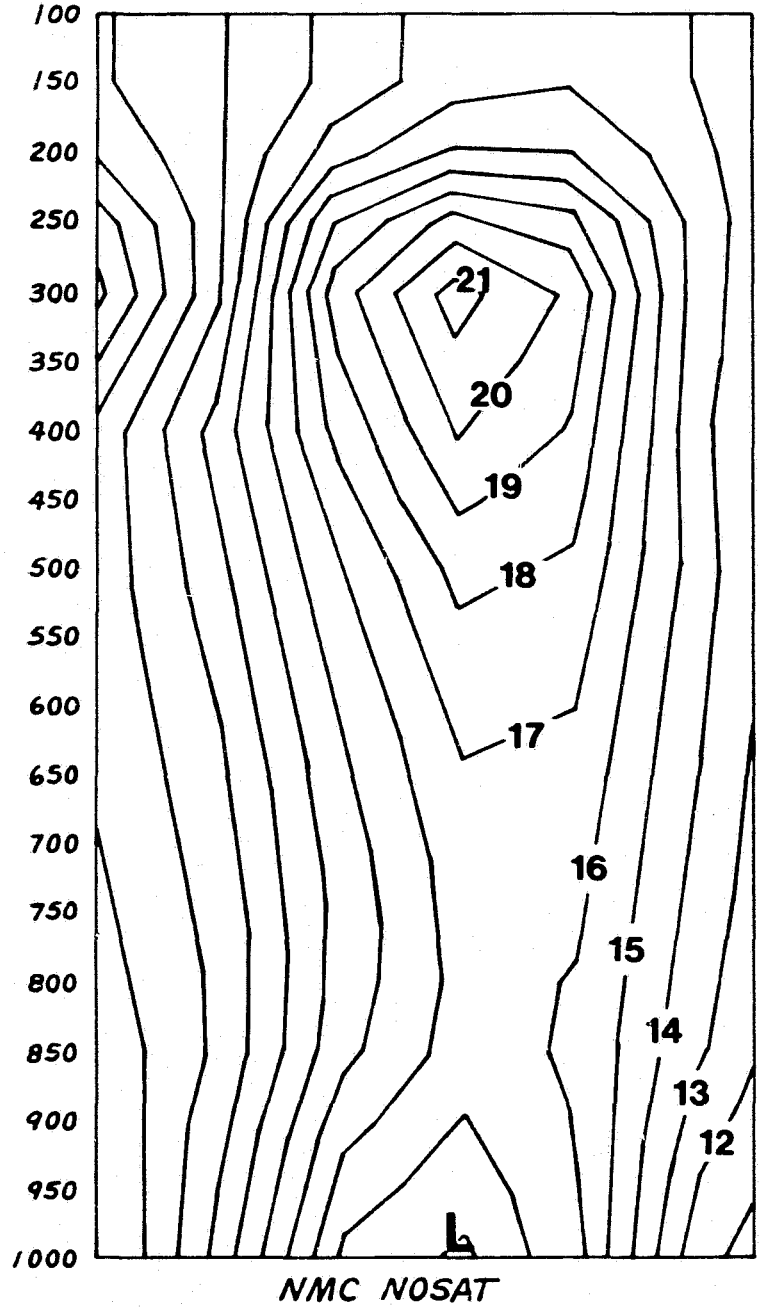

Fig. 7a. NMC NOSAT vertical cross section of absolute vorticity above surface low on 0000 GMT

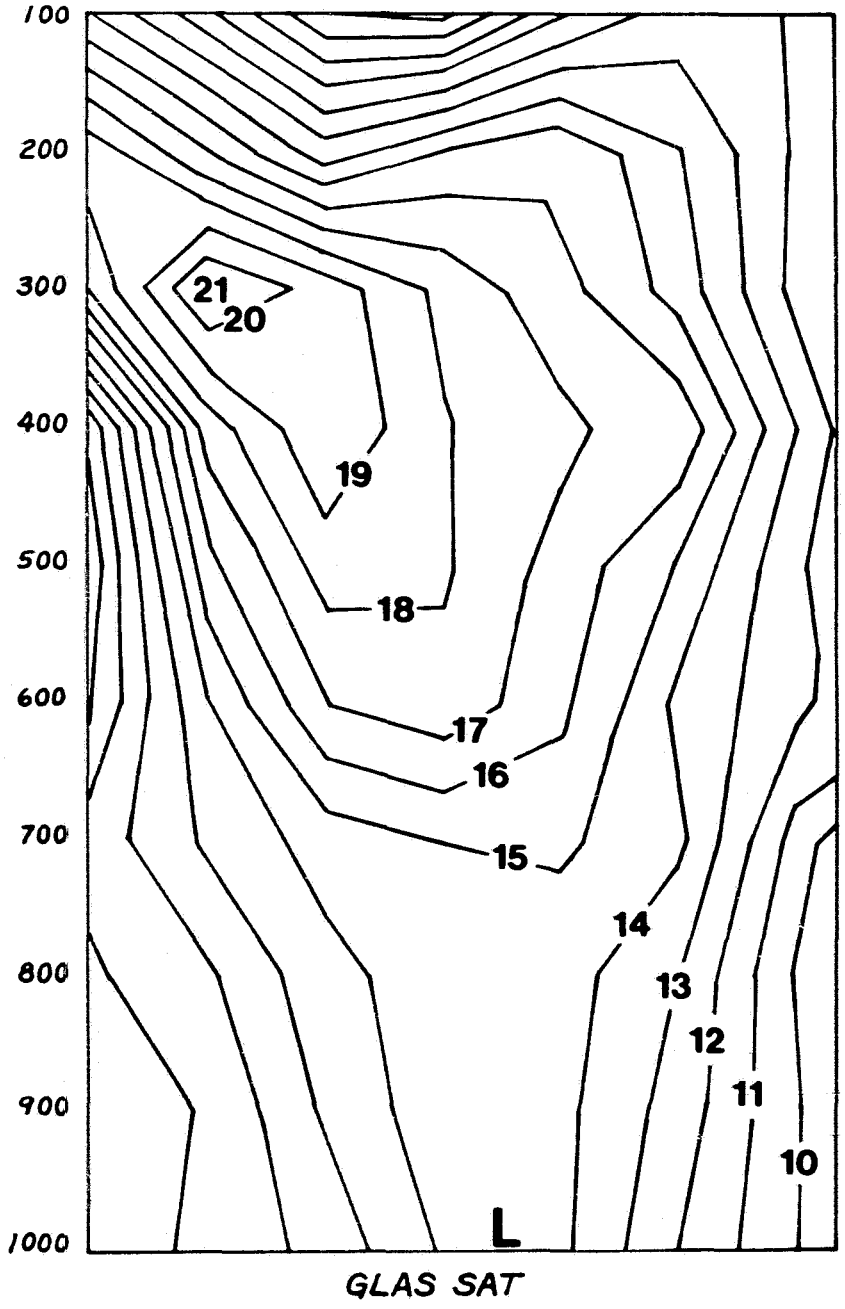

Fig. 7b. As in Fig. 7a except for GLAS SAT.

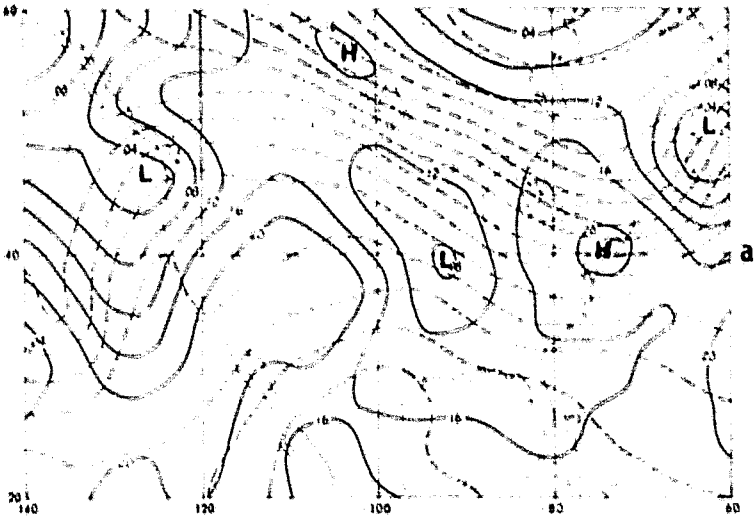

a. 72-h NMC 7L NOSAT forecast

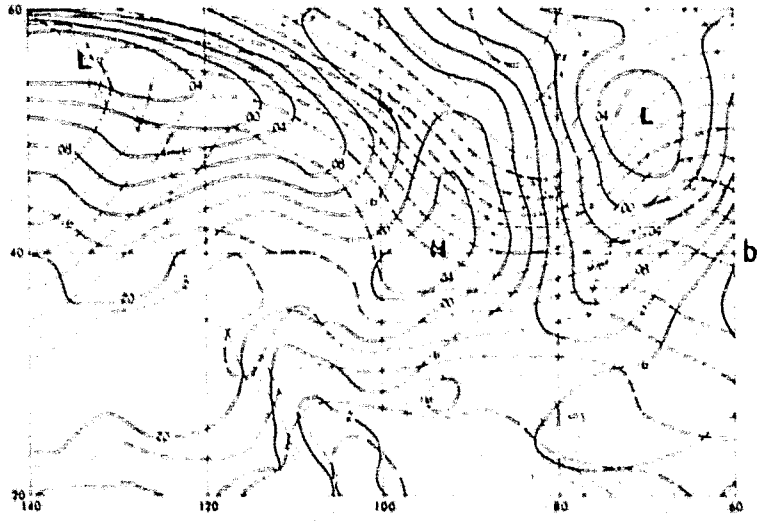

b. 72-h GLAS SAT forecast

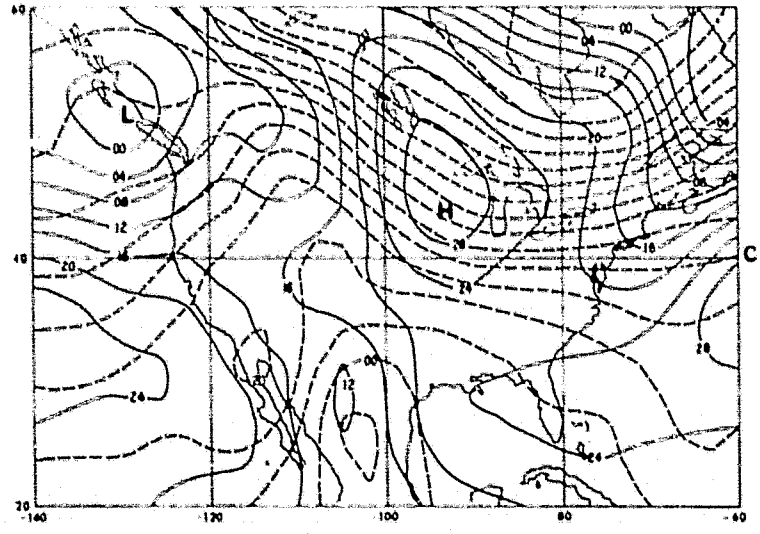

c. Analysis

Fig. 8. As in Fig. 1 except for 0000 GMT 14 February 1976.

Acknowledgment

The author wishes to acknowledge Drs. J. Brown and J. Stackpole of the Development Division at NMC, for providing copies of their 7-level model forecast outputs for these case studies.

References

Atlas, R., 1978: Development of a computerized procedure for the prediction of severe local storm potential. NASA Tech. Memo. 80253, Atmos. and Oceano. Res. Rev.-1978, NASA Goddard Space Flight Center, Greenbelt, Maryland, 7-13.

_____, 1979: A Comparison of GLAS SAT and NMC High Resolution NOSAT Forecasts from 19 and 11 February 1976. NASA Tech. Memo. 80591, NASA Goddard Space Flight Center, Greenbelt, Maryland.

_____, M. Halem, and M. Ghil, 1980: The combined influence of satellite temperature sounding data and increased horizontal resolution on GLAS model forecasts. NASA Tech. Memo. (herein), Atmos. and Oceano. Res. Rev.-1979, NASA Goddard Space Flight Center, Greenbelt, Maryland.

SUPPLEMENTARY NOTES ON THE DEVELOPMENT AND VERIFICATION OF THE AUTOMATED FORECASTING METHOD (AFM)

(R. Atlas and R. Rosenberg)

Prior to beginning assimilation experiments with data from the January-March 1976 Data Systems Test (DST-6), research was initiated to develop improved measures for assessing the impact of remote sounding data on weather forecasting. Previously, numerical measures of forecast accuracy such as the RMS error or S1 score had been the main tool used for this purpose. However, impacts in RMS or S1 are often difficult to interpret in terms of impact on local weather forecasting (Druyan et al., 1975; Houghton and Irvine, 1976; Sanders, 1973). This is due to the large-scale averaging inherent in this type of verification procedure as well as the methodology by which weather forecasts are actually produced. Local weather forecasting is not based solely on the one or two fields for which numerical scores are routinely computed, rather a variety of prognostic primary variables and derived quantities are considered in combination (George, 1960; Naval Education and Training Command, 1974). Quasi-geostrophic theory forms the underlying framework for much of subjective weather forecasting through the omega and geopotential tendency equations (Holtan, 1979).

Recognizing the need for evaluating the impact of satellite data on local weather forecasting, a subjective forecast experiment was conducted and, utilizing the results of this experiment, the AFM was developed. In the subjective forecast experiment, a series of numerical forecasts from initial conditions, which included satellite temperature soundings (referred to as SAT) and initial conditions which excluded satellite soundings (referred to as NOSAT), were generated. For each forecast case, a set of SAT and NOSAT prognostic packages (consisting of most of the charts available at local weather stations) was delivered to two experienced forecasters. These forecasters would then compare prognostic charts, note changes in meteorological variables, and then issue a weather forecast at a few preselected cities scattered throughout the United States. Each forecast was based completely on the subjective interpretation of the SAT or NOSAT prognostic charts. This experiment revealed that the impact of satellite sounding data was large enough to influence local weather forecasts (Atlas and Sakal, 1978) but was limited in utility because of the large amount of time required to produce weather forecasts at even a small number of cities and because of the subjectivity involved.

The attempt was then made to simulate the forecaster's interpretation of the complete prognostic package. Objective algorithms were developed which correlated well with the subjective judgment of the magnitude and importance of each of the prognostic quantities that were utilized. The objective quantities were then combined sequentially in approximately the same order as had been employed by the forecasters to form the AFM. Minor modifications to the AFM were then incorporated to minimize bias and to account for local topographical differences. The AFM is thus based primarily on subjective forecasting experience, which is to a large extent in agreement with quasi-geostrophic theory.

As mentioned in our paper, the AFM was verified in terms of its accuracy when applied to a perfect prognoses (i.e., an analysis) and its agreement with experienced forecasters, prior to being applied to model prognoses. It was found to be 93 percent accurate in determining whether or not precipitation would occur, and agreed with the subjective judgments of three forecasters (two of which did not take place in the original experiment on which the AFM was based) 94 percent of the time on the average. The AFM was then utilized to evaluate the impact of satellite sounding data assimilation on local precipitation forecasts at 128 cities in the United States as reported by Ghil et al. (1979).

Recently, GLAS model forecasts of measurable precipitation and AFM forecasts of precipitation occurrence have been compared. Ten different 72-h forecasts from February 1976 have been verified at 12-h intervals at 128 cities, for a total of 7,680 precipitation forecast comparisons. Of these, the AFM and model forecasts differed 29 percent of the time. Where they were different, the AFM was more accurate in its determination of precipitation occurrence 67 percent of the time. The greater accuracy of the AFM is related to the deficiencies of the model vertical motion predictions, as described by Ghil et al. (1979) and to the inclusion of routines to account for frontal precipitation in the AFM.

To determine the effectiveness of the AFM's combination of parameters, we have compared its accuracy when applied to perfect prognoses with simple forecast schemes in which the prediction is based on a single parameter. Table 1 presents the results of this evaluation for the AFM versus selected cutoff values of 500 mb vorticity advection, 850 mb temperature advection, or 850 mb dewpoint depression. Comparisons with observed precipitation events were made every 12 h for the entire month of February 1976 for the same cities that were utilized in our original verification of the AFM. Statistics verified included percentual correctness, bias, prefigurance, post agreement, and threat score; for a definition of these statistics see, for instance, Ghil et al. (1979) and Tracton and Stackpole (in Murphy and Williamson, 1976, p. 736).

The table shows the relationship of each of the single predictors to precipitation occurrence, and the relative utility of each prediction scheme. From the prefigurances, we see that 70 percent of all precipitation events occurred in conjunction with positive vorticity advection, as compared to 49 percent occurring with warm advection and 57 percent with dewpoint depressions less than 5°C. However, the forecasts based on weak vorticity or thermal advection have higher bias and corresponding lower values of percentual correctness, post agreement, and threat score than those based on dewpoint depressions less than 5°C. The AFM, with near-perfect bias, accounts for 76 percent of all precipitation events and verifies 76 percent of all positive precipitation forecasts. This results in a 10 percent increase in the total number of correct forecasts, and an increase in threat score of .23, relative to the best single parameter prediction. We conclude that: a) vorticity advection is a useful predictor of precipitation occurrence, b) dewpoint depression is the most accurate single predictor, and c) the combination of parameters in the AFM yields a substantial increase in accuracy over any single predictor.

Table 1. Verification of AFM and single parameter predictions of precipitation occurrence for February 1976.

Forecast scheme	Percent correct	Bias	Pre-figurance	Post-agreement	Threat score
Precipitation occurs when 500 mb vorticity advection:					
$> 0 \times 10^{-9}sec^{-2}$	55	3.03	.70	.23	.21
$> .5 \times 10^{-9}sec^{-2}$	79	.92	.35	.37	.22
$> 1 \times 10^{-9}sec^{-2}$	83	.30	.17	.55	.15
Precipitation occurs when 850 mb temperature advection:					
$> 0 \times 10^{-9}sec^{-2}$	49	2.91	.49	.17	.14
$> .5 \times 10^{-9}sec^{-2}$	74	.99	.24	.24	.14
$> 1 \times 10^{-9}sec^{-2}$	79	.39	.10	.25	.08
Precipitation occurs when 850 mb dewpoint depression:					
$< 5°C$	83	1.12	.57	.51	.37
$< 2.5°C$	83	.16	.16	.63	.10
AFM	93	.99	.76	.76	.60

In summary, the AFM was developed in response to the need for improved automated measures for assessing forecasting impact. It simulates subjective interpretation of an ensemble of prognostic and diagnostic quantities. The AFM has been verified from the standpoint of its accuracy when applied to analyses and of its agreement with experienced forecasters. Its actual prognostic accuracy was tested for a relatively large number of cases; these cases, however, were drawn from a limited number of model forecasts. The AFM appears to be comparable in performance to the average skilled weather forecaster's interpretations of large-scale numerical guidance and is thus a useful tool for evaluating the accuracy and utility of large-scale numerical forecasts.

References

Atlas, R., and D. Sakal, 1978: Evaluation and verification tests. The GISS Sounding Temperature Impact Test. NASA Tech. Memo. 78063, p. 5-1, NASA Goddard Space Flight Center, Greenbelt, Maryland.

Druyan, L. M., R. C. J. Somerville, and W. J. Quirk, 1975: Extended-range forecasts with the GISS model of the global atmosphere. Mon. Wea. Rev., 103, 779-795.

George, J. J., 1960: Weather Forecasting for Aeronautics. Academic Press, 673 pp.

Ghil, M., M. Halem, and R. Atlas, 1979: Time-continuous assimilation of remote sounding data and its effect on weather forecasting. Mon. Wea. Rev., 107, 140-171.

Holtan, J. R., 1979: An Introduction to Dynamic Meteorology. Academic Press, 416 pp.

Houghton, D. D., and W. S. Irvine, 1976: A case study comparison of the performance of operational prediction models used in the United States. Mon. Wea. Rev., 104, 817-827.

Naval Education and Training Command, 1974: Aerographer's Mate 1 & C, NAVEDTRA 10362-B. U.S. Government Printing Office, Washington, DC, 659 pp.

Sanders, F., 1973: Skill in forecasting daily temperature and precipitation: some experimental results. Bull. Amer. Meteor. Soc., 54, 1171-1179.

FORECAST SKILL AS A FUNCTION OF THE DATA ASSIMILATED AND METHOD OF OBJECTIVE ANALYSIS

(W. Baker, D. Han, and G. Chatters)

The current skill of numerical weather forecasts degrades rapidly in the first 48 to 72 h due to inaccurate initial conditions as well as model deficiencies. Recent estimates of the sources of forecast error (e.g., Miyakoda, 1975; Robert, 1976; Somerville, 1976) indicate that inaccurate initial data may contribute substantially to the rapid error growth. Errors in the specification of the initial conditions are due to both inadequacies in the observing systems and data analysis techniques. With the aim of extending the limits of predictability, we are evaluating the usefulness of new observing systems and the accuracy of different methods of data analysis.

We have tested two different approaches to the objective analysis of the observational data as outlined below:

Objective Analysis Scheme A

- Temperature analysis at the mandatory pressure levels
- Cressman (1959) weighting with fixed scanning radii
- No horizontal consistency checks
- Hydrostatic consistency is not imposed
- A 5-point smoother is applied to the surface pressure after each analysis
- 12-h assimilation cycle with a ±3-hour window used on all conventional data. Time-continuous assimilation of satellite sounding data (Ghil et al., 1979).

Objective Analysis Scheme B

- Geopotential height analysis at the mandatory pressure levels
- Cressman (1959) weighting modified such that the scanning radius is a function of the data density (Stephens and Stitt, 1970)
- Horizontal consistency checked after each scan for all data
- Vertical consistency maintained
- A smoother (Shuman, 1957) is applied to all fields after each analysis
- 6-h assimilation cycle with a ±3-h window used on all data.

As may be seen, Scheme B analyzes the thickness of the vertical column, maintains horizontal and vertical consistency, determines the radius of influence about each model grid point as a function of the data density, and utilizes a 6-h assimilation cycle. Scheme A, on the other hand, analyzes temperature at each level, does not check for data consistency, has a fixed radius of influence for all model grid points, and assimilates the conventional data every 12 h with a time-continuous assimilation of satellite sounding data (Ghil et al., 1979).

Assimilation/Forecast Experiments

To examine the differences in the objective analysis methods and the usefulness of various data for numerical weather prediction, a series of assimilation/forecast experiments has been run, using analysis Schemes A and B with different combinations of observational data as summarized in Table 1. The first four experiments (1405, 1444, 8449, 8939) utilize the 2.5° x 3° version of the 2nd-order GLAS GCM (Somerville et al., 1974) as the assimilation and forecast model. In Experiment 1425, the data are assimilated with the 2.5° x 3° GLAS model, and the forecast is generated on the 4° x 5° 4th-order GLAS model (Kalnay-Rivas et al., 1977). The 2.5° x 3° GLAS model is utilized as the forecast model in Experiment 1298 for the initial conditions provided by the National Meteorological Center (NMC) at 0000 GMT 19 February 1976 from their operational cycle with the 9-level assimilation model (Stackpole, 1976) using the Flattery (1971) analysis.

Table 1. Description of assimilation/forecast experiments for the 0000 GMT 19 February 1976 case.

Model exp.	Description	Assimilation model	Objective analysis scheme	Forecast model	Satellite data	Aircraft temp. data
1405	NOSAT	2.5° x 3°	B	2.5° x 3°	No	No
1444	NOSAT	2.5° x 3°	B	2.5° x 3°	No	Yes
8449	NOSAT	2.5° x 3°	A	2.5° x 3°	No	Yes
8939	SAT	2.5° x 3°	A	2.5° x 3°	Yes	Yes
1425	SAT	2.5° x 3°	A	4° x 5°	Yes	Yes
1298	VTPR+BOGUS	NMC	Hough	2.5° x 3°	Yes	No

In Experiment 8449, Scheme A objectively analyzed rawinsonde, surface, and aircraft wind and temperature data every 12 h from 0000 GMT 29 January 1976 through 0000 GMT 19 February 1976. For Experiment 1444, Scheme B analyzed pilot balloon wind data[1] in addition to those data analyzed in Experiment 8449.

Experiment 1444 began from the initial conditions provided by Experiment 8449 at 0000 GMT 17 February 1976 with the observational data analyzed every 6 h through 0000 GMT 19 February 1976. In Experiment 1405, Scheme B analyzed the same observational data as in Experiment 1444 except that aircraft temperature data were excluded in Experiment 1405 with the initial conditions provided by the NMC operational analysis at 0000 GMT 17 February 1976. For Experiment 8939, Scheme A analyzed the same data as in Experiment 8449. In addition, satellite sounding data obtained from the NOAA-4 Vertical Temperature Profile Radiometer (VTPR) and from the High-Resolution Infrared Spectrometer (HIRS) and Scanning Microwave Spectrometer (SCAMS) on NIMBUS 6 were also assimilated.

Evaluation of the Analysis Methods and Observing Systems

To illustrate the differences in the analysis schemes and the importance of various data assimilated, the 500 mb geopotential height and wind direction are shown in Figs. 1-3. The differences in the height analysis from the final analysis of the assimilation among the various experiments should be noted in the enclosed region off the west coast of North America. In particular, the amplitude of the short-wave trough is greater in Experiments 1444 (Fig. 1), 8449 (Fig. 2), and 8939 (Fig. 2) with aircraft temperature data than in Experiment 1405 (Fig. 1) where it was excluded. The NMC analysis in Experiment 1298 (Fig. 3) also excluded aircraft temperature data, but comparison of Experiment 1298 with the other experiments is difficult because the data were assimilated with a different model. Bogus data were also used in the NMC analysis in addition to other differences.

The experiments which utilized Scheme B (1405 and 1444) are less noisy than those in which Scheme A was used (Experiments 8449 and 8939). This is due in part to the application of a smoother (Shuman, 1957) on the height and wind fields in Scheme B, whereas those fields were not smoothed in Scheme A. The lack of vertical consistency in Scheme A also contributes to the noise.

The S1 scores for a series of 72-h forecasts generated from the initial conditions presented in Fig. 1 are summarized in Table 2. The following points are noted:

1. Of the five forecasts from initial conditions generated on the 2.5° x 3° GLAS model (Experiments 1405, 1444, 8449, 8939, and 1425), the two which included satellite sounding data and aircraft temperature data (Experiments 8939 and 1425) are the most skillful over North America.

---

[1] For the purposes of our discussions here, the effects of the pilot balloon data may be considered negligible.

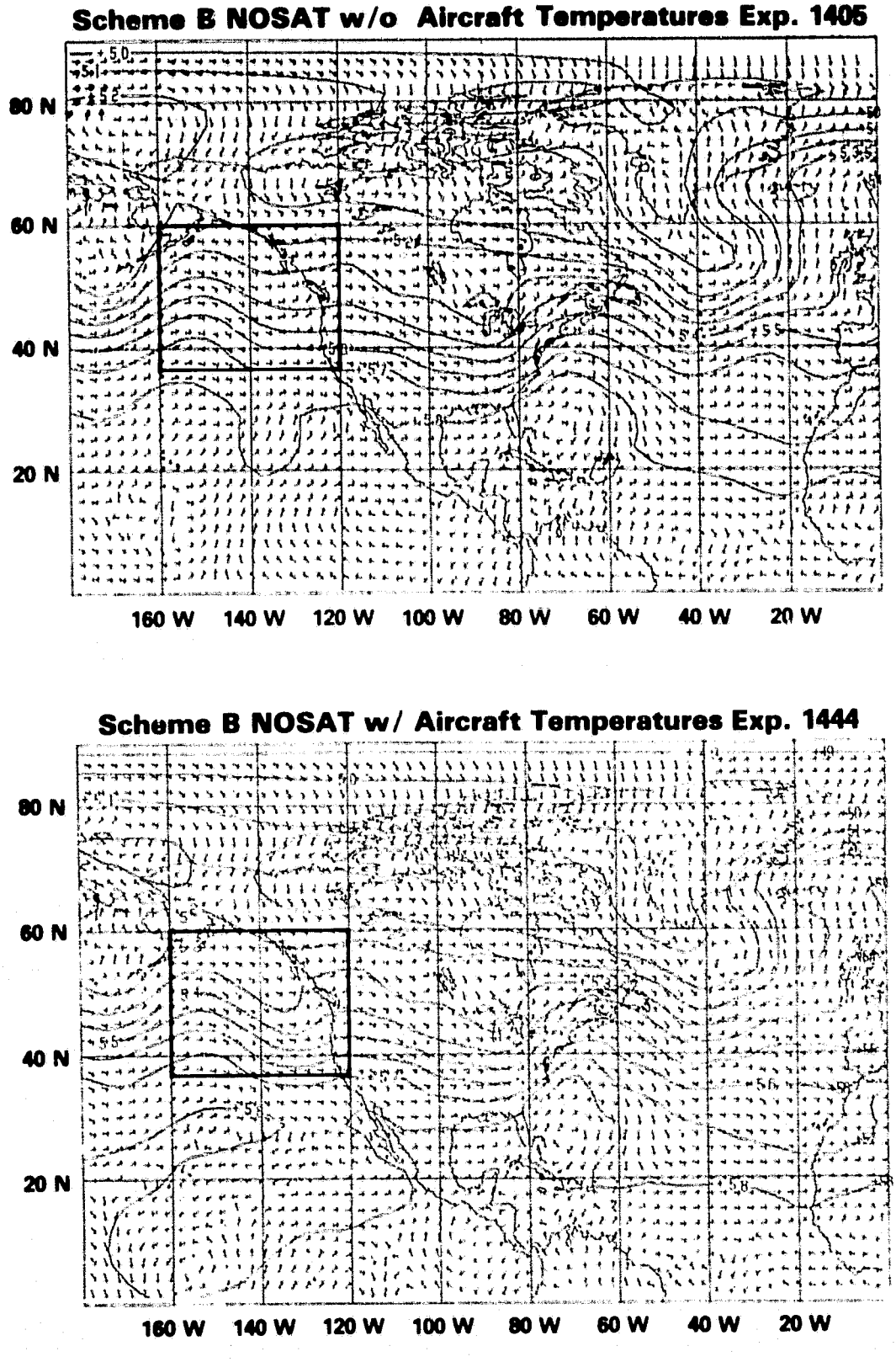

Fig. 1. 500 mb geopotential height and wind direction for 0000 GMT 19 February 1976 for Experiments 1405 and 1444. 500 mb height contours are at 100 dam intervals.

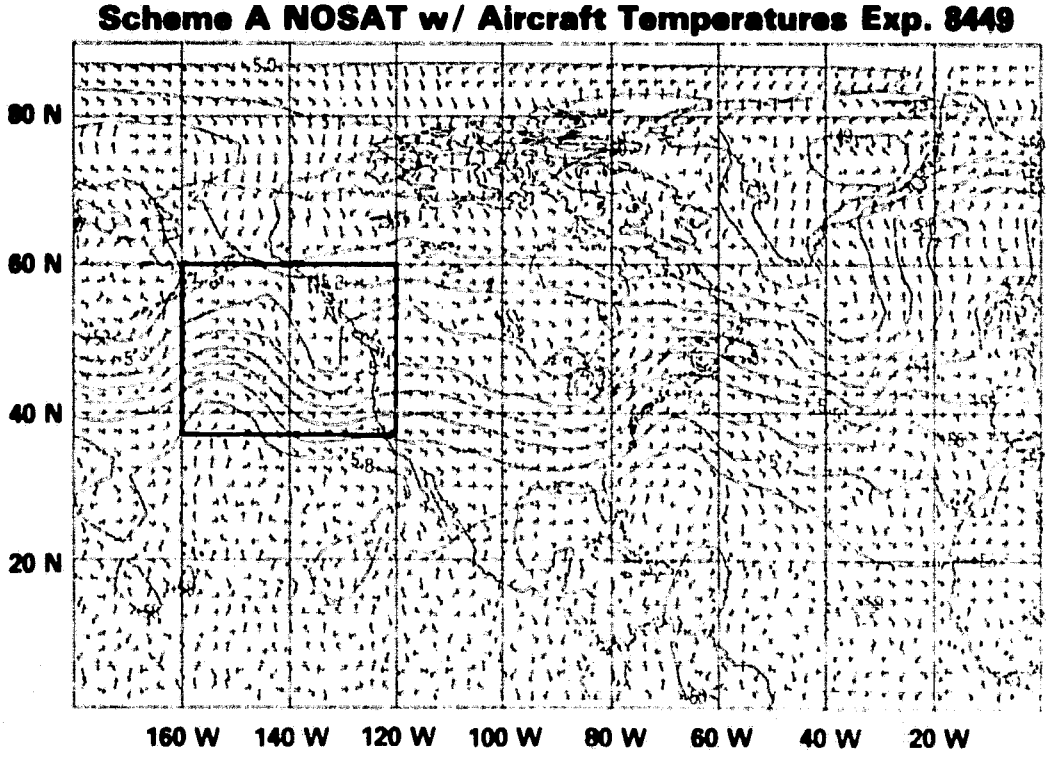

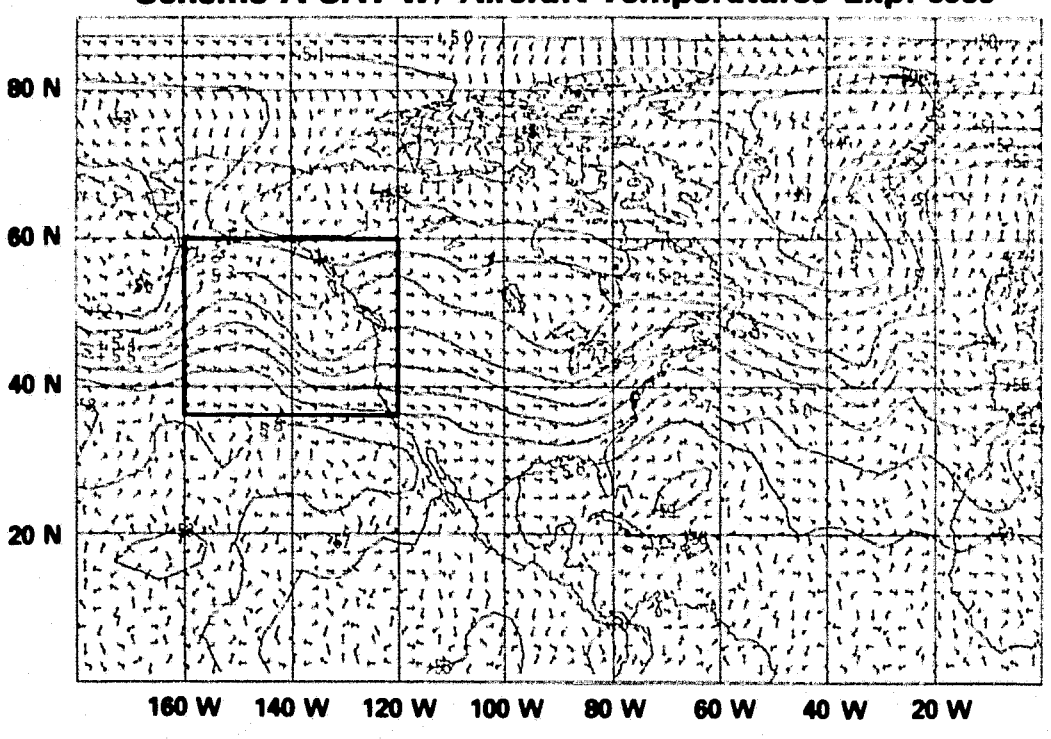

Fig. 2. As in Fig. 1 except for Experiments 8449 and 8939.

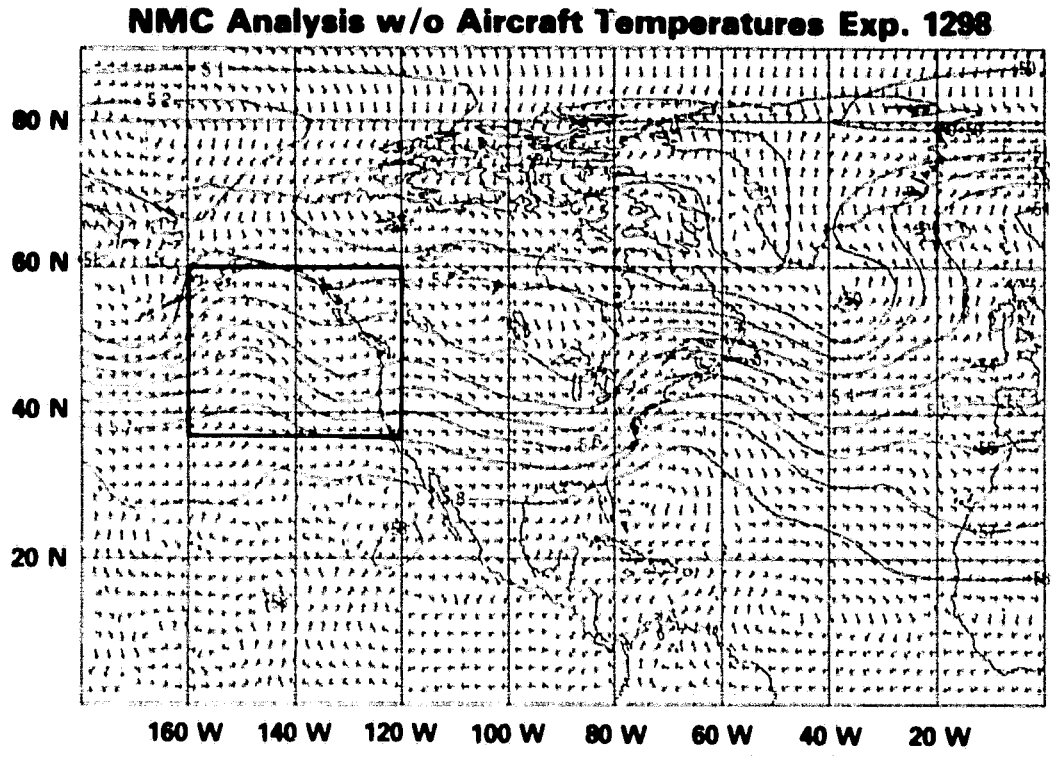

Fig. 3. As in Fig. 1 except for Experiment 1298.

A number of points may be made in regard to the diagrams in Figs. 4 and 5. The long wave error fields shown on the left are quite similar in Experiments 1444 (Fig. 4), 8449 (Fig. 5), and 8939 (Fig. 5) during the first 48 h over Europe (stippled region from 10W to 40E longitude). Aircraft temperature data are common to all three experiments. Experiment 1405 (Fig. 4), which had neither aircraft temperatures nor satellite sounding data, has substantially less error over the same region during the first 48 h of the forecast. Comparing Experiments 8449 and 8939 over North America (stippled region from 130W to 75W longitude), there is no apparent improvement in the forecast of the long waves with the addition of satellite sounding data (Experiment 8939). However, when Experiments 8449 and 8939 are compared over the same region for the baroclinic waves, shown on the right in Fig. 4 and 5, a significant improvement is noted, particularly in the last 12 h. This pattern also holds for the short waves (k = 8-12) not shown here.

It is also worth noting that both Experiments 1405 and 8939 are generally free of the rapid error growth in the baroclinic waves, characterizing the other experiments in the last 12 h of the forecast. It seems likely that, when aircraft temperatures and satellite sounding data are assimilated together (e.g., Experiment 8939), systematic errors are controlled in the baroclinic-wave range and smaller. The rapid error growth seen in Experiments 1444 and 8449 in waves 5-7 seems consistent with the findings of Baumhefner and Julian (1972). In a later study, Baumhefner and Julian (1975) found a rapid error growth from initial conditions obtained using simulated cloudy retrievals with systematic errors.

References

Baumhefner, D. P., and P. R. Julian, 1972: The reference-level problem: its location and use in numerical weather predictions. J. Atmos. Sci., 29, 285-299.

_____, and _____, 1975: The initial structure and resulting error growth in the NCAR GCM produced by simulated, remotely sensed temperature profiles. Mon. Wea. Rev., 103, 273-284.

Cressman, G. P., 1959: An operational objective analysis system. Mon. Wea. Rev., 85, 367-374.

Flattery, T. W., 1971: Spectral models for global analysis and forecasting. Air Weather Service Tech. Rep. No. 242, 42-54.

Ghil, M., M. Halem, and R. Atlas, 1979: Time-continuous assimilation of remote-sounding data and its effect on weather forecasting. Mon. Wea. Rev., 107, 140-171.

Kalnay-Rivas, E., A. Bayliss, and J. Storch, 1977: The 4th order GISS model of the global atmosphere. Cont. to Atmos. Phys., 50, 306-311.

Miyakoda, K., 1975: Weather forecasts and the effects of the subgrid scale processes. Seminars on Scientific Foundation of Medium Range Wea. Forecasts, Reading, England, 380-593.

References (Continued)

Robert, A., 1976: Sensitivity experiments for the development of NWP models. Proc. Eleventh Stanstead Seminar, Publ. Meteor. No. 114. McGill Univ., 68-81.

Shuman, F. G., 1957: Numerical methods in weather prediction: II, Smoothing and filtering. Mon. Wea. Rev., 85, 357-361.

Somerville, R. C. J., 1976: Sensitivity of large-scale numerical weather forecasts to deficiencies in models. Ann. Meteor. (NF), 11, 266-268.

_____, P. H. Stone, M. Halem, J. E. Hansen, J. S. Hogan, L. M. Druyan, G. Russell, A. A. Lacis, W. J. Quirk, and J. Tenenbaum, 1974: The GISS model of the global atmosphere. J. Atmos. Sci., 31, 84-117.

Stackpole, J. D., 1976: The National Meteorological Center eight-layer global model. Preprints Sixth Conf. Numerical Wea. Forecasting and Analysis, AMS, Albany, New York, 112-116.

Stephens, J. J., and J. M. Stitt, 1970: Optimum influence radii for interpolation with the method of successive corrections. Mon. Wea. Rev., 98, 680-687.

2. The same pair of experiments, however, are less skillful over Europe than Experiment 1405, in which satellite sounding data and aircraft temperature data are not assimilated.

3. Differences in the forecasts with the 4° x 5° 4th-order model and the 2.5° x 3° 2nd-order model from the same initial conditions (Experiments 1425 and 8939) are smaller than the differences in the forecasts from different initial conditions with the same model (e.g., Experiments 1405 and 8939).

Table 2. Sensitivity of forecast skill to the data assimilated and method of objective analysis for the 0000 GMT 19 February 1976 case.

Model exp.	Sea level pressure (S1)				500 mb Z (S1)			
	48h N.Am.	72h N.Am.	48h Eur	72h Eur	48h N.Am.	72h N.Am.	48h Eur	72h Eur
1405	76.8	73.1	48.8	67.9	41.0	38.3	46.1	50.5
1444	70.6	72.2	53.1	70.9	42.5	45.0	52.7	51.3
8449	69.5	77.5	52.0	80.1	39.5	44.8	53.2	52.2
8939	56.4	54.3	54.3	81.6	33.2	37.1	54.5	62.3
1425	61.9	56.7	57.9	82.8	31.6	35.1	48.9	63.2
1298	58.6	58.8	48.4	68.7	31.2	35.3	46.8	47.2

Analysis of Forecast Error by Wavenumber Decomposition

To further examine the effects of the objective analysis schemes and data assimilated on the forecast skill, Figs. 4 and 5 show the error in the long waves (wavenumbers 1-4) and baroclinic waves (wavenumbers 5-7) as a function of time at 40N for 500 mb. The forecast error fields presented are relative to the NMC operational analysis and are, therefore, not a measure of the "true" observational error. Nevertheless, they provide useful insight into the effects of the data and the analysis schemes on the forecast.

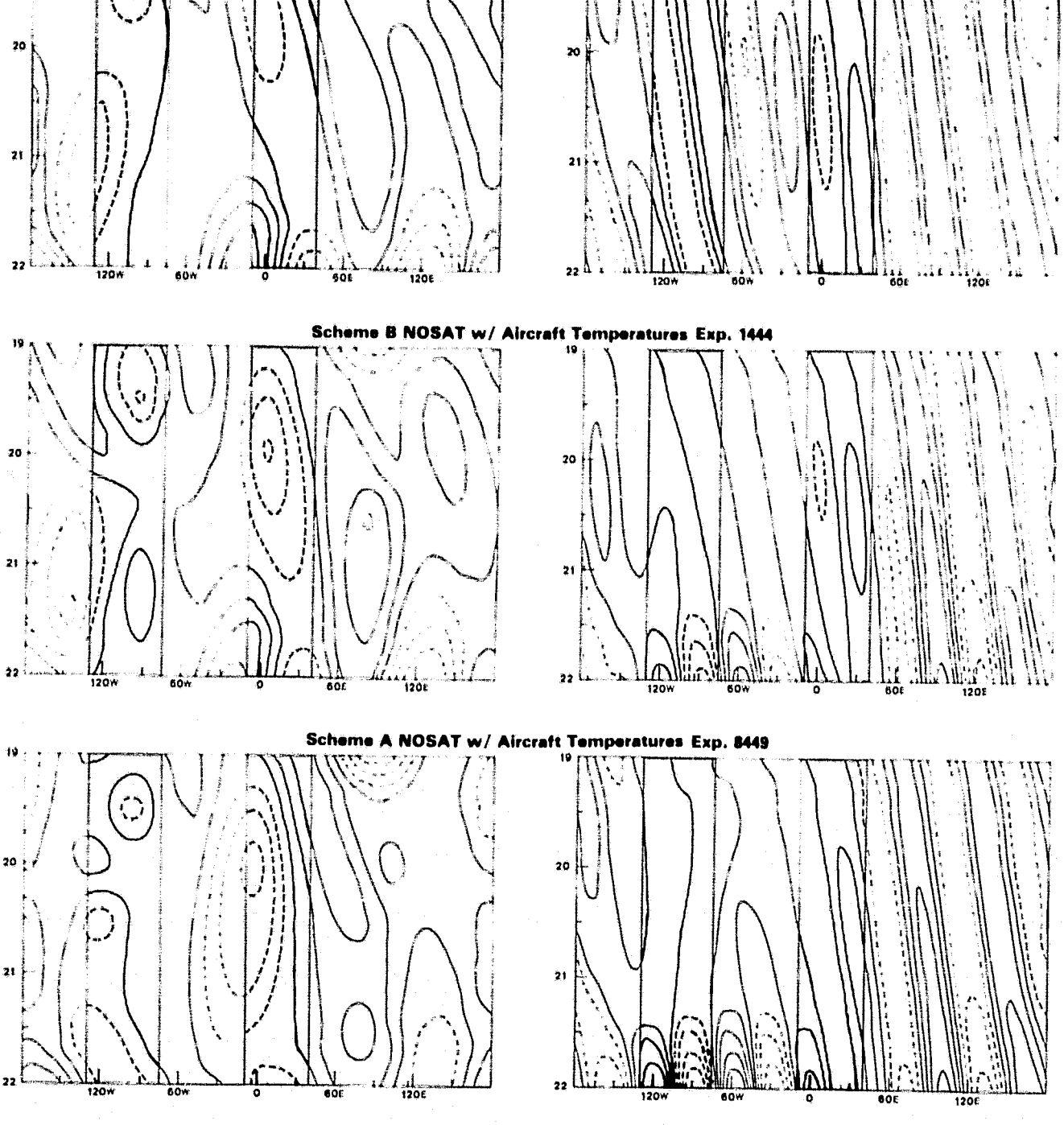

Fig. 4. Longitude-time plot of forecast errors at 40N at 500 mb for the 0000 GMT 19 February 1976 case for Experiments 1405, 1444, and 8449. Errors for waves 1-4 are shown on the left and those for waves 5-7 on the right. The contour interval is 20 m.

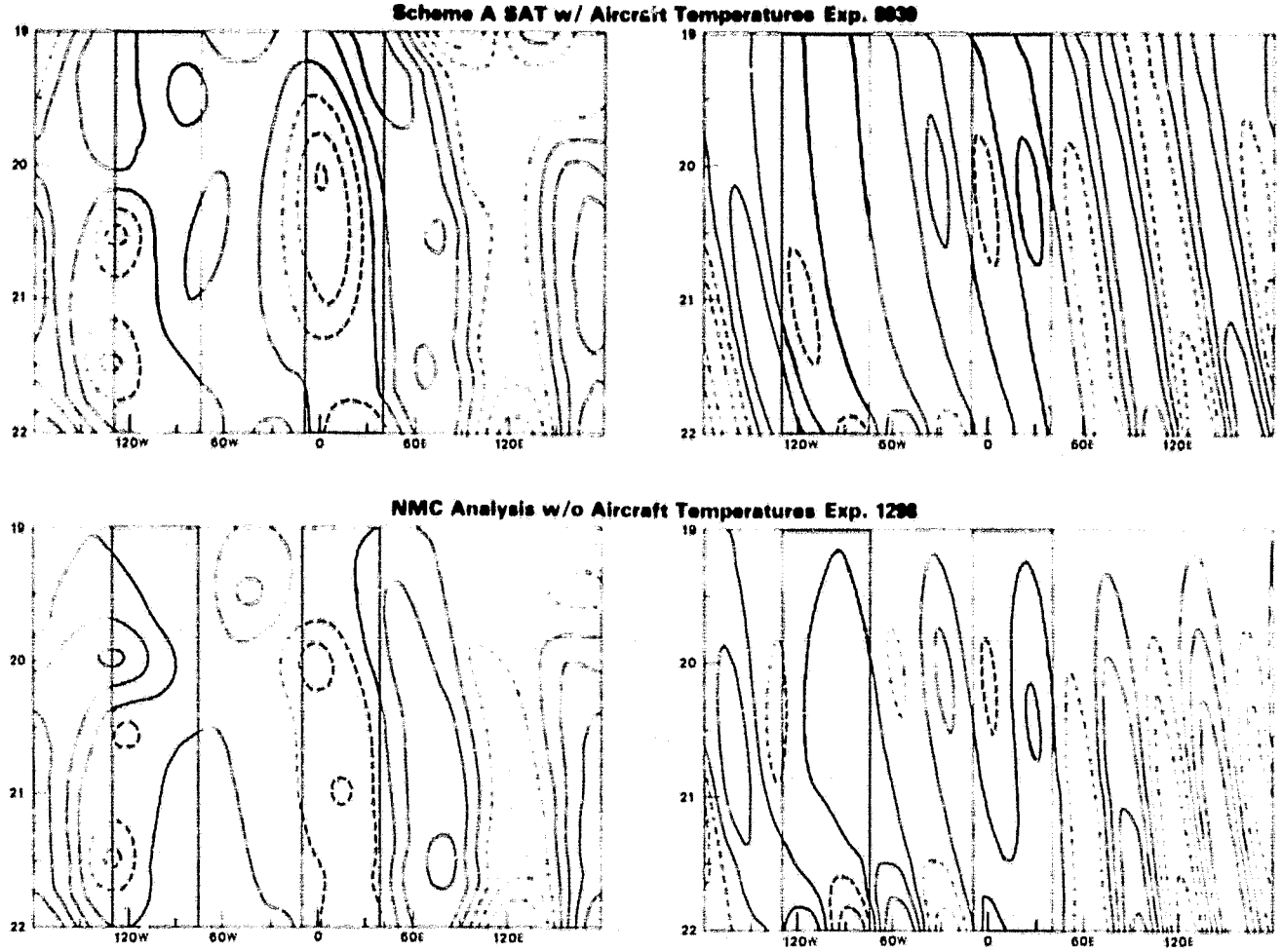

Fig. 5. As in Fig. 4 except for Experiments 8939 and 1298.

ASSIMILATION AND FORECAST EXPERIMENTS WITH THE GLAS 4TH-ORDER GLOBAL ATMOSPHERIC MODEL

(E. Kalnay-Rivas, W. Baker, and D. Han)

The new 4th-order GLAS global atmospheric model (Kalnay-Rivas and Hoitsma, 1979) is based on an energy-conserving scheme, with all horizontal differences computed with 4th-order accuracy. A 16th-order Shapiro filter is applied every 2 h to the fields of sea level pressure and potential temperature, which are rather insensitive to the presence of topography. In this scheme, waves with wavelengths longer than four grid lengths are resolved accurately without damping. Waves shorter than four grid lengths, which would otherwise be grossly misrepresented by the finite differences, are filtered out while they are still infinitesimal. These shortest waves, which in the new 4th-order model are considered to be part of the subgrid scale, act as a "sponge layer" in the spectral domain, allowing energy to trickle down from longer waves and avoiding the accumulation of energy which would otherwise occur at the short wave cutoff. Shallow water experiments indicate that such a scheme in practice conserves potential enstrophy to a high degree of accuracy.

The new model has similar computation time and memory requirements as the present 2nd-order GLAS model with the same 4° latitude, 5° longitude, and 9 vertical-level resolution (Somerville et al., 1974). However, the 4th-order forecasting skill is nearly as skillful as the 2.5° lat. by 3° long. 2nd-order GLAS model. Figs. 1 through 4 show a comparison of the 3-day forecast from 0000 GMT 19 February 1976 during the DST-6 period made with the low resolution 2nd- and 4th-order models, and with the high resolution 2nd-order model. A less skillful forecast from 0000 GMT 1 February 1976 is shown in Figs. 5 through 8. The relative differences between the models are typical of other integrations. The 4th-order forecast for the 19 February 1976 case (Fig. 3) was continued for 2 days (Fig. 9), still showing considerable skill. Another advantage of this model is that vertical motion is clearly associated with only the large-scale field, even over regions with topography (Fig. 10). In the 2nd-order models, small-scale noise dominates the instantaneous field of vertical motion, especially over topography.

The analysis and assimilation "Scheme B" (Baker et al., 1980) has been adapted to the 4th-order model. The scheme has been tested with Level II-a (operational) data corresponding to the period 6-9 January 1979 during the FGGE SOP-1. Fig. 11 shows the 300 mb initial analysis at 9 January 1979 obtained using the 4th-order assimilation model and used as initial conditions for the 4-day prediction of Fig. 13. In the eastern hemisphere, the flow is rather zonal. After 4 days (13 January), a deep trough developed over Central Europe and an intense blocking high, with a low to the south located at about 60E (Fig. 12). The basic characteristics of this development are well predicted by the 4th-order model (Fig. 13). A similar forecast, made from the NMC analysis with the high resolution 2nd-order GLAS model, predicts a less intense development (Fig. 14).

Assimilation and forecast experiments with Level II-b data using both the 2nd-order high resolution and the 4th-order low resolution GLAS models are presently being conducted.

References

Baker, W., D. Han, and G. Chatters, 1980: Forecast skill as a function of the data assimilated and the method of objective analysis. NASA Tech. Memo. (herein), Atmos. and Oceano. Res. Rev.-1979, NASA Goddard Space Flight Center, Greenbelt, Maryland.

Kalnay-Rivas, E., and D. Hoitsma, 1979: The effect of accuracy, conservation and filtering on numerical weather forecasting. AMS Fourth Conf. on Numerical Weather Prediction, Silver Spring, Maryland, 29 October-1 November, Preprint Volume, 302-312.

Somerville, R. C. J., P. H. Stone, M. Halem, J. E. Hansen, J. S. Hogan, L. M. Druyan, G. Russell, A. A. Lacis, W. J. Quirk, and J. Tenenbaum, 1974: The GISS model of the global atmosphere. J. Atmos. Sci., 31, 84-117.

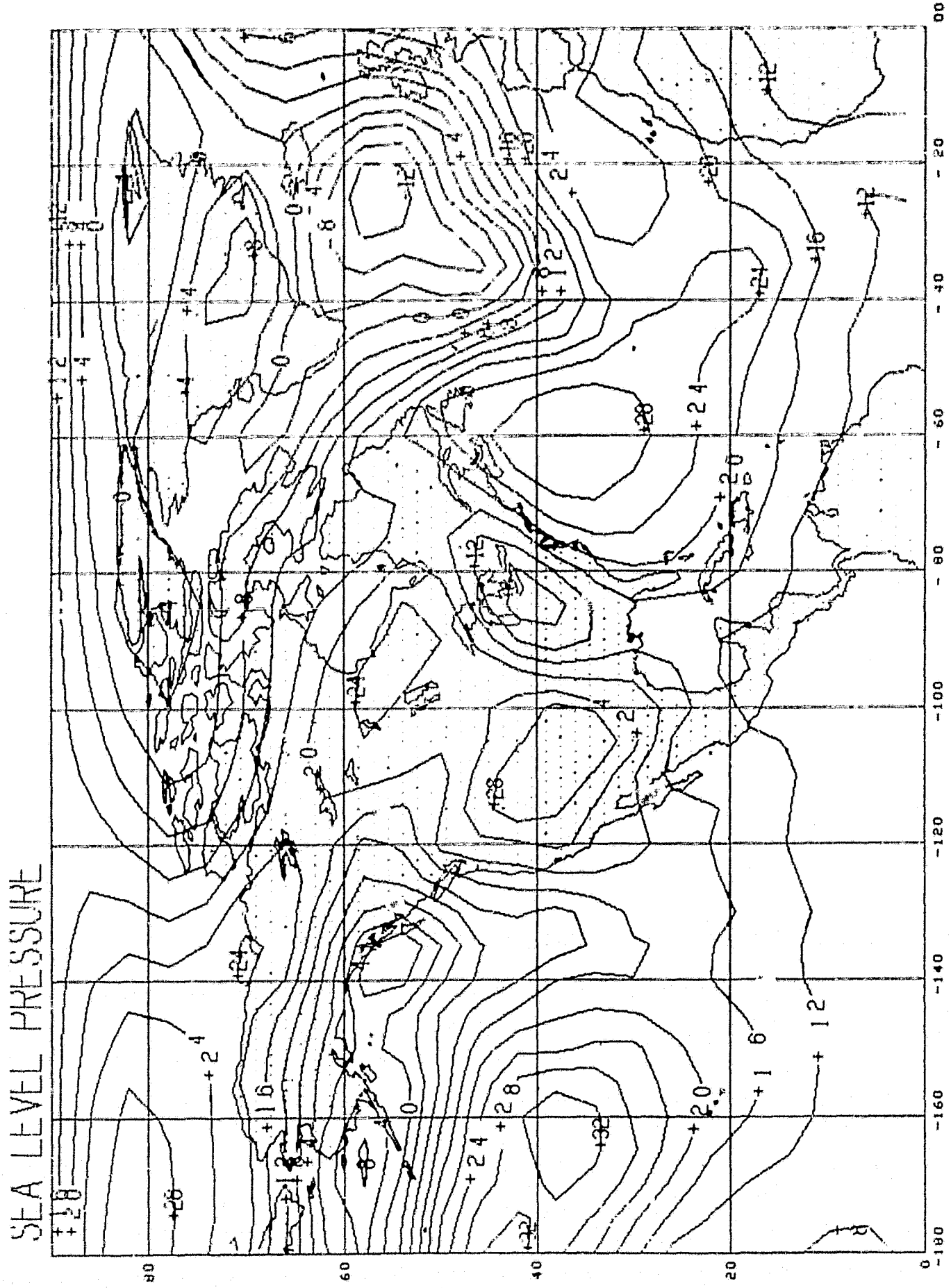

Fig. 1. NMC analysis for 0000 GMT 22 February 1976.

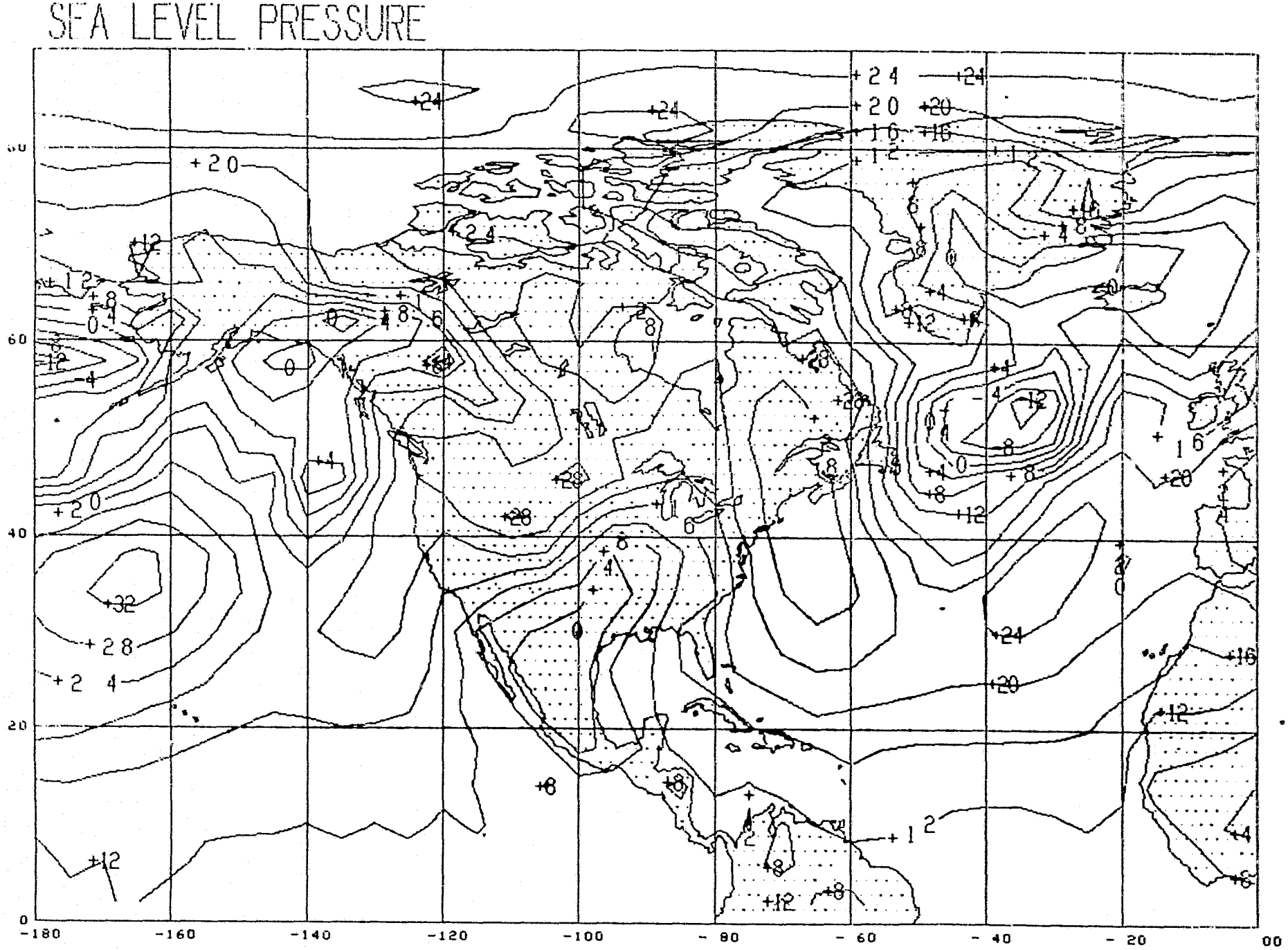

Fig. 2. GLAS 2nd-order, 4° x 5°, 3-day forecast at 0000 GMT 22 February 1976.

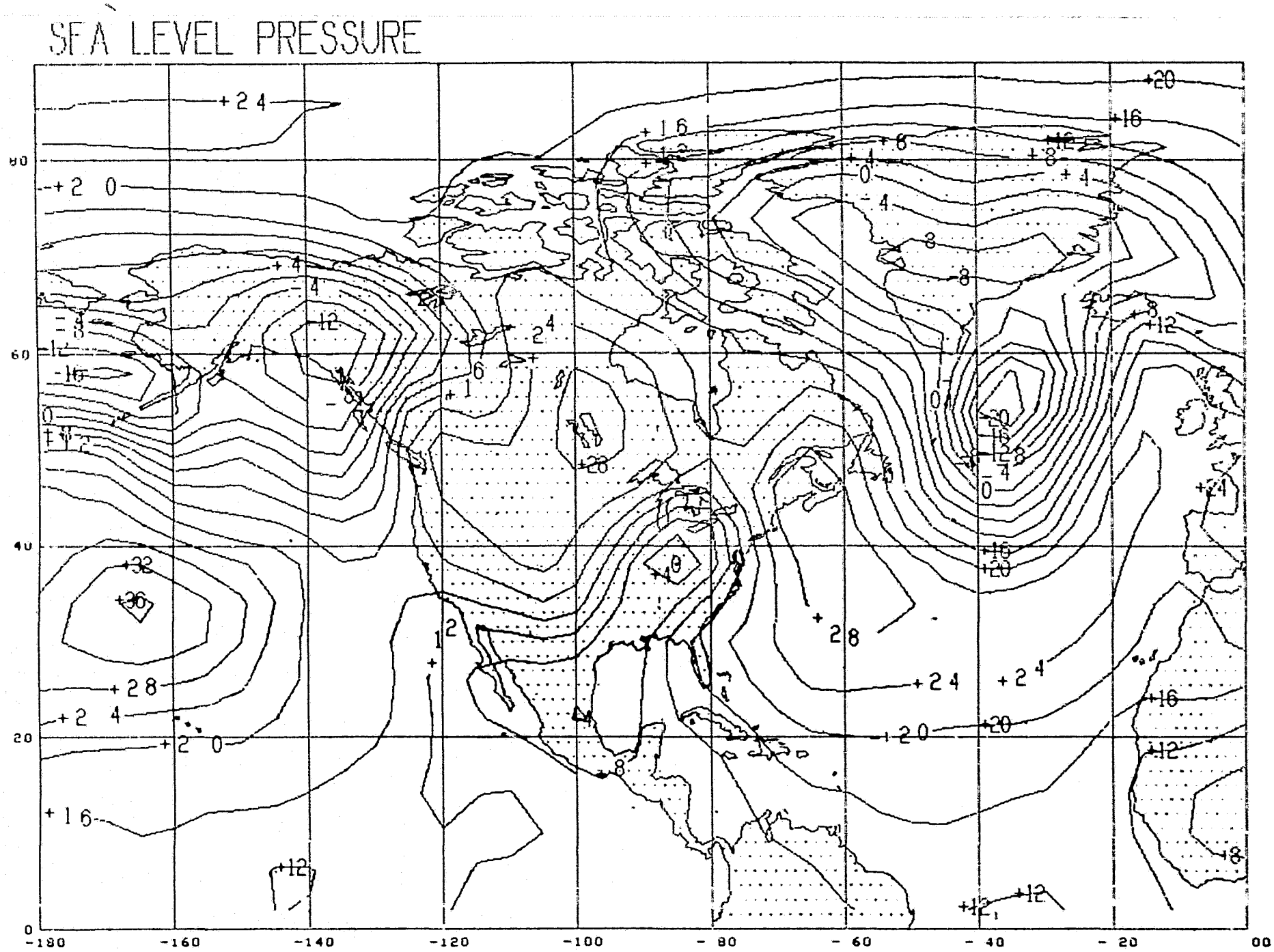

Fig. 3. GLAS 4th-order, 4° x 5°, 3-day forecast at 0000 GMT 22 February 1976.

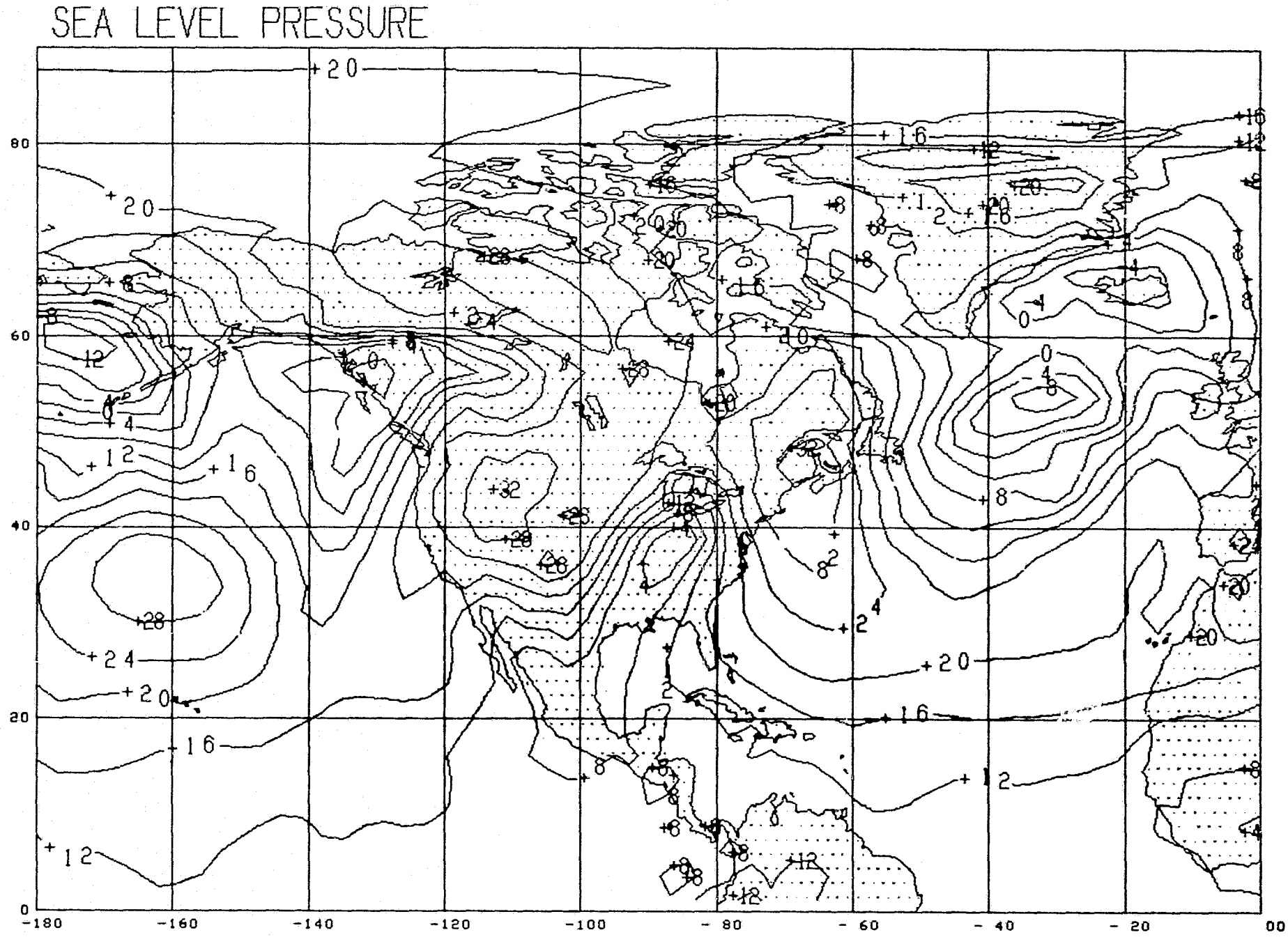

Fig. 4. GLAS 2nd-order, 2.5° x 3°, 3-day forecast at 0000 GMT 22 February 1976.

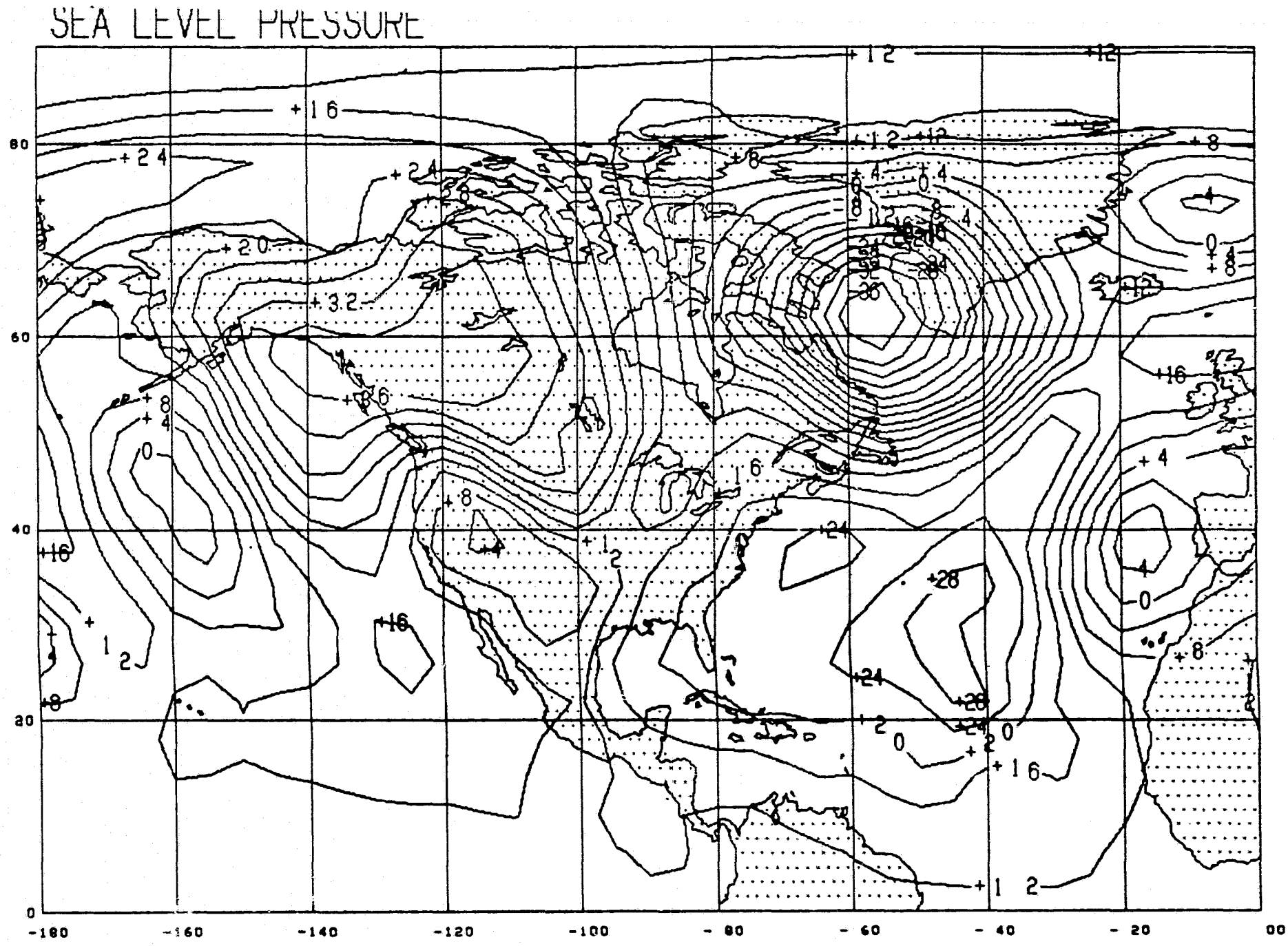

Fig. 5. NMC analysis for 0000 GMT 4 February 1976.

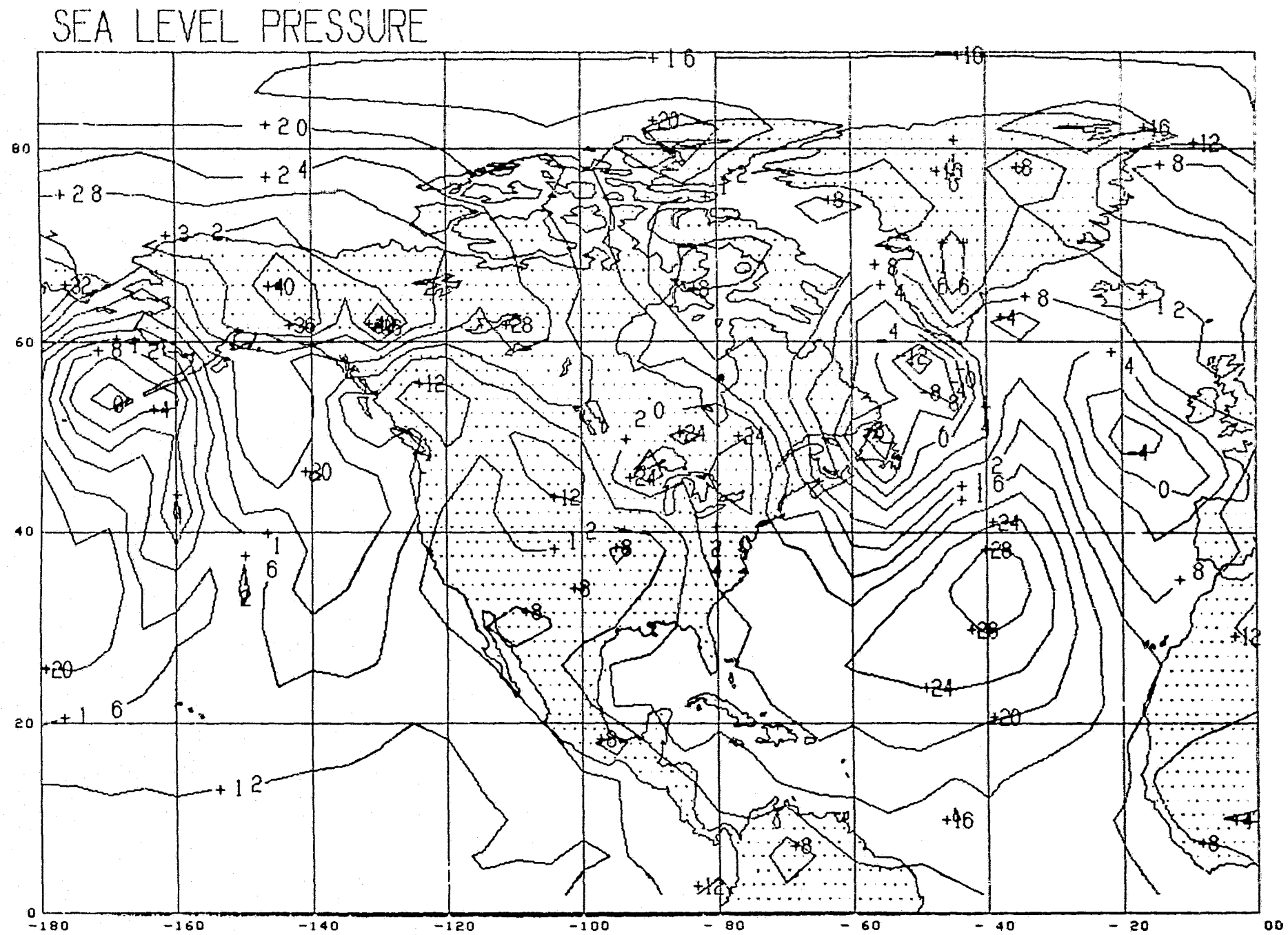

Fig. 6. GLAS 2nd-order, 4° x 5°, 3-day forecast at 0000 GMT 4 February 1976.

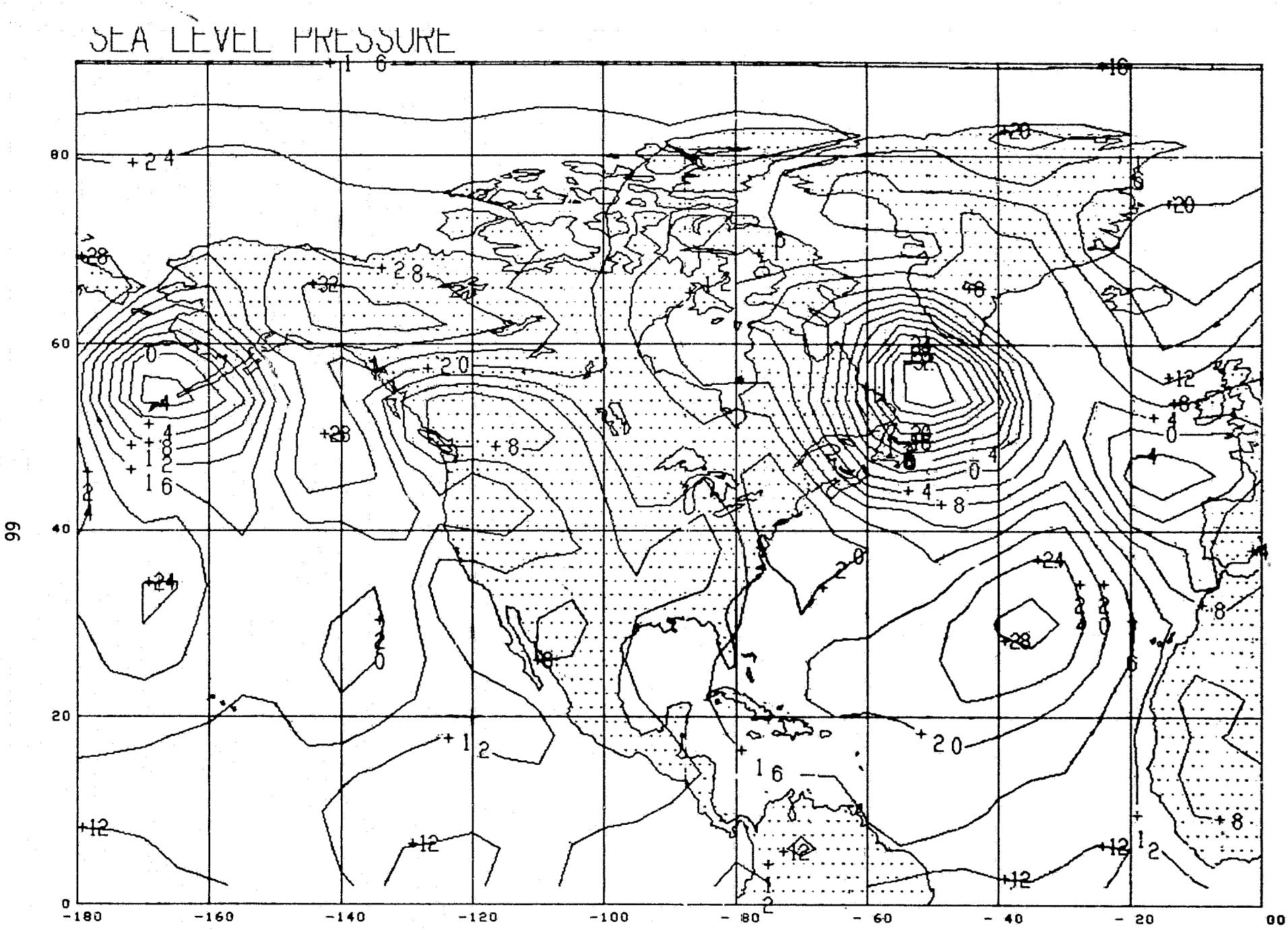

Fig. 7. GLAS 4th-order, 4° x 5°, 3-day forecast at 0000 GMT 4 February 1976.

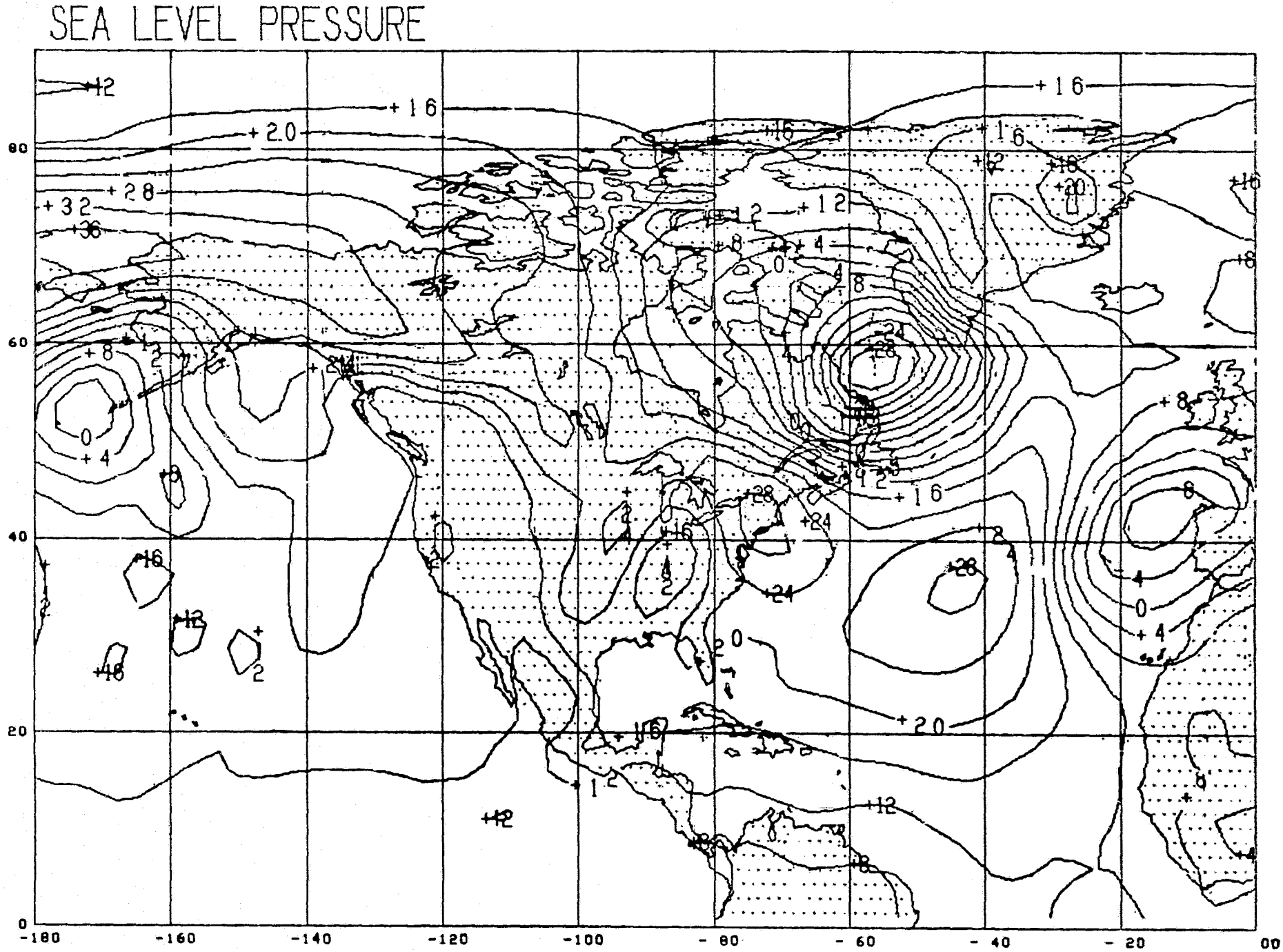

Fig. 8. GLAS 2nd-order, 2.5° x 3°, 3-day forecast at 0000 GMT 4 February 1976.

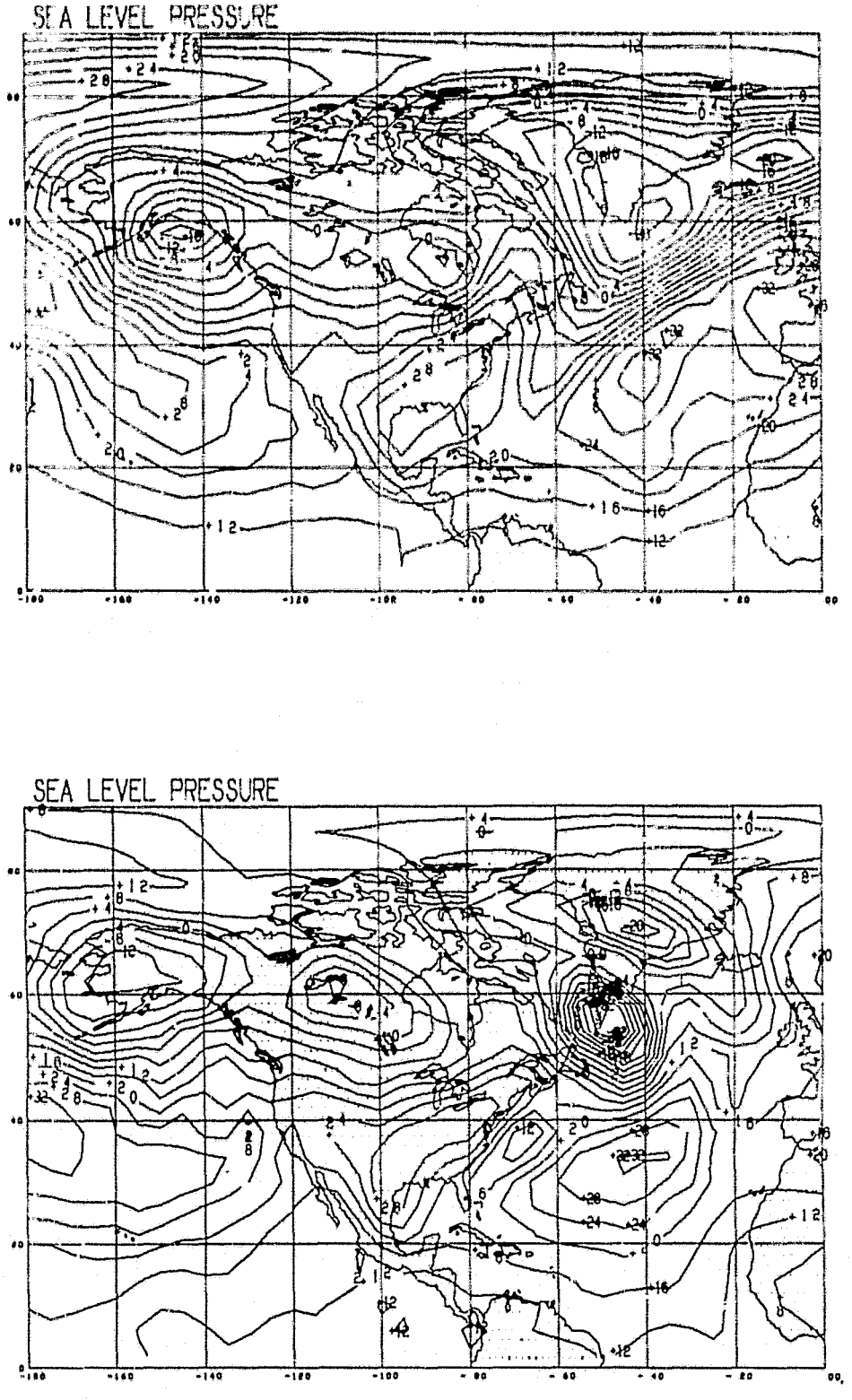

Fig. 9. Five-day forecast at 0000 GMT 19 February 1976.

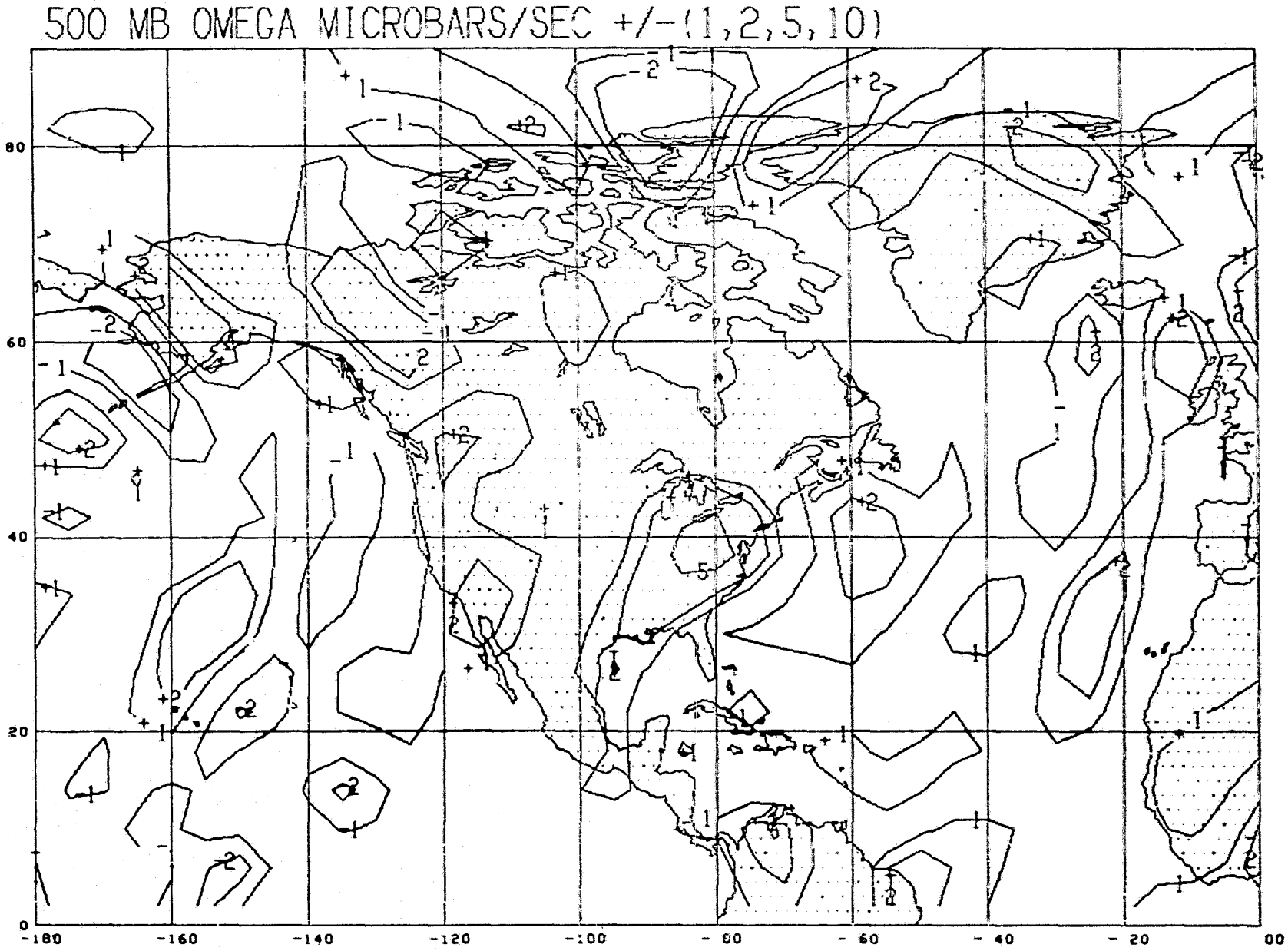

Fig. 10. 500 mb vertical velocity field, corresponding to Fig. 3.

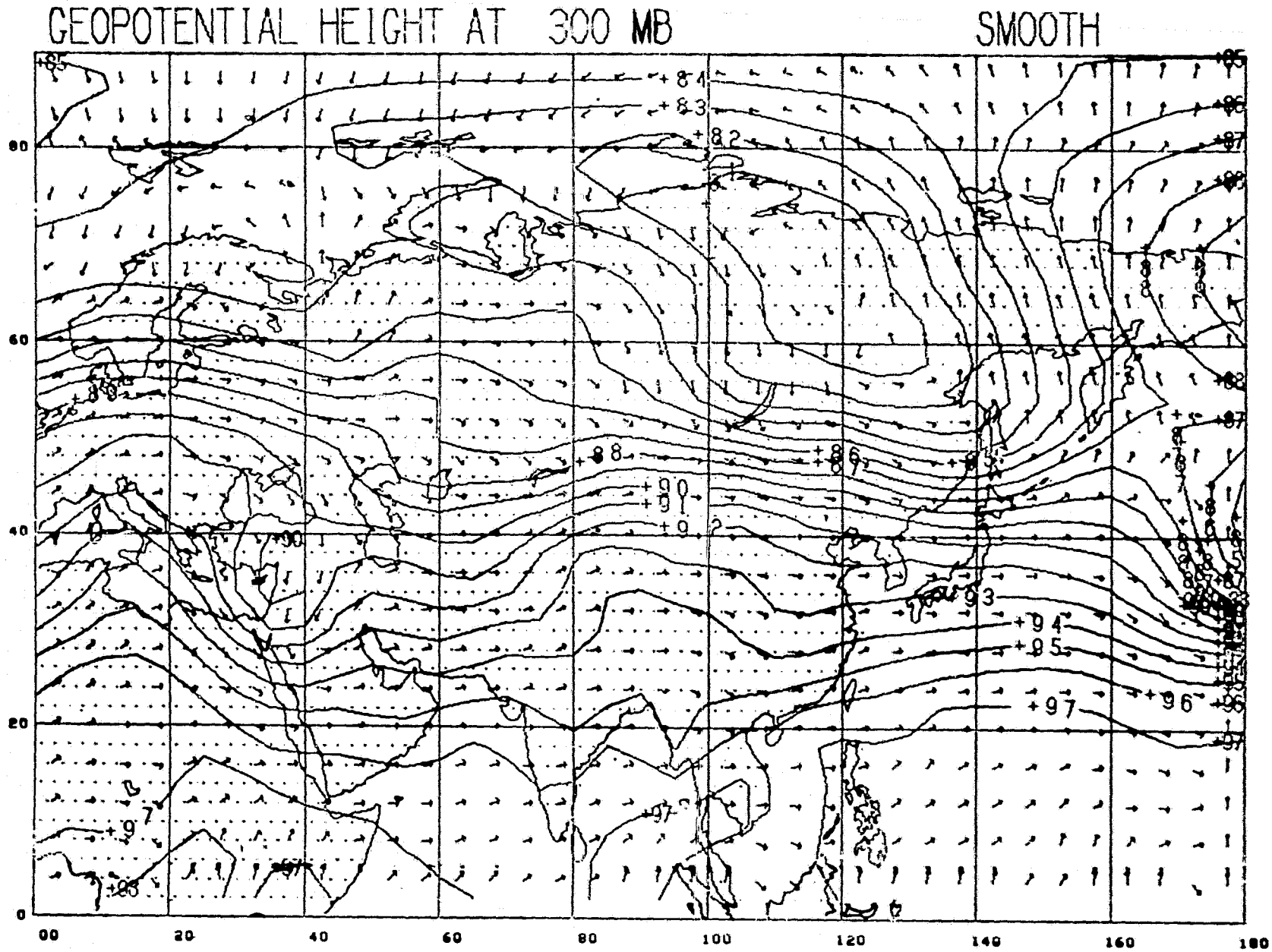

Fig. 11. GLAS 4th-order 300 mb analysis for 0000 GMT 9 January 1979.

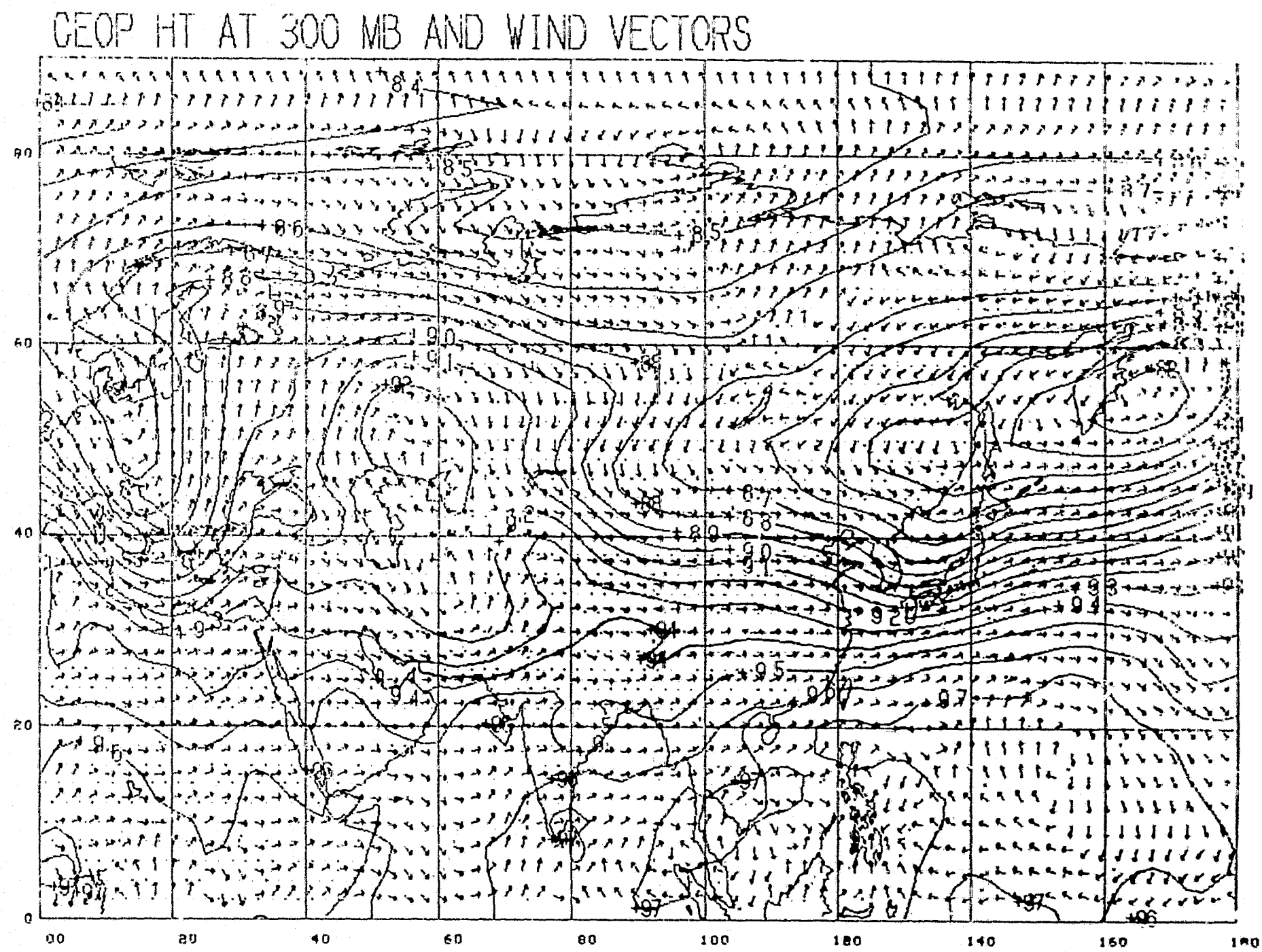

Fig. 12 NMC analysis for 0000 GMT 12 January 1979

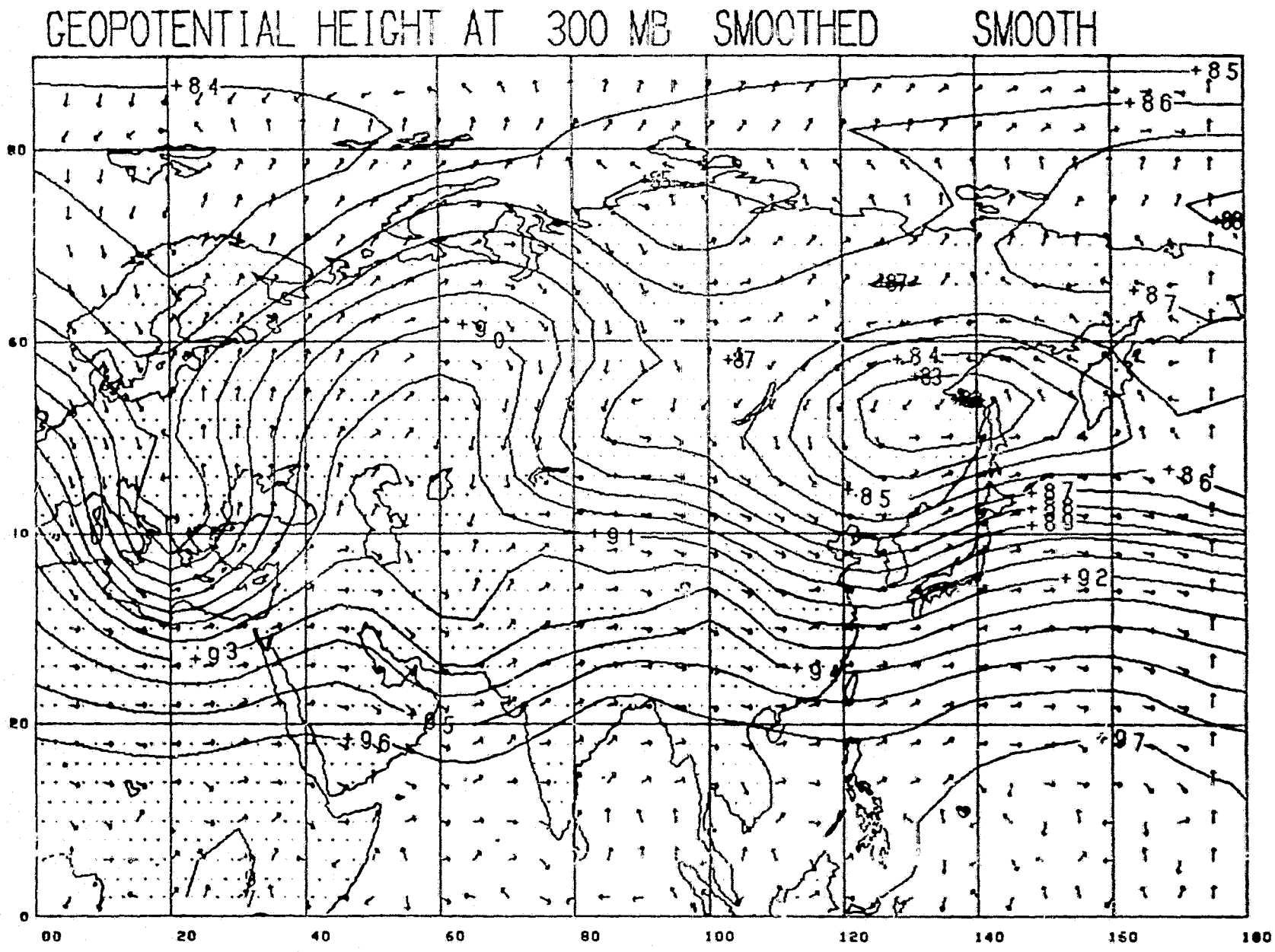

Fig. 13. GLAS 4th-order, 4° x 5°, 4-day forecast at 0000 GMT 9 January 1979.

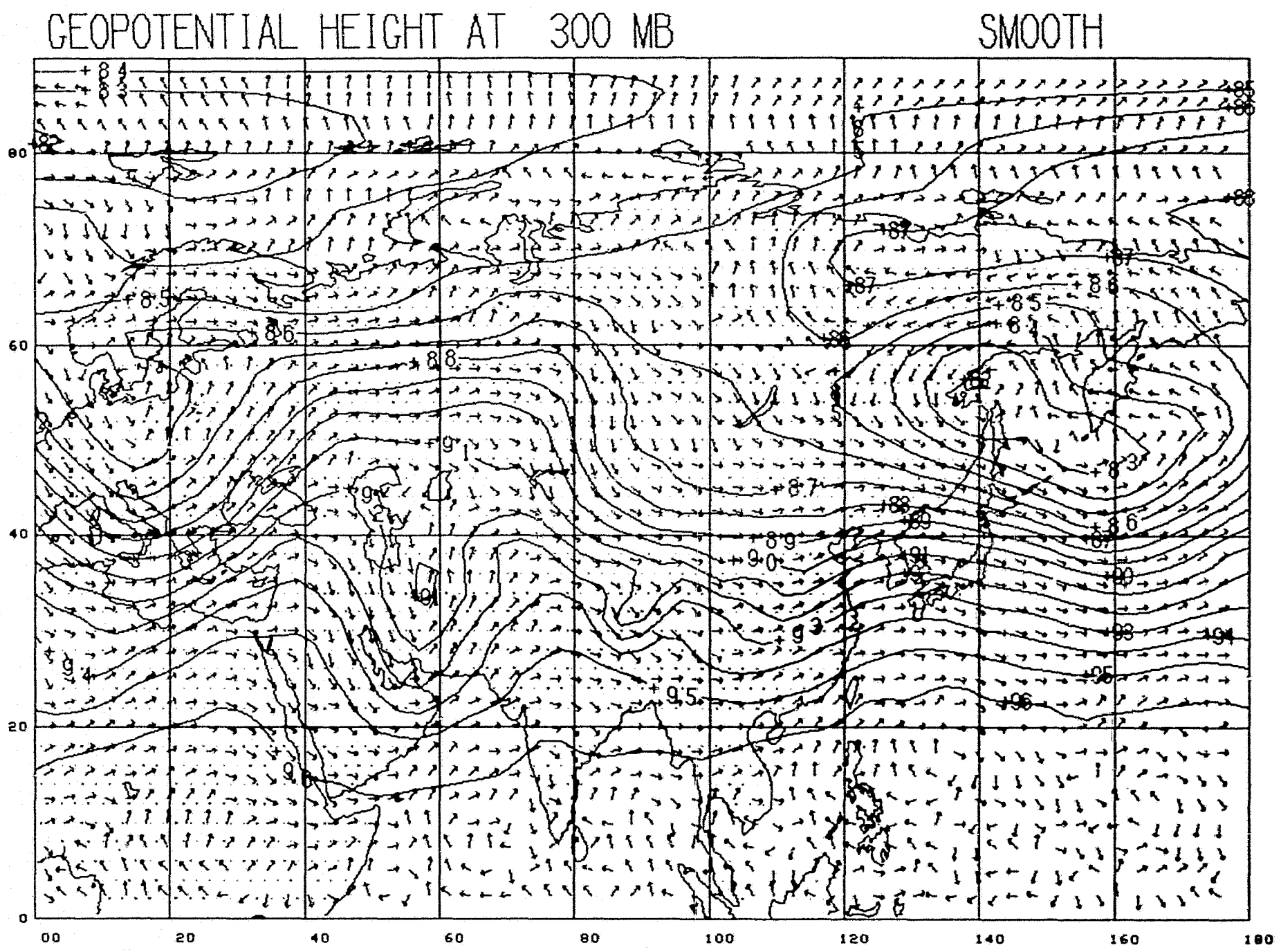

Fig. 14. GLAS 2nd-order, 2.5° x 3°, 4-day forecast at 0000 GMT 9 January 1979.

AN IMPLICIT SCHEME FOR METEOROLOGY

(E. Isaacson and D. Marchesin)

A compact implicit scheme with accuracy of 4th order in space and 2nd order in time is developed. The size of the time step is determined by the speed of the significant waves in the flow, rather than by the sound speed. For a shallow water atmospheric model over a spherical earth, the implicit scheme is shown to be more efficient than an explicit scheme, for fine grids.

Meteorological data is becoming available more densely over the earth through satellite and other soundings. Numerical methods that can use this information to make accurate and longer range forecasts are being intensively developed (e.g., Kalnay-Rivas and Hoitsma, 1979). Implicit schemes have the advantage that they do not require that the time step be decreased proportionately when the spatial interval is reduced. That is, the time step of an implicit method is chosen to be small enough to resolve time change of the motion and not the "sound" speed of the system. An efficient implicit scheme for dealing with the horizontal (longitude, latitude) shallow water atmospheric model on a spherical earth, with orography, has been tested. For each time step, the implicit scheme required slightly more than four times the number of arithmetic operations that were needed for each time step of a 4th-order explicit scheme developed by Williamson and Browning (1973). With a spatial resolution of (360/128)°, the implicit scheme required a 15-minute time step for a rapidly changing flow pattern, whereas the explicit scheme required a 3-minute time step, because of the "sound" speed. That is, for this grid of slightly less than 3°, the implicit scheme used 0.8 as much computer time as did the explicit scheme for a forecast. If the grid size were to be halved, the implicit scheme would use 0.4 as much computer time. Thus, for practical application to the primitive forecast equations, it is expected that the implicit method will be more efficient than the explicit method.

The shallow water equations can be written in divergence form by introducing the momentum variables $U = hu$ and $V = hv$, where h is the depth of the atmospheric layer and u,v the relative tangential velocity components from west to east and from south to north, respectively. That is, the equations may be written as

$$W_t + F(W)_\lambda + G(W)_\theta + E(W) = 0 \qquad (1)$$

where

$$W = \begin{bmatrix} h \\ U \\ V \end{bmatrix},$$

F, G, and E are vector functions of the components of W, and λ and θ are longitude and latitude, respectively (see Stoker and Isaacson, 1975, p. 40, with R = 0, for the momentum equations in divergence form, without orography).

By integrating Eq. (1) from $n\Delta t$ to $(n+1)\Delta t$ by the trapezoidal rule, one obtains implicit equations involving F, G, and E at W^{n+1} and at W^n. The vector functions may be linearized about W^n, which leads to the implicit system

$$[I + \frac{\Delta t}{2}(\frac{\partial}{\partial \lambda} A^n + \frac{\partial}{\partial \theta} B^n + D^n)]\Delta W^n = R^n + O(\Delta t^3) \ , \qquad (2)$$

where

$$\Delta W^n = W^{n+1} - W^n \ ,$$

A, B, D are the Jacobian matrices of F, G, E, respectively, relative to the components of W; R^n represents quantities known at time $n\Delta t$; and the partial derivatives are to be applied through ΔW^n.

In any difference approximation of Eq. (2), a two-dimensional system of linear equations is found for ΔW^n. But, it would be a formidable task to solve this system directly. Instead, by following the formulation of Beam and Warming (1976, 1977), the difference operator is factored into the product of one-dimensional operators.

$$[I + \frac{\Delta t}{2}(\frac{\partial}{\partial \lambda} A^n + K^n)]\,[I + \frac{\Delta t}{2}(\frac{\partial}{\partial \theta} B^n + L^n)]\Delta W^n = R^n + O(\Delta t^3), \qquad (3)$$

where

$$K^n + L^n = D^n \ .$$

Experiments were performed with various methods of factoring Eq. (2). The following observations were made:

(a) In some of these methods, the block tri-diagonal, periodic matrices that result by replacing the derivatives by a 4th-order rational Padé approximation have a structure that permits the 3 by 3 blocks to be treated as 2 by 2 blocks along with a scalar system.

(b) Furthermore, although the block systems are periodic, the detection of underflows in the bottom row and rightmost column of their LU decomposition makes it possible to perform the Gaussian elimination process in only about 10 percent more time than would be required for the Dirichlet data block system.

These two observations are primarily responsible for the fact that the implicit scheme required only slightly more than four times the number of arithmetic operations as are required by the explicit scheme. A 4th-order Shapiro filter is applied after each of the spatially differenced factors is "inverted." Since this filter is applied to the "change," rather than to the function W^{n+1}, no apparent dissipation of the solution is detected (see Kalnay-Rivas and Hoitsma, 1979, for discussion of such dissipative effects). A recent paper by Navon and Riphagen (1979) carries out a similar implicit procedure for the shallow water equations over a rotating rectangle, with periodic boundary conditions.

Test Calculations

The implicit scheme was tested with three kinds of initial data: the steady zonal flow, the nearly geostrophically balanced initial data derived from prescribing three subtropical highs symmetrically placed in northern and southern hemispheres, and a four-mode Haurwitz wave (see Phillips, 1959; Sadourny, 1975).

The flow resulting from the initial highs quickly developed lows (one for each high and bordering it on the east side) and the pattern moved to the west. This rapidly changing flow was a more severe test for the implicit scheme. The accuracy of the solution was estimated by comparison with the solution produced by an explicit scheme. It was found that the solution of the implicit scheme at a time step of 15 minutes agreed quite well (by overlaying contour maps) with the solution of the explicit scheme. Fig. 1 shows the contours of the initial height field with arrows indicating the initial velocity field, in a stereographic projection of the northern hemisphere. Fig. 2 shows the contours of the height field and the velocity arrows after 1 day as produced by the implicit scheme. In these calculations, no mountains were present.

Summary

An efficient two-dimensional implicit scheme has been developed for the shallow water model over the earth. The scheme conserves total mass, energy, and potential enstrophy reasonably well and, when it is required to do so, a corrective modification step can be added to ensure proper conservation as indicated in Isaacson et al. (1979). Application of the implicit technique to the primitive equation model is being developed. Here it is planned to use time-splitting to aid in separating the vertical dimension from the tangential dimensions.

Acknowledgment

The authors were supported in part under NASA Research Grant NSG-5034. Professor Isaacson was supported in part under DOE Contract EY-76-C-02-3077. The DOE computing facility at the Courant Institute was used for some of the numerical experiments. The computing facility of the Laboratory for Atmospheric Sciences was used for most of the numerical experiments.

References

Beam, R. M., and R. F. Warming, 1976: An implicit finite-difference algorithm for hyperbolic systems in conservation-low form. J. Comp. Phys., 22, 87-110.

_____, and _____, 1977: An implicit factored scheme for the compressible Navier-Stokes Equations. AIAA Third Comp. Fl. Dyn. Conf., Paper No. 77-645, 130-140, Albuquerque, New Mexico, June.

Isaacson, E., D. Marchesin, and G. Zwas, 1979: Numerical methods for meteorology and climatology. NASA Conf. Publ. 2076, Fourth NASA Wea. and Clim. Prog. Sci. Rev., 183-190, Greenbelt, Maryland.

References (Continued)

Kalnay-Rivas, E., and D. Hoitsma, 1979: The effect of accuracy, conservation and filtering on numerical weather forecasting. AMS Fourth Conf. on Numerical Weather Prediction, Silver Spring, Maryland, 29 October-1 November, Preprint Volume, 302-312.

Navon, I. M., and H. A. Riphagen, 1979: An implicit compact fourth-order algorithm for solving the shallow-water equations in conservation-low form. Mon. Wea. Rev., 107, 1107-1127.

Phillips, N. A., 1959: Numerical integration of the primitive equations on the hemisphere. Mon. Wea. Rev., 87, 333-345.

Sadourny, R., 1975: Compressible model flows on the sphere. J. Atmos. Sci., 32, 2103-2110.

Stoker, J. J., and E. Isaacson, 1975: Research in Climatology. Final Report, I., Courant Inst. Rep. IMM-407, 76 pp.

Williamson, D. L., and G. L. Browning, 1973: Comparison of grids and difference approximations for numerical weather prediction over a sphere. J. Appl. Meteor., 12, 264-274.

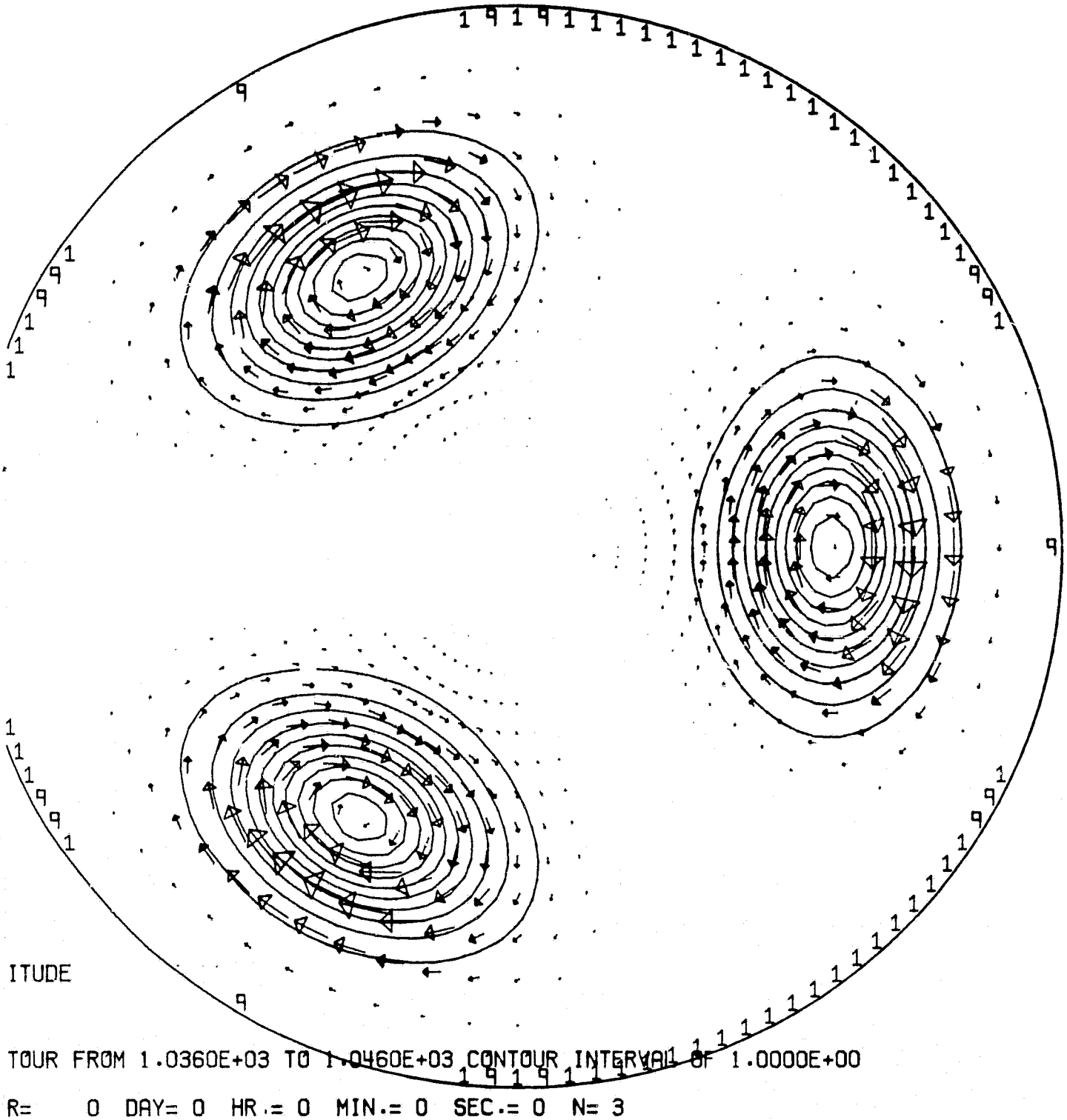

Fig. 1. Contour levels of initial height field, from h = 8500 m to h = 8585 m. Maximum initial geostrophic velocity is about 13 m/s. Arrow size is proportional to speed.

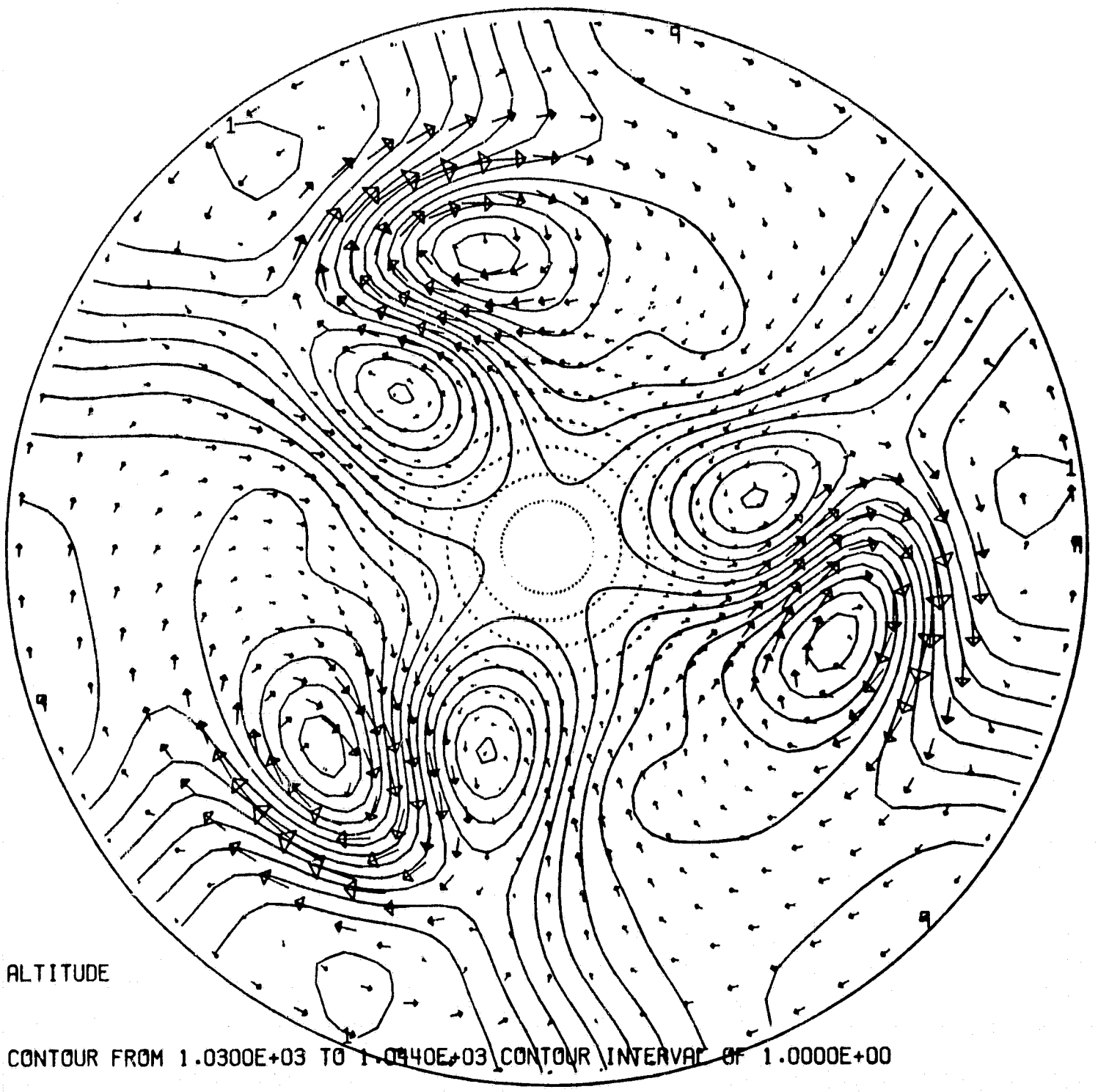

Fig. 2. Contour levels of height field and velocity vectors after 1 day, with same scale as in Fig. 1.

A LANGEVIN EQUATION FOR LARGE-SCALE ATMOSPHERIC FLOW

(M. Ghil and R. Balgovind)

The purpose of this study is to derive on a theoretical basis optimal interpolation coefficients for the assimilation of the First GARP Global Experiment (FGGE) data. In the process, hopefully, a better understanding of the stochastic-dynamic behavior of large-scale motions of the atmosphere will be obtained. Previous attempts at modeling the statistics of atmospheric fields in a systematic way by multi-dimensional autoregressive processes have been made by Thiebaux (1977, and references therein). A general theory of statistical interpolation on the sphere with application to meteorological problems is in the process of being formulated by Wahba (1979, and references therein).

The short-time dynamics of extratropical large-scale atmospheric flow are governed by the conservation equation of potential vorticity:

$$(d/dt)(\nabla^2-\lambda^{-2})\phi = 0 . \qquad (1)$$

In it, d/dt is the material derivative, ∇^2 the horizontal Laplacian, λ the Rossby radius of deformation, and ϕ the height of the 500 mb pressure surface. The radius λ, $\lambda^2 = \Phi/f^2$, represents a characteristic length scale of quasi-geostrophic flow, with Φ a characteristic magnitude of ϕ and $f = 2\Omega \sin\phi$ the Coriolis parameter, Ω being the angular velocity of the earth and θ latitude. A stochastic perturbation of this equation on the sphere, for an atmosphere near geostrophic equilibrium, is considered:

$$(\nabla^2 - \lambda^{-2})\phi = W , \qquad (2)$$

where W is uncorrelated white noise representing smaller scale nongeostrophic phenomena; more precisely, $E\,W(\nu,\theta) = 0$, $E\,W(\nu+\nu', \theta+\theta')W(\nu,\theta) = \sigma^2\,\delta(\nu',\theta')$, with E the expectation operator, ν longitude, and σ^2 a prescribed variance.

Numerical solutions of Eq. (2) for different values of the parameter are obtained. A comparison is made of $R_N(\nu';\theta) = E_N\,\phi(\nu+\nu',\theta)\,\phi(\nu,\theta)$ with the corresponding spatial correlations of the atmospheric temperature field, obtained from satellite observations during the Data Systems Test, DST-6 (February 1976), for FGGE (Ghil et al., 1979). Here E_N is the finite-sample correlation based on N realizations of the equation.

The major feature of the data (Fig. 2 of Ghil et al., 1979), namely, a general $R_N(s;\theta) \sim \exp(-s/s_0(\theta))$ behavior, is reproduced by the solutions of Eq. (2), with $s_0(\theta) \sim f \sim \sin\theta$. For realistic values of Φ, the fit between solution correlations and data correlations is rather good (Fig. 1). This seems to indicate that a single vertical mode strongly dominates the error structure of the temperature field.

The theoretical correlation function for Eq. (2) has also been obtained, i.e., $R(s;\theta)=\lim_{N\to\infty} R_N(s;\theta)$. This will be further compared with the error structure of other atmospheric fields, namely, geopotential heights

at 500 mb and at 850 mb, and sea level pressures, using the 15-year NMC data set, as well as recent FGGE data. Furthermore, the full baroclinic version of Eqs. (1,2) will be considered, and the contribution of the different vertical modes to the error structure analyzed.

Acknowledgment

It is a pleasure to acknowledge useful discussions with E. Isaacson, C. E. Leith, G. Papanicolaou, J. Shukla, H. J. Thiebaux, and G. Wahba. E. Kalnay-Rivas suggested the dynamical interpretation (1) of Eq. (2) and provided continuous encouragement.

References

Ghil, M., M. Halem, and R. Atlas, 1979: Time-continuous assimilation of remote-sounding data and its effect on weather forecasting. Mon. Wea. Rev., 107, 140-171.

Thiebaux, H. J., 1977: Extending estimation accuracy with anisotropic interpolation. Mon. Wea. Rev., 105, 691-699.

Wahba, G., 1979: Spline interpolation and smoothing on the sphere. Tech. Rep. No. 584, Dept. of Statistics, Univ. of Wisconsin, Madison, 38 pp.

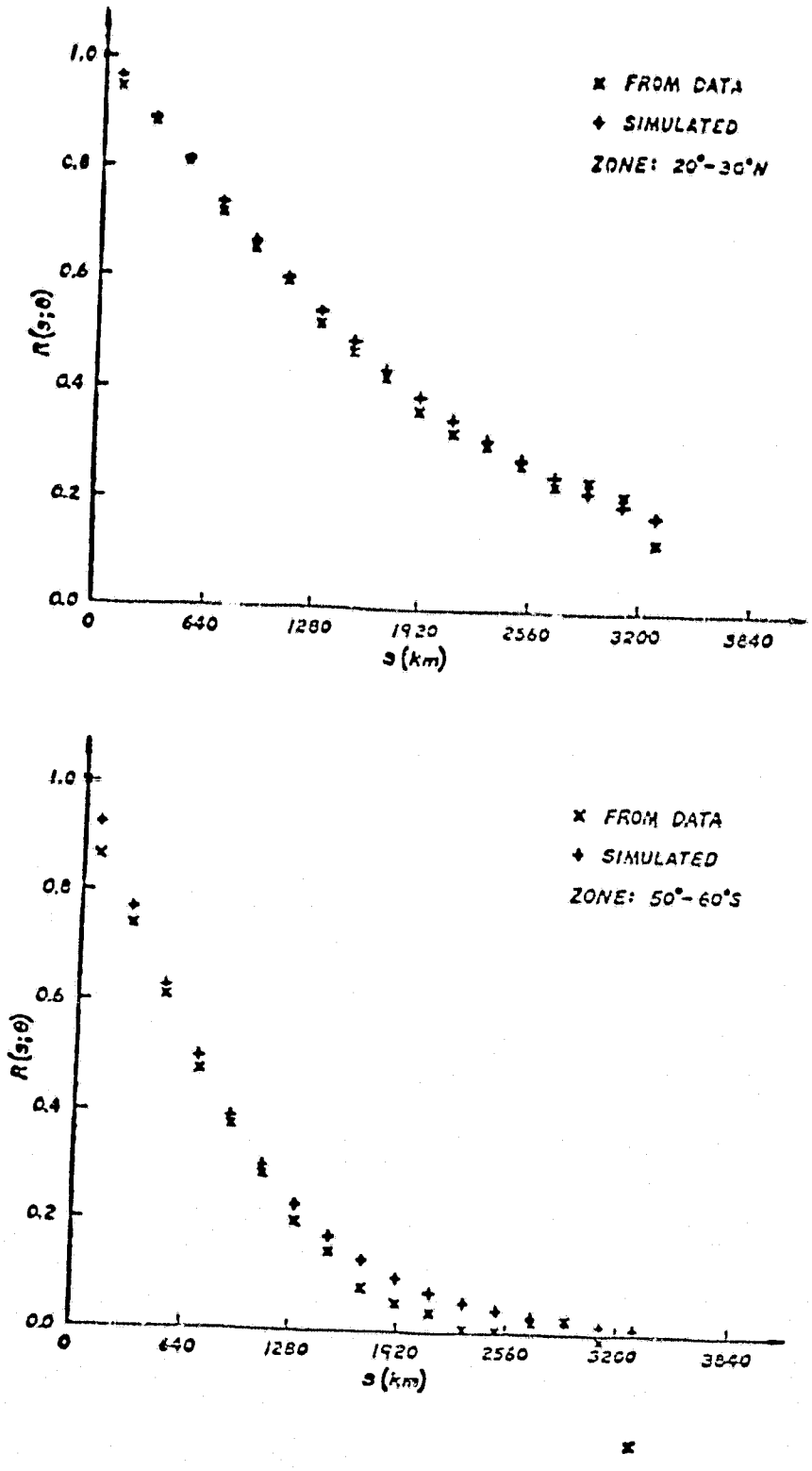

Fig. 1. A comparison of the correlation function R(s;θ), obtained from Eq. (2) (identified by +), with the correlation function computed from DST-6 data (see Ghil et al., 1979, for details) (identified by x). For some 10° lat. bands near the poles and the equator, the fit between theoretical (+) and observed (x) correlation functions was not as good. The two zones shown are typical, though, of the goodness of fit for subtropical and mid-latitude bands.

APPLICATIONS OF ESTIMATION THEORY TO NUMERICAL WEATHER PREDICTION

(M. Ghil, J. Tavantzis, K. Bube, and E. Isaacson)

Numerical weather prediction (NWP) is an initial-value problem for a system of nonlinear partial differential equations (PDEs) in which the initial values are known only incompletely and inaccurately. Data at initial time are supplemented, however, by observations of the system distributed over a time interval preceding it. Estimation theory has been successful in approaching such problems for models governed by systems of ordinary differential equations (ODEs) and of linear PDEs. An attempt to apply it to NWP is being made.

A model exhibiting many features of large-scale atmospheric flow important in NWP is the one governed by the shallow-fluid equations. Currently, the estimation problem for a linearized version of these equations is being studied (Ghil and Tavantzis, 1978). A discrete Kalman-Bucy (K-B) filter is applied to a finite-difference version of the equations, which simulates the numerical models used in NWP. The filter has been modified in order to eliminate fast inertia-gravity waves in the solution, as well as reduce the error in the estimate of the atmospheric state. The vector of observations corresponds to the different atmospheric quantities measured and space-time patterns associated with conventional and satellite-borne meteorological observing systems.

The specific character of the equations' dynamics gives rise to the necessity of modifying the usual K-B filter. The modification consists in eliminating the high-frequency inertia-gravity waves which would otherwise be generated by the insertion of observational data. The modified filtering procedure developed here combines in an optimal way dynamic initialization (i.e., elimination of fast waves [Baer and Tribbia, 1977; Ghil et al., 1977; Ghil, 1980]) and four-dimensional (space-time) assimilation of observational data (Bengtsson, 1975; Ghil et al., 1979; Bube, 1978), two procedures which traditionally have been carried out separately in NWP.

Optimal error reduction in the initial-state estimate is studied for the different observation patterns. Comparisons between the modified filter and the standard K-B filter have been made. Also the filter discussed will be compared with operational methods of four-dimensional data assimilation currently used by meteorological services.

References

Baer, F., and J. J. Tribbia, 1977: On complete filtering of gravity modes through nonlinear initialization. Mon. Wea. Rev., 12, 1536-1539.

Bengtsson, L., 1975: Four-Dimensional Assimilation of Meteorological Observations, GARP Publ. Series, No. 15, WMO Int'l. Council of Scient. Unions, Geneva, Switzerland, 76 pp.

Bube, K. P., 1978: The Construction of Initial Data for Hyperbolic Systems from Nonstandard Data, Ph.D. Thesis, Stanford Univ., 114 pp. (Available from Univ. Microfilms Int'l., Ann Arbor, Michigan 48106.)

References (Continued)

Ghil, M., 1980: The compatible balancing approach to initialization, and four-dimensional data assimilation. Tellus, in press.

_____, M. Halem, and R. Atlas, 1979: Time-continuous assimilation of remote-sounding data and its effect on weather forecasting. Mon. Wea. Rev., 107, 140-171.

_____, B. Shkoller, and V. Yangarber, 1977: A balanced diagnostic system compatible with a barotropic prognostic model. Mon. Wea. Rev., 105, 1223-1238.

_____, and J. Tavantzis, 1978: Recursive estimation for numerical weather prediction. NASA Tech. Memo. 80253, 34-41, Atmos. and Oceano. Res. Rev.-1978, NASA Goddard Space Flight Center, Greenbelt, Maryland.

INTEGRATED AND SPECTRAL ENERGETICS OF THE GLAS GCM

(J. Tenenbaum)

Analysis of the generation, transport, and dissipation of energy represents one of the primary methods of studying geophysical fluid flows. Lorenz proposed subdividing atmospheric energy into kinetic and available potential forms and in turn subdividing these into zonal kinetic (KO) and eddy kinetic (KE) categories. Further subdivision in the spectral domain was suggested by Saltzman (1970) and followed by similar observational and model studies (Tenenbaum, 1976; Baker et al., 1978). One purpose of this project is to examine both the integrated and spectral energetics for two versions of the GLAS general circulation model.

The most direct test of a model over a period of several days is the quality of the prediction of standard meteorological variables. One knows that this approach should theoretically give an essentially random result at a predictability limit on the order of 14 days, and in practice does so in about 5 days.

To extract further information in spite of these limits, one employs various space and time averages applied to both meteorological variables and energetics quantities. These averaged quantities may show skill for periods approaching the predictability limit; indeed, current general circulation models are characterized by quite reasonable model "climates." In this project, we will examine to what extent low wave number spectral quantities may qualify as "averaged" quantities.

Central results of this project concern the interplay of the eddy kinetic energy and its spectral subcomponents. Figs. 1 and 2 show the observational and model values of KO and KE for the first 2 weeks of each time period for two sets of model runs. Figs. 1a and 1b refer to a GLAS model with no filtering of diagnostic variables and a radiation routine comparable to the GISS version of the model (Somerville et al., 1974). Figs. 2a and 2b refer to a GLAS model with filtering of diagnostic variables and a new radiation routine due to Wu.

For the no-filtering version, the KE agreement for January 1977 (Fig. 1a) is quite good. Note that for the KE rise in January 1977 there appears to be a 1-day lag. A reasonable interpretation is the clear evidence of predictive skill in an averaged quantity out to the predictability limits. With the same model for January 1975 (Fig. 1b), the observational KE dip is not followed downward.

For the filtered version of the model, this same case (January 1975) is well modeled (Fig. 2a). The accurate tracking of the dip in KE is a result which is consistent with the filtering out of extraneous small-scale energy. A second filtered case, however, shows far less success: for January 1976 (Fig. 2b), the model seems unable to generate the KE needed to follow the atmosphere's rise.

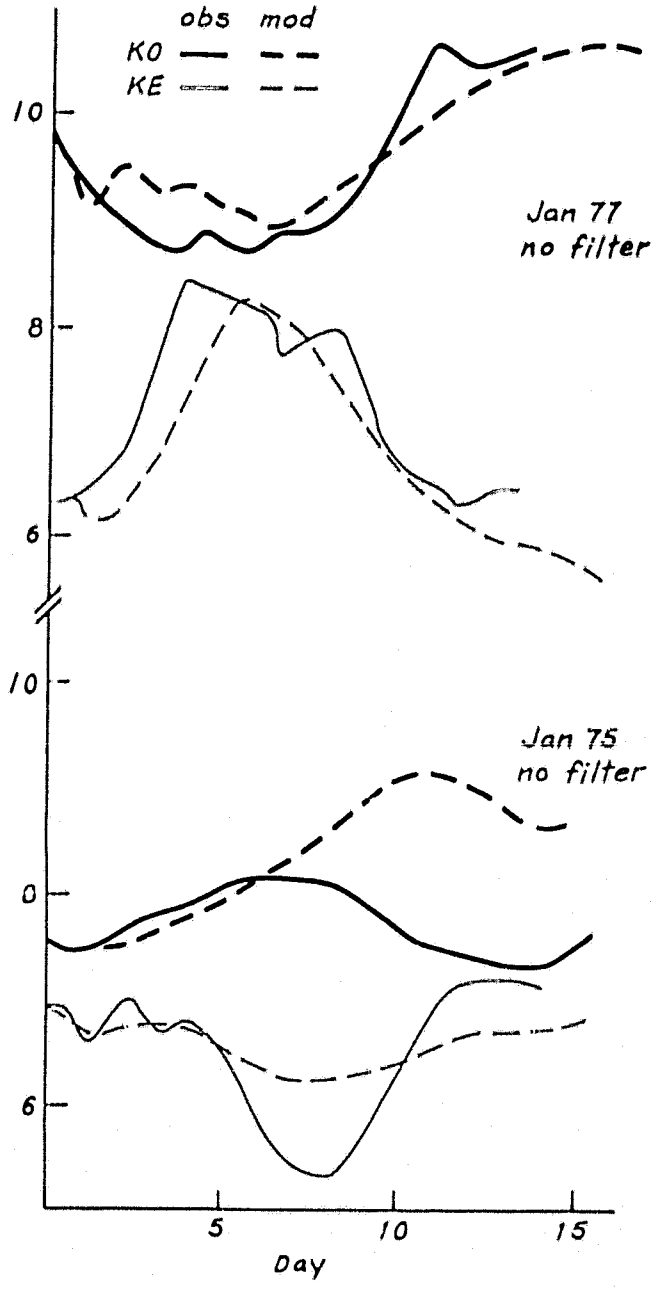

Fig. 1. Time history of the tropospheric mean kinetic energy, KO, and eddy kinetic energy, KE, for the first two weeks of each case using an unfiltered model. (a) January 1977 (b) January 1975. Units $10^5 J/m^2$.

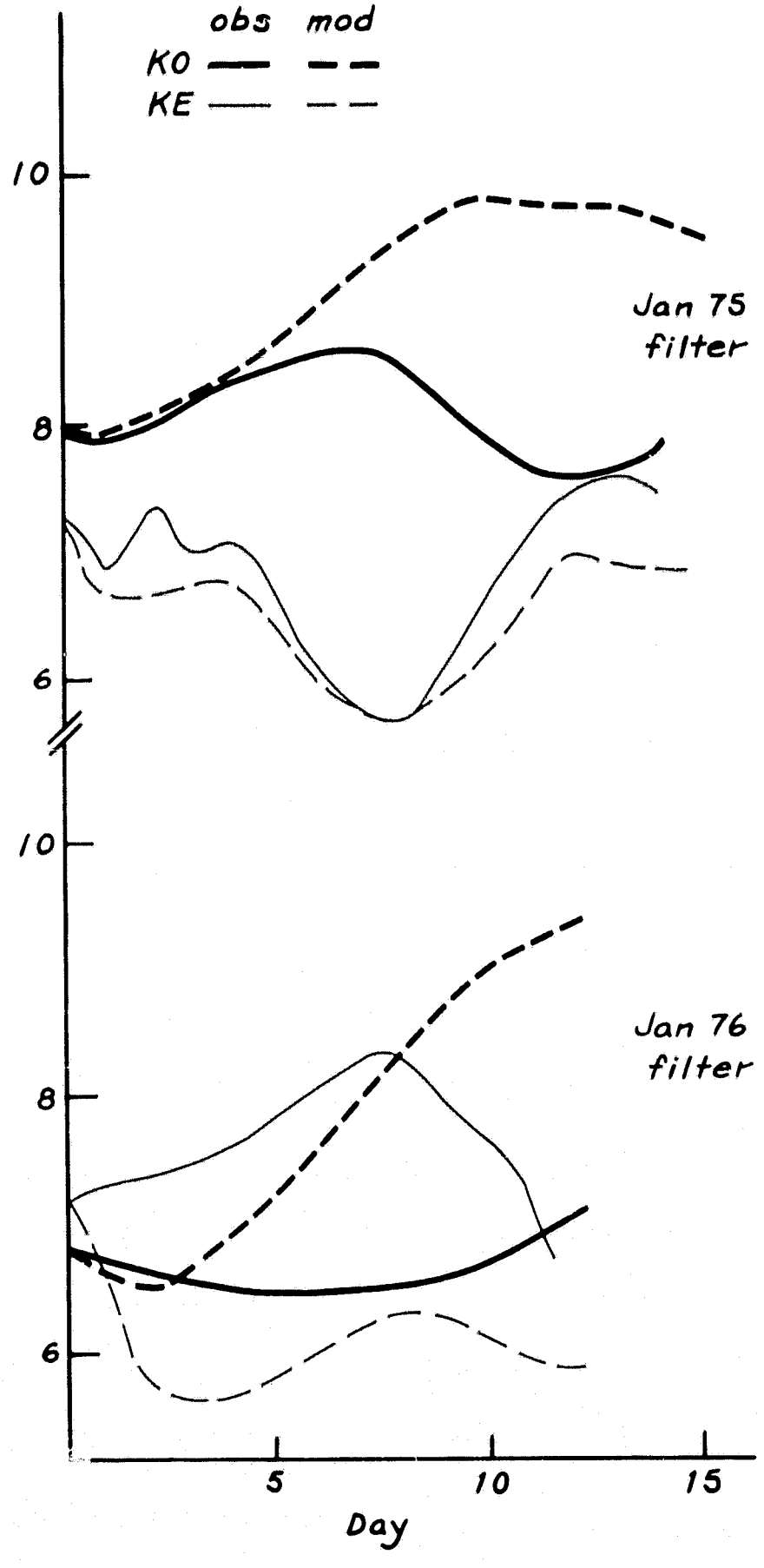

Fig. 2. Same as Fig. 1 using a filtered model: (a) January 1975; (b) January 1976. Units 10^5 J/m^2.

One uniform pattern does appear in KO for both versions. The initial states consist of one low KO state (January 1976), one average KO state (January 1975), and one strikingly high KO state (January 1977). The latter case is unusual and was sustained at, or near, this high value throughout the 2 weeks. Both models, in contrast, for the four cases have only one pattern: monotonic growth. Some of the success of January 1977 is clearly due to the atmosphere happening to match this built-in bias of the model.

Upon studying spatial displays of KO, excess energy is found collecting in the model's topmost layer. Since there are no significant dissipative mechanisms at that level, the excess energy appears to remain trapped there, functioning as a source of the model's total KE, but feeding the individual wave numbers erroneously. As shown, a related study in conjunction with E. Kalnay-Rivas of GLAS, this effect is an initial condition shock which induces major oscillations over periods from 2 h to 4 days. Enhanced vertical resolution near the tropopause decreases the amplitude of the initial shock.

In striking contrast to the successful KE predictions for January 1975 and January 1977 is the behavior of the individual K_n, the coefficient of kinetic energy for wave number n. One can isolate the one or two dominant wave numbers with little difficulty. Fig. 3 shows the time history of K_1 and K_3 for January 1977. In spite of the noisier signal, one sees a much more discrepant behavior with gross errors at times when the summed KE remains correct. Note particularly the behavior of n = 3. In terms of model development, the fundamental question is "What process or processes in the model are producing the difficulties?"

In terms of Saltzman's spectral energetics analysis, one can imagine two possibilities: (1) erroneous transports in or out of the northern hemisphere troposphere, or (2) erroneous conversions from zonal potential or kinetic energy. A third possibility, erroneous transports within the northern hemisphere troposphere, should not logically affect the results since integrated quantities are considered. Such erroneous transports may, however, be suggestive of other problems. Inevitably, the sorting out of cause and effect will probably be difficult.

For January 1977, there is evidence of transport difficulties. Northward transport starts in the subtropics and feeds first the large K_3 peak at 38N, and then the stratospheric warming at 50N. For January 1975, evidence indicates erroneous conversion in the term expressing nonlinear redistribution of energy to wave number 3 from all other wave numbers (Saltzman's L). At the time (2 January 1975) when K_3 for observation and model are just starting to diverge, one sees a discrepancy centered at 36N and 285 mb. No corresponding effect appears before the much stronger n = 3 divergence of 6 January 1977. No other conversion term shows significant causal discrepancies though a fair number of correlations are observed, i.e., D_3 (the dissipation in wave number 3) showing significant disagreements when K_3 does.

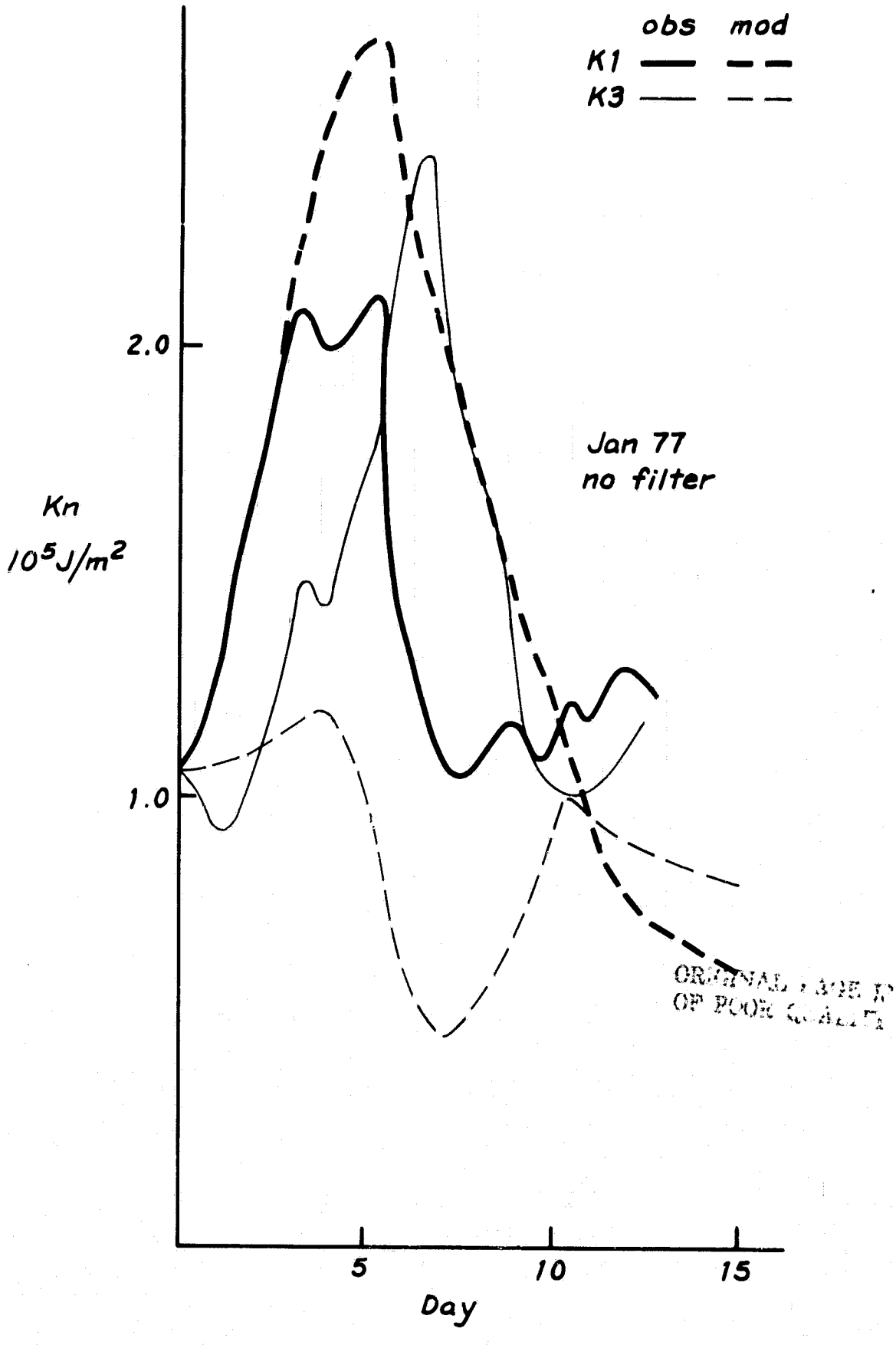

Fig. 3. Time history of eddy kinetic energy of wavenumbers 1 and 3 for January 1977. Units 10^5 J/m^2.

C-2

Some general questions remain concerning the consistency of results obtained from Saltzman's spectral energetics analysis. The equations themselves are not in question but rather the quality of results from their application to either model or observational data. Saltzman's equations provide a closed system with respect to conversions into and out of individual K_n. The algebraic sum of the conversions integrated over an appropriate space and time period should equal the secular change in the corresponding K_n. While such a result requires assuming the validity of dissipation calculations, D, the lack of agreement gives some sense of overall confidence in the results. Because of the unavailability of independent data for D, Saltzman had to calculate it only as a residual.

The results are not encouraging. Table 1 presents this type of calculation for a sampling of model and observational runs. For most cases, the sign of the change is incorrect and, in some cases, the individual K_n should have been driven solidly and unphysically negative. Three possible explanations seem most likely: errors in Cn, Dn, and in the vertical transports. The conversion Cn and, to a lesser extent, some others depend on the vertical velocity, W. For the observations, this is a notoriously difficult quantity to evaluate. Dn is a parameterized quantity whose physical basis is known in broad terms but whose detailed quantitative evaluation requires confidence in surface winds and boundary layer effects. Vertical transports are clearly a problem for the model and may be a problem for the observations.

The vertical velocity problem is being examined in detail in a subsequent paper (Tenenbaum and Reddi, 1980, to be published). Preliminary results show that alternate formulations for omega (changing from mass convergence to iterative solution of the diagnostic omega equation) can yield major changes in long- and synoptic-scale values of Cn and extensive smoothing of the higher wave numbers.

The model's medium-range skill and climatology using various possible integrated quantities have been studied. Major conclusions are as follows:

(1) The model can show medium-range skill in an integrated quantity, KE, the northern hemisphere tropospheric eddy kinetic energy, out to the predictability limit of 2 weeks. When the atmosphere's KO matches the model's bias towards monotonic growth in KO, the predictions are most successful.

(2) The model retains a bias in accumulating KO in the topmost, stratospheric level and in the initial monotonic growth of tropospheric KO.

(3) Low wave number spectral coefficients appear questionable in the role of integrated energetics quantities: KE can show agreement while individual Kn are erroneous. An expanded version of Saltzman's spectral analysis (including transports) does provide a useful tool in showing cause-and-effect relations for where the model is failing to match significant energy flow in the atmosphere. In the near future, more synoptic cases will be studied, both randomly chosen, and specially chosen to explore synoptic dependence.

Table 1. Conversions to and from K_3 for wave number 3 for January 1975 (5 to 7 days) and January 1977 (3 to 6 days).

Conversions to and from K_3 (W/m^2)	January 1975 (5 to 7 days)		January 1977 (3 to 6 Days)	
	Observations	Model	Observations	Model
$+C(P_3,K_3) = C_3$	-0.3	0	-0.5	0.3
$+C(K_n,K_3) = L_3$	0	-0.3	0.3	0
$-D_3$	0.1	0.1	0.25	0.25
$-C(K_3,K_0) = M$	0.2	0.4	0.1	0.3
Net conversion (W/m^2)	-0.6	-0.8	-0.55	0.25
X time (sec)	1.7×10^5	1.7×10^5	2.6×10^5	2.6×10^5
Net conversion (10^5 J/m^2)	-1.0	-1.4	-1.3	0.7
K_3 (final)	1.5	1.5	2.5	0.5
$-K_3$ (initial)	0.6	1.5	1.5	1.2
Net change (10^5 J/m^2)	0.9	0	1.0	-0.7

References

Baker, W. E., E. C. Kung, and R. C. J. Somerville, 1978: An energetics analysis of forecast experiments with the NCAR general circulation model. Mon. Wea. Rev., 106, 311-323.

Saltzman, B., 1970: Large scale atmospheric energetics in the wavenumber domain. Rev. Geophys. Space Phys., 8, 289-302.

Tenenbaum, J., 1976: Spectral and spatial energetics of the GISS model atmosphere. Mon. Wea. Rev., 104, 15-30.

_____, and M. Reddi, 1980: In preparation to be submitted to Mon. Wea. Rev.

III. CLIMATE

FRACTIONAL CLOUDINESS AND VARIABLE CLOUD EMISSIVITY IN THE GLAS GCM

(G. F. Herman and V. Krishnamurthy)

The recent analysis of cloud-radiation experiments conducted with the GLAS GCM (cf. Herman et al., 1980) clearly pointed to the fact that the average infrared opacity of the GLAS model atmosphere was too large. This is attributed to two factors: First, since all model clouds, including those which are intended to represent cirrus clouds in nature, are assumed to have unit emissivity (zero transmissivity), the model did not transmit enough long wave radiation to space. Secondly, all model clouds, including those intended to represent subgrid scale cumulus convection, were assumed in the radiation calculation to occupy the entire 4° latitude by 5° longitude grid area. The net result of both of these features of the radiation calculation was to maintain an excessively positive global radiation balance, and possibly have a detrimental effect on such dynamical processes as the formation of the Siberian anticyclone.

If the spectra of atmospheric absorbers, namely water vapor and cloud droplets, are uncorrelated (cf. Goody, 1964, p. 123), then a particularly simple treatment of both variable cloud emissivity and fractional cloudiness follows from the so-called multiplicative property.

Suppose that f is the fraction of a grid square that contains any cloud at any level, and also that f is constant with respect to height. Then the flux, $\overline{F}_c$, at any height, z, in this cloudy region is

$$\overline{F}_c(z) = \overline{T}_c(0,z)\,\pi(B(0) - B_g) - \int_0^\infty \overline{T}_c(z,z')\,\pi\frac{dB(z')}{dz'}\,dz' \quad , \tag{1}$$

where T_c is the frequency-averaged transmittance that includes the presence of the cloud droplets, B is the Planck intensity, and B_g corresponds to the temperature of the ground.

For cloud-free regions of the atmosphere, the net flux due to gaseous absorption, F_g, is

$$\overline{F}_g(z) = \overline{T}_g(0,z)\,\pi(B(0) - B_g) - \int_0^\infty \overline{T}_g(z,z')\,\pi\frac{dB(z')}{dz'}\,dz' \quad , \tag{2}$$

where the mean transmittance, $\overline{T}_g$, accounts only for gaseous absorption. We define the average flux, F, of the partially cloudy region as the weighted mean,

$$F = fF_c + (1-f)F_g \quad . \tag{3}$$

Then from (1) and (2)

$$F = \pi(B(0) - B_g)\,[f\bar{T}_c\,(0,z) + (1-f)\bar{T}_g(0,z)] - \int_0^\infty \pi \frac{dB(z')}{dz'} dz'\; f\bar{T}_c(z,z') + (1-f)\bar{T}_g(z,z')] \quad . \tag{4}$$

The bracketed term $[f\bar{T}_c + (1-f)\bar{T}_g]$ represents the average transmittance of the partially cloudy regions.

Using the multiplicative property, the mean transmittance, $\bar{T}$, of the cloud-plus-gas mixture is

$$\bar{T}(z,z') = \bar{T}_g(z,z') \times \bar{T}_c(z,z') \quad . \tag{5}$$

The <u>effective</u> transmittance, $\bar{T}_e$, of the partially clouded region is thus

$$\bar{T}_e = \bar{T}_g(1-f+f\bar{T}_c) \quad . \tag{6}$$

Equation (4) becomes simply

$$F = \pi(B(0) - B_g)\bar{T}_e - \int_0^\infty dB(z')\;\bar{T}_e(z,z') \quad . \tag{7}$$

Equation (7), as derived, applies only to the situation where cloud fraction does not vary with height. However, it is readily generalized to account for cloud fractions that may vary from layer to layer.

The transmittance of the cloud may thus be adjusted directly in the term $\bar{T}_c$. Note that the cloud fraction and cloud transmissivity occur as a product; the average opacity of the atmosphere may be adjusted by alternatively varying the cloud fraction or the cloud emissivity.

Table 1 illustrates the effect that variable cloud fraction and cloud transmissivity have on fluxes and cooling rates. Here f denotes the fractions of a grid square that contains any cloud, and T_c the cloud transmissivity. Thus, f=0 corresponds to a completely clear grid, while f=1.0 corresponds to a complete overcast. Similarly $\bar{T}_c$=0 corresponds to a completely transparent cloud, while $\bar{T}_c$=1.0 denotes a cloud that is perfectly opaque. For illustration it is assumed that a single cloud layer is found in layer 5. The effect of the cloud on the fluxes is shown in upper section of Table 1. As the average opacity increases due to either increasing the fraction or decreasing the transmittance, the net flux beneath the cloud layer decreases monotonically, which is due to the enhanced downward flux. The flux <u>above</u>

the cloud layer also diminishes with increasing opacity because the upward radiation is less intense, having originated at comparably colder temperatures.

The effect on cooling rates is illustrated in the lower section of Table 1. Cooling below the cloud is smaller as the opacity increases because of the decreased importance of cooling to space. Cooling at and above the cloud increases with increasing opacity. These dependencies are illustrated in Fig. 1.

When introduced to the GLAS GCM, the cloud fraction, f, will likely be a parameter to which the model's radiation and dynamics are very sensitive. Clearly, a major problem will be in determining the most realistic value of this parameter.

Reference

Goody, R. M., 1964: Atmospheric Radiation. Oxford University Press.

Herman, G. F., M. L. Wu, and W. T. Johnson, 1980: The effect of clouds on the earth's solar and infrared radiation budgets. To appear in J. Atmos. Sci.

Table 1. Clouds in layer 5. Latitude = 46°, Day = 1 February.

Level	Pressure (mb)	Flux(W m^{-2})				
		Cloudless $f=0.0, \overline{T}_c=1.0$	$f=0.25, \overline{T}_c=0.0$ or $f=1.0, \overline{T}_c=0.75$	$f=0.5, \overline{T}_c=0.0$ or $f=1.0, \overline{T}_c=0.5$	$f=0.75, \overline{T}_c=0.0$ or $f_c=1.0, \overline{T}_c=0.25$	$f=1.0$ $\overline{T}_c=0.0$
1	10	211	195	179	164	148
2	120	205	189	173	157	141
3	230	197	181	164	148	131
4	340	187	170	153	136	119
5	450	170	152	134	116	98
6	560	151	126	100	75	49
7	670	134	113	92	72	51
8	780	118	101	83	66	48
9	890	104	89	74	59	44
10	1000	90	77	64	51	39

Layer	Pressure at Center of Layer (mb)	Cooling Rate (°C/Day)				
		Cloudless $f=0.0, \overline{T}_c=1.0$	$f=0.25, \overline{T}_c=0.0$ or $f=1.0, \overline{T}_c=0.75$	$f=0.5, \overline{T}_c=0.0$ or $f=1.0, \overline{T}_c=0.5$	$f=0.75, \overline{T}_c=0.0$ or $f=1.0, \overline{T}_c=0.25$	$f=1.0$ $\overline{T}_c=0.0$
1	65	0.4	0.5	0.5	0.5	0.6
2	175	0.6	0.6	0.7	0.7	0.7
3	285	0.8	0.9	0.9	0.9	0.9
4	395	1.3	1.4	1.4	1.5	1.6
5	505	1.4	2.0	2.6	3.2	3.8
6	615	1.3	1.0	0.6	0.2	-0.2
7	725	1.2	1.0	0.7	0.5	0.2
8	835	1.1	0.9	0.7	0.5	0.3
9	945	1.1	0.9	0.8	0.6	0.4

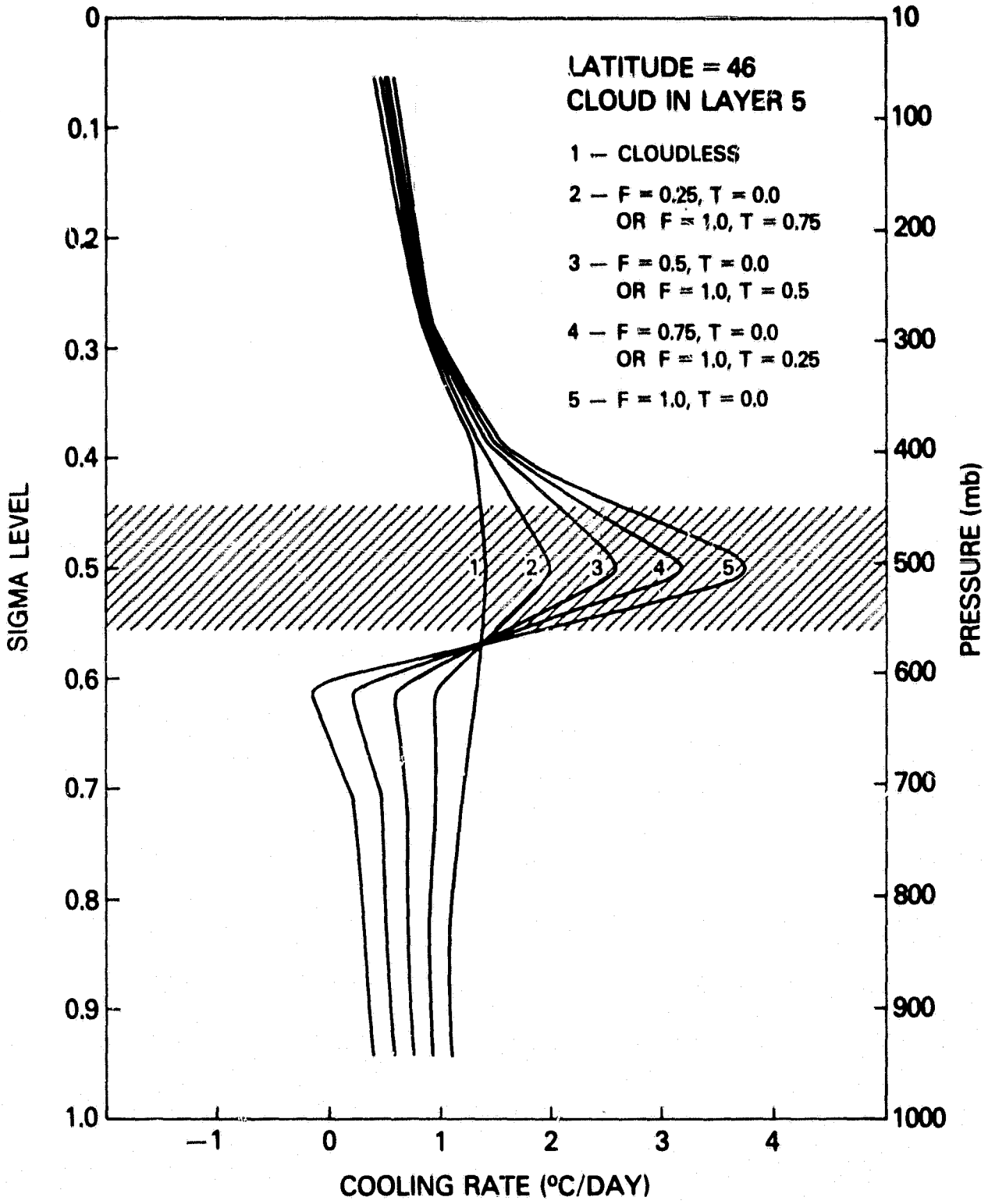
LATITUDE = 46
CLOUD IN LAYER 5
1 — CLOUDLESS
2 — F = 0.25, T = 0.0
OR F = 1.0, T = 0.75
3 — F = 0.5, T = 0.0
OR F = 1.0, T = 0.5
4 — F = 0.75, T = 0.0
OR F = 1.0, T = 0.25
5 — F = 1.0, T = 0.0
SIGMA LEVEL
PRESSURE (mb)
COOLING RATE (°C/DAY)
0
0.1
0.2
0.3
0.4
0.5
0.6
0.7
0.8
0.9
1.0
10
100
200
300
400
500
600
700
800
900
1000
−1
0
1
2
3
4

Fig. 1.

ABSORPTION OF SOLAR RADIATION IN THE GLAS GCM: THE INFLUENCE OF SOLAR ZENITH ANGLE

(R. Davies)

The current parameterization of the absorption of solar radiation in the GLAS GCM is relatively unchanged from the initial scheme developed by Lacis and Hansen (1974), referred to hereafter as the LH code. While the LH code explicitly includes the effect of the solar zenith angle, θ_0, on the absorption of solar radiation in cloud-free atmospheres, it fails to include this effect in the two critical areas of surface absorption and cloud scattering. The consequences of such an omission with regard to climatic effects and to model development are discussed below.

Surface Absorption

Following the observations of many investigators, which have been summarized by Paltridge and Platt (1976), it is now recognized that the surface albedo of most natural surfaces under clear sky conditions shows a pronounced dependence on θ_0 at low solar elevations. If $\bar{a}_g$ is the clear sky surface albedo for $\theta_0 \lesssim 40°$, this dependence may be modeled as

$$a_g(\theta_0) = \bar{a}_g + (1 - \bar{a}_g)\exp\{-0.1(90° - \theta_0)\} \quad , \qquad (1)$$

so that $a_g \to 1$ as $\theta_0 \to 90°$, but remains close to $\bar{a}_g$ for $\theta_0 \lesssim 40°$. While this effect may be incorporated into the GCM by a relatively trivial change to the code, the consequences to the model-generated planetary albedo and surface heating are quite significant. One should note that θ_0 is greater than 40° for at least 50 percent of the day, even at equatorial latitudes.

The most pronounced effect of this change is on the amount of absorbed radiation by the earth's surface. Using model-generated values for cloud, water vapor, etc., at 1200 GMT 1 January, zonally averaged values of surface absorption were produced using the LH code and the new code (NC). Fig. 1 shows the difference values (LH results - NC results) as a function of latitude.

The LH code systematically overestimates the surface absorption by up to ~45 ly/day, with the worst bias at high latitudes. On a global basis, the bias is ~30 ly/day for this particular case, representing an error of ~5 percent. If this difference were to be applied continuously to the snow line, the LH code would melt an extra inch of snow every 2-3 days. This error may also be partially responsible for the abnormally high surface temperatures produced by the GCM at high latitudes.

Cloud Scattering

The effect of solar zenith angle on the transfer of solar radiation in an isolated plane parallel cloud layer with homogeneous intrinsic parameters τ, a, and g is modeled first. Here τ is the optical thickness, a is the single scatter albedo and g is the asymmetry factor of the scattering phase function. The required output quantities are the amounts of solar energy absorbed, transmitted and reflected by the cloud layer. Distinction will be made between two forms of these quantities: those arising from a direct solar beam of irradiance F_0 from zenith angle θ_0, and those arising from unit diffuse irradiance on the top surface of the layer. The total problem of multiple cloud layers, cloud-free intervening atmosphere and underlying surface may then be solved by a suitable combination of the isolated layer results, as discussed below.

In modeling the transfer of solar radiation in clouds, the LH code uses a diffuse version of the two-stream approximation (Sagan and Pollack, 1967), whereas the new code employs the delta Eddington approximation (Joseph et al., 1976) for large τ and a delta version of the Coakley and Chylek (1975) two-stream approximation for small τ. Both the delta Eddington and the delta two-stream models explicitly include solar zenith angle effects.

Fig. 2 presents comparative results from the LH and new codes for the transmitted energy through a conservative cloud of optical thickness $\tau = 30$ as a function of $\mu_0 = \cos \theta_0$ resulting from an incident direct beam with $F_0 = 2880$ ly/day. Also shown are results from the accurate doubling model of Hansen (1971). While the delta Eddington model provides excellent comparative results to the doubling model, the LH version is seen to systematically underestimate the transmission for large values of μ_0 and to overestimate it for low values of μ_0. Due to the nonlinearity of the radiative transfer problem, it appears unwise to rely on averaging to cancel the errors, as was suggested by Lacis and Hansen (1974).

Figs. 3 and 4 address another important feature of cloud scattering, namely its effect on absorption within an individual cloud layer. The absorbed energy is presented as a function of τ for $a = 0.7$ and $\mu_0 = 1.0$ in Fig. 3, and as a function of a for $\tau = 3$ in Fig. 4. The new code and the doubling model give virtually identical results in Fig. 3 and excellent agreement in Fig. 4, whereas the LH code continues to show systematic errors in both figures.

While the LH code failed to adequately account for the directionality of the incident solar beam, it gave relatively good values for the transmitted, reflected and absorbed flux resulting from diffuse incident irradiance. An example of this is shown in Fig. 5, which compares the results for the transmitted fraction of diffuse irradiance from the LH version and the doubling model as a function of τ for different a.

In developing the new code, solutions to the complete multi-layered problem were obtained by a combination of the individual layer solutions. This was accomplished in two stages. Upwelling and downwelling irradiances from each cloud layer and the upwelling irradiance from the surface due to

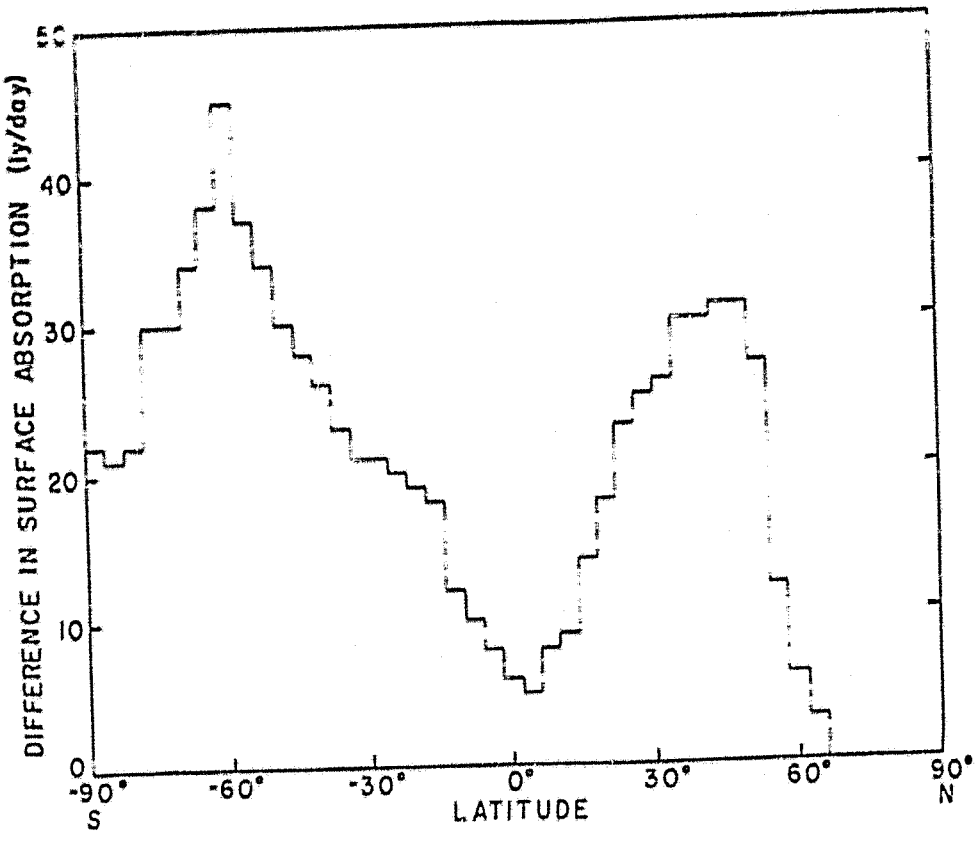

Fig. 1. GCM results for the difference in surface absorption (LH results - new results). Model time is 1200 GMT 1 January.

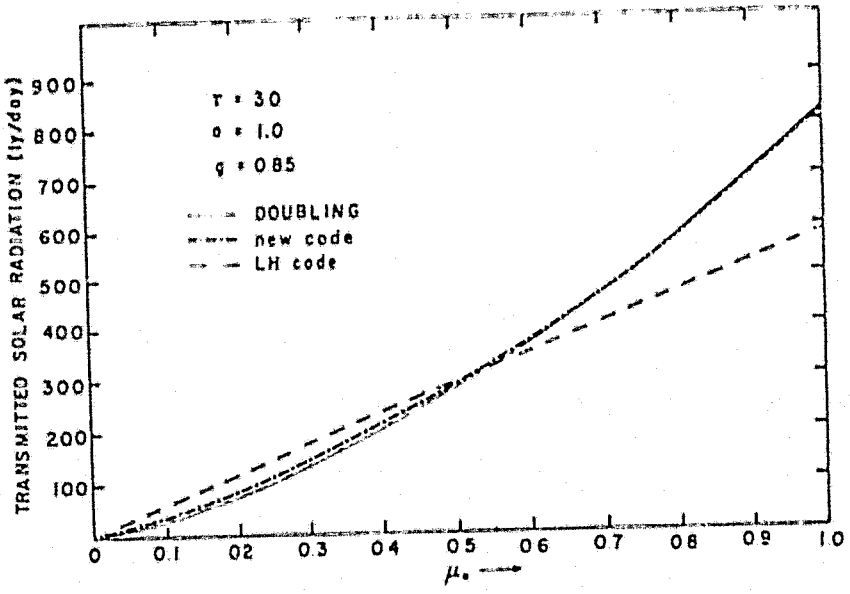

Fig. 2. Transmitted solar flux as a function of μ_0. The incident irradiance, F_0 = 2880 ly/day.

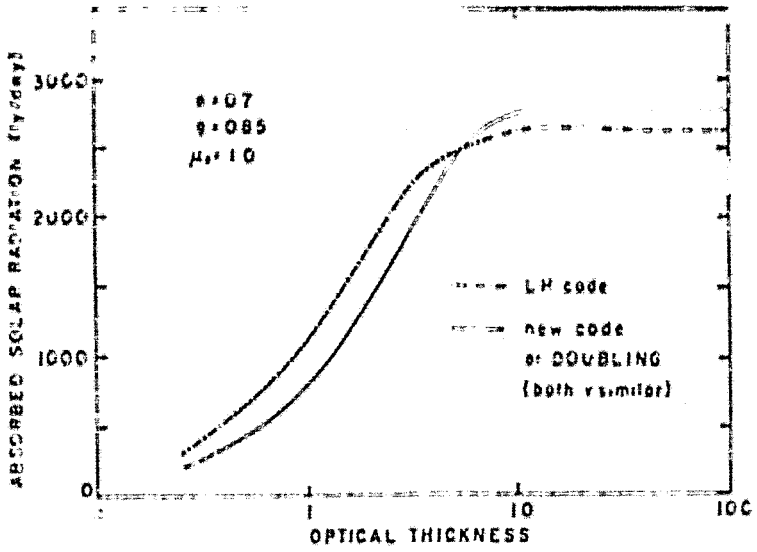

Fig. 3. Absorbed solar irradiance as a function of cloud optical thickness for F_0 = 2880 ly/day.

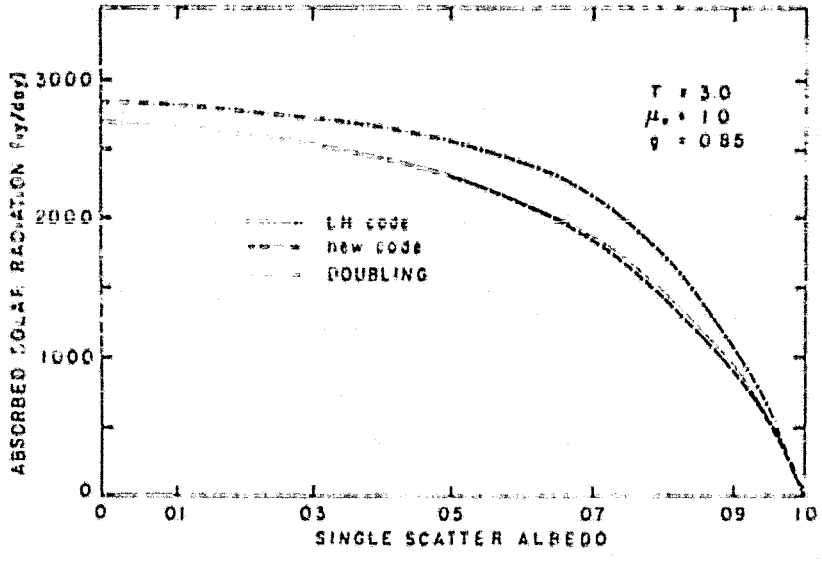

Fig. 4. Absorbed solar flux as a function of single scatter albedo for F_0 = 2880 ly/day.

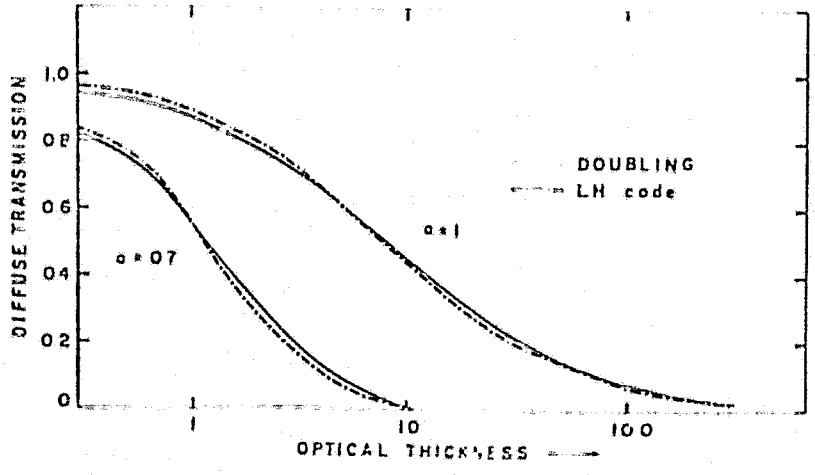

Fig. 5. Relative transmission of solar flux for diffuse incidence as a function of cloud optical thickness.

the attenuated solar beam at each level were first calculated. The resulting interaction of these irradiances with the complete multilayered system was then obtained by applying an advanced adding technique, utilizing the diffuse coefficients for reflection and transmission. The solar zenith angle dependence was thus preserved while still allowing the complete problem to be solved in a computationally efficient manner. Preliminary estimates using the new code to generate the global results below, for example, indicated an increase of less than 10 percent in the running time of the solar radiation portion of the GCM.

On applying the revised treatment to a typical time step of the GCM, the main effect on the zonally averaged solar radiation was an increase in planetary albedo and a decrease in atmospheric absorption. Fig. 6 shows an example of the difference between the new and old codes in generating total atmospheric absorption. The original treatment of surface albedo was used in this comparison, so that the differences resulted entirely from the new treatment of radiation in clouds. The values were zonally averaged for the same case as in Fig. 1. The LH code again systematically overestimates absorption for most latitudes, but with a latitude dependence that strongly reflects the amount of cloud cover. The maximum difference is thus now in equatorial latitudes where there is both significant cloud cover as well as substantial insolation. On a global basis, the LH code overestimates the atmospheric absorption for this case by ~20 ly/day or ~20 percent.

The present study has demonstrated that the absorption of solar radiation both at the earth's surface and within the atmosphere is noticeably affected by the directionality of the insolation at the top of the atmosphere. The combined effect of the above revisions on the zonally averaged planetary albedo is presented for the 1 January case in Fig. 7, which shows both the new and LH results. The increased surface albedo for clear skies and the increased cloud albedo for cloudy skies resulted in an increase of the planetary albedo at virtually all latitudes. On a global basis, the albedo for this particular case rose from the LH value of 0.29 to 0.34. In terms of absorbed solar energy, this has an equivalent climatic effect of a decrease of 7 percent in the solar constant.

Further developments along the above lines are planned to more accurately account for spectral effects and to more faithfully model situations involving fractional cloudiness.

Acknowledgment

Financial support under NASA Research Grant NSG 5223 is gratefully acknowledged.

References

Coakley, J. A., and P. Chylek, 1975: The two-stream approximation in radiative transfer: including the angle of the incident radiation. J. Atmos. Sci., 32, 409-418.

Hansen, J. E., 1971: Multiple scattering of polarized light in planetary atmospheres. Part I. The doubling method. J. Atmos. Sci., 28, 120-125.

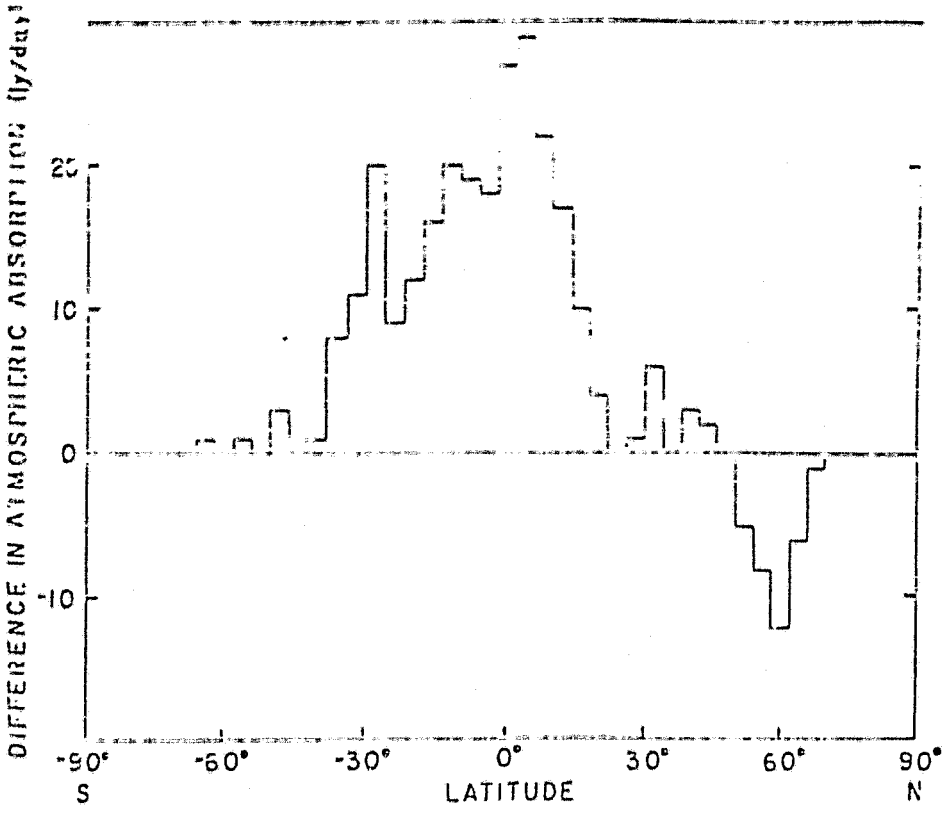

Fig. 6. GCM results for the difference in zonally averaged atmospheric absorption (LH results - new results). Model time is 1200 GMT 1 January.

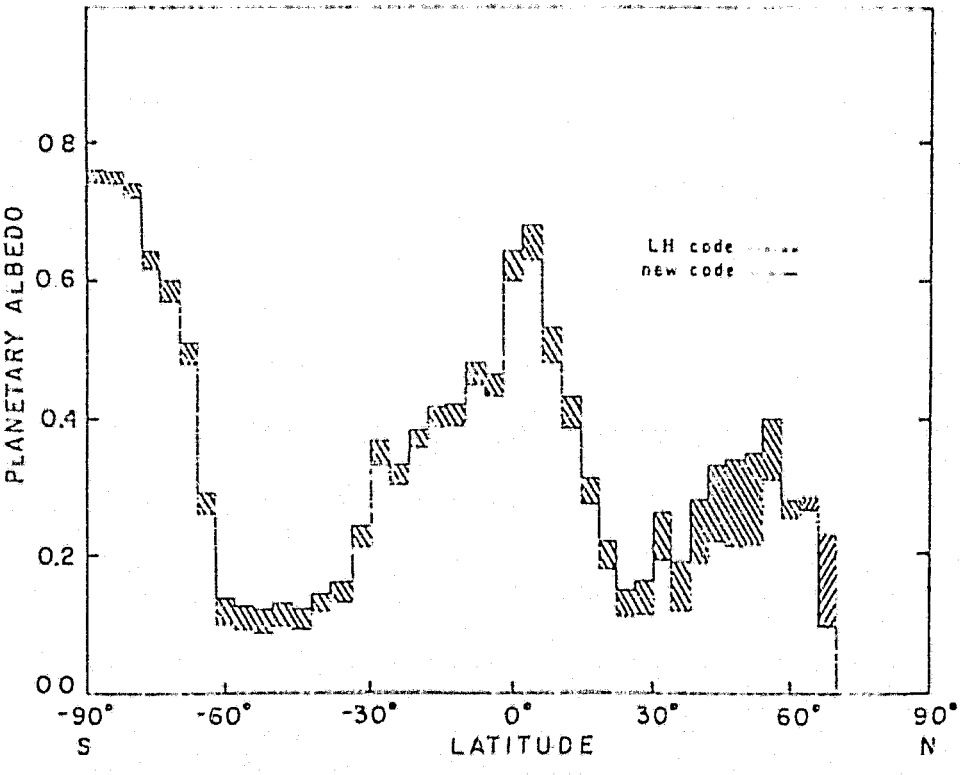

Fig. 7. Zonally averaged planetary albedo produced by the LH and new codes in the GCM. Model time is 1200 GMT 1 January.

References (Continued)

Joseph, J. H., W. J. Wiscombe, and J. A. Weinman, 1976: The delta-Eddington approximation for radiative flux transfer. J. Atmos. Sci., 33, 2452-2459.

Lacis, A. A., and J. E. Hansen, 1974: A parameterization for the absorption of solar radiation in the earth's atmosphere. J. Atmos. Sci., 31, 118-133.

Paltridge, G. W., and C. M. R. Platt, 1976: Radiative Processes in Meteorology and Climatology, Elsevier Sci. Publ. Co., New York.

Sagan, C., and J. B. Pollack, 1967: Scattering in the Venus clouds. J. Geophys. Res., 72, 469-477.

TESTS OF GROUND HYDROLOGY PARAMETERIZATIONS

(J. D. Lin, P. Bock, and J. J. Alfano)

A global ground hydrology model (GHM) is being developed for use in the GLAS GCM. Parameterization of land surface hydrologic processes at the grid scale of the GCM is the central problem in the model development and research. Ground temperature and soil moisture are employed in the GCM as prognostic variables and thus must be used as basic hydrologic variables in the GHM for parameterization of the latent heat flux (evapotranspiration) and sensible heat flux at the atmospheric-land interface. To account for the pathways through which the moisture and heat are transported, a computational grid in the GHM is divided horizontally into two portions: the bare soil and the vegetated surface, and vertically into two active layers: the surface layer and the root zone, as depicted schematically in Fig. 1. The subgrid parameterization is considered to be a minimum requirement for a physically realistic GHM. The purpose of this report is to present the test results of the GHM by using the field-observed data that were obtained from two experimental sites on bare soils and one on winter wheat crop. The data consist of:

(1) soil moisture, ground temperature, and evaporation of bare soil from the U. S. Water Conservation Laboratory, Phoenix, Arizona (Jackson, 1973; Jackson et al., 1975).

(2) soil moisture and ground temperature of bare soil from the Southern Piedmont Conservation Research Center, Watkinsville, Georgia (Bruce et al., 1977).

(3) soil moisture, canopy temperature, and evapotranspiration of winter wheat crop from U. S. Water Conservation Laboratory, Phoenix, Arizona (Jackson et al., 1977).

The formulations that are involved in the one-dimensional transport of moisture and heat in the tests of a soil-atmosphere or soil-plant-atmosphere column are summarized as follows. A detailed presentation of the GHM is given in Lin et al. (1979). The ground temperature is calculated by the force-restore method, as derived by Deardorff (1978) and recently modified by Lin (1979), i.e.,

$$\alpha \frac{dT_g}{dt} = \frac{2\pi^{1/2} G}{\rho_{s1} c_{s1} \bar{d}_1} - \frac{2\pi (T_g - \bar{T})}{\tau_1} \tag{1}$$

and

$$\frac{d\bar{T}}{dt} = G/(\rho_{s2} c_{s2} \bar{d}_2) \tag{2}$$

where $\alpha = 1 + \sqrt{\pi}\ \delta/\bar{d}_1$ and the ground heat flux

$$G = R_n - \lambda E_a - H_s \tag{3}$$

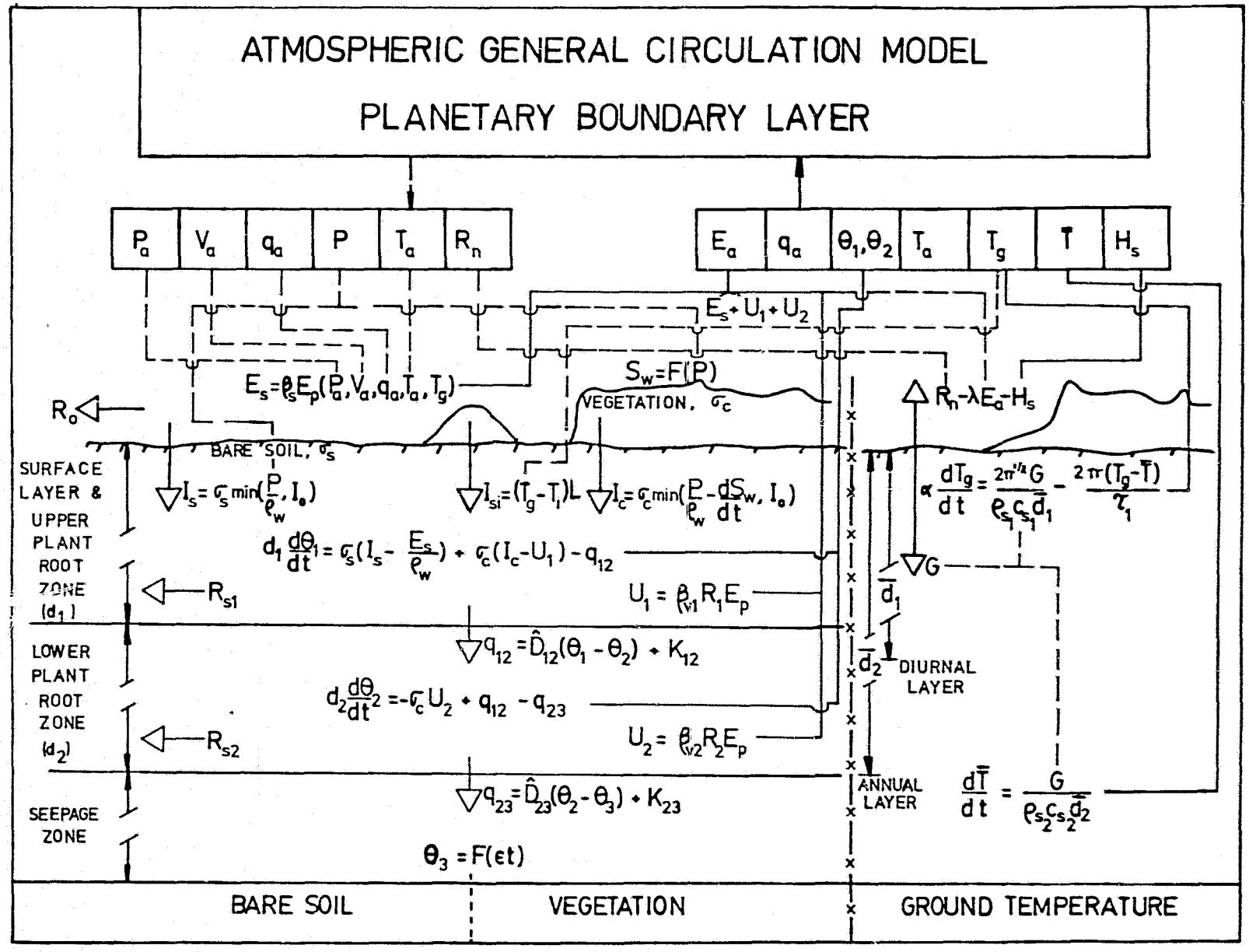

Fig. 1. The Ground Hydrology Model.

The soil moisture is governed by

$$d_1 \frac{d\theta_1}{dt} = \sigma_s(I_s - \frac{E_s}{\rho_w}) + \sigma_c(I_c - U_1) - q_{12} \tag{4}$$

for the surface layer or upper root zone and

$$d_2 \frac{d\theta_2}{dt} = \sigma_c U_2 + q_{12} - q_{23} \tag{5}$$

for the intermediate layer or lower root zone, while θ_3 = constant. No surface and/or subsurface runoff is allowed in the tests. All rain and irrigated water are allowed to infiltrate into the layers. The vegetation fraction σ_c was set to unity for the vegetation test, while the bare soil fraction σ_s was set to unity for the bare soil tests. The evapotranspiration is parameterized by scaling from the potential evaporation

$$E_p = \rho_a C_m V_a [q^*(T_g) - q_a] \tag{6}$$

as follows. For bare soil

$$E_s = \beta_s E_p \ , \ \beta_s = \min (a \bar{\theta}_{ai}^{\,b}, 1) \tag{7}$$

where the normalized available soil moisture is defined as

$$\bar{\theta}_{ai} = (\theta_1 - \theta_{pwp})/(\theta_{fc} - \theta_{pwp}) \ , \ i = 1,2 \tag{8}$$

The soil at the Arizona site is Adelanto loam with a = 1.95 and at the Georgia site is Cecil sandy loam with a = 4.63, and in both cases, b = 3. The a- and b- values were determined by calibration. For a vegetated surface, the uptakes of moisture from the upper and lower root zone are parameterized, using the concept of soil water stress and the unstressed transpiration. The transpiration is the sum of the uptakes

$$E_T = U_1 + U_2 \tag{9}$$

and

$$U_1 = E_u \ , \qquad \text{if } \bar{\theta}_{a1} \geq 1 \tag{10a}$$

$$\{$$

$$U_2 = 0$$

or

$$U_1 = \beta_1 R_1 E_u, \qquad \text{if } 1 > \bar{\theta}_{a1} \geq 0 \tag{10b}$$

$$\begin{cases} U_2 = (1-\beta_1 R_1)\, E_u, & \text{if } \bar{\theta}_{a2} \geq 1 \\ \quad = \beta_2 R_2 E_u, & \text{if } 1 > \bar{\theta}_{a2} \geq 0 \end{cases}$$

where

$$\beta_i = \min\left[\bar{\theta}_{ai}/\bar{\theta}_{at},\ 1\right] \tag{11}$$

The threshold value of the normalized available soil moisture depends on the atmospheric demand such that

$$\bar{\theta}_{at} = (CE_u/d\theta_{am})^k \tag{12}$$

For the Arizona winter wheat, k = 0.8, C = 35 h, and d = 50 cm were used. Finally, the unstressed transpiration can be related to the potential evaporation in Equation (6) by

$$E_u = \alpha E_p \tag{13}$$

where can be estimated from the type of vegetation canopy, e.g., α = .8 for crops.

The soil moisture flux q_{ij} in Equations (4) and (5) is the average flux in a layer in the neighborhood of the interface, in which the soil moisture content of the profile changes from θ_i to θ_j, i.e.

$$q_{ij} = \hat{D}_{ij}\,(\theta_i - \theta_j) + K_{ij}, \qquad i = 1, 2 \text{ and } 2, 3 \tag{14}$$

To evaluate $\hat{D}_{ij}$ and K_{ij}, the soil moisture diffusivity and conductivity are assumed as an exponential function of θ, thus

$$\hat{D}_{ij} = \{D(\theta_i) - D(\theta_j)\}/d_{ij} \ln\{D(\theta_i)/D(\theta_j)\} \tag{15}$$

Similarly,

$$K_{ij} = \{(\theta_i) - K(\theta_j)\}/\ln\{K(\theta_i)/K(\theta_j)\} \quad (16)$$

It is found that d_{ij} can be estimated by the following scheme:

$$d_{12} = 1/2\ (d_1 + d_2) \text{ and } d_{23} = 1/\ d_2 \quad (16a)$$

if $\theta_1 > \theta_2 > \theta_3$ or $\theta_1 < \theta_2 < \theta_3$

or

$$d_{12} = 1/4(d_1 + d_2) \quad \text{and} \quad d_{23} = 1/4\ d_2 \quad (16b)$$

otherwise.

The GHM was forced by the observed atmospheric data consisting of specific humidity, wind speed, net radiation, and air temperature, and the ground temperature and soil moisture were also initialized by the data as shown at the upper four graphs in Figs. 2-4. In the Arizona experiments, the plot was irrigated prior to the initial time as indicated by the initial moisture content in Layer 1. There were two rain events in the Georgia experiment: 9.7 and 4.1 mm during the 5th and 6th day, which substantially increased the soil moisture in Layer 1, as seen in Fig. 3. Calculated results of θ_1, θ_2, Tg, and Ea were compared with the observed data in Figs. 2-4, except that Ea was not measured at the Georgia site. All calculated soil moisture contents agree very well with the observed data for the weighted-average values in each layer. In Figs. 2 and 3, the bare soil ground surface temperature was calculated on the basis of $\delta = 2$ and 1 cm, while the observed data were taken at a depth of 1 and 0.5 cm for the Arizona and George site, respectively. In Fig. 4, the observed canopy temperature was used for comparison. The calculated evaporation for the bare soil at the Arizona site in Fig. 2 agrees with the observed data when the soil is wet and there is only an overall agreement when the soil becomes dry (note the missing data for the 2nd and 3rd day). In the Georgia experiment in Fig. 3, the evaporation was not measured; however, the calculated evaporation was nearly equal to the potential evaporation during 2 days after the rain events. The transpiration from the winter wheat crop in Fig. 4 shows a good agreement for the whole experiment (note the missing lysimeter data on the 6th day).

The tests of the GHM using these field-observed data sets have provided a useful means to evaluate the parameterizations of soil moisture, ground surface temperature, and evapotranspiration. Good agreement was found between calculated and observed values. Further testing is being conducted for the parameterization of vegetated surface, using observed data in a forest site.

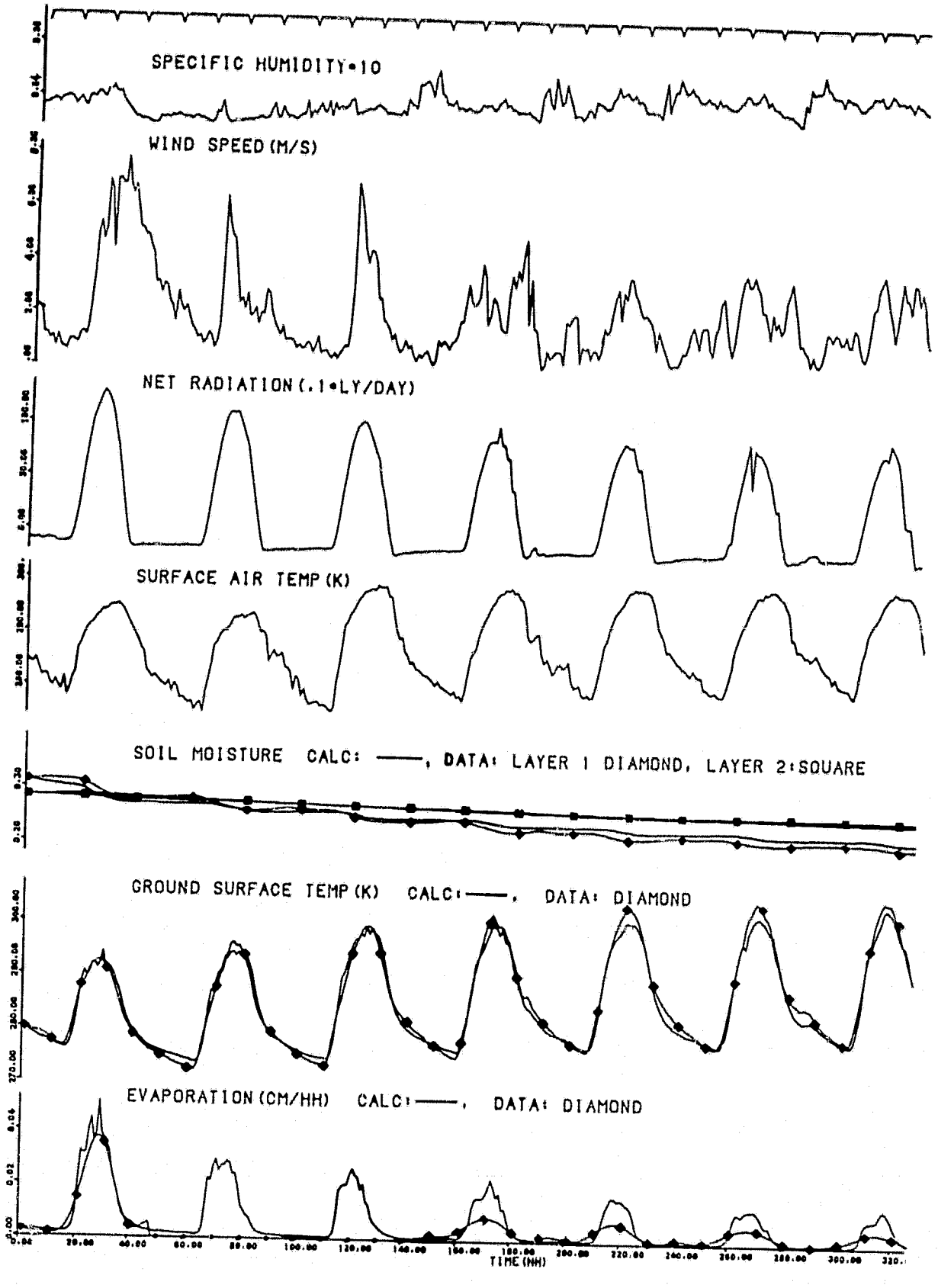

Fig. 2. Arizona Base Soil Experiment.

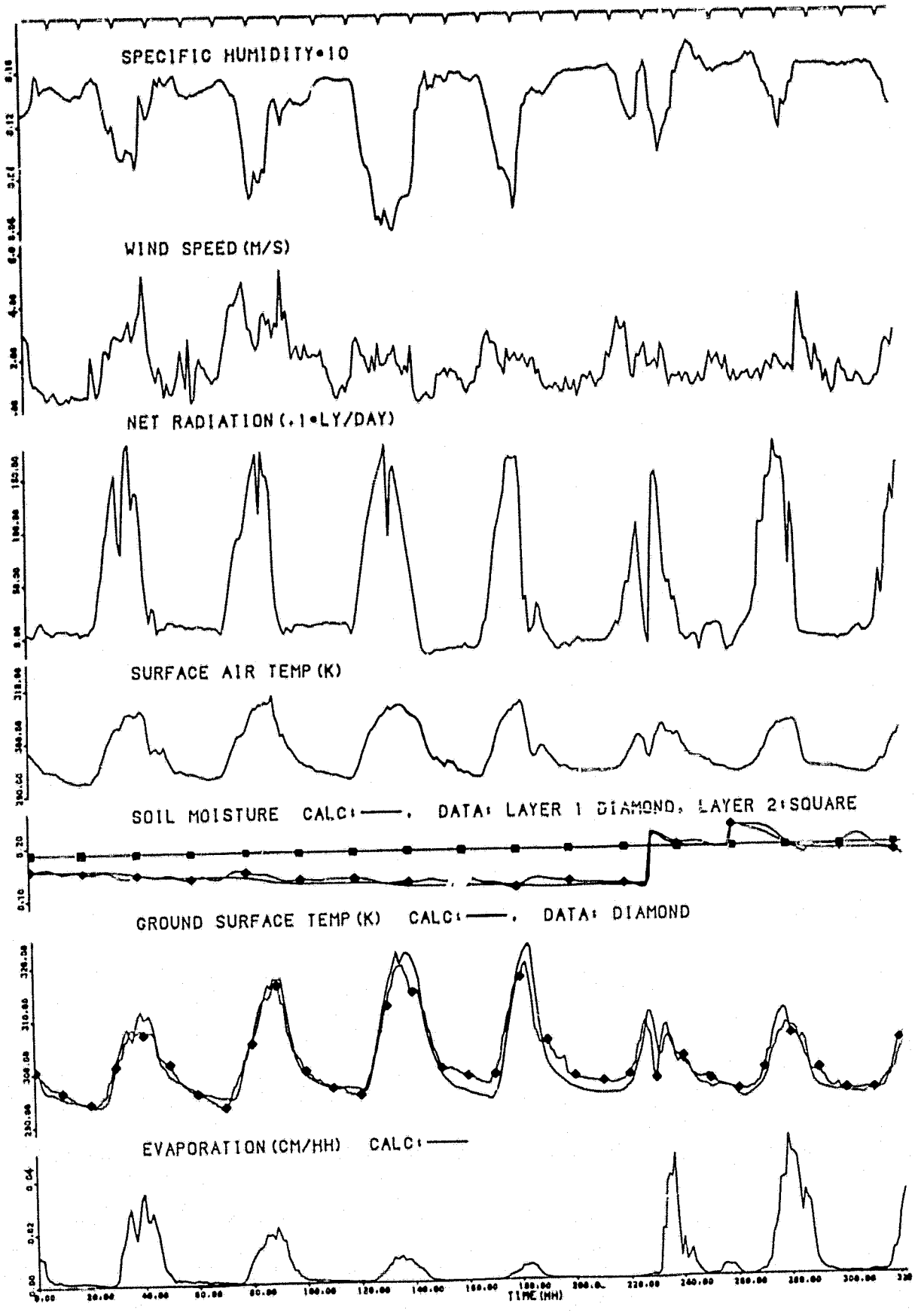

Fig. 3. Georgia Base Soil Experiment.

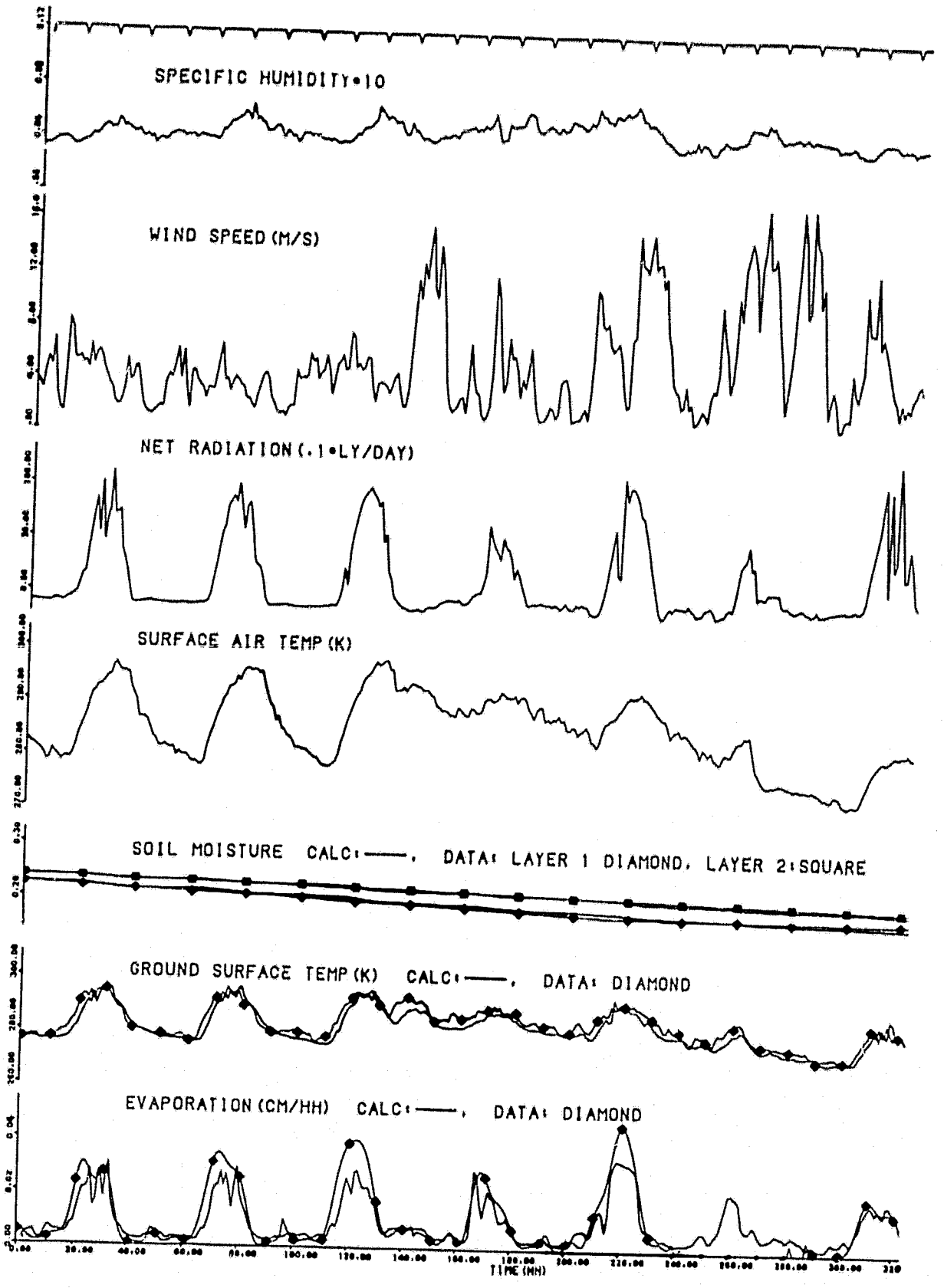

Fig. 4. Arizona Crop.

NOTATIONS

a,b,C,k	constants
C_m	moisture transfer coefficient
c_s	soil specific heat
$\hat{D}_{12},\hat{D}_{23}$	moisture transfer coefficient
d	sum of d_1 and d_2
$d_1,d_2,\bar{d}_1,\bar{d}_2$	depth for θ_1,θ_2, diurnal and annual temperature wave
E_a	total evaporative flux, $E_a = E_s + U_1 + U_2$
E_p,E_s	potential and bare soil evaporation
E_u	unstressed transpiration
G	ground heat flux
H_s	sensible heat flux
I_s,I_c	infiltration on soil and under vegetated surface
I_o	infiltration capacity
I_{si}	infiltration from snow or ice melt
K_{12},K_{23}	soil conductivity
P	precipitation or throughfall
p_a	air surface pressure
q^*,q_a	specific humidity at saturation and at reference height
q_{12},q_{23}	soil moisture flux
R_1,R_2	fraction of plant roots
R_n	net radiation
R_o,R_s	surface and subsurface runoff
$\bar{T}$	depth-average ground temperature
T_a	air temperature at reference height
T_i	ice temperature

NOTATIONS (Continued)

T_g	cell-average ground temperature
U_1, U_2	moisture uptake by plants
V_a	wind speed at reference height
β_s	scaling factor for bare soil
β_{vi}	scaling factor for evapotranspiration
$\theta_1, \theta_2, \theta_3$	volumetric soil moisture content
θ_a	available soil water content
$\theta_{fc}, \theta_{pwp}$	soil moisture at field capacity and permanent wilting point
λ	latent heat of vaporization
ρ_a, ρ_w, ρ_s	density of air, water, and soil
σ_s, σ_c	fraction of bare soil and vegetated surface
τ_1	diurnal period
α	depth correction factor for calculating T_g
γ	ratio of E_u/E_p
δ	thickness of thin surface layer for calculating T_g

References

Bruce, R. R., A. W. Thomas, L. A. Harper, and R. A. Leonard, 1977: Diurnal soil water regime in the tilled plow layer of a warm humid climate. Soil Sci. Soc. Amer. J., 41, 455-460.

Deardorff, J. W., 1978: Efficient prediction of ground surface temperature and moisture with inclusion of a layer of vegetation. J. Geophys. Res., 83, 1889-1903.

Jackson, R. D., 1973: Diurnal changes in soil-water content during drying. Field Soil Water Regimes, R. R. Bruce (ed.), Soil Sci. Soc. Amer. Sp. Publ. 5, 37-55.

_____, B. A. Kimball, R. J. Reginato, S. B. Idso, and S. A. Nakayama, 1975: Heat and water transfer in natural soil environment. Heat and Mass Transfer in the Biosphere. Part I. Transfer Processes in the Plant Environment, Scripter Book Publ. Co., Washington, DC, 67-76.

_____, R. J. Reginato, and S. B. Idso, 1977: Wheat canopy temperature: a practical tool in evaluating water requirements. Water Resources Res., 13, 652-656.

Lin, J. D., 1979: On the force-restore method for prediction of ground surface temperature. Submitted for publication.

_____, J. J. Alfano, and P. Bock, 1979: Modeling and terrestrial hydrology for the global atmosphere. I. The ground hydrology model; II. Tests of the ground hydrology model. In preparation to be submitted to J. Geophys. Res.

INTERANNUAL VARIATIONS OF SEA LEVEL PRESSURE

(R. Godbole)

In present-day climate modeling, attention is focused on the use of climate models for short-range climate predictions on a time scale of a season or a year. An important question to be addressed in this connection is the predictability of observed variations in monthly or seasonal means from one year to another. A logical prerequisite, therefore, is to examine and document these observed year-to-year variations.

The purpose of this paper is to examine the spatial patterns of sea level pressure and their interannual variations during the past 16 years. The period covers from 1961 through 1976 and the region considered is the whole globe. January and July monthly mean sea level pressure data for individual stations have been plotted and subjectively analyzed. The data were extracted from NCAR data sets.

Figs. 1a and 1b show the 16-year mean sea level pressure for January and July, respectively. The major centers of action such as the Aleutian low, the Icelandic low, the Siberian high in January, the monsoon low over Africa and Asia in July and also the subtropical highs in both January and July have the right locations and intensities when compared to any corresponding climatological or long-term mean sea level pressure field (Shutz and Gates, 1971; Crutcher and Meserve, 1970).

Fig. 2 represents a typical example of the variation of sea level pressure for January of two different years: 1974 and 1976. It is observed that in 1974 (Fig. 2a), the Icelandic low is an intense, huge system apparently dominating the circulation of the northern hemisphere. The Aleutian low is weak and the Siberian high, although strong, is broken into small circulation cells. In 1976, on the other hand, the Icelandic low is weak having a secondary center lying over northern Europe. The Siberian high shows a single and relatively weak cell whereas the Aleutian low shows intensification. Similar interannual variations are noticed for July also but their amplitude is considerably less than that observed in January. This is clearly borne out from Fig. 3 which shows year-to-year variations of central pressure of a major system in January and July. For an Icelandic low in January, the maximum range of variation of central pressure is about 32 mb whereas for a monsoon low over Asia in July, the maximum range is hardly 5 mb.

Fig. 4 shows the range of variability in the location of the major centers of action for January and July. The results again point out that the variability in January is more than the variability for July. Also, these year-to-year displacements are stretched more in east-west rather than in north-south extent.

Table 1 presents anomalies of sea level pressure for some of the major systems in January. The anomalies were obtained as the difference between central pressure in an individual year and that of a long-term mean (Fig. 1a) for a given major system. The results reveal a very interesting

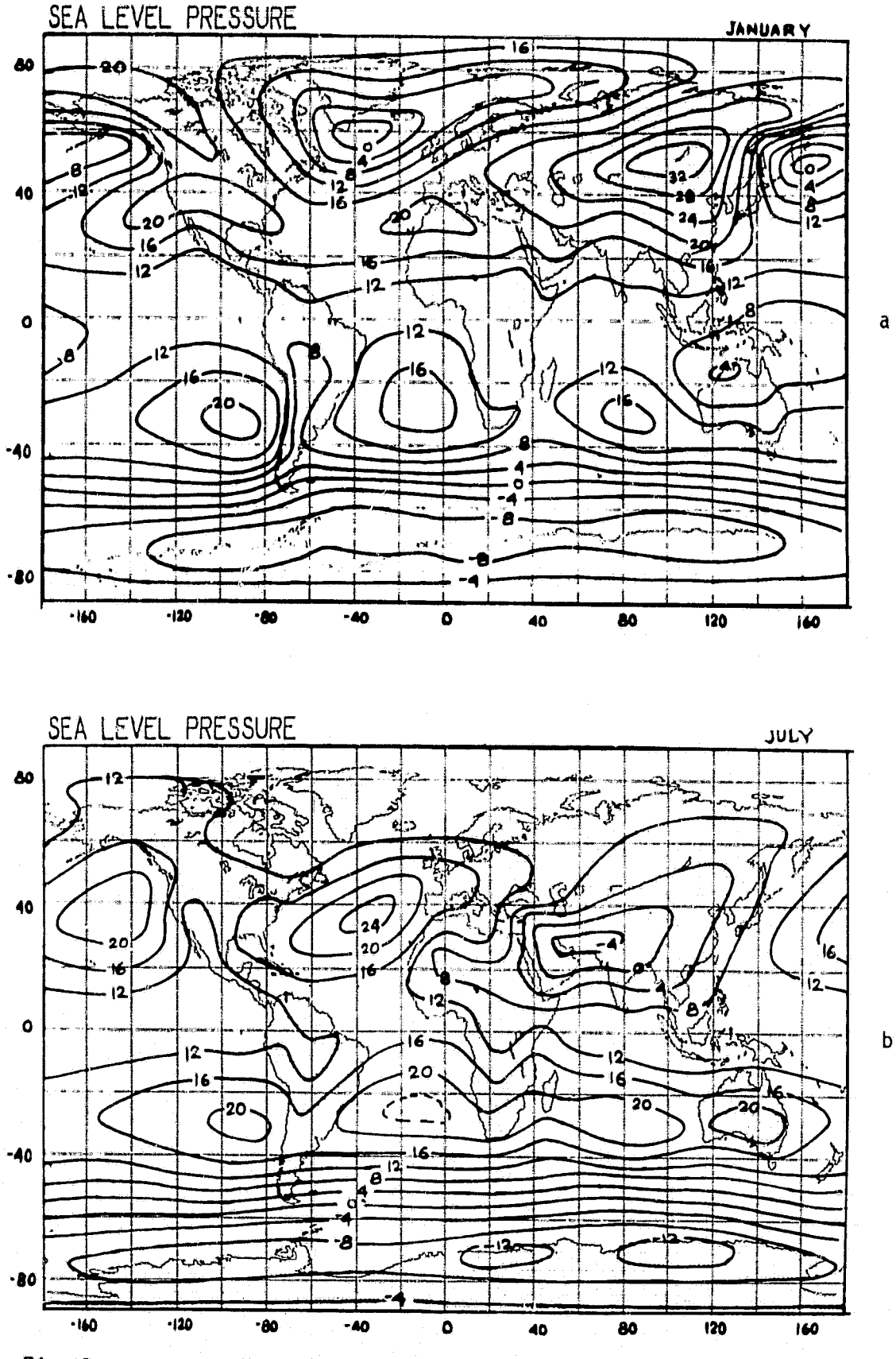

Fig. 1. Monthly mean sea level pressure ($\bar{P}$) for (a) January and (b) July (1961-1976). Values are expressed as ($\bar{P}$-1000) mb.

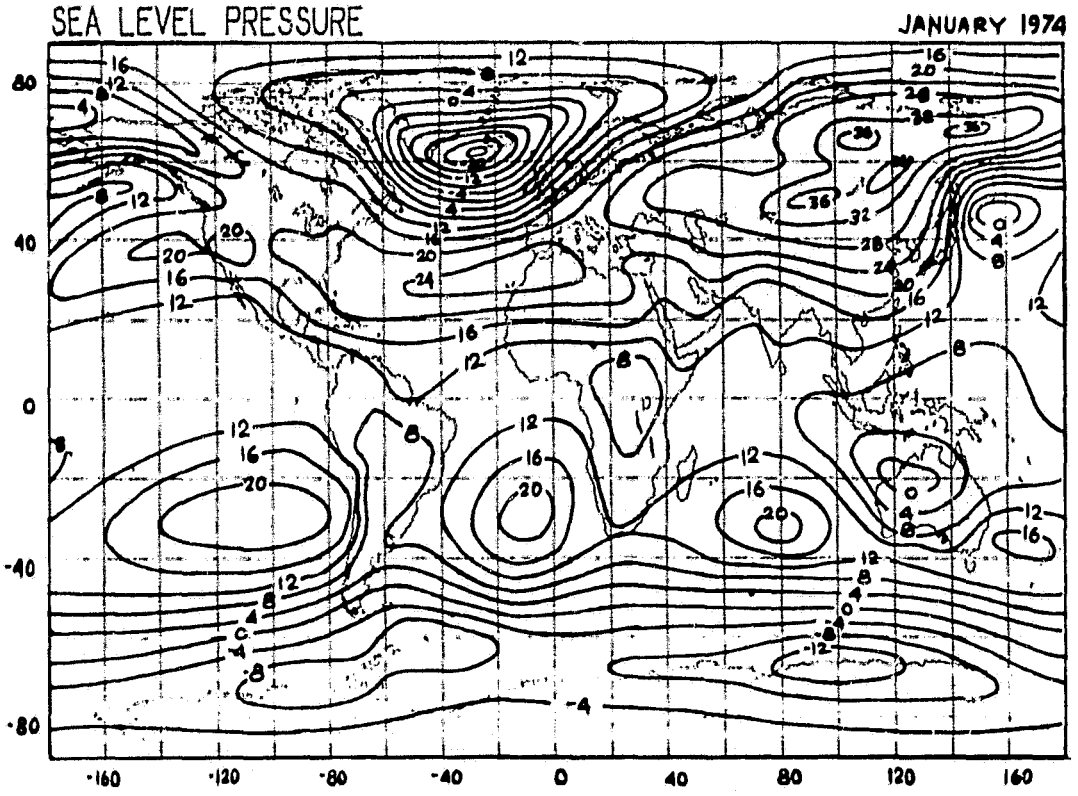

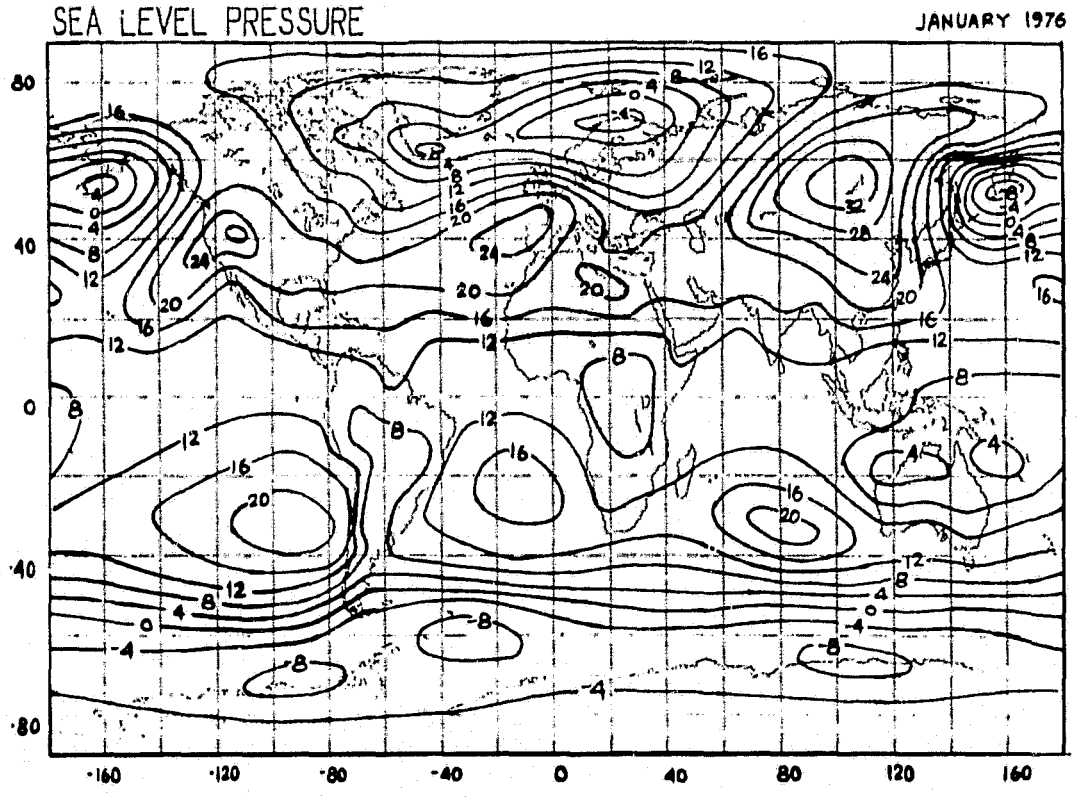

Fig. 2. Monthly mean sea level pressure ($\bar{P}$) for (a) January 1974 and (b) January 1976. Values are expressed as ($\bar{P}$-1000) mb.

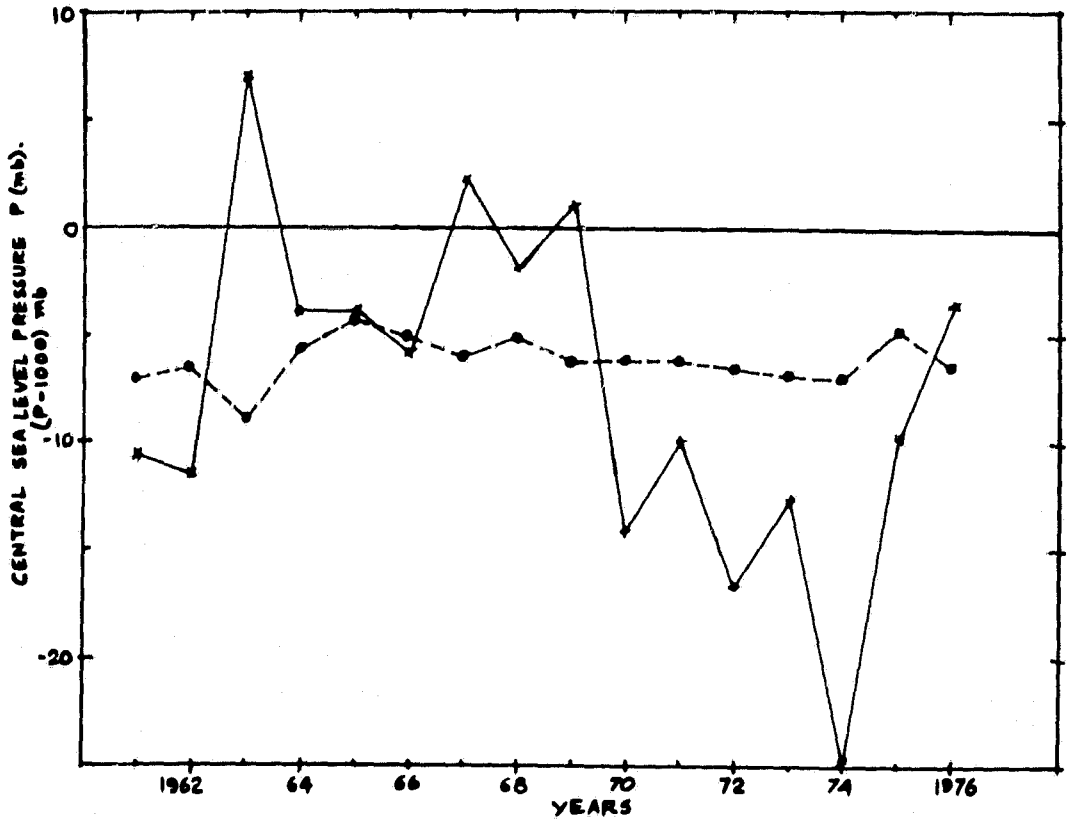

Fig. 3. Year-to-year variation of central pressure (P-1000) for Icelandic low in January (solid line) and for monsoon low in July (broken line).

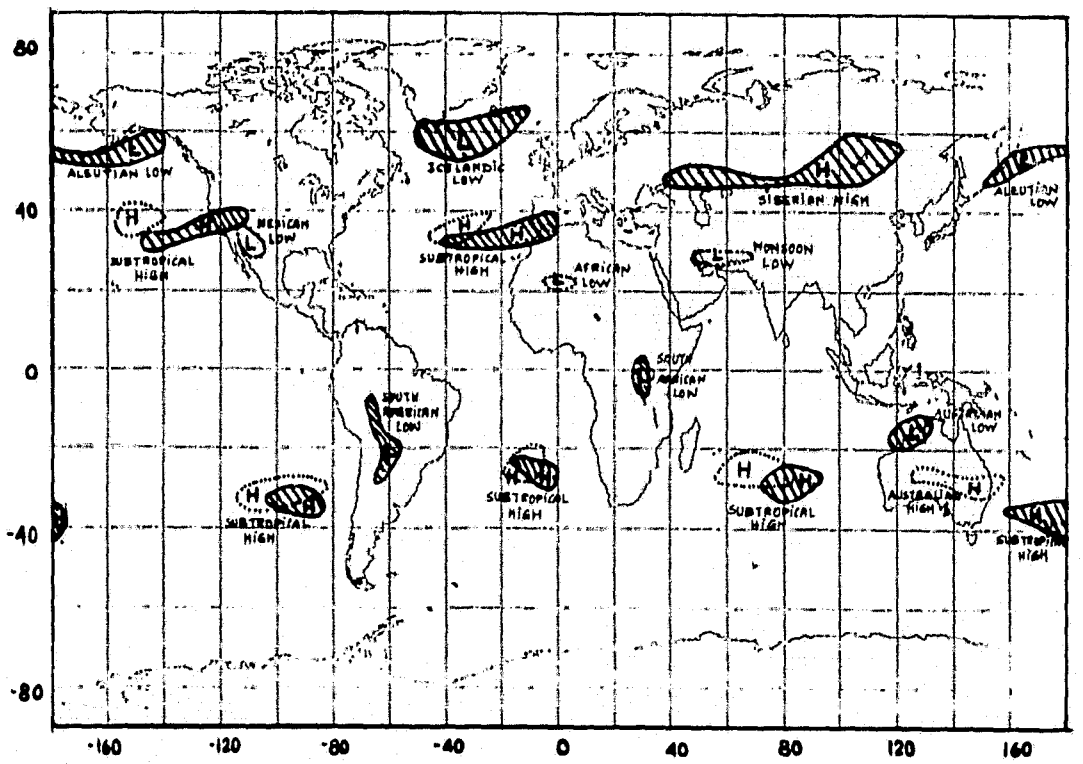

Fig. 4. Range of variation of the location of centers of action for January (hatched) and July (dotted).

Table 1. Monthly mean sea level pressure anomaly ($P-\overline{P}$) for Icelandic low, Aleutian low, and Siberian high in January.

Year	Icelandic low - strong + weak	Aleutian low - strong + weak	Siberian low - weak + strong
1961	- 8.0	- 8.5	+ 1.0
1962	- 9.0	+ 0.5	+ 1.0
1963	+11.0	- 3.8	+ 4.8
1964	+ 0.0	- 8.0	+ 4.0
1965	+ 0.0	- 1.5	+ 1.0
1966	- 2.0	-10.1	+ 0.0
1967	+ 6.3	- 4.8	+ 4.0
1968	+ 2.2	+ 2.6	+ 0.0
1969	+ 5.1	- 5.5	+ 5.1
1970	-10.1	+ 2.1	+ 2.6
1971	- 6.0	+ 7.5	+ 4.0
1972	-12.8	+ 3.5	+ 2.0
1973	- 8.6	+ 2.3	- 1.0
1974	-20.6	+ 0.5	+ 3.0
1975	- 5.8	+ 1.1	+ 1.0
1976	+ 0.4	- 7.8	- 1.2

feature. It is seen that, with the exception of 2 to 3 years, the Icelandic low bears an inverse relationship with the Aleutian low. This means that, in a given year, if the Icelandic low is strong, the Aleutian low is weak and vice versa. Further, the behavior of these two lows seems to be somewhat associated with that of the Siberian high. The relationship, however, is not as strong as that noticed between the two lows. Nevertheless, one cannot fail to notice that in a majority of cases, a weak Icelandic low tends to associate with a weak Siberian high whereas a weak Aleutian low tends to associate with a strong Siberian high. A somewhat similar relationship appears to exist between the subtropical highs also. The findings have a very important implication: these seasonal centers of action which act as internal forcing in a climate model dynamics have an impact not only restricted locally where they are produced but rather their impact is global in nature.

Acknowledgments

The author wishes to express his sincere thanks to Dr. J. Shukla for his helpful comments during discussions with him.

References

Crutcher, H. L., and J. N. Meserve, 1970: Selected level heights, temperatures and dew points for the northern hemisphere. NAVAIR 50-1C-52 Revised, Naval Weather Service Command, Washington, DC.

Schutz, C., and W. L. Gates, 1971: Global climate data for surface, 800 mb, 400 mb; January. Report R-915-ARPA, Rand, Santa Monica, California.

PRELIMINARY RESULTS OF A JANUARY SIMULATION WITH AN IMPROVED VERSION OF THE GLAS MODEL

(J. Shukla, Y. Sud, and E. Sabatino)

Several aspects of the weaknesses and strengths of winter and summer simulations with the GLAS model are described in a recent paper by Halem et al. (1979), which points out that one of the weaknesses of the model is its lower evaporation over the oceans. This, along with smoothing of orography over high mountain peaks, was suspected to be responsible for weaker amplitudes of stationary waves in these simulations. We have introduced several modifications in the earlier version of the GLAS model. These were comprised of modified boundary layer calculations which led to an improvement in the fields of boundary layer fluxes and a stable calculation of surface temperature. This parameterization is discussed in a paper by Sud and Abeles (1979). In addition, the ground albedo over snow-ice covered surfaces of the earth are prescribed from an analysis of satellite observation of Matson (1978) and Rayner and Howarth (1977). This snow-ice data is combined with the bare land albedos of Posey and Clapp (1964). Furthermore, the model has been initialized for a long climate run by making the permanent ice depth equal to 3 meters and transient snow depth of 0-2 cm, depending upon its reflectivity. Sea surface temperatures from a 2° x 2° GFDL data set were interpolated to the 4° x 5° grid of the GLAS model. All the prescribed boundary conditions are now interpolated on a daily basis.

Furthermore, as a result of detailed examination of the code and the diagnostics of various calculations, a few additional modifications have been made. These consist of the following: elimination of Shapiro-filter on humidity field, maintaining conservations in strapping and unstrapping of cloud layer in the model, calling short wave radiation every half hour while maintaining long wave calls at 5-h frequency but with net radiative temperature modification to be made every half hour using the saved fluxes of long wave radiation, changes for correction of radiative heating rates over the mountains, and correcting a coding error in the interpolation of level-8 winds in the split-grid regions.

Preliminary results of first 31 days which consist of simulated month of January (starting from the initial conditions of 1 January 1975 from NMC analysis) are compared with the simulation with the earlier model run of Halem et al. (1979) of which February simulation has been presented in their paper. Some basic fields which show an impact from these changes are presented and compared with the earlier run.

Analysis of Results

An important result from these modifications was the improvement of one of the most serious deficiencies in the model, i.e., the lower amplitude of the stationary component of its general circulation. It is well known that the stationary waves are forced by diabatic heating sources and orography.

Since the earlier model produced an evaporation field which was significantly less than the observed over the oceans (Charney et al., 1977), an improvement in diabatic heating through increased boundary layer fluxes of evaporation and sensible heating over the oceans was expected to improve the stationary component of general circulation. This has happened in the new model simulation.

The following results compare the modified model with its earlier version. Figure captions (a) and (b) are used for the modified and earlier model results, respectively. Figs. 1a and 1b show the sea level pressure maps. Fig. 1a has better subtropical highs and a pronounced Siberian high. Also, the low over the coast of Japan is much better defined and the sea level pressure fields off the coast of Greenland have a better structure.

Figs. 2a and 2b show zonal plots of evaporation over the land and oceans in the two simulations. Increased evaporation over the oceans and lower evaporation over land in the modified model run are seen. This corrects a well known weakness of the model. Figs. 3 and 4 show the zonally averaged evaporation and precipitation fields. There is an increase in evaporation and precipitation in the new model.

An analysis of amplitude of stationary component of circulation geopotential height fields are presented. Tables 1a and 1b show the variance of geopotential height fields at the mandatory pressure levels. The values of variances for the new run compare well with the observations (as shown in Table 1c) of Oort and Rasmusson (1971) and show a considerable improvement over those of the old model shown in Table 1b. In Fig. 5 the plots of variance of geopotential height fields at 500 mb are shown. The new model results are in good agreement with observations. The peaks of variances in the baroclinic regions improve by a factor of two over the old model.

References

Charney, J. G., W. J. Quirk, S. H. Chow, and J. Kornfield, 1977: A comparative study of the effects of albedo changes on drought in semi-arid regions. J. Atmos. Sci., 34, 1366-1385.

Halem, M., J. Shukla, Y. Mintz, M. L. Wu, R. Godbole, G. Herman, Y. Sud, 1979: Comparisons of observed seasonal climate features with a winter and summer numerical simulation produced with the GLAS general circulation model. Report of the JOC Study Conf. on Climate Models: Performance, Intercomparison and Sensitivity Studies, GARP Publ. Series No. 22, 207-253, WMO, Geneva, Switzerland.

Matson, M., 1978: Winter Snow-Cover Maps of North America and Eurasia, 1966-1976.

Oort, A. H., and E. R. Rasmusson, 1971: Atmospheric circulation statistics. NOAA Prof. Paper 5, U.S. Dept. of Comm.

Posey, J. W., and P. F. Clapp, 1964: Global distribution of normal surface albedo. Geofisica Int'l., Vol. 4, 33-48.

References (Continued)

Rayner, J. N., and D. A. Howarth, 1977: Analysis of Spatial and Temporal Variation of the Ice in Antarctica. Vol. I-2, Final Report, Dept. of Geography and Inst. of Polar Studies, the Ohio State Univ., Columbus, Ohio.

Sud, Y., and J. Abeles, 1980: Calculation of surface temperature and surface fluxes in the GCM. Submitted to ASME for publication in Appl. Meteor. (Also in NASA Tech. Memo. (herein), Atmos. and Oceano. Res. Rev.-1979, NASA Goddard Space Flight Center, Greenbelt, Maryland.)

Table 1a.

MODIFIED MODEL

VARIANCE OF STATIONARY GEOPOTENTIAL HEIGHT(Z) FOR THE MONTH

SOUTHERN HEMISPHERE 10(GPM**2)

J A N U A R Y

P(MB)	90S	86S	82S	78S	74S	70S	66S	62S	58S	54S	50S	46S	42S	38S	34S	30S	26S	22S	18S	14S	10S	6S	2S
50.	0	60	384	662	1838	2418	2828	2631	2440	1853	907	450	231	182	171	152	118	90	78	91	80	70	70
100.	0	487	1082	1304	2089	2029	2147	2228	1666	1397	907	507	368	319	207	146	203	270	292	344	279	186	159
200.	0	81	276	726	238	411	524	923	1071	877	699	483	397	322	167	140	284	376	314	208	130	88	82
300.	0	9	94	35	73	91	163	435	628	586	500	420	377	310	168	91	127	177	144	86	48	27	18
400.	0	28	140	61	104	80	101	250	398	386	378	305	288	250	154	69	43	50	39	22	11	6	4
500.	0	22	68	32	65	59	68	161	249	249	230	200	202	186	129	64	33	26	17	12	5	4	2
700.	0	9	14	11	35	26	33	58	86	95	94	97	117	124	98	61	38	36	33	31	17	10	7
850.	0	4	21	37	38	26	33	34	40	43	53	77	103	108	96	76	58	53	46	37	28	17	14
900.	0	7	33	70	56	29	36	29	32	34	46	77	104	107	102	90	76	67	54	41	27	20	17
950.	0	11	63	142	91	35	36	30	31	31	45	82	110	113	118	120	116	102	74	56	37	27	22
1000.	0	17	81	186	138	49	37	31	32	32	48	90	120	124	140	162	172	152	105	78	50	35	29
MEAN	0	68	195	274	434	476	545	620	675	485	360	254	218	195	142	107	116	127	111	91	64	44	37

VARIANCE OF STATIONARY GEOPOTENTIAL HEIGHT(Z) FOR THE MONTH

NORTHERN HEMISPHERE 10(GPM**2)

J A N U A R Y

P(MB)	2N	6N	10N	14N	18N	22N	26N	30N	34N	38N	42N	46N	50N	54N	58N	62N	66N	70N	74N	78N	82N	86N	90N
50.	69	68	60	70	150	373	640	869	1139	1460	2016	2716	3491	4185	3987	3221	1941	1172	768	529	248	67	0
100.	146	175	235	350	634	1039	1495	1748	1614	1327	1919	2662	3220	3341	3065	2260	1520	772	554	445	208	95	0
200.	69	79	127	231	405	622	744	563	380	860	1859	2573	2678	2225	1590	1078	861	578	592	470	305	116	0
300.	18	28	45	86	169	219	243	188	446	1231	2104	2506	2298	1663	1145	869	907	593	515	390	281	90	0
400.	4	6	13	24	42	65	90	174	557	1192	1769	1917	1689	1179	850	663	788	483	382	254	194	59	0
500.	3	5	9	12	19	32	60	181	476	915	1267	1313	1156	805	606	507	581	339	266	162	126	40	0
700.	8	11	18	23	29	35	56	126	272	471	601	624	547	376	295	245	256	149	102	63	81	17	0
850.	14	15	19	20	21	26	40	79	180	304	413	428	366	269	224	142	136	103	66	32	33	9	0
900.	19	17	20	20	20	27	45	81	177	286	386	392	336	277	246	150	164	144	85	37	36	8	0
950.	21	23	27	27	23	31	58	93	193	291	377	383	321	302	313	213	240	223	155	52	40	6	0
1000.	27	30	40	42	32	41	78	113	221	315	392	391	339	358	423	326	365	346	278	85	55	6	0
MEAN	34	41	56	82	142	228	323	384	504	787	1191	1447	1495	1360	1157	883	784	446	382	227	145	49	0

Table 1b

EARLIER MODEL

VARIANCE OF STATIONARY GEOPOTENTIAL HEIGHT(Z) FOR THE MONTH

SOUTHERN HEMISPHERE 10(GPM**2)

J A N U A R Y

P(MB)	90S	86S	82S	78S	74S	70S	66S	62S	58S	54S	50S	46S	42S	38S	34S	30S	26S	22S	18S	14S	10S	6S	2S
50.	0	42	372	668	1305	1372	926	774	714	578	481	404	319	255	173	100	68	58	65	83	71	62	59
100.	0	566	837	1138	1242	907	960	946	669	489	402	444	510	379	253	170	142	143	132	155	125	82	60
200.	0	288	664	652	865	470	593	460	260	208	261	443	532	322	141	165	227	247	169	93	46	21	14
300.	0	91	237	312	337	297	390	301	176	213	318	499	572	347	122	80	101	117	78	42	19	9	5
400.	0	38	143	135	226	191	267	254	150	194	278	420	499	329	127	45	34	41	25	15	6	3	2
500.	0	19	79	55	132	124	185	185	105	138	196	312	383	279	131	47	26	26	14	8	3	1	1
700.	0	6	18	17	23	56	110	68	49	57	95	139	211	183	123	60	41	30	18	8	3	1	1
850.	0	20	50	117	140	51	63	43	46	39	61	90	128	125	111	97	84	69	46	26	11	5	5
900.	0	35	90	181	234	88	75	41	48	37	52	84	109	113	112	113	109	93	64	39	18	9	8
950.	0	54	148	266	306	111	73	46	38	39	47	74	97	111	124	145	156	140	94	59	29	17	15
1000.	0	78	202	368	383	176	73	51	62	82	44	66	90	113	144	188	217	200	133	87	45	27	24
MEAN	0	113	260	192	507	319	331	280	213	186	205	272	313	211	142	109	110	105	76	56	34	21	17

VARIANCE OF STATIONARY GEOPOTENTIAL HEIGHT(Z) FOR THE MONTH

NORTHERN HEMISPHERE 10(GPM**2)

J A N U A R Y

P(MB)	2N	6N	10N	14N	18N	22N	26N	30N	34N	38N	42N	46N	50N	54N	58N	62N	66N	70N	74N	78N	82N	86N	90N
50.	63	63	61	48	57	79	98	148	435	1049	1953	2870	3289	3530	3434	3081	2527	1940	1479	984	548	88	0
100.	87	89	73	93	113	182	209	265	590	1180	2046	2630	2695	2720	2421	2071	1827	1567	1006	802	485	189	0
200.	14	20	42	83	163	231	206	213	274	551	919	1116	1292	1416	1377	1250	1221	1073	910	805	614	198	0
300.	5	8	19	46	97	149	188	214	298	439	621	769	922	1068	1099	1063	1018	897	841	801	559	162	0
400.	2	3	8	23	51	85	128	177	252	352	471	591	697	812	823	795	779	691	639	628	421	133	0
500.	1	2	3	12	24	48	88	130	187	266	357	438	501	567	556	510	512	419	421	385	273	105	0
700.	1	0	1	1	3	22	42	68	96	143	191	215	220	230	207	145	194	140	127	52	67	45	0
850.	2	6	9	16	20	32	59	70	75	66	104	116	121	119	109	66	89	70	56	20	44	11	0
900.	5	11	19	24	29	43	86	95	91	52	75	86	95	106	100	86	100	80	53	31	58	5	0
950.	16	19	36	42	43	63	133	139	123	47	54	65	81	107	141	138	126	133	106	56	60	3	0
1000.	26	31	56	68	64	93	196	197	168	52	45	64	98	154	224	237	201	242	221	109	71	3	0
MEAN	16	27	31	43	65	94	135	155	236	381	621	816	911	980	955	859	785	655	532	425	290	88	0

* Table 1c. Variance of geopotential height resulting from stationary eddies [$\overline{Z}^{*2}$] for the month.

(units in $10^2 gpm^2$)

[$\overline{Z}^{*2}$]	January																($10^2 gpm^2$)
P(mb)	10S	5S	EQ	5N	10N	15N	20N	25N	30N	35N	40N	45N	50N	55N	60N	65N	70N	75N
50	6.4	6.4	13.6	18.7	22.2	25.8	25.6	29.2	32.3	41.0	54.1	85.9	111.4	150.4	178.3	189.8	145.0	71.8
100	1.9	3.3	6.0	7.3	9.0	11.7	13.5	14.6	21.1	41.6	75.8	136.2	191.0	223.7	257.4	253.1	209.8	124.7
200	1.6	1.6	2.9	4.3	7.0	11.7	16.9	20.0	31.4	71.7	135.8	219.3	258.4	243.6	206.5	164.1	122.1	72.5
300	.2	.7	1.4	2.3	4.0	6.3	9.1	14.3	36.6	92.7	168.2	249.5	268.9	223.8	167.7	122.5	92.5	59.4
400	.2	.3	.7	1.1	1.8	3.1	5.6	12.0	32.9	79.9	140.2	198.4	199.6	158.9	121.4	97.6	79.6	58.3
500	.2	.2	.4	.7	1.0	1.8	4.1	9.8	25.3	57.3	94.4	132.2	135.5	108.3	81.5	66.9	56.8	41.6
700	.3	.3	.3	.4	.5	.9	2.1	4.9	11.6	25.1	43.4	63.6	72.5	58.9	37.5	25.7	22.2	16.4
850	.5	.4	.3	.3	.4	.8	1.6	2.9	6.2	12.0	20.9	34.5	46.0	38.5	18.8	10.7	12.0	11.5
900	.6	.5	.4	.4	.5	.8	1.6	2.9	5.8	10.3	16.4	27.5	40.3	35.3	17.1	9.8	11.9	12.1
950	.2	.3	.4	.5	.6	.9	1.9	3.3	6.1	9.7	15.1	24.1	35.0	32.6	17.5	11.3	13.6	12.7
1000	.7	.6	.6	.6	.8	1.4	2.5	3.8	7.3	10.7	15.7	23.2	31.2	30.6	20.1	15.6	17.3	13.8
Mean	.5	.7	1.2	1.6	2.4	3.8	5.8	9.3	20.3	45.9	81.3	122.1	137.9	122.0	98.2	79.5	64.5	42.7

* As taken from Table B11b of Oort and Rasmusson (1971).

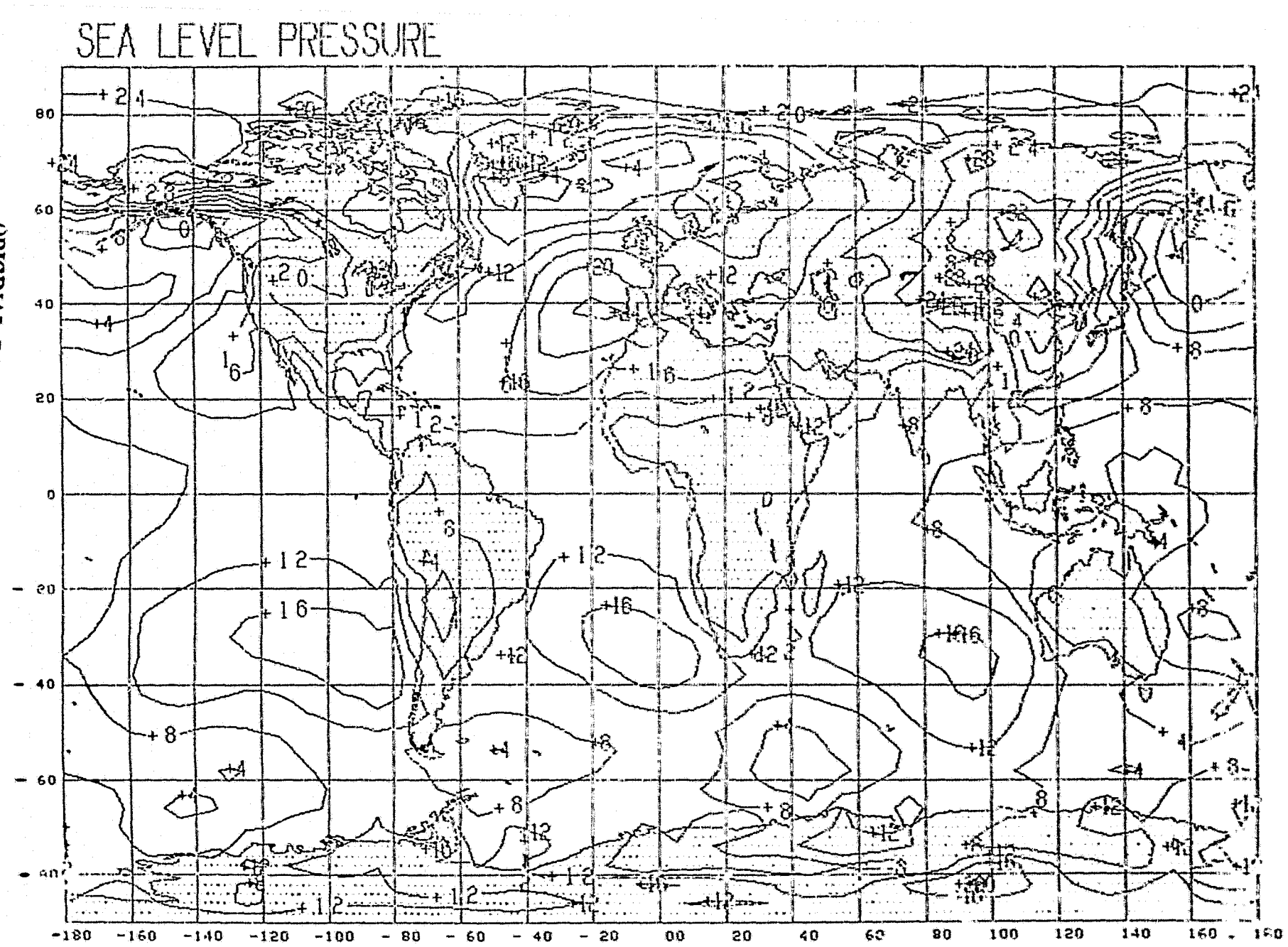

Fig. 1a. Sea level pressure plots for mean monthly January simulation with the modified GLAS model.

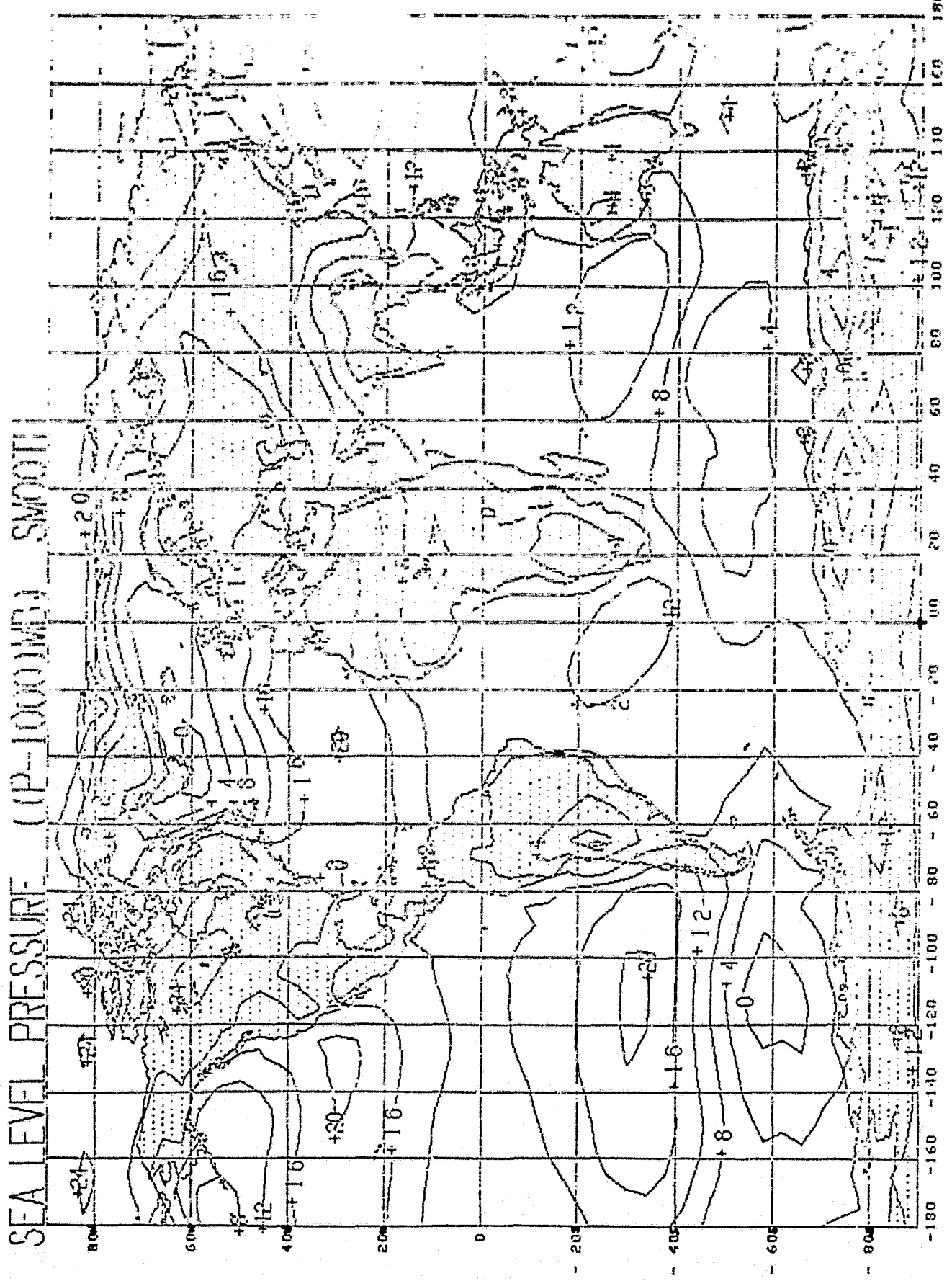

Fig. 1b. Sea level pressure plots for mean monthly January simulation with the earlier GLAS model.

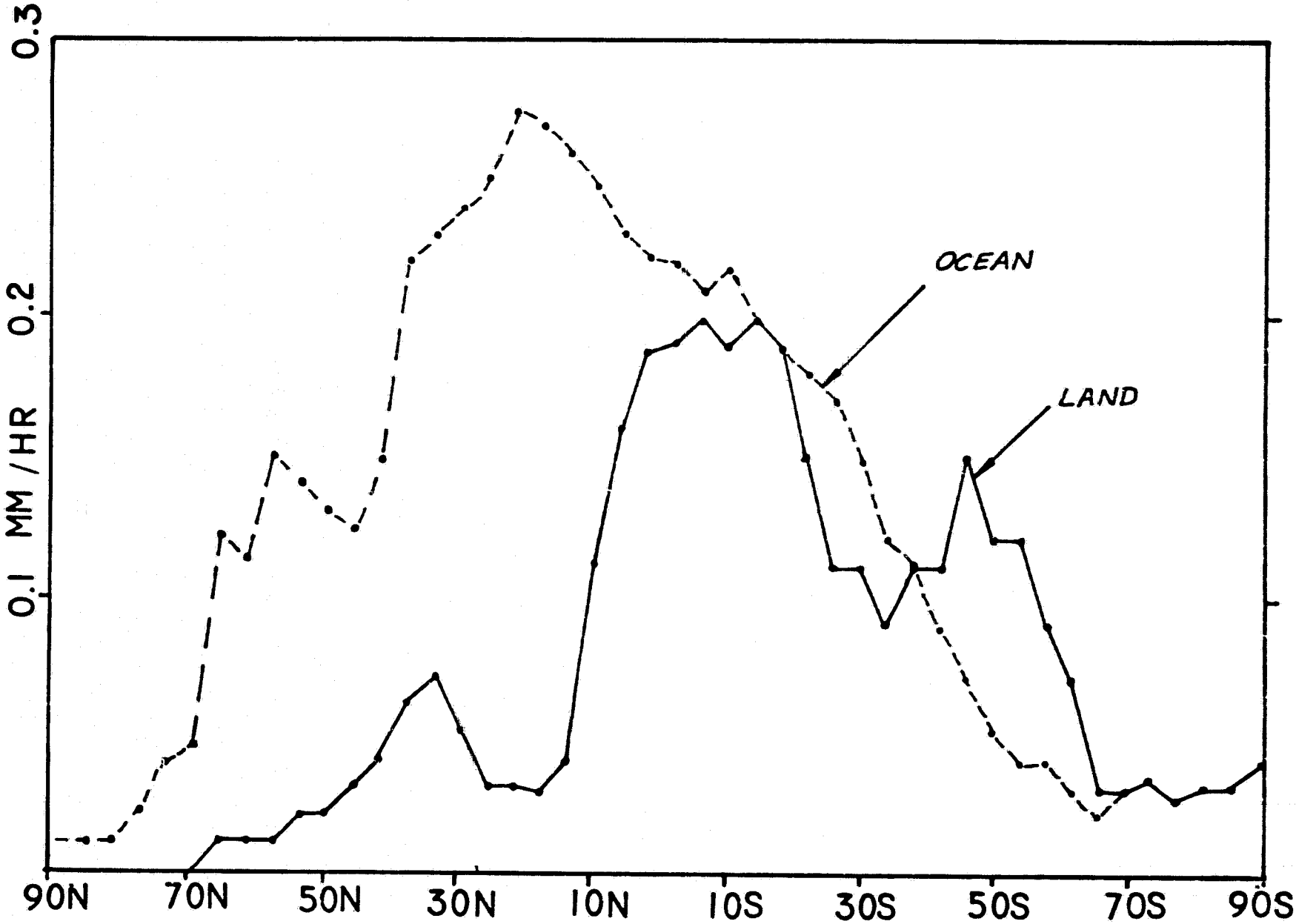

Fig. 2a. Zonal fields of evaporation over land and ocean for the modified GLAS model.

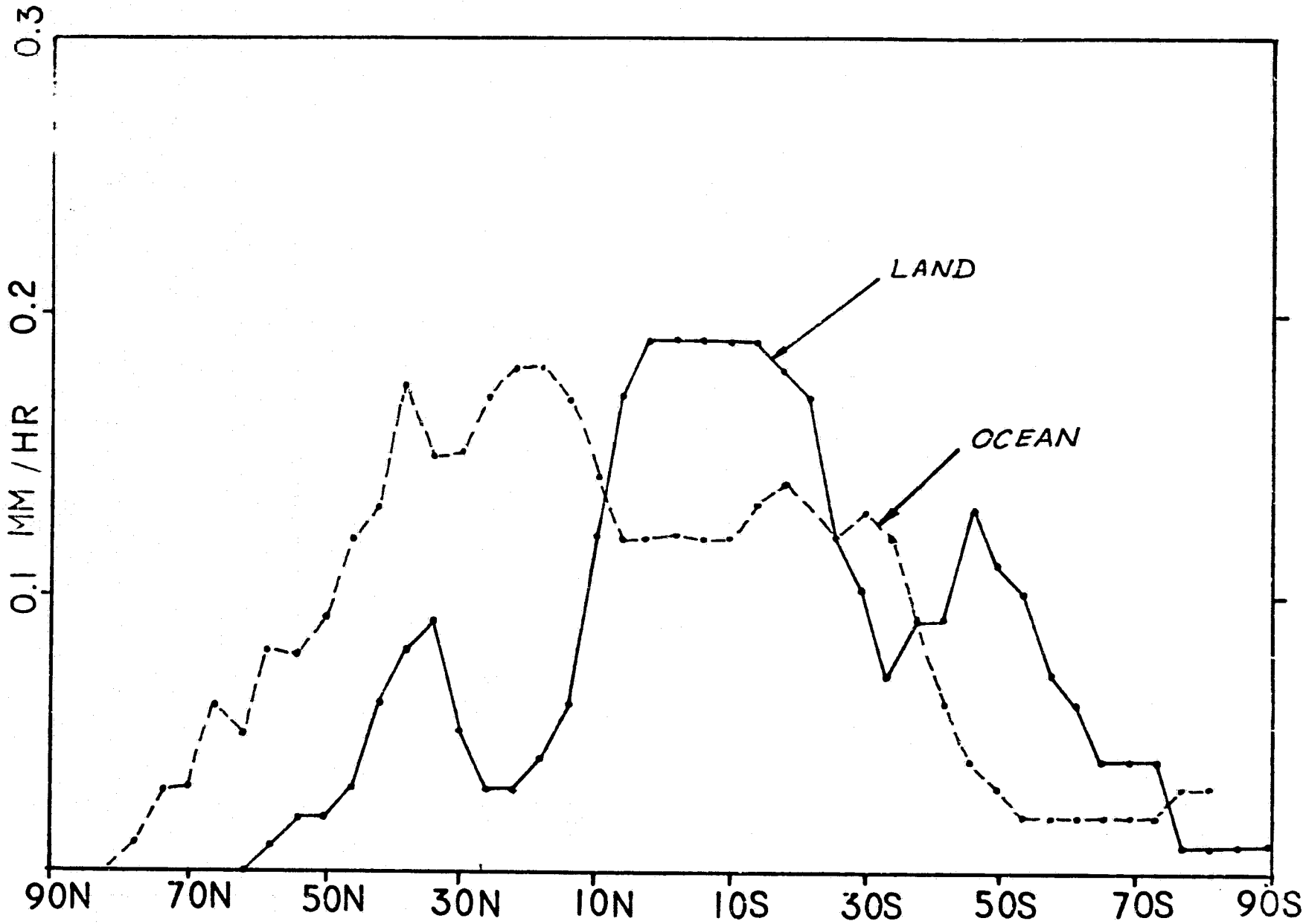

Fig. 2b. Zonal fields of evaporation over land and ocean for the earlier GLAS model.

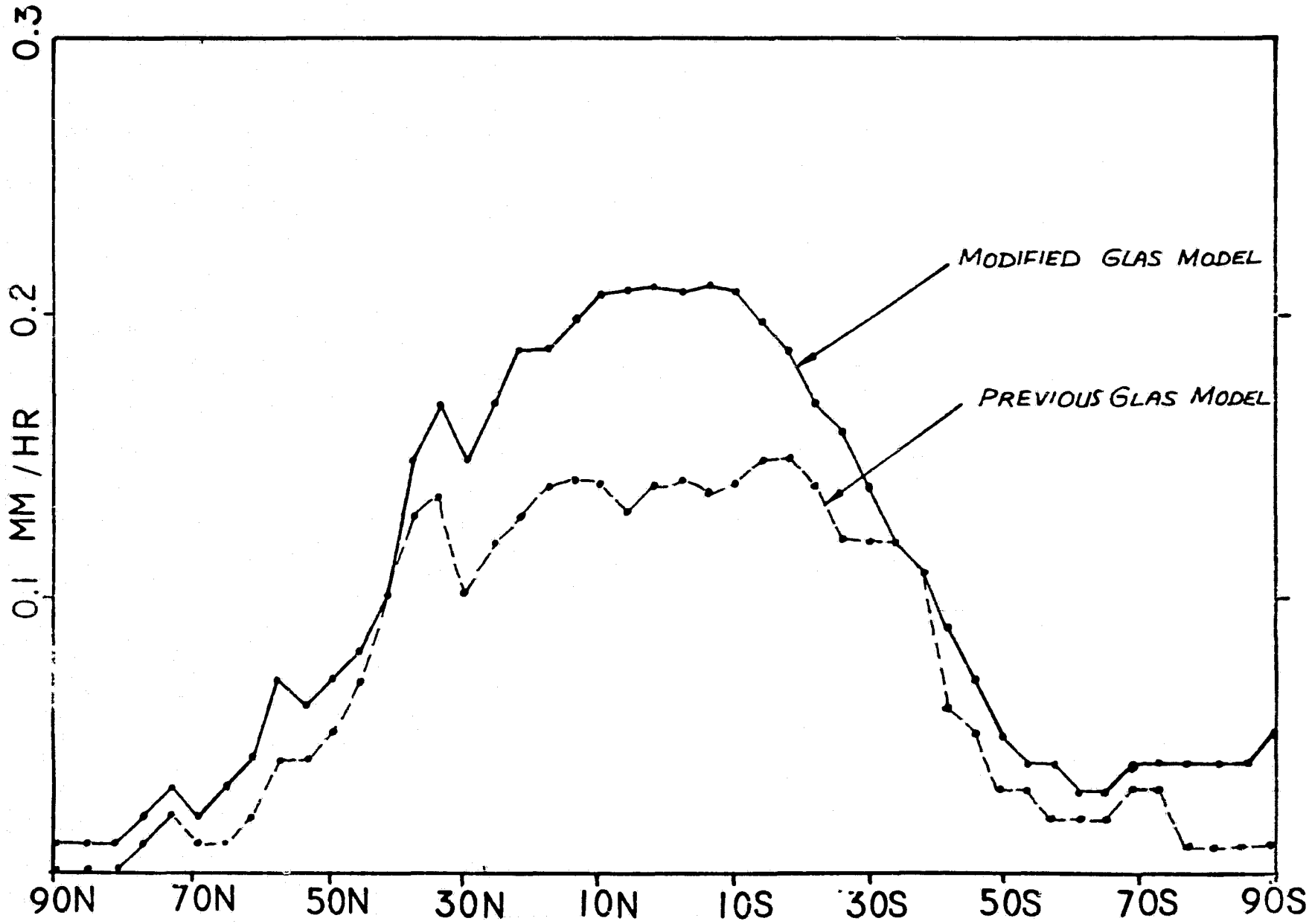

Fig. 3. Zonally averaged evaporation for the modified and earlier GLAS models.

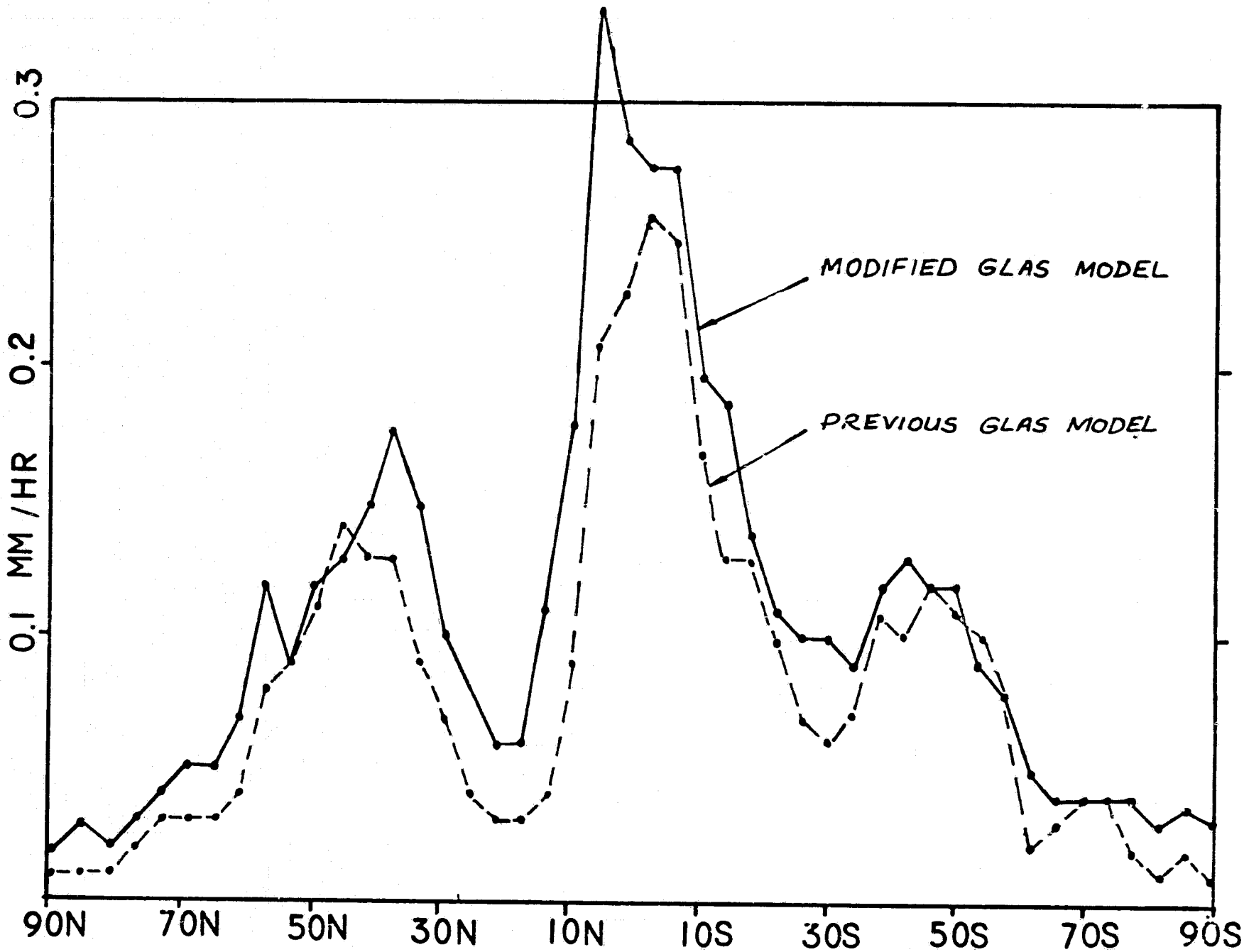

Fig. 4. Zonally averaged precipitation for the modified and earlier GLAS models.

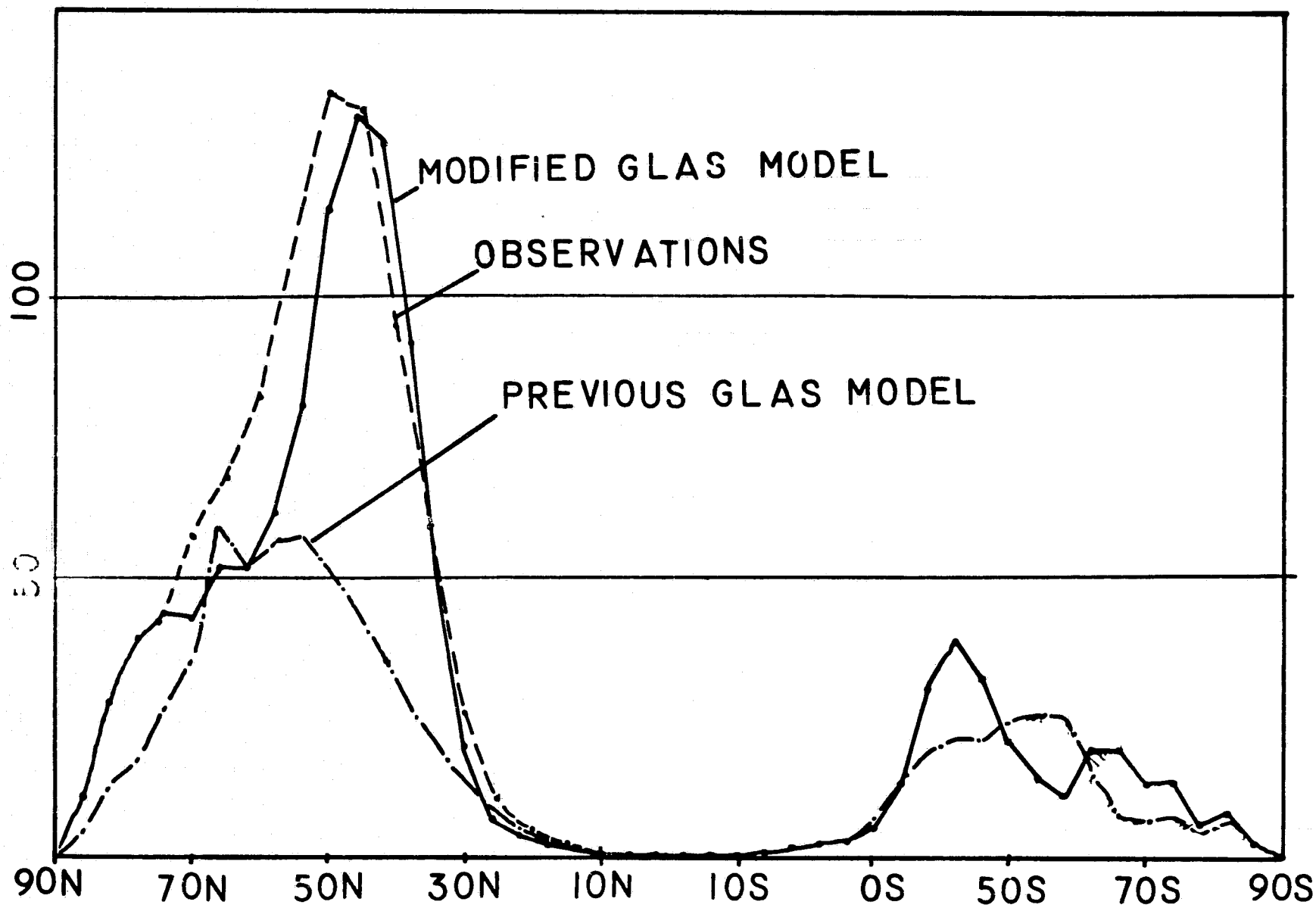

Fig. 5. Variance of 500 mb geopotential height for the modified and earlier GLAS models and observations.

MOISTURE AND ENERGY BALANCE STUDY FOR A SET OF WINTER AND SUMMER SIMULATIONS WITH THE GLAS MODEL

(Y. Sud)

A heat budget analysis of the earth atmosphere system yields heat balance fields separately at the surface of the earth, within the atmosphere, and at the top of the atmosphere. Basically the analysis is helpful in understanding the nature of energy and moisture storage in the atmosphere, transfers at the boundaries of the atmosphere, and transport within the atmosphere. The analysis is useful in correlating the dynamical processes with the energy transfers and transformations. In a GCM simulation, it has yet another very useful purpose, i.e., checking the conservation of energy and moisture globally. In the GLAS climate model, lack of conservation in the Shapiro filter is well known. Certain other ad hoc adjustments such as zeroing out of negative humidity and making the minimum specific humidity equal to 10^{-8} also contribute to lack of conservation. There are similar nonconservative simplifications in the physical calculations. Whereas in the next climate model all these inconsistencies will be eliminated to get even better conservation, the present model does yield some unaccounted energy and moisture in the atmosphere.

The circulation of global atmosphere is supported by thermal forcing. There are two basic sources of thermal forcing on the time scale of a season, which is 3 months or less in these studies: solar insolation and the fluxes of heat and moisture from the surface of the earth including oceans. Oceans are represented by a prescribed water surface temperature which varies steadily over a month. This implies that the oceans are infinite sources of sensible and latent energy. In a realistic interaction between the oceans and the atmosphere, a reasonable balance between the net radiation into the oceans and the fluxes of sensible and latent energy from the oceans is vital. On the surface of land, a simple conservative slab model is used. The change in soil temperature and soil moisture is determined by the net heat and moisture flux (precipitation-evaporation-runoff) to the soil. Over snow and ice on land, a part of the heat flux to the land may be used in melting ice or snow. This flux is lost for the surface heat balance through runoff. All energy and moisture balances are based on the conservation principle and may be derived from energy and moisture-conservation equations. A detailed discussion of the GLAS global circulation model may be found in Somerville et al. (1974) and Halem et al. (1979).

The GLAS model climate simulations generate diagnostics of energy and moisture fluxes at the top and bottom boundaries of the atmosphere. In conjunction with this, the initial and final states of the atmosphere for the simulation period may be used to obtain a complete energy and moisture cycle analysis of the earth-atmosphere system. The net surface balance can also be used to give the energy flux to the ocean. From all this data, calculations can be made to obtain energy transport in the atmosphere as well as the ocean. Similar calculations for moisture field yield moisture transport in the atmosphere. This study examines these quantities in great detail. Presented here is an analysis of a set of three summer and three winter runs. Each set

consists of a control run from the observed initial state of the atmosphere plus two predictability runs in which only the wind fields at the initial time are perturbed by 3 m sec^{-1}. The heat balance is obtained in the form of two-dimensional, zonal, hemispheric and global distributions of the sought quantities. Also, energy balance at the top of the atmosphere, energy balance at the surface of the earth, and moisture and heat balance in the atmosphere are obtained. Taking into account the storage of moisture and other forms of energy, the transport of heat and moisture in the atmosphere and transport of heat in the oceans are calculated.

Governing Equations

The energy and moisture flux diagnostics for the atmosphere are generated for an overall vertical column of air. There is no information about breakdown of these fluxes for individual σ-levels of the model. Water balance may be calculated from the balance between the fluxes of evaporation and precipitation. The following fluxes are written out as diagnostics every 6 h and their values are accumulated means over various model time steps in a given time interval. The units of each quantity are cal cm^{-2} day^{-1}.

F_S = Upward evaporation flux at the surface
P_S = Precipitation flux to the surface
H_S = Upward sensible heat flux at the surface
S_T = Incoming short wave radiation at the top of the atmosphere
S_a = Absorbed short wave radiation by the atmosphere
S_S = Upward long wave radiation at the surface
L_T = Upward long wave radiation at the top
L_S = Upward long wave radiation at the surface
H_p = Heat storage in melting/freezing water and heat conduction through sea ice.

The above diagnostics along with the initial and final states of the atmosphere are used to obtain a complete heat and moisture balance. The basic equations follow:

The total change of a conservative variable, ε, representing energy or mass as the case may be, can be written as,

$$\frac{\partial \varepsilon}{\partial t} = (\varepsilon_f - \varepsilon_i)/\Delta t \qquad (1)$$

Also,

$$\frac{d\varepsilon}{dt} = \frac{\partial \varepsilon}{\partial t} + \nabla.(\varepsilon v) - \frac{\partial}{\partial \sigma}(\varepsilon \sigma) \quad , \qquad (2)$$

substituting for $\frac{\partial \varepsilon}{\partial t}$ from (1) and taking $\frac{d\varepsilon}{dt} = \frac{ds}{dt}$, one obtains

$$\frac{ds}{dt} = (\varepsilon_f - \varepsilon_i)/\Delta t + \nabla.(\varepsilon v) \quad . \qquad (3)$$

Obviously $\frac{\partial}{\partial\sigma}(\epsilon\sigma) = 0$ for a column of air. Here ds/dt is the source term. It represents net flux from the source, s, which may be calculated from the diagnostics as follows:

For heat flux absorbed by the atmosphere,

$$\frac{ds}{dt} = S_a + H_s + P_s + (L_s - L_T) \quad , \tag{4}$$

For moisture flux to the atmosphere,

$$\frac{ds}{dt} = F_s - P_s \quad . \tag{5}$$

For energy flux to the oceans/land,

$$\frac{ds}{dt} = S_s - L_s - F_s - H_s + H_p \quad . \tag{6}$$

Similarly, ϵ_f or ϵ_i can be calculated at the final and initial time by: vertical integrals of enthalpy plus kinetic energy of the air, and vertical integrals of specific humidity for moisture in the air. The time integration of product $C_z T_g$ summed over land gives the heat absorbed by the ground. Here C_z is the thermal capacity of the ground and T_g is the ground temperature.

Global Integrals

The advection calculation in Eq. (3) applies to a finite area. If the equation is integrated over the entire globe, the advection integral must vanish. Therefore,

$$\frac{1}{A}\int_A \frac{ds}{dt}\,dA = \frac{1}{A}\int_A [(\epsilon_f - \epsilon_i)/\Delta t]\,dA \quad . \tag{7}$$

Since both the RHS and LHS of Eq. (7) can be independently calculated over the globe, the two sides should be equal in a conservative model. Any difference between the two represents lack of conservation. This difference is obtained for the energy and moisture balance in the atmosphere as well as the net heat flux to the oceans. Satellite observations analyzed by Barrett (1974), and Vonder Haar and Suomi (1971) show that global integrals of energy flux to the earth-atmosphere system should be vanishingly small. This implies thermal equilibrium of the oceans with the atmosphere which is a consequence of oceans attaining equilibrium with the atmosphere for millions of years.

Analysis of Results

From the monthly average of flux fields, we obtain their zonal, hemispheric and globally averaged distributions. Tables 1a and 1b show the hemispheric and global heat balances for February and July simulations. The mean fields and their standard deviations between the three runs for each hemisphere as well as over the entire globe are also shown. From the fluxes

Table 1a. February 1976 energy balance (cal/cm^2/day).

Items	Analysis of heat budget fields					
	S. hemisphere		N. hemisphere		Global	
	Mean	SD	Mean	SD	Mean	SD
Top boundary of atmosphere						
Incoming short wave flux	915.90	0.00	565.80	0.00	740.90	0.00
Outgoing short wave flux	284.50	1.35	170.60	1.03	227.60	1.19
Outgoing long wave flux	429.70	2.10	402.50	1.80	416.60	1.95
Within the atmosphere						
S.W. absorbed	125.60	0.52	78.40	0.14	102.00	0.33
L.H. release by precipitation	164.20	1.20	134.20	1.00	149.20	1.10
S.H. increase (atmosphere)	-9.40	1.30	3.75	0.80	-2.84	0.57
KE increase (atmosphere)	-0.15	0.07	-0.01	0.11	0.07	0.08
LE increase (moisture)	-0.80	0.41	1.11	0.80	0.16	0.22
Bottom boundary of atmosphere						
S.W. absorbed	505.70	1.78	316.70	0.66	411.20	1.22
L.W. outgoing	113.80	0.82	115.90	0.39	114.90	0.60
S.H. flux outgoing	48.00	0.53	70.00	0.67	59.00	0.60
L.H. flux outgoing	145.40	0.67	145.00	0.51	145.00	0.59
Net energy absorbed						
Land	-	-	-	-	10.76	-
Ocean	-	-	-	-	136.30	0.32
All surfaces	198.40	1.00	-14.08	0.84	92.18	0.92
At the top (atmosphere)	-201.60	0.56	8.34	0.18	-96.65	1.37
Unaccounted quantity						
Heat in the atmosphere	-	-	-	-	11.23	0.32
Moisture in the atmosphere	-	-	-	-	-4.14	0.12
Planetary albedo	0.31	0.15	0.30	0.18	0.30	0.16

Table 1b. July 1974 energy balance (cal/cm^2/day).

Items	Analysis of heat budget fields					
	S. hemisphere		N. hemisphere		Global	
	Mean	SD	Mean	SD	Mean	SD
Top boundary of atmosphere						
Incoming short wave flux	442.30	-	948.90	-	695.60	-
Outgoing short wave flux	129.50	1.37	307.49	2.95	218.52	2.06
Outgoing long wave flux	388.70	0.61	438.26	1.06	413.46	0.84
Within the atmosphere						
S.W. absorbed	66.00	0.08	142.79	0.23	104.40	0.16
L.H. release by precipitation	95.10	1.30	135.90	1.75	115.50	1.53
S.H. increase (atmosphere)	-7.89	0.70	18.18	0.19	5.14	0.38
KE increase (atmosphere)	0.62	0.06	0.02	0.01	0.32	0.03
LE increase (moisture)	-3.28	0.62	7.11	0.09	1.92	0.46
Bottom boundary of atmosphere						
S.W. absorbed	246.75	1.29	498.61	2.83	372.68	2.06
L.W. outgoing	148.44	0.67	178.25	1.10	163.35	0.89
S.H. flux outgoing	41.55	1.05	43.08	0.91	42.31	0.98
L.H. flux outgoing	112.03	1.14	112.94	0.79	112.48	0.97
Net energy absorbed						
Land	-	-	-	-	5.63	-
Ocean	-	-	-	-	75.27	4.06
All surfaces	-55.27	2.41	164.35	0.84	54.54	1.62
At the top (atmosphere)	-75.90	0.97	203.15	1.85	63.62	1.47
Unaccounted quantity						
Heat in the atmosphere	-	-	-	-	14.68	4.28
Moisture in the atmosphere	-	-	-	-	-13.70	3.96
Planetary albedo	0.29	0.003	0.32	0.003	0.31	0.003

at the top and bottom of the atmosphere, the net energy balance at the top and bottom of the atmosphere is calculated. The surface energy balance is further subdivided into its land and ocean distributions. Land is treated as a slab of finite but small heat and moisture capacity. Therefore, averaged over a month, the surface heat and moisture balance over land should be negligible. On the other hand, over the oceans the net surface fluxes may be substantial depending upon the region. However, in a realistic model, the net globally averaged surface flux over the ocean must be small. This is found in observations (Vonder Haar and Suomi, 1971). This result also must follow as a natural consequence of oceans equilibrating with all its environments over millions of years. In fact, this is one of the basic assumptions in simpler climate models which neglect oceanic storage (e.g., Sellers, 1967). However, this is not the case with our model simulations.

There is a large net globally averaged heat flux sinking into the oceans both in the February and July simulations. This situation in turn leads to reduced outgoing long wave flux at the top of the atmosphere. This reduced flux must be supported by lower upper level temperatures of the simulation model which is indeed one of the weaknesses of our simulation model. Thus, too cold upper atmosphere simulated by the model seems to be consistent with sinking of heat in the oceans. However, it is not clear how the two effects are dynamically related. We know that the present climate model oceans do not evaporate sufficiently. Past attempts to increase evaporation by an ad hoc increase in the boundary layer transport coefficients in the model were not successful because the final equilibrium of ocean-atmospheric interactions brought the two to a state which leads to very little change in the fluxes of sensible heat and evaporation over the ocean. All these findings point out that the main weakness may be in the upward transport of energy. In whatever way this discrepancy is resolved, it appears that cooling of upper model levels and sinking of net energy in the oceans are manifestations of the same problem.

In Table 2 computed upwelling long wave fluxes are shown for two cloud-free columns of air which have temperature and humidity profiles for the mean monthly February zonally averaged at 50N for the model simulations and analyzed observations (Oort and Rasmusson, 1971). Notice the model temperature profile has typically colder upper atmosphere and yields 8.2 percent lower outgoing long wave flux at the top of the atmosphere. The reduction in cooling is of the order of heat sunk in the oceans. The heat balance is shown schematically in Figs. 1(a) and 1(b) for the data in Tables 1a and 1b for February and July, respectively.

Conclusions

The heat balance analysis of February and July simulations with the GLAS model reveals that the GLAS model energy and moisture balance fields are in good agreement with observations and present a consistent picture. Conservation is reasonable but is not within the limits of round-off errors.

Table 2. Computed upwelling long wave fluxes for two cloud-free columns of air for February, zonally averaged at 50N.

Pressure (mb)	Model simulation			Observed†		
	Temperature (°K)	Humidity (g/kg)	Upward long wave flux ($cal/cm^2/day$)	Temperature (°K)	Humidity (g/kg)	Upward long wave flux ($cal/cm^2/day$)
65	203.6	0.02	415.8	218.2	0.02	449.9
175	205.9	0.12	404.2	217.2	0.15	427.3
285	214.3	0.31	391.5	220.2	0.35	406.8
395	228.7	1.34	372.8	232.2	2.50	383.3
505	242.0	4.10	339.1	244.2	4.00	343.2
615	252.3	7.90	300.6	253.2	8.00	309.4
725	259.5	11.90	264.8	259.2	12.50	274.3
835	264.5	16.80	233.5	264.2	17.50	244.7
945	267.0	26.40	203.6	268.2	27.80	216.8
1000	268.3	30.00	175.2	270.2	30.00	186.9

† Observed data represents winter season mean taken from Oort and Rasmusson (1971).

HEAT BALANCE GLAS GCM

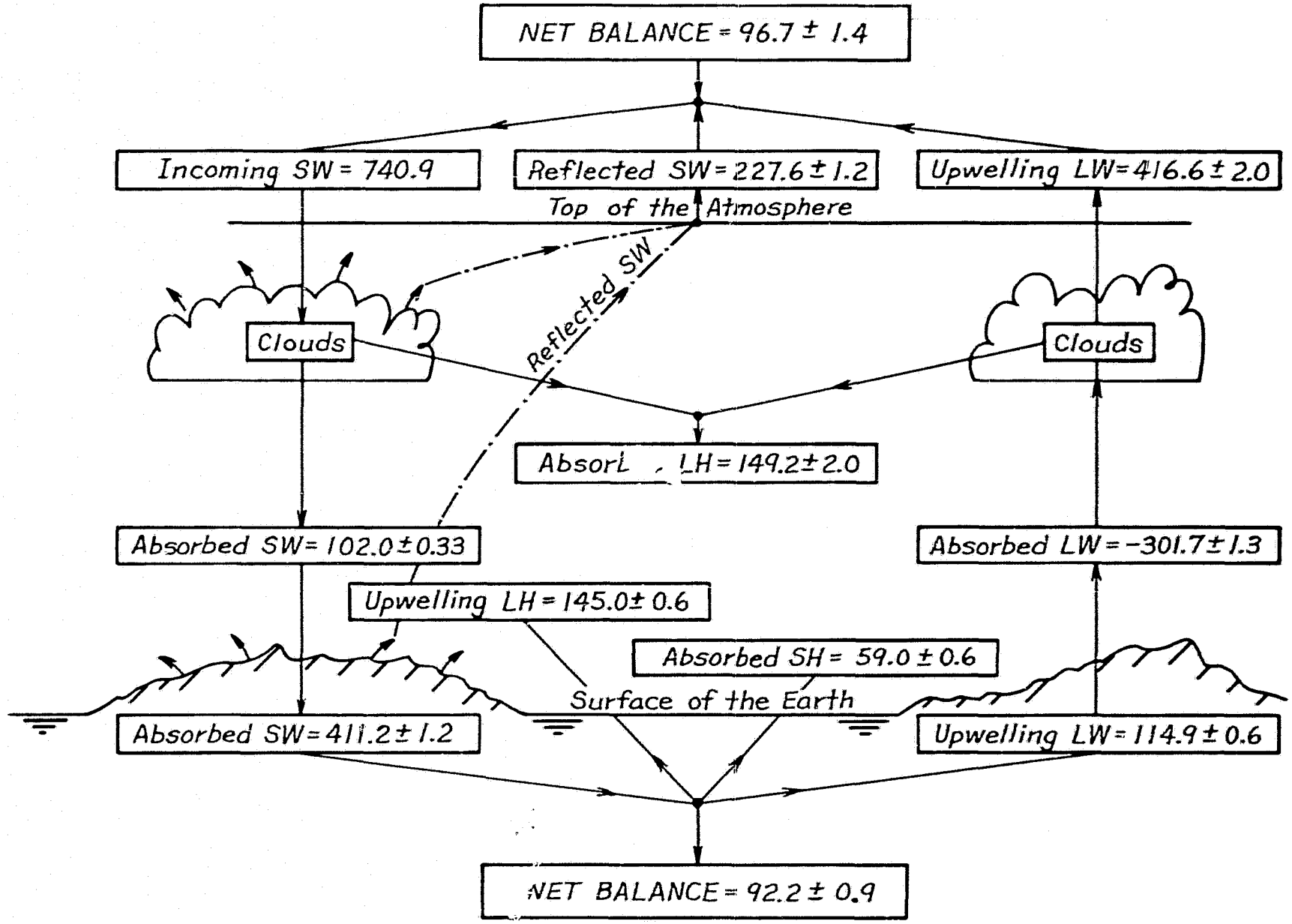

Fig. 1a

HEAT BALANCE GLAS GCM

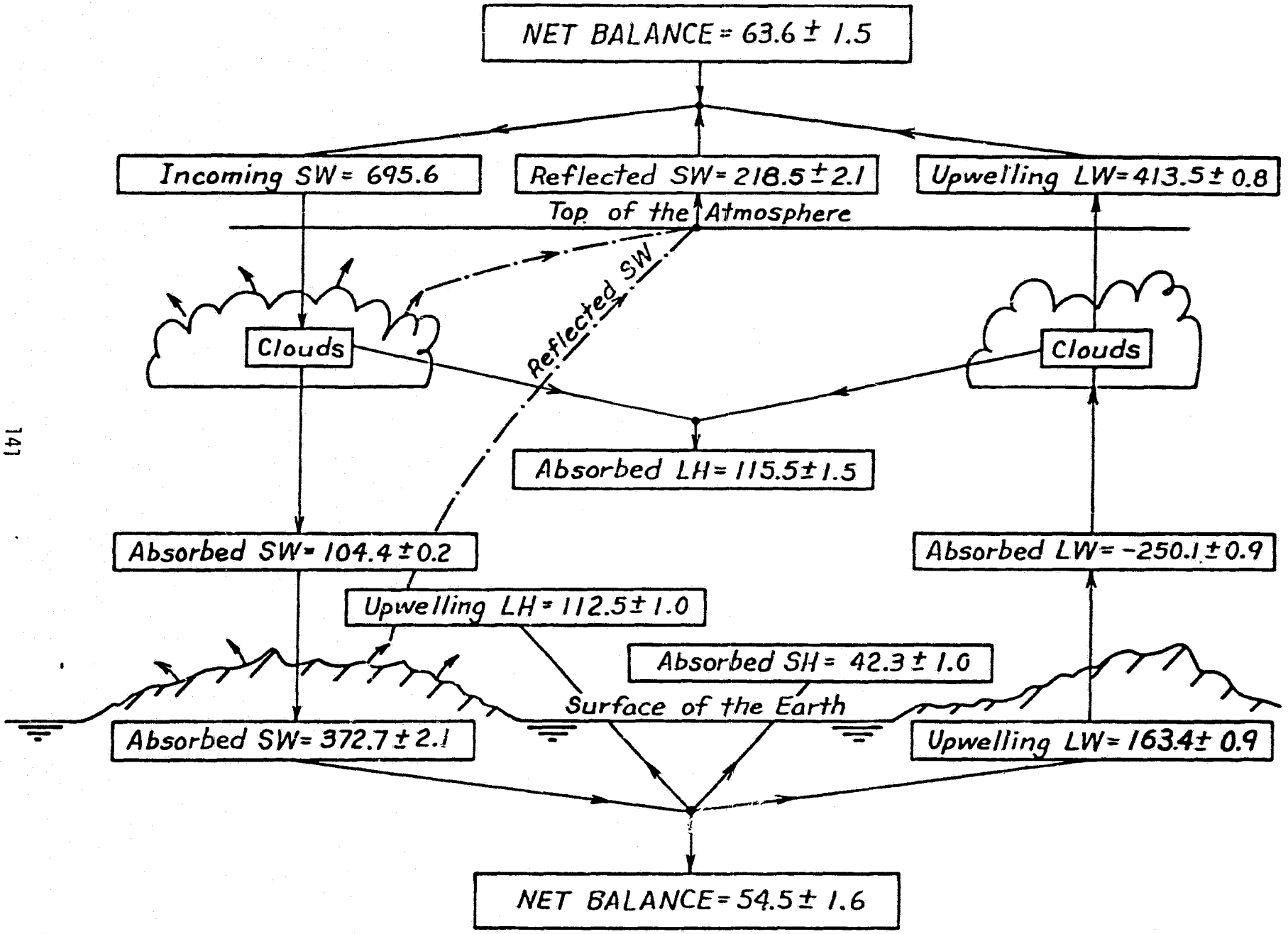

Fig. 1b

The model loses .02 mb/day of air mass which is within the limits of round-off. However, making up this loss by adding mass uniformly itself contributes to lack of conservation. The major factors for the lack of model conservation are: use of nonconservative Shapiro filter, model round-off, and some other nonconservative calculations discussed in the introduction. Another major weakness of the model is its sinking of large amounts of energy in the oceans. The next climate model which uses a modified boundary layer to enhance fluxes of moisture and sensible heat over the oceans (Sud and Abeles, 1980) is expected to correct this situation. The study reveals that upper level cooling of air may be a consequence of lack of surface energy balance in the model brought about by adjustment through dynamical transport processes. If it turns out that this is indeed the case, then the finding is important because it points out that the boundary layer processes can affect the upper levels of the atmosphere on a climate scale. However, this result is merely an indirect inference and needs further evidence.

Acknowledgments

Heat balance analysis of the model simulations with the GLAS model started with the JOC Study Conference on Climate Models held in Washington, DC, in April 1978. On the suggestion of Dr. J. Shukla, the present detailed heat balance analysis of the model simulations was undertaken. I wish to sincerely thank Dr. J. Shukla for his support and encouragement in taking the analysis to its present stage.

References

Barrett, E. C., 1974: Climatology from Satellites. Fletcher and Sons Ltd., Norwick, United Kingdom, 147-195.

Halem, M., J. Shukla, Y. Mintz, M-L. Wu, R. Godbole, G. Herman, Y. Sud, 1979: Comparisons of observed seasonal climate features with a winter and summer numerical simulation produced with the GLAS general circulation model. Report of the JOC Study Conf. on Climate Models: Performance, Intercomparison and Sensitivity Studies, GARP Publ. Series No. 22, 207-253, WMO, Geneva, Switzerland.

Oort, A. H., and E. M. Rasmusson, 1971: Atmospheric Circulation Statistics, Environmental Research Laboratories, Geophysical Fluid Dynamics Laboratory, Princeton, New Jersey, NOAA Professional Paper 5. U.S. Department of Commerce, Rockville, Maryland.

Sellers, W. D., 1967: A global climate model based on the energy balance of the earth-atmospheric system. J. Appl. Meteor., 8, 392-400.

Somerville, R. C. J., P. H. Stone, M. Halem, J. E. Hansen, J. S. Hogan, L. M. Druyan, G. Russell, A. A. Lacis, W. J. Quirk, and J. Tenenbaum, 1974: The GISS model of the global atmosphere. J. Atmos. Sci., 31, 84-117.

References (Continued)

Sud, Y., and J. Abeles, 1980: Calculation of surface temperature and surface fluxes in the GCM. Atmos. and Oceano. Res. Rev.-1979, NASA Tech. Memo. (herein), NASA Goddard Space Flight Center, Greenbelt, Maryland. (Also, submitted to ASME for publication in J. Appl. Meteor.)

Vonder Haar, T. H., and V. E. Suomi, 1971: Measurements of earth radiation budget from satellites during a five year period, Part I, extended time and space means. J. Atmos. Sci., 19, 369-384.

ARCTIC AND ANTARCTIC CLIMATOLOGY OF THE GLAS GCM

(G. F. Herman and W. T. Johnson)

A detailed study of the high latitude climatology of the GLAS GCM was conducted in order to assess the reliability of the model for high latitude climate studies, such as those involving changes in atmospheric carbon dioxide or sea ice boundaries.

The model-generated January climatology was constructed from eight simulations (Runs No. D058, D077, D084, D091, D092, D093, D094, D095), while the July climatology was based on seven simulations (Runs No. D115, D116, D119, D120, D126, D127, D129). These runs differed from one another by either small, randomly distributed values in the initial conditions, by variations in sea surface temperature or sea ice margin, or by minor variations in model physics. The selection of runs involving both different initial conditions and different boundary conditions is an attempt to represent some of the processes in nature that cause one January (or July) to differ from another.

The January climatology of the model was computed by forming the average of eight 30-day simulations, which in turn were each formed by averaging the model-generated fields sampled at 12-h intervals. A comparison is made between these results and the NCAR data set made available by Jenne (1975).

Fig. 1 illustrates the distribution of sea level pressure for January in the northern hemisphere as obtained in the model and given by the NCAR climatology. The dominant features of the observed circulation are the major low pressure systems over the North Atlantic and North Pacific, the broad and intense Siberian anticyclone, and a somewhat weaker anticyclone over northwest Canada. The Icelandic low in the model's climatology is in excellent agreement with observations, but appears to be about 4 mb too deep. The model's Aleutian low is not quite as extensive as observed, and its center is located about 15° longitude too far to the east. The major deficiency of the model's high latitude climatology is its failure to represent in any realistic way the Siberian anticyclone. In nature, this high pressure center extends over a vast region of the central U.S.S.R. from the Caspian Sea to the Sea of Japan, with a central pressure exceeding 1032 mb. The high in the model is confined to northwest Siberia, with central pressures on the order of 1024 mb.

The distribution of pressure during the northern hemisphere summer is shown in Fig. 2. During the summer, the observations show that the winter-time lows over the oceans have been replaced by broad regions of high pressure, while weak thermal lows dominate the continents. An area of weak low pressure is found in the Central Arctic. In the model climatology, the maritime high pressure areas tend to be too weak by about 4-6 mb, and the continental lows too deep, particularly over Asia. A weak ridge of high pressure spans the Central Arctic.

Sea level pressure over Antarctica is not well defined because of the difficulty both in the model and in the observations of reducing surface pressure to sea level. However, a comparison can be made over the peripheral

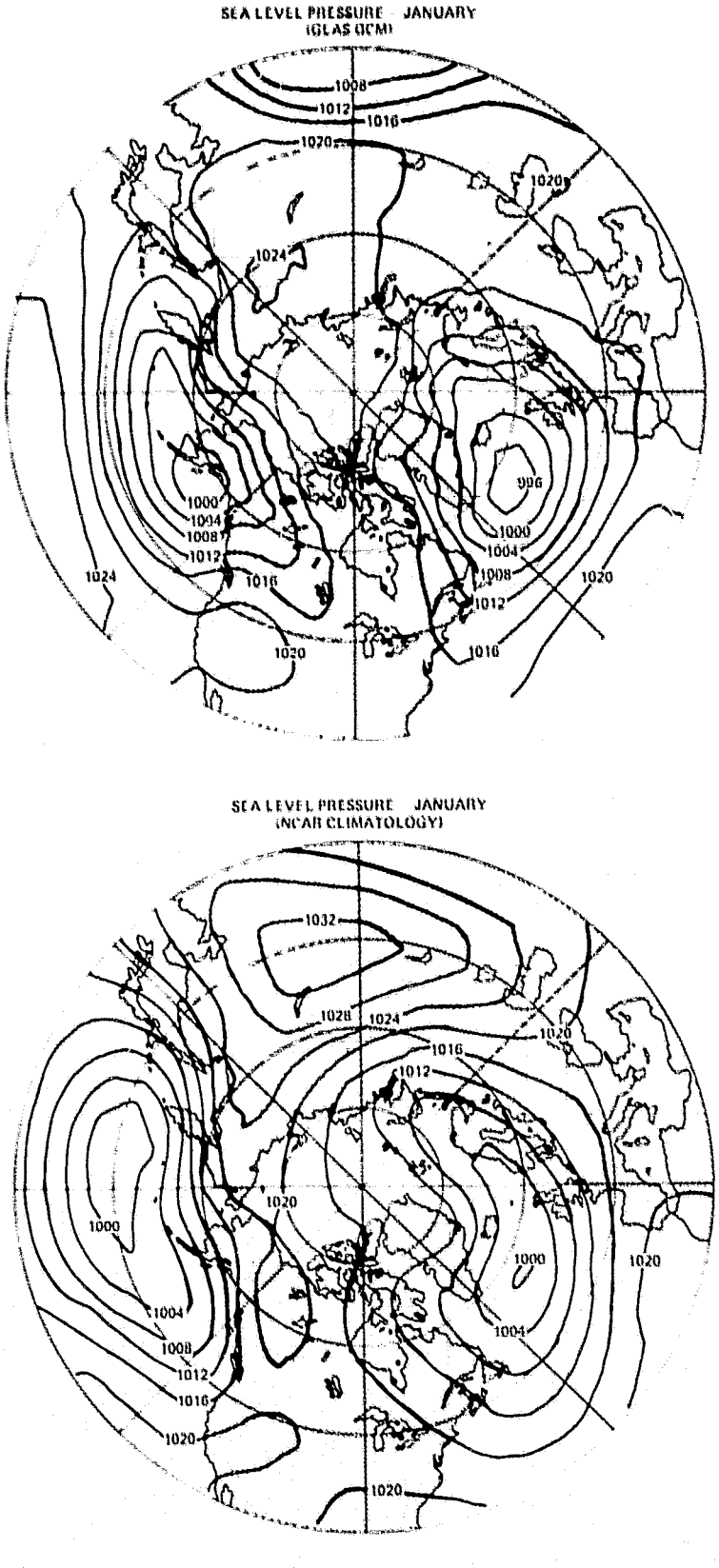

Fig. 1. January-February sea level pressure distribution for GLAS GCM (top) and NCAR climatology (bottom).

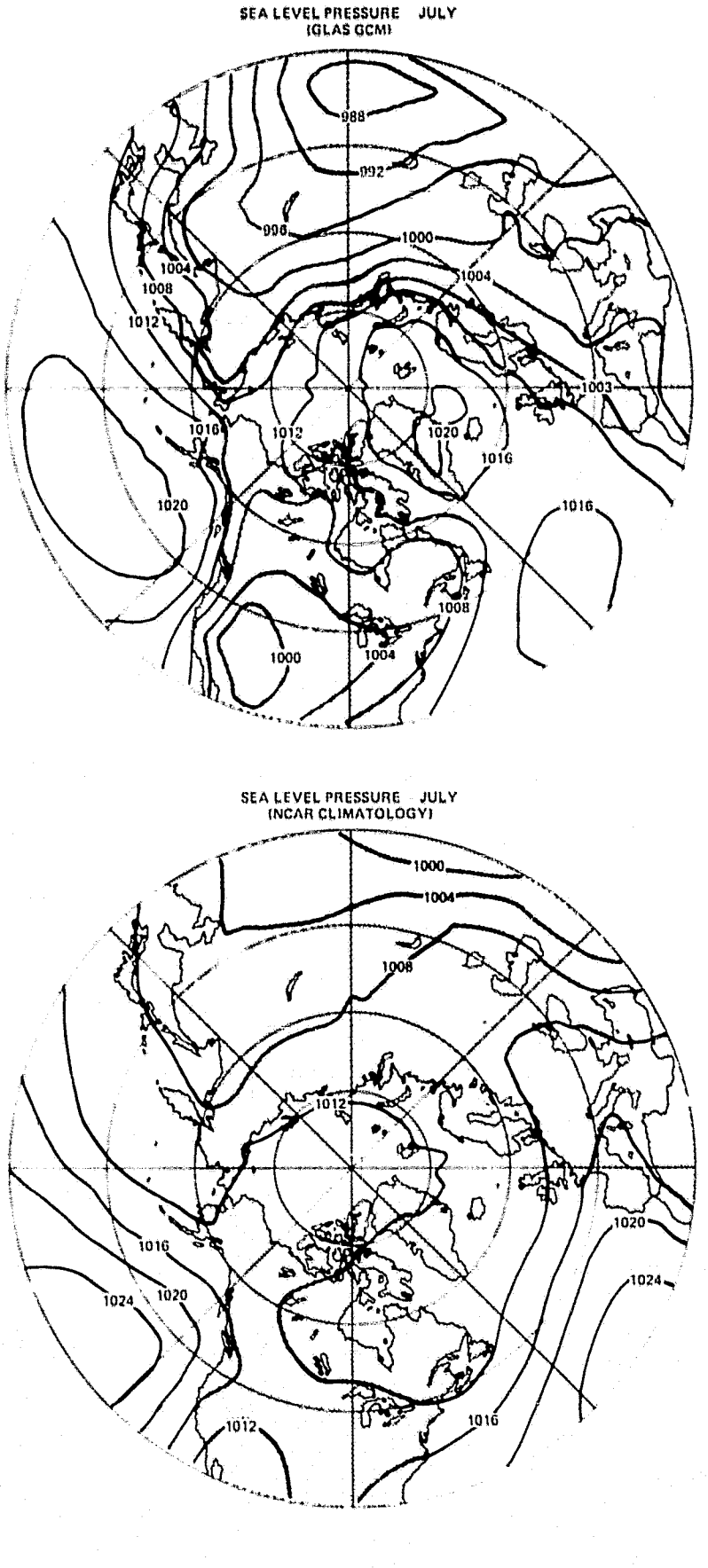

Fig. 2. As in Fig. 1 except for July.

sub-Antarctic oceans. Observations indicate that during the winter (July) (Fig. 3), the Antarctic continent is encircled by deep low pressure regions found in the Ross, Weddell, and Bellinghausen Seas. Broad regions of high pressure are found in the central regions of the Atlantic, Pacific, and Indian Oceans. The July model climatology misses most of these features. While the ridge of high pressure in the South Pacific is well simulated, that in the Indian Ocean is missing, while that in the South Atlantic is underestimated. The stationary low pressure centers around Antarctica do not occur in the model, and this points to a problem that the model has in generating baroclinic eddies in the high latitudes of the southern hemisphere. During the summer (January) (Fig. 4), the high pressure regions over the oceans are even more expansive, and a number of low pressure centers continue to ring the Antarctic continent. The model does a reasonable job of reproducing the oceanic highs in January, but is capable of producing only a weak low pressure center (996 mb) in the high latitudes of the South Pacific.

The mean flow at 500 mb during January is shown in Fig. 5. The dominant features of the observed January climatology are deep troughs located over the Hudson Bay and the Sea of Okhotsk, and a weaker trough over the western U.S.S.R. Maximum zonal flow occurs in midlatitudes off the east coast of Japan and over the eastern U.S. In the model both the midlatitude jet and the Canadian trough are well represented, but the axis of the trough is located about 15° longitude too far to the east. A Eurasian trough appears, and also is slightly displaced to the east. The most glaring deficiency of the model appears to be its failure to reproduce the Pacific trough, which is a difficulty likely to be associated with problems in treating adequately the Himalayan topography.

It appears that, at the surface in the northern hemisphere, the model does its best at reproducing circulation features over the oceans. This is not surprising since the oceans exert such a strong influence on surface features and have their temperatures specified in the model. The agreement with observations is not as good over land, and it is speculated that this is a consequence of problems in treating the interaction between the surface radiation budget and cloudiness.

The long wave structure of the model's climatology appears reasonable in the western hemisphere but not in the eastern hemisphere.

Reference

Jenne, R. L., 1975: Data sets for meteorological research. NCAR Tech. Note TN/IA-111, 194 pp.

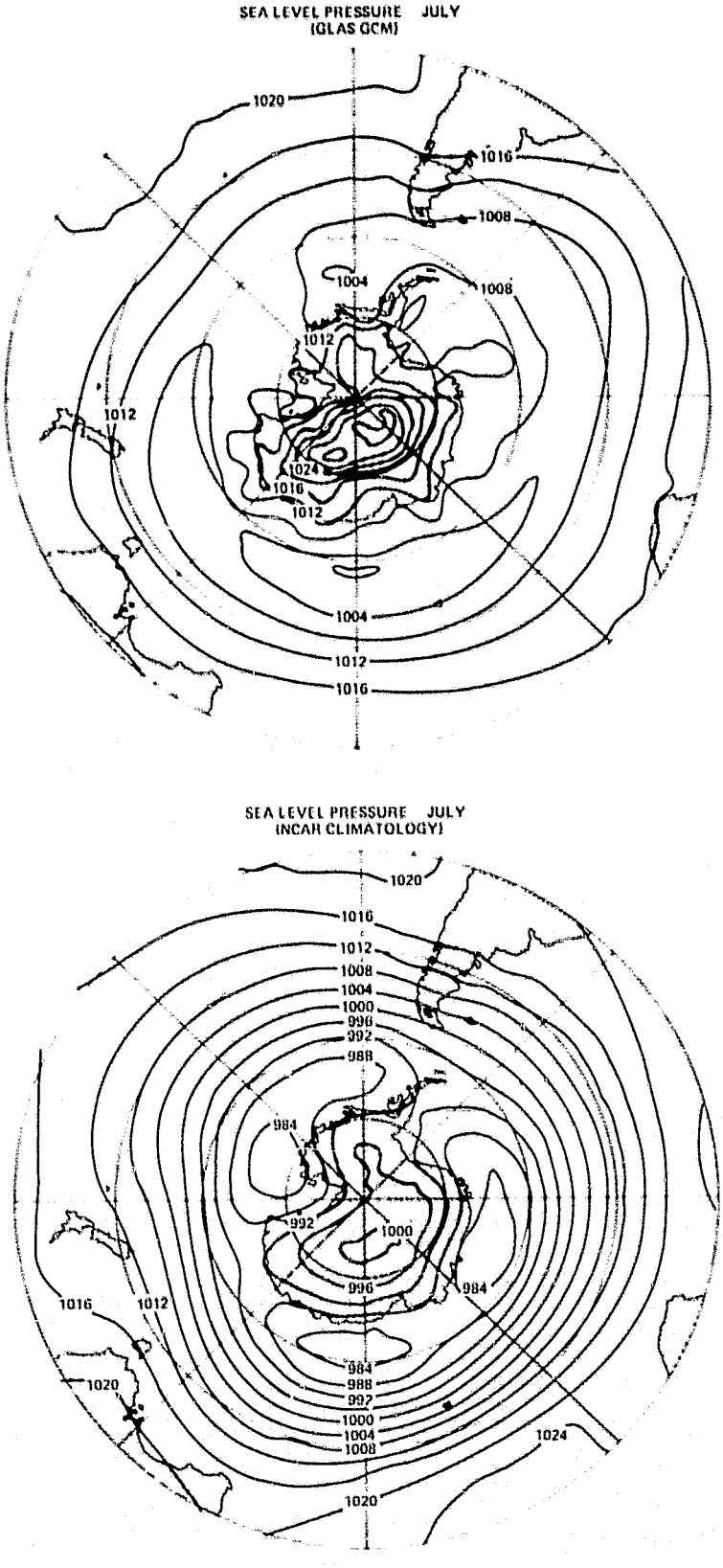

Fig. 3. As in Fig. 2 except for southern hemisphere.

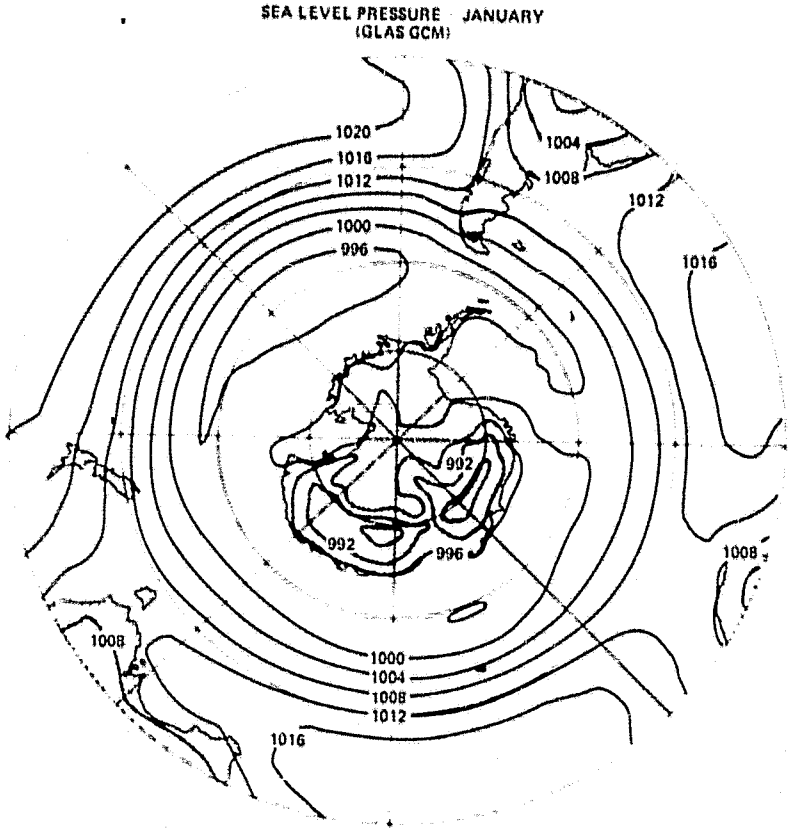

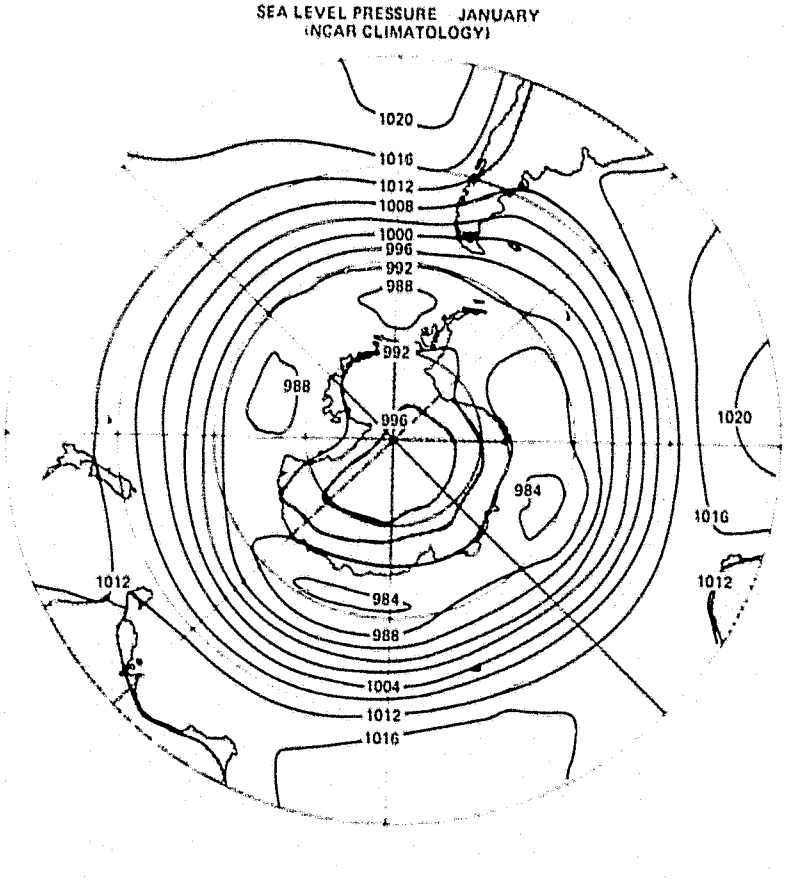

Fig. 4. As in Fig. 3 except for January-February.

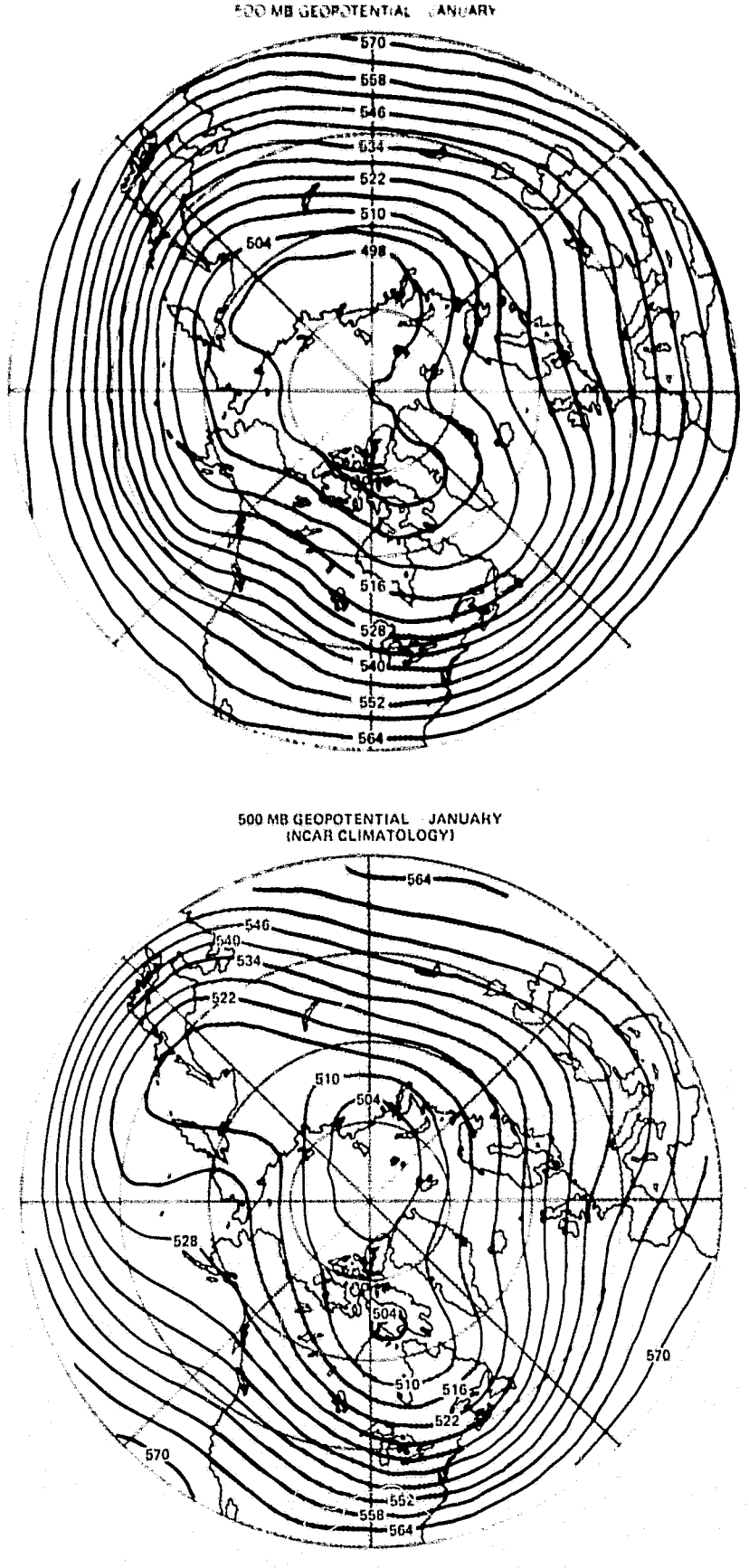

Fig. 5. January-February 500 mb geopotential height field for GLAS GCM (top) and NCAR climatology (bottom).

SEA ICE SIMULATIONS BASED ON GLAS GCM OUTPUT

(C. L. Parkinson, G. F. Herman, M. R. Good, and W. T. Johnson)

The sea ice cover of the north and south polar seas plays an important role in determining the energy balance of the surface through its effect on surface albedo and its influence on heat and moisture transport at the air-sea ice interface. At the present time, the sea ice coverage of the GLAS GCM is a specified parameter, i.e., it varies according to a predetermined climatology and does not alter the value of model-generated variables.

As a preliminary step in the development of a fully coupled ice-atmosphere-ocean model, an "offline" sea ice simulation is being conducted in which the atmospheric fields calculated with the GLAS GCM have been used as forcing for a sea ice model, but in turn are not affected by the resulting distribution of sea ice.

The sea ice model employed is essentially the thermodynamic portion of the Parkinson and Washington (1979) model. It includes a snow layer, an ice layer, and a lead percentage within each grid square. The calculation involves energy balances at the water-ice, ice-snow, snow-air, and water-air interfaces. The incoming short and long wave radiation and precipitation amounts are based directly on the GCM output, while the sensible and latent heat fluxes are calculated through bulk aerodynamic formulae which use GCM-generated air temperatures, specific humidities, and wind speeds.

The GCM calculation was a 3-month run (GMSF reference No. D122) based on 00Z 1 January 1975 NMC initial conditions. Initial sea ice concentrations for the same date were estimated from maps of average brightness temperature recorded by the Electrically Scanning Microwave Radiometer (ESMR) on NIMBUS 5 over the 3-day period, 30 December 1974-1 January 1975. Initial ice thicknesses were estimated based on climatology. The initial ice extents and thicknesses are shown in Fig. 1.

The results of the simulation are shown in Figs. 2 through 4. In the Arctic, there is some adjustment to the relatively thick initial ice cover, and ice in the coastal region melts during January. However, in February and March the ice thickens again, as would be expected for that time of year. The northern hemisphere ice extents move equatorward from January to March, with retreat of the ice beginning by 1 April.

In the southern hemisphere (Figs. 1-2), the ice melts during January and February (i.e., during the Antarctic summer). Although the ice thickens somewhat from mid-February to mid-March (Figs. 2-3), the ice edge retreats, especially in the Bellingshausen and Amundsen Seas. The continued ice retreat into March does not correspond well with the observed seasonal cycle as interpreted from the ESMR imagery for 1975. The simulated ice expands outward during the latter half of March (Figs. 3-4), and it appears that the simulation has simply extended the melt season by 1/2-1 month. A likely cause of the extended melt season in the Antarctic may be the unrealistically high surface temperatures which characterize the model's Antarctic climatology

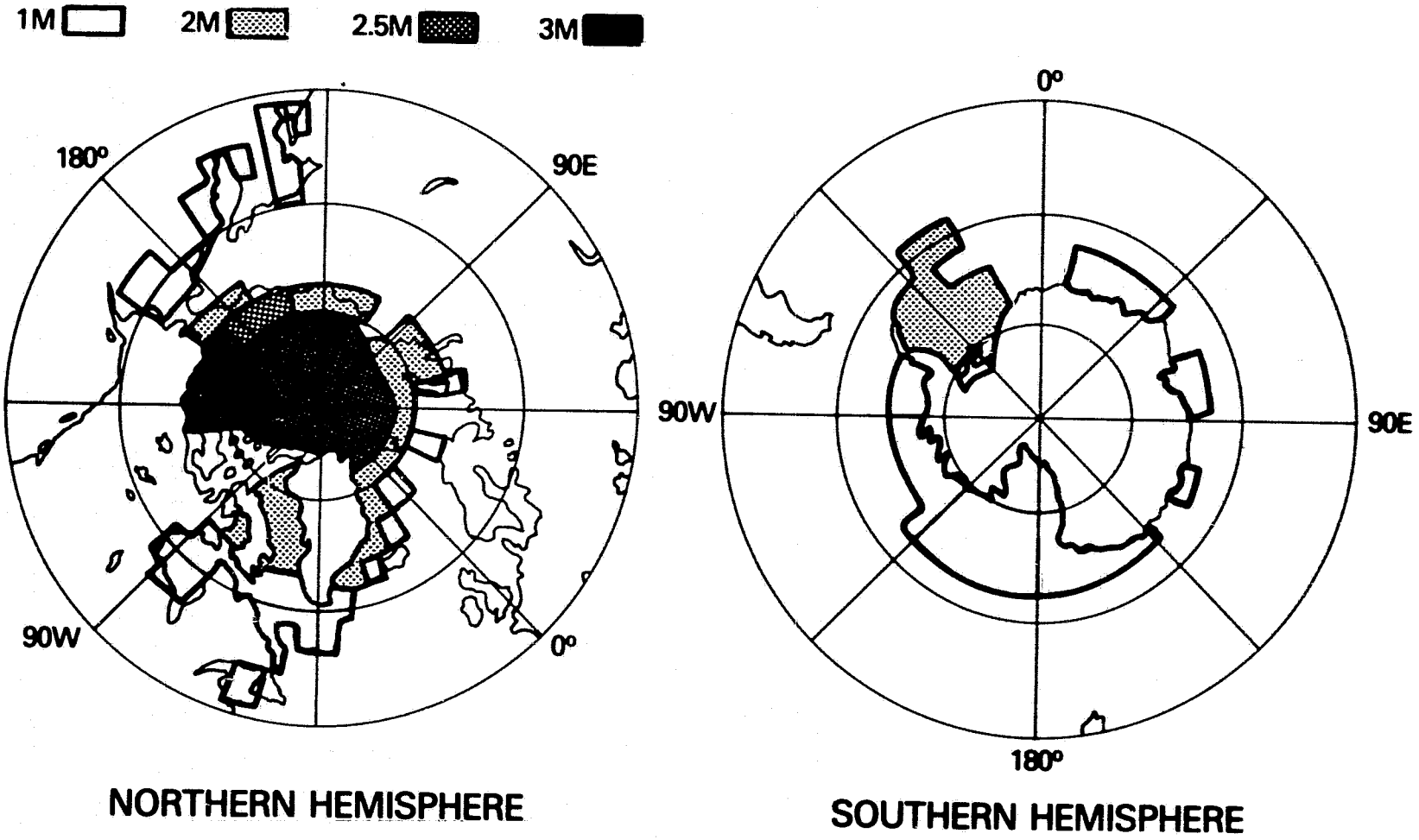

Fig. 1. Initial conditions--ice thicknesses, 1 January 1975.

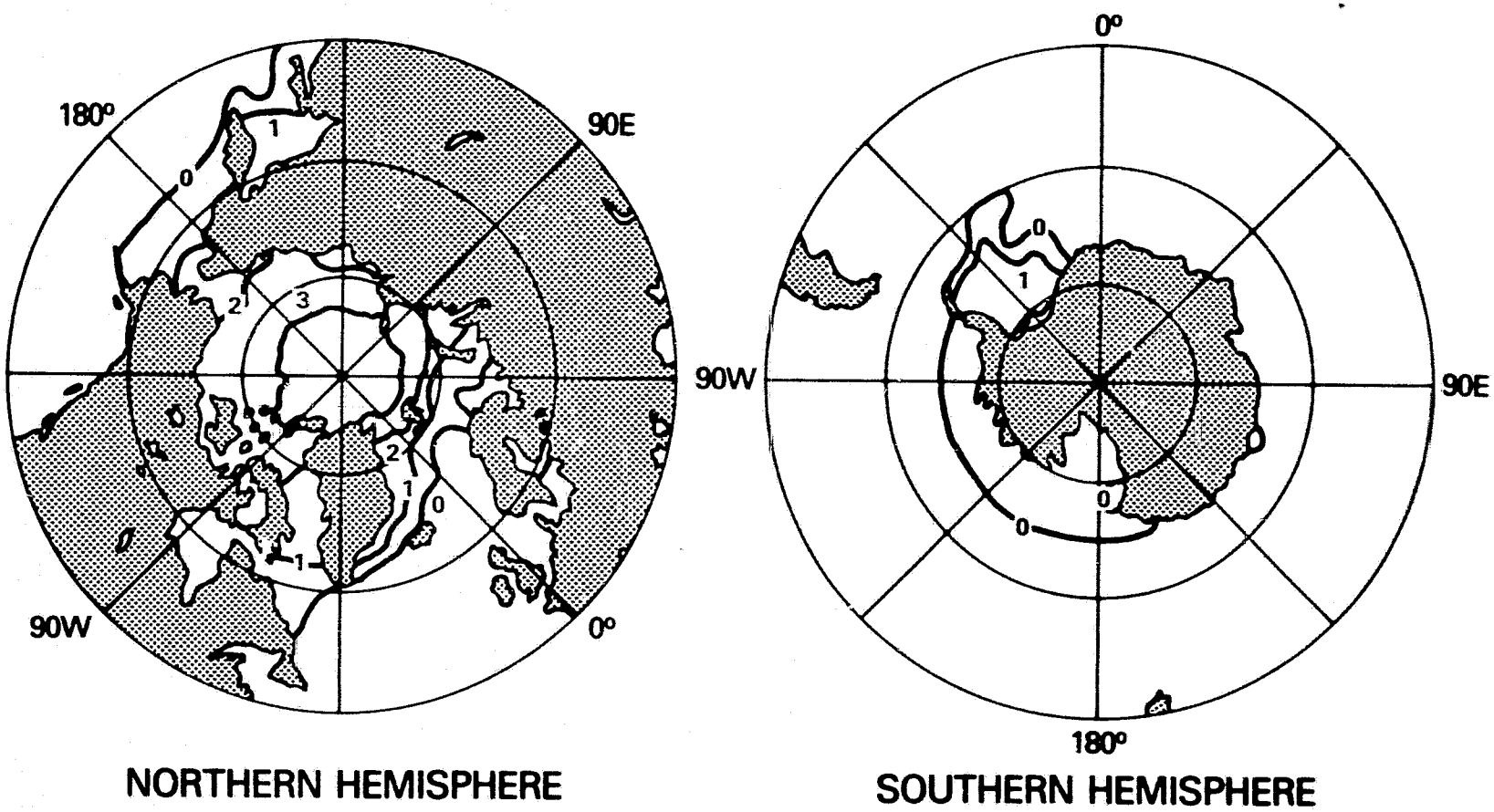

Fig. 2. Contours of ice thickness in meters, simulated for 15 February.

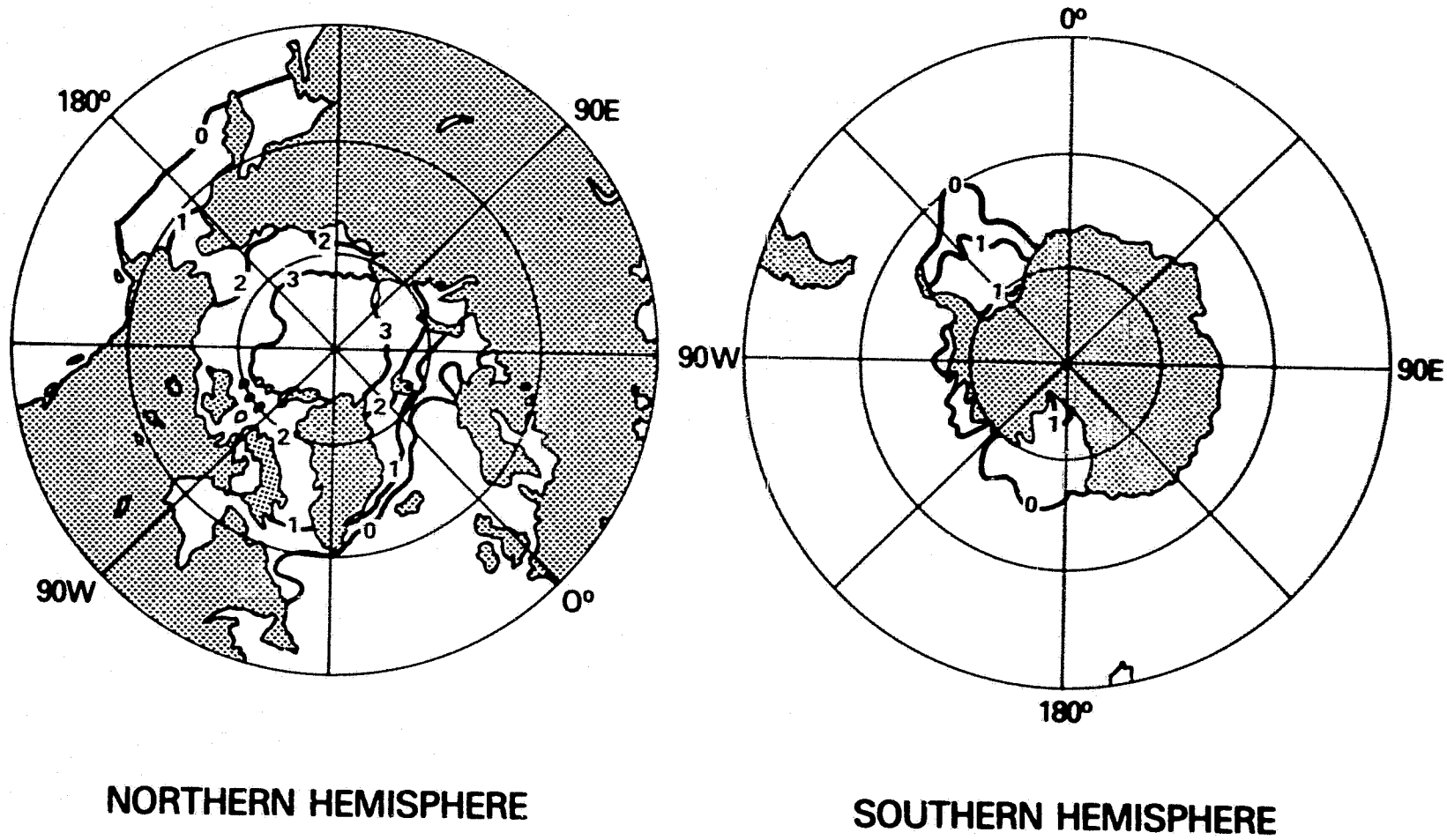

Fig. 3. Contours of ice thickness in meters, simulated for 15 March.

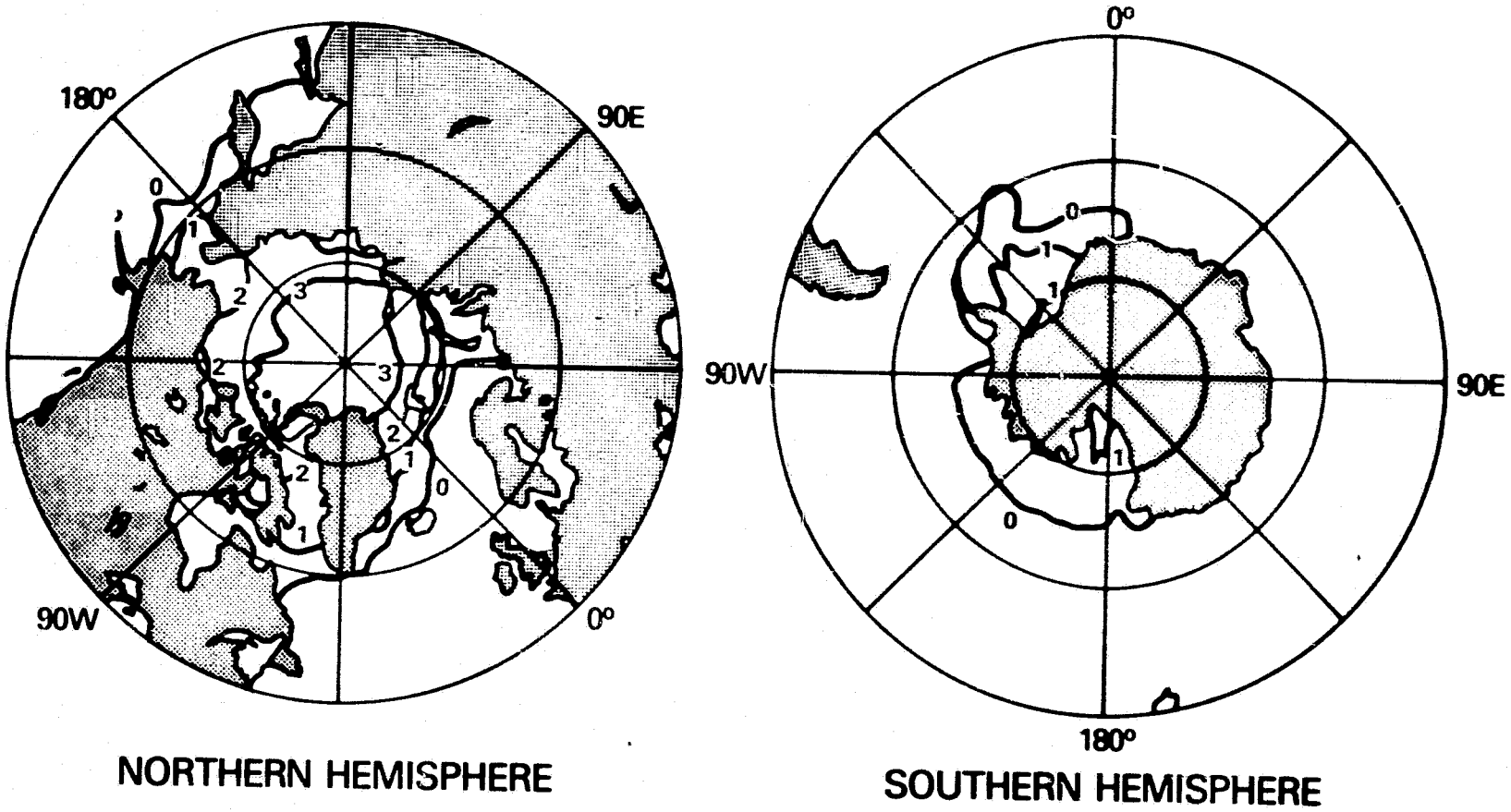

Fig. 4. Contours of ice thickness in meters for 1 April, following 3 months of numerical simulation.

Actual thickness and concentration values are listed in Table 1 for the Weddell Sea, East Greenland Sea, and Central Arctic. The values confirm the extension of the melt season into mid-March in the Weddell Sea, but also point out the increase in concentration from the start to the middle of the month. The full (99.5-100 percent) ice cover in the Central Arctic throughout this period is realistic, though thicknesses of 2.7-2.8 m are about 0.5 m below those typically cited.

Table 1. Areally averaged ice thickness and concentration.

	Weddell Sea	E. Greenland Sea	Central Arctic
Thickness (Meters)			
1 January	1.81	1.66	2.73
15 January	1.59	1.51	2.73
1 February	1.35	1.39	2.72
15 February	1.19	1.29	2.72
1 March	1.09	1.23	2.72
15 March	0.99	1.08	2.74
1 April	1.01	0.90	2.76
Concentration (Percent)			
1 January	60	62	100
15 January	53	70	100
1 February	48	73	100
15 February	45	74	100
1 March	43	74	100
15 March	47	79	100
1 April	67	79	100

References

Herman, G. F., and W. T. Johnson, 1980: Arctic and Antarctic climatology of the GLAS GCM. Submitted to Mon. Wea. Rev.

Parkinson, C. L., and W. Washington, 1979: A large-scale numerical model of sea ice. J. Geophys. Res., 84, 311-337.

THE EFFECT OF CLOUDS ON THE EARTH'S SOLAR AND INFRARED RADIATION BUDGETS

(G. F. Herman, M-L. C. Wu, and W. T. Johnson)

A series of numerical experiments were conducted with the GLAS GCM to demonstrate the effect that the global distribution of cloudiness has on the solar and infrared components of the radiation balance, and in particular to determine the relative role of the albedo and greenhouse effects of clouds when they are considered in the global aggregate. The complete analysis of this experiment has been published elsewhere (Herman et al., 1980), and some aspects of the discussion of the clouds' effect on the earth's radiation balance were presented at the Fourth NASA Weather and Climate Program Science Review (cf. Herman et al., 1979) and will not be repeated here. The focus here is on cloud effects on surface and atmospheric temperature, and the resultant influence ("feedback") on cloud formation processes.

In the control run for this experiment, solar and thermal radiation calculations were fully consistent and interactive with the model's predicted cloud fields. Solar radiation was calculated according to the method of Lacis and Hansen (1974), which explicitly treats cloud absorption and multiple scattering processes. Long wave radiation was computed and summed over ten spectral intervals using a technique developed by M-L. C. Wu and L. D. Kaplan. Cloud solar optical properties were fixed according to cloud type as described by Somerville et al. (1974, Table 2), and unit cloud emissivity was assumed in the infrared spectrum. Since the model does not treat fractional cloudiness that occurs on the subgrid scale, clouds were assumed to cover an entire 4° latitude by 5° longitude grid area.

In one experiment ("inactive solar"), all cloud formation processes and radiative transfer were calculated as they were in the control, except that cloud coverage was fixed at zero in the solar radiation calculation. Thus, clouds formed, liberated latent heat, and participated in vertical mixing processes, but were otherwise transparent ot the streams of solar radiation. The second experiment ("inactive thermal") specified zero cloud coverage in the long wave radiation calculation, but explicitly treated all other cloud processes, including solar radiation.

The initial state was defined from the 0000 GMT 1 January 1975 National Meteorological Center (NMC) global analysis, and the integration period was 30 days. Conclusions therefore refer to an average January circulation for a model atmosphere in which the ocean surface temperature, surface albedo and sea ice extent are prescribed and non-interactive. Thus, there is no means to determine from these experiments whether the annual average planetary mean surface temperature would increase or decrease in association with global cloud coverage changes. The differences between the control and experimental ("transparent") simulations represent only the responses of the atmospheric and land components of the model's earth-atmosphere system.

Analysis of these experiments determined that the radiation balance of the January control was more positive (less negative) than the observations of Raschke et al. (1973) in the northern and southern hemispheres, and globally by 14, 28, and 22 W m^{-2}, respectively. This discrepancy is a likely consequence of the model's treatment of thermal absorption in high clouds, or the absence of partially clouded areas. When clouds do not interact with solar radiation, substantially more energy is available to the system because of the diminished planetary albedo, and the balance became more positive (and less negative) than the control by 26, 87, and 56 W m^{-2} in the northern and southern hemispheres and globally. The balance became more negative (and less positive) in these same regions when clouds are transparent to thermal radiation by 35, 45, and 40 W m^{-2}, respectively.

Under certain circumstances, it is possible to compute the net effect of the clouds on the radiation balance simply by combining the radiation loss due to the albedo effect, and the gain due to the greenhouse effect. Thus, the net cloud effect on the global net radiation balance is -16 W m^{-2}, i.e., the albedo effect makes the balance more negative by 56 W m^{-2} (39 minus 95), while the greenhouse effect makes it more positive by only 40 W m^{-2} (39 minus -1). Similarly, in the southern hemisphere, a cloud effect of -42 W m^{-2} is obtained and in the northern hemisphere, +9 W m^{-2}. Hence, during the month of January, the albedo effect dominates the greenhouse effect in the radiation budgets of the globe and of the southern hemisphere. The greenhouse effect dominates the budget of the northern hemisphere winter because there is less solar radiation available than in the southern hemisphere due to geometrical factors.

It is possible to deduce the net effect of clouds on the net radiation as the difference between the albedo and greenhouse effects only if the changes caused by the two processes are independent. It is possible to imagine a variety of coupling mechanisms or feedbacks that might relate the cloud-solar and cloud-long wave processes. For example, ground temperature differences induced by solar radiation changes might change the long wave loss at the top of the atmosphere through cloud formation processes related to stability and cumulus convection.

Table 1 illustrates the effects of cloud-radiative interactions on surface and atmospheric temperatures. Values are spatial averages with appropriate areal weighting. The surface temperatures over oceans do not change because ocean tempertures are specified in the model. When clouds are not present in the solar radiation calculation, surface temperatures over land (Row 1) increase in the northern and southern hemispheres and globally by 2, 3, and 3°C, respectively, due to the increased direct solar heating of the ground. When clouds are absent in the long wave calculation, back radiation from the atmosphere decreases substantially and hence averaged surface temperatures decrease by 5, 2, and 3°C. Spatially averaged atmospheric temperatures behave in the same fashion, over both land and ocean; i.e., temperatures increase by 1-2°C without solar interactions and decrease by 1-2°C without thermal interactions.

Table 1. Spatially averaged temperatures for radiative-interactive and non-interactive cloudiness (°K).

	(A) January control		(B) Inactive thermal minus control		(C) Inactive solar minus control	
	Land	Oceans	Land	Oceans	Land	Oceans
Surface temperature						
N. hemisphere	271	293	-5	0	2	0
S. hemisphere	285	291	-2	0	3	0
Global	275	292	-3	0	3	0
Average atmospheric temperature						
N. hemisphere	240	252	-1	-1	2	1
S. hemisphere	249	253	-1	-1	2	2
Global	243	253	-1	-2	2	1

The degree of coupling between the radiation and the cloudiness is illustrated in Table 2, which shows the differences between the cloudiness calculated in the control and in the transparent cloud simulations. As a measure of "cloudiness", cloud frequency is used, which is defined as the fraction of the total integration time during which a specified cloud type occurred at a grid point.

The supersaturation (or stratus) cloud frequencies increase by 1-2 percent when cloud-long wave interactions are absent because of the cooler atmospheric temperatures (cf. Table 1). The cloud frequencies decrease by comparable amounts due to warmer atmospheric temperatures when solar interactions are absent, except over continental regions of the southern hemisphere. Evidently, there is a negative correlation in the model between the occurrence of layered cloudiness and average atmospheric temperatures.

Table 2. Spatially averaged cloud frequency for radiatively interactive and non-interactive clouds (%).

	(A) January control		(B) Inactive thermal minus control		(C) Inactive solar minus control	
	Land	Oceans	Land	Oceans	Land	Oceans
Supersaturation clouds						
N. hemisphere	47.9	39.9	1.3	1.9	-1.6	-3.1
S. hemisphere	50.2	40.8	0.3	1.5	0.5	-2.1
Global	48.6	40.4	1.1	1.7	-0.8	-2.5
Convective clouds						
N. hemisphere	8.9	12.0	-1.6	4.3	0.6	-2.7
S. hemisphere	23.0	8.5	-2.7	3.1	-0.4	-2.0
Global	13.5	10.0	-1.9	3.6	0.4	-2.3
All clouds						
N. hemisphere	50.8	43.8	1.4	3.7	-1.5	-4.1
S. hemisphere	57.6	43.8	1.5	2.9	-0.8	-3.2
Global	53.1	43.8	1.4	3.2	-1.3	-3.6

The model's convective clouds, which represent cumulus clouds in nature, generally form less frequently than supersaturation clouds. However, the relative changes in their frequency caused by eliminating radiative interactions are much larger. The frequency changes over the oceans are correlated in a negative sense with the induced atmospheric temperature change, i.e., convective cloud frequencies decrease when the atmosphere is heated by enhanced solar radiation, and increase when it is cooled through enhanced long wave emission. Changes are on the order of 2-4 percent.

The opposite is true of convective cloud frequencies over land, where frequencies increase by about 0.5 percent when there is stronger heating (except in the southern hemisphere) and decrease by 2 percent when there is enhanced cooling. Globally, the convective frequencies decrease from January control value of 11.2 percent to 9.8 percent with solar transparency and increase to 12.9 percent with thermal transparency. Since the convective cloud frequencies over the oceans are more sensitive to solar radiation changes than those over land, model-generated convective cloudiness apparently is more strongly correlated with atmospheric temperature and stability than with surface temeprature. On a global basis, the combined frequency of all cloud types decreases from the control value of 46.9 percent to 44.1 percent without solar interactions and increases to 49.6 percent without thermal interactions.

Recently there has been active debate over the relative roles of the solar and infrared effects of clouds in the global climate system. In particular, would an increase in cloud cover be associated with a surface warming due to "greenhouse" type processes, or to a surface cooling due to albedo effects? Is there a simultaneous redistribution of clouds that accompanies and possibly compensates for differences in the radiation balance by total cloud amount changes?

On the basis of theoretical models of radiative equilibrium and radiative energy balances for specified cloud conditions (e.g., Manabe and and Strickler, 1964; Manabe and Wetherald, 1967), it appears that increases in the amount of low and middle level clouds cause the surface temperature to decrease. But it also appears that increasing the upper level (e.g., cirriform) cloud amount increases the surface temperature, although this latter conclusion is more sensitive to assumptions about cloud optical properties and cloud temperature. Thus, the albedo effect tends to dominate when changes in low cloud amount occur, while the infrared effect dominates when the changes involve upper level clouds. Clearly, any discussion of the radiative effect of changing global cloud amounts must consider the possibility of changes in the distribution and type of cloud as well, a point stressed by Cess and Ramanathan (1978). In fact, Cess (1976) suggests that changes in global cloudiness occur in such a fashion that the net radiation balance is essentially unchanged.

The results presented here indicate that some geographical redistribution of cloudiness does accompany changes in the visible or infrared opacity of the atmosphere, and redistribution takes place in the vertical direction as well. The increase in globally averaged cloud frequency for the transparent infrared case is effected by an increase at virtually all levels in the model, except for supersaturation clouds at level 2 and convective clouds at level 5. The decrease in total cloudiness for the solar transparent case is caused by a decrease of frequencies at most levels, although convective and supersaturation cloud frequency each increase slightly at one level. There is some tendency at most levels for the changes in the cloud frequency caused by infrared transparency to compensate partially for the changes due to solar transparency, but complete cancellation does not occur.

A comparison is also made between the results of the GLAS GCM and the radiation balance study of Ellis (1978) based on satellite radiometer measurements. For the December-February period, Ellis concluded that the cloud effect on the radiation balance, N, which was obtained by subtracting cloud-free values from values obtained with actual cloudiness was -12, -42, and -27 W m^{-2} for the northern hemisphere, southern hemisphere, and globe, respectively. For comparison, the same GCM values obtained here were +9, -42, and -16 W m^{-2}, which agree well globally and in the southern hemisphere, but not in the northern hemisphere. As with the results from the GCM, Ellis' values do not apply to small changes in cloud amount. However, they are valuable because they are measurements of actual atmospheric cloud fields that contain the true feedback between cloud formation and cloud radiative processes.

References

Cess, R. D., 1976: Climate change: An appraisal of atmospheric feedback mechanisms employing zonal climatology. J. Atmos. Sci., 33, 1831-1843.

_____, and V. Ramanathan, 1978: Averaging of infrared cloud opacities for climate modeling. J. Atmos. Sci., 35, 919-922.

Ellis, J. S., 1978: Cloudiness, the Planetary Radiation Budget, and Climate. Ph.D. Thesis, Colorado State Univ., 129 pp.

Herman, G. F., M. L. Wu, and W. T. Johnson, 1979: The effect of clouds on the earth's radiation balance. Fourth NASA Wea. and Cli. Prog. Sci. Rev., NASA Conf. Report #2069, 159-162, NASA Goddard Space Flight Center, Greenbelt, Maryland 20771.

_____, _____, and _____, 1980: The effect of clouds on the earth's solar and infrared radiation budgets. To appear in J. Atmos. Sci., 37.

Lacis, A. A., and J. E. Hansen, 1974: A parameterization for the absorption of solar radiation in the earth's atmosphere. J. Atmos. Sci., 31, 118-133.

Manabe, S., and R. F. Strickler, 1964: Thermal equilibrium of the atmosphere with a convective adjustment. J. Atmos. Sci., 21, 361-385.

_____, and R. T. Wetherald, 1967: Thermal equilibrium of the atmosphere with a given distribution of relative humidity. J. Atmos. Sci., 24, 241-259.

Raschke, E., T. H. Vonder Haar, M. Pasternak, and W. R. Bandeen, 1973: The radiation balance of the earth-atmosphere system from NIMBUS 3 radiation measurements. NASA Tech. Note D7249 [NTIS-N-73-21702].

Somerville, R. C. J., P. H. Stone, M. Halem, J. E. Hansen, J. S. Hogan, L. M. Druyan, G. Russell, A. A. Lacis, W. J. Quirk, and J. Tenenbaum, 1974: The GISS model of the global atmosphere. J. Atmos. Sci., 31, 84-117.

REVISION OF GLOBAL TOPOGRAPHY ARRAYS

(D. Randall and J. Abeles)

In preparation for the testing of a new climate model based on the C-grid (Randall et al., 1980), it was necessary to create a new global topography array. We averaged the Scripps 1° x 1° topography data set (Gates et al., 1975) onto a 4° x 5° C-grid. Comparing the result with the standard GLAS B-grid topography, we found that the new topography shows much greater relief over all mountainous regions of the world and that the land surface elevations of Greenland, in particular, were much higher than in the standard GLAS topography array.

To study these discrepancies more carefully, we recomputed the topography for the 4° x 5° B-grid, so that a direct comparison could be made with the standard GLAS topography. As shown in Fig. 1., in the new array, the highest elevations of the Himalayas are over 1 km greater, the Andes are more than 600 m higher, and there are similar large differences in many other parts of the world. Fourier analysis along latitude circles shows significant differences in low wave numbers (Fig. 2). At some latitudes, the topographic forcing at low wave numbers is more than twice as strong for the new topography as for the old.

These findings are of potentially great significance for the GLAS climate modeling effort because, to the extent that the model responds linearly to topographic forcing, a doubling of the forcing will produce a doubling of the model's response. In fact, one deficiency of past GLAS climate simulations has been an underprediction of the amplitudes of the long planetary waves.

Preparations are underway to determine by numerical experiment how much impact the revised topography has on climate runs. Preliminary tests of the topography in the GLAS 4° x 5° fourth-order forecasting model have shown improvements in the forecasts. Revision of the topography used in the GLAS 2.5° x 3° forecasting model is also planned.

Acknowledgment

Thanks to Professor Mike Schlesinger of Oregon State University for providing the Scripps topography tape.

References

Gates, W. L., and A. B. Nelson, 1975: A new (revised) tabulation of the Scripps topography on a 1° global grid. Part I: terrain heights. Report R-1276-1-ARPA, Rand, Santa Monica, California, 132 pp.

Randall, D., J. Abeles, and C-H. Moeng, 1980: Testing of a potential enstrophy-conserving momentum advection scheme based on the C-grid. NASA Tech. Memo. (herein), Atmos. and Oceano. Res. Rev.-1979, NASA Goddard Space Flight Center, Greenbelt, Maryland.

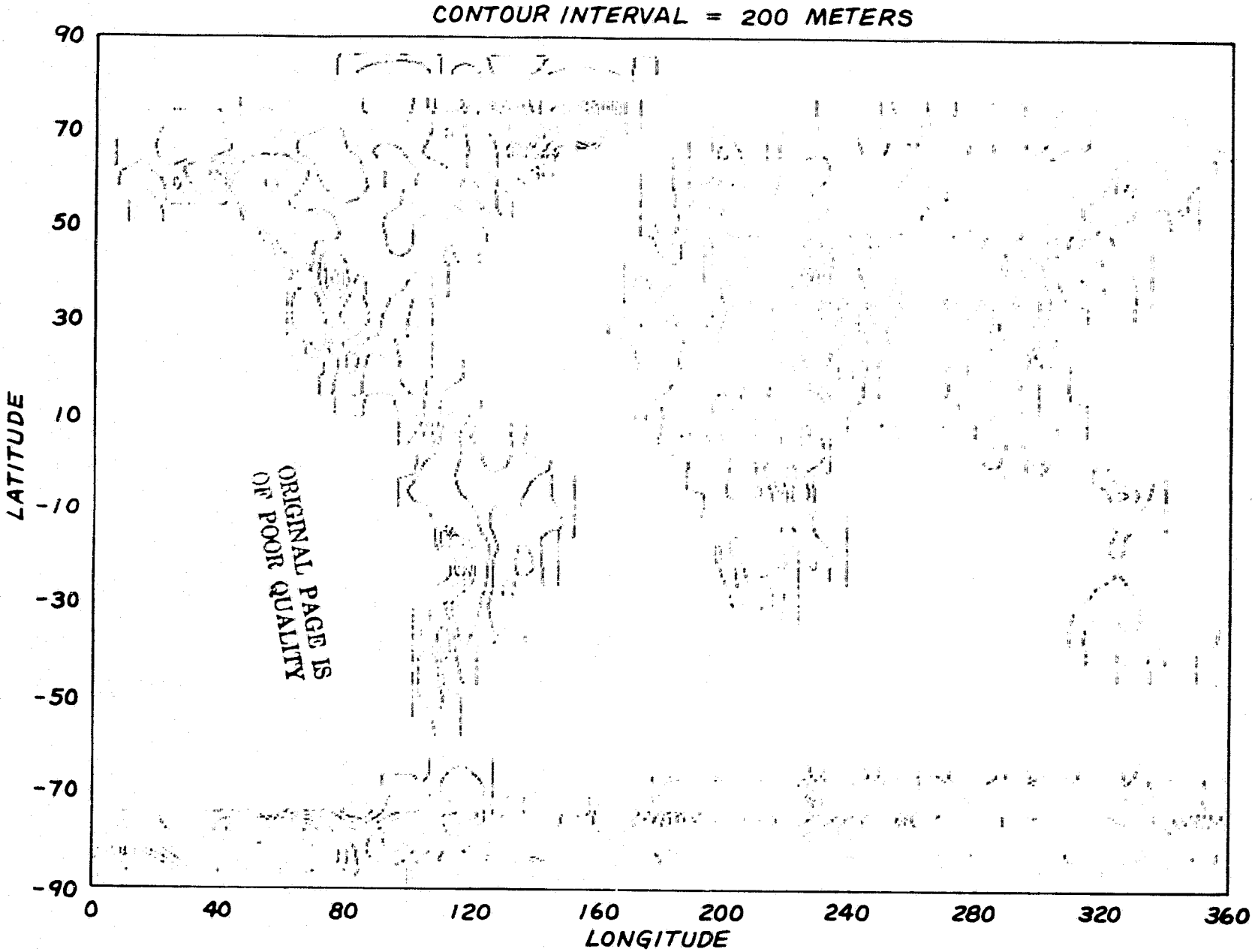

Fig. 1. Differences between the land surface height computed from the Scripps topography and those traditionally used in the GLAS model. The new topography is higher than the old at virtually all land points.

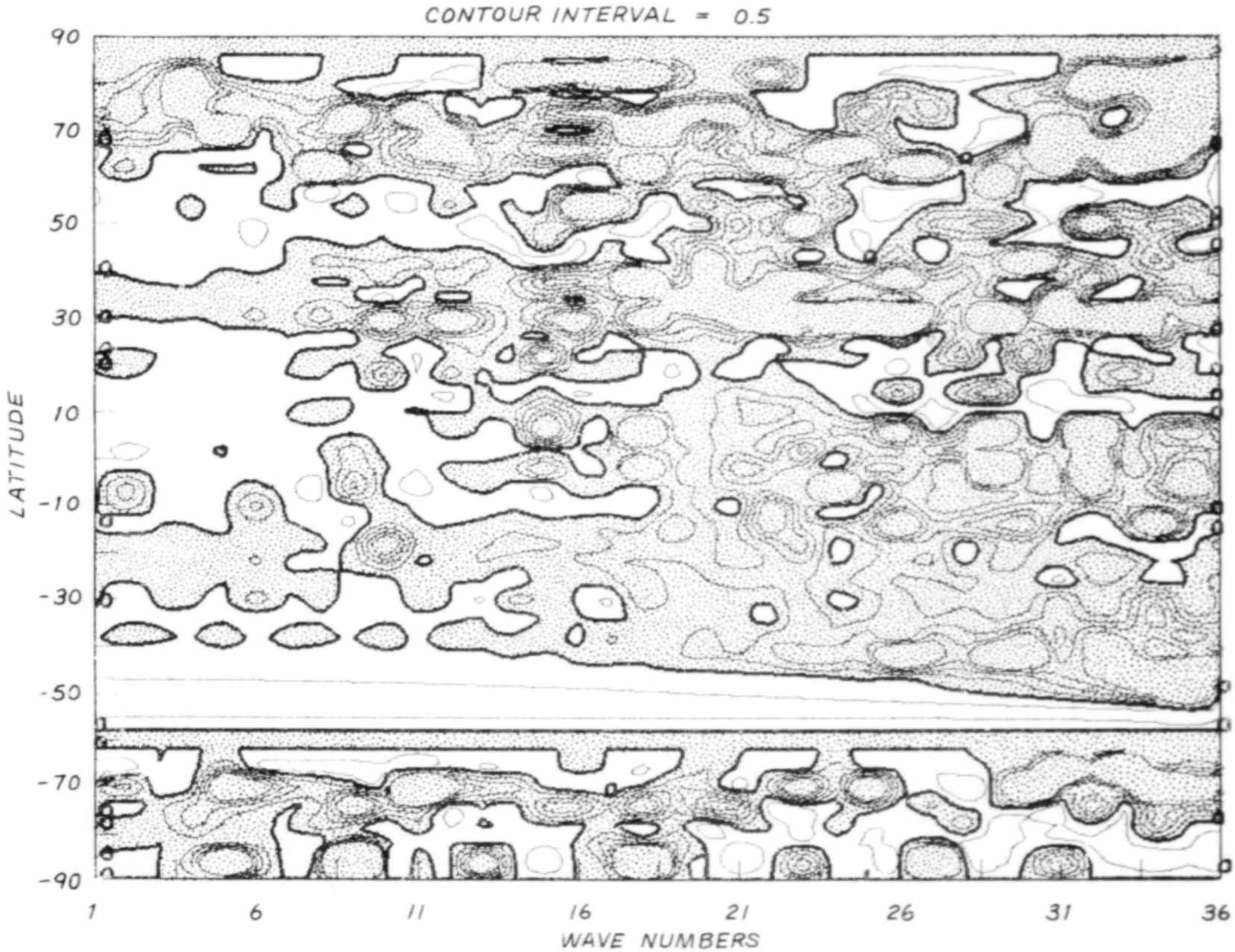

Fig. 2. For both the new and old topographies, we computed the square root of the sum of the squares of the Fourier sine and cosine coefficients along latitude circles. This figure shows the difference in results for the new and old topography arrays, normalized by the results for the old topography. The zero contour is heavy and positive values are shaded.

TESTING OF A POTENTIAL ENSTROPHY-CONSERVING MOMENTUM ADVECTION SCHEME BASED ON THE C-GRID

(D. A. Randall, J. Abeles, and C-H. Moeng)

Early attempts to simulate the general circulation of the atmosphere (Phillips, 1956) were plagued by nonlinear computational instability, which occurred as finite difference truncation errors allowed a false cascade of energy to the smallest resolvable scales (Phillips, 1959). The instability can be prevented by selectively smoothing the smallest scales, but objections can be raised against such smoothing. When the smoothing increases the simulated rate of dissipation (e.g. Smagorinsky, 1963), it is sometimes interpreted as a parameterization of unresolved subgrid scale diffusion, but in practice the smoothing techniques are ad hoc and are not derived from turbulence theories. On the other hand, if the smoothing is nondissipative, then it cannot represent the effects of subgrid scale turbulence.

Arakawa (1966) showed that the nonlinear instability could be avoided through the use of a finite difference momentum advection scheme which conserves kinetic energy and, in the limit of two-dimensional nondivergent flow, also conserves enstrophy. Arakawa emphasized that his scheme not only prevents the nonlinear instability, but also allows simulation of the statistics of the general circulation over simulated times far longer than those over which the details of the circulation can be predicted. In short-to-medium range forecasting (up to about 2 weeks), deterministic prediction of individual synoptic features is a credible objective, and one of the most important factors determining a model's suitability for such forecasting is the local spatial and temporal accuracy of its finite difference scheme. Especially for short forecasts, prediction of the statistics of the circulation is not crucial, since over such short periods no reasonable scheme will allow the statistics to wander far from those of the initial condition. But for climate modeling, the required simulation times are so long that deterministic prediction is hopeless, and therefore local accuracy is almost irrelevant. Instead, the statistical accuracy of the scheme mostly determines the model's predictive skill.

The present GLAS climate model is based on Arakawa's (1966) scheme, and on other aspects of the version of the UCLA model described by Arakawa (1972). In spite of the demonstrated success of the present scheme, the following three difficulties remain. First, in the limit of two-dimensional nondivergent flow, the present scheme conserves enstrophy only in case the grid increments are spatially uniform; on a spherical grid, this is true only near the equator. Second, as discussed by Arakawa and Lamb (1977), the B-grid used in the GLAS climate model is less suitable for simulation of the geostrophic adjustment process than the C-grid. Finally, as discussed by Arakawa and Lamb (1980), the present scheme does not guarantee conservation of potential enstrophy in a divergent flow. As a result, the scheme is not well suited to simulation of the strongly divergent circulations forced by sharp topographic features.

Suarez and Arakawa (1979) have presented preliminary results from a new version of the UCLA GCM, which incorporates a revised finite difference scheme based on the C-grid and designed to conserve potential enstrophy on the sphere. The new scheme is thus free from the three deficiencies of the current GLAS scheme. But the new UCLA model also incorporates several additional major new features, including a vertical coordinate system in which the planetary boundary layer top is a coordinate surface. For this reason, it is difficult to isolate the impact of the new horizontal differencing scheme on the model results.

We have incorporated the new UCLA horizontal differencing scheme into the GLAS climate model, without making any other changes. By comparing the results of this new model with those of the current GLAS climate model, we plan to identify and evaluate the impact of the new scheme through a series of controlled experiments, including both short-range forecasts and climate simulations. At present (February 1980), all coding changes have been completed, and the model has been successfully tested in a 7-day run, starting from idealized initial conditions and using idealized topography, without any physical parameterizations except dry convective adjustment.

We have also constructed shallow water models based on the current GLAS scheme and on the new scheme. These models incorporate all the essential new elements of the respective schemes, but little else. They therefore serve as ideal test beds for the schemes, and a large number of experiments have already been performed with them. These experiments have shown that the new scheme is considerably less noisy than the old, and that even such gross statistics as the simulated zonal mean water depth differ significantly between the two schemes. Further tests are planned, with varying horizontal resolutions, to establish which scheme requires less resolution for a given accuracy of approximation to the "exact" (high-resolution) solution. We also plan to test a fourth-order version of the new scheme.

References

Arakawa, A., 1966: Computational design for long-term numerical integration of the equations of fluid motion: Two-dimensional incompressible flow. Part I. J. Comp. Phys., 1, 119-143.

_____, 1972: Design of the UCLA general circulation model. Numerical Simulation of Weather and Climate, Tech. Rep. No. 7, Dept. of Meteorology, Univ. of California, Los Angeles, 116 pp.

_____, and V. R. Lamb, 1977: Computational design of the basic dynamical processes of the UCLA general circulation model. Methods in Comp. Phys., 17, Academic Press, New York, 173-265.

_____, and V. R. Lamb, 1980: A potential enstrophy and energy conserving scheme for the shallow water equations. Submitted for publication.

Phillips, N. A., 1956: The general circulation of the atmosphere: a numerical experiment. Quart. J. R. Met. Soc., 82, 123-164.

References (Continued)

_____, 1959: An example of non-linear computational instability. In The Atmosphere and Sea in Motion, Bert Bolin, ed., Rockefeller Inst. Press, New York, 501-504.

Smagorinsky, J., 1963: General circulation experiments with the primitive equations. Mon. Wea. Rev., 91, 99-164.

Suarez, M. J., and A. Arakawa, 1979: Description and preliminary results of the 9-level UCLA general circulation model. AMS Fourth Conf. on Numerical Weather Prediction, Silver Spring, Maryland, 29 October-1 November, Preprint Volume, 290-297.

A NON-ITERATIVE CALCULATION PROCEDURE FOR SURFACE TEMPERATURE AND SURFACE FLUXES IN THE GLAS GCM

(Y. Sud and J. Abeles)

The present GLAS model has been described by Somerville et al. (1974), Stone et al. (1977), and more recently by Halem et al. (1979). Its surface fluxes of sensible and latent heat were found to exhibit strong 2-δt oscillations at the individual grid points as well as in the zonal and hemispheric averages. In addition, it was pointed out by Charney et al. (1977) that a basic weakness of the GLAS model has been its lower evaporation over oceans and higher evaporation over land in a typical monthly simulation. On examining the planetary boundary layer (PBL) parameterization, it was found that the approximations used in the calculation of surface temperature and the use of ad hoc constants in the eddy diffusivity calculation for the mixed layer were primarily responsible for these deficiencies.

By using a quadratic equation for a stable PBL and by a curve-fit relation for an unstable PBL, the GLAS model PBL parameterization has been changed to calculate the mixed layer temperature gradient. The basic formulae used to determine the drag coefficient, its stability dependence and the effect of moisture on the temperature gradient remain unchanged. This calculation in the PBL removed the 2-δt oscillations in the surface temperature and surface fluxes. Also, the geographical distributions of the surface fluxes were improved.

Another advantage of this calculation was to avoid iteration in the surface flux calculation thereby producing some speed improvements. Comparisons of the evaporation over land and ocean are shown for the old and new calculations. The basic quantities and useful variables are defined below:

T_g = ground temperature, °K

q_g^* = saturation mixing ratio at the ground

T_9, θ_9 = physical and potential temperature of layer 9 in the model

q_9 = mixing ratio at level 9 of the atmosphere

q_s = surface mixing ratio

U_s, V_s = surface U,V winds, in ms^{-1}

U_9, V_9 = level 9 U,V winds, in ms^{-1}

$W_s = (U_s^2 + V_s^2)^{1/2}$

K = Eddy diffusivity of the mixed layer cal $m^{-1}k^{-1}$

L = latent heat of evaporation $calg^{-1}$

C_p = specific heat at constant pressure

R = gas constant

$\kappa = R/C_p$

ε = ratio of molecular weights of water and air

Fig. 1 shows a schematic sketch of a potential temperature profile in a stable and an unstable PBL. The temperature difference across the mixed layer, , is modified to reflect the moist adiabatic lapse rate as follows:

$$\gamma_c = \gamma_d + r_s \frac{g}{c_p} \Delta Z_B \left[1 - \frac{\frac{L}{cp\kappa}\left(\frac{q^*}{Ts}\right)}{1 + 5418 \frac{L}{C_p}\left(\frac{q}{T^2_s}\right)} \right] .$$

Define $$\Delta T_c = \Gamma r_s \cdot \Delta Z_B ,$$

$$\Delta T_d = \Gamma_d \Delta Z_B ,$$

and

$$\gamma_c = r_s \frac{g}{C_p} Z_B \left[\frac{1 - \frac{1 + \frac{L}{cpk}\left(\frac{q^*}{Ts}\right)}{}}{1 + 5418 \frac{L}{C_p}\left(\frac{qs^*}{T^2_s}\right)} \right] ,$$

The above equations yield

$$T_c = T_d + \gamma_c .$$

Assuming that D_R is prescribed on a grid cell, the surface heat flux, F_s, may be obtained as follows:

$$F_s = \rho C_p D_R (\theta_g - \theta_s)$$

where

$$D_R = C_D W_s^3/(W_s^2 - 7x(\Delta\theta - \theta)) \qquad \text{if } T_g < T_s ,$$

$$D_R = C_D(W_s + \sqrt{\Delta\theta - \theta}) \qquad \text{if } T_g > T_s .$$

The mixed-layer heat flux, F_{ml}, is given by

$$F_{ml} = - C_p K/Z_B(\Delta T - \Delta T_c) ,$$

First, for the stable case

$$K = 60./(1 + 40.*R_i) ,$$

where

$$R_i = -\delta\Delta\, gZ_B/[\theta_g^* \ (U_g-U_s)^2 + (V_g - V_s)^2 \ ].$$

Second, for the unstable case

$$K = 60. + 100. \ [1 - \exp(-1.2 \frac{\delta\theta}{\delta z})[=]$$

By equating F_s and F_m, we find that

$$D_R(\theta_g - \theta_s) = -K/Z_B \ (\Delta T - \Delta T_d - \gamma_c) = K/Z_B(d\theta + \gamma_c).$$

(a) Solution of $\delta\theta$ (Stable Case)

The following equation for the stable case is obtained by using the above equations:

$$\underbrace{(7 \times 60/Z_B C_D W_s^3 - 40gZ_B/ \ gD_w^2)}_{A}\delta\theta^2 +$$

$$\underbrace{(1 + 60/Z_B C_D W_s - 7x60 \ /Z_B C_D W_s^3 + 40gz_B C_D/ \ gD_w^2)}_{B}\delta\theta = \Delta\theta \ ,$$

from which $\delta\theta$ may be obtained. However, if A approaches zero in the above quadratic equation, the limiting solution is

$$\delta\theta = -\Delta\theta/B(1 - A.\Delta\theta/B^2).$$

The boundary layer height Z_B is of the order of 500 m. However, a stable PBL is generally shallow. Its height is of the order of 100 m. A limiting value of K = 2.0 is reached when the limiting critical Richardson

number 3.05 is attained (Deardorff, 1967). Also, the constant (40.) is adjusted to (8.) to reflect use of 500 m for the PBL height. The minimum value of $\delta\theta$ is obtained by

$$\delta\theta = \Delta\theta/[1. + (K_{min}/Z_B C_D W_s)(1 - 7.\Delta\theta/w_s^2)] \quad .$$

(b) Solution of (Unstable Case)

In an unstable case, a transcendental is involved. Therefore, an exact solution is not possible. Hence, an attempt is made to obtain $\delta\theta$ as a function of $\Delta\theta$, w_s, and C_D, for a range of values. Figs. 2a, 2b, and 2c show $\delta\theta$ as a function of $\Delta\theta$ for values of C_D between .001 and .005 and surface wind magnitudes of 2-12 m s^{-1}. From these solutions, graphs are obtained for $\delta\theta/\Delta\theta$ versus C_D, for various values of the winds (Fig. 2d) and $\delta\theta/\Delta\theta$ versus surface wind for various values of C_D. A relation between $\delta\theta$ and $\Delta\theta$, C_D and W_s, was curve fitted to give

$$\delta\theta = (0.1382 \cdot W_s \cdot C_D^{1/2} + 13.67\ C_D) \quad .$$

(c) Wind Field Modification by Surface Drag

In the old code, first the wind fields were interpolated to primary points, then momentum deficit was calculated for the interpolated wind fields. Having done that, the momentum deficit was reinterpolated to secondary points. This back-and-forth interpolation does not allow a direct coupling between wind velocity and momentum deficit. Replacement of this procedure by the one used in the new boundary layer calculation helps to partially eliminate a 2- x oscillation. In the new procedure, first a factor, D_R, is calculated at each primary point, as before. It is then interpolated linearly to secondary points. The momentum deficit is now calculated by multiplying this factor by winds at level 9. Also, wind velocity updates are saved in an array. These are made simultaneously at the end.

Analysis of Results

(1) First, a time step invoking one call each of radiation and physics and three calls of hydrodynamics was completed to compare the results. The only striking difference was larger evaporative tendencies over oceans and some large differences in surface temperature. Fig. 3 shows the digitized maps of surface temperature differences. A large difference of 10-20°C may be seen in regions marked (I). These differences occur because in this region the air aloft the surface is very cold. The old model makes T_s close to the ground temperature, whereas the new model makes it close to level 9 potential temperature. This is so because in the new calculation the eddy exchange coefficient has increased by an order of magnitude for the unstable atmosphere.

In a 1-day simulation, the 2-δt oscillation in the surface temperature and surface fluxes was eliminated over land and ocean. See Figs. 4a and 4b for changes in the fluxes of evaporation and sensible heat over land and

ocean in the two hemispheres separately. The previous PBL model runs exhibit a very noisy field compared to the new PBL model. Consistent changes in daily averages of sensible heat and evaporative fluxes on individual grid points are now simulated.

The new PBL parameterization has been tested with a unique solution of surface temperature instead of an iterative and time-averaged solution. Also, the original formulation of the eddy diffusion coefficient of Deardorff (1967) has been incorporated. The results from the new parameterization show desirable effects of increased evaporation over ocean, reduced evaporation over land along with elimination of 2-δt oscillation in the surface fluxes of the old model. Also, a short-range forecast revealed small but beneficial effects on surface temperatures, sea level pressure and geopotential heights at 500 mb.

References

Charney, J. G., W. J. Quirk, S. H. Chow, and J. Kornfield, 1977: A comparative study of the effects of albedo change on drought in semi-arid regions. J. Atmos. Sci., 34, 1366-1385.

Deardorff, J. W., 1967: Empirical dependence of the eddy coefficients for heat upon stability above the lowest 50 m. J. Appl. Meteor., 6, 631-643.

Halem, M., J. Shukla, Y. Mintz, M. L. Wu, R. Godbole, G. Herman, Y. Sud, 1979: Comparisons of observed seasonal climate features with a winter and summer numerical simulation produced with the GLAS general circulation model. Report of the JOC Study Conf. on Climate Models: Performance, Intercomparison and sensitivity Studies, GARP Publ. Series No. 22, 207-253, WMO, Geneva, Switzerland.

Somerville, R. C. J., P. H. Stone, M. Halem, J. E. Hansen, J. S. Hogan, L. M. Druyan, G. Russell, A. A. Lacis, W. J. Quirk, and J. Tenenbaum, 1974: The GISS model of the global atmosphere. J. Atmos. Sci., 31, 84-117.

Stone, P. H., S. Chow and W. J. Quirk, 1977: The July climate and a comparison of the January and July climates simulated by the GISS general circulation model. Mon. Wea. Rev., 105, 170-194.

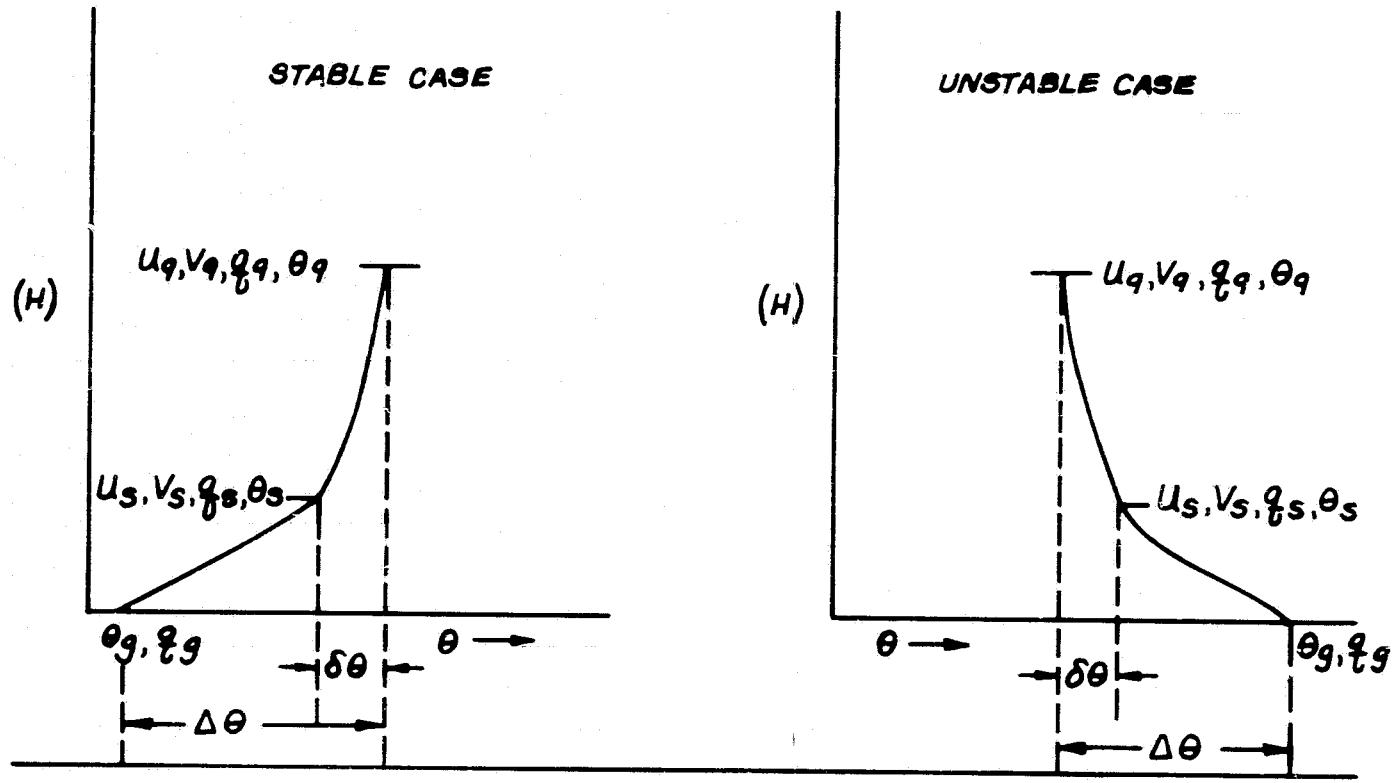

Fig. 1. Schematic sketch of potential temperature profile in a boundary layer for stable and unstable PBL's.

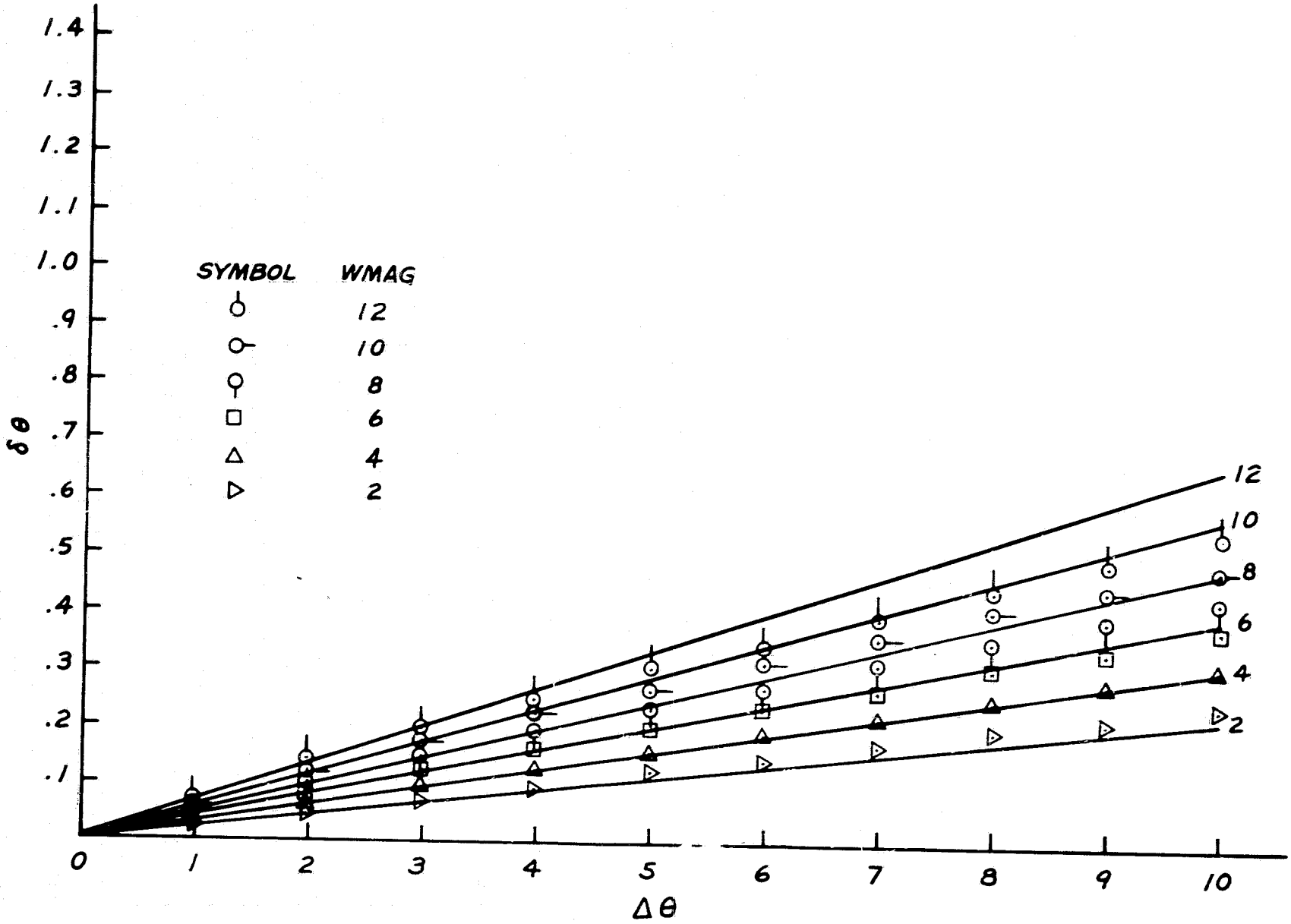

Fig. 2a. Graphs showing $\delta\theta$ vs. $\Delta\theta$ for various values of wind magnitudes and $C_D = 0.001$ for unstable PBL. Exact calculations are points shown on curve fit solutions drawn as lines.

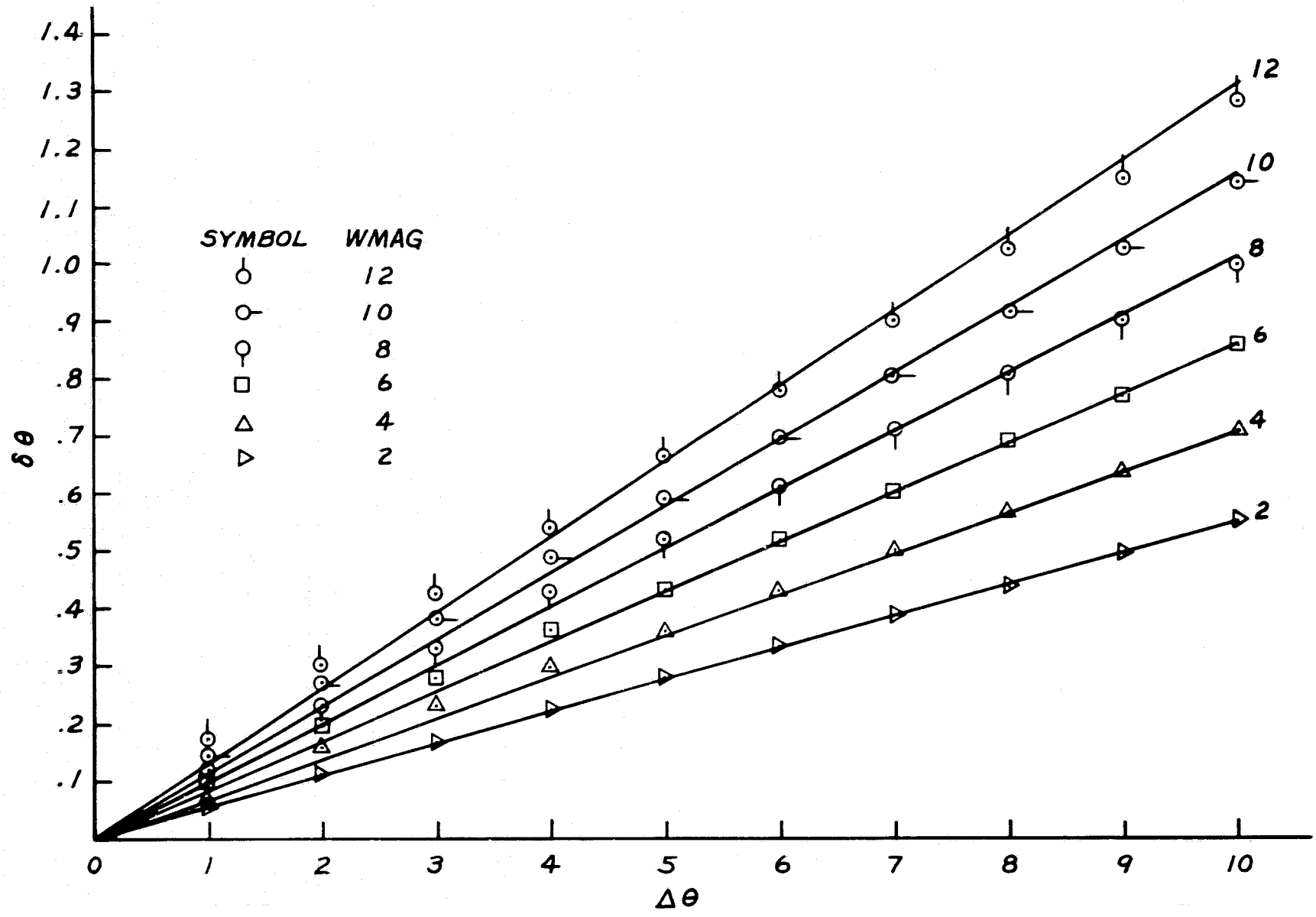

Fig. 2b. As in Fig. 2a, except C_D = 0.003 for unstable PBL.

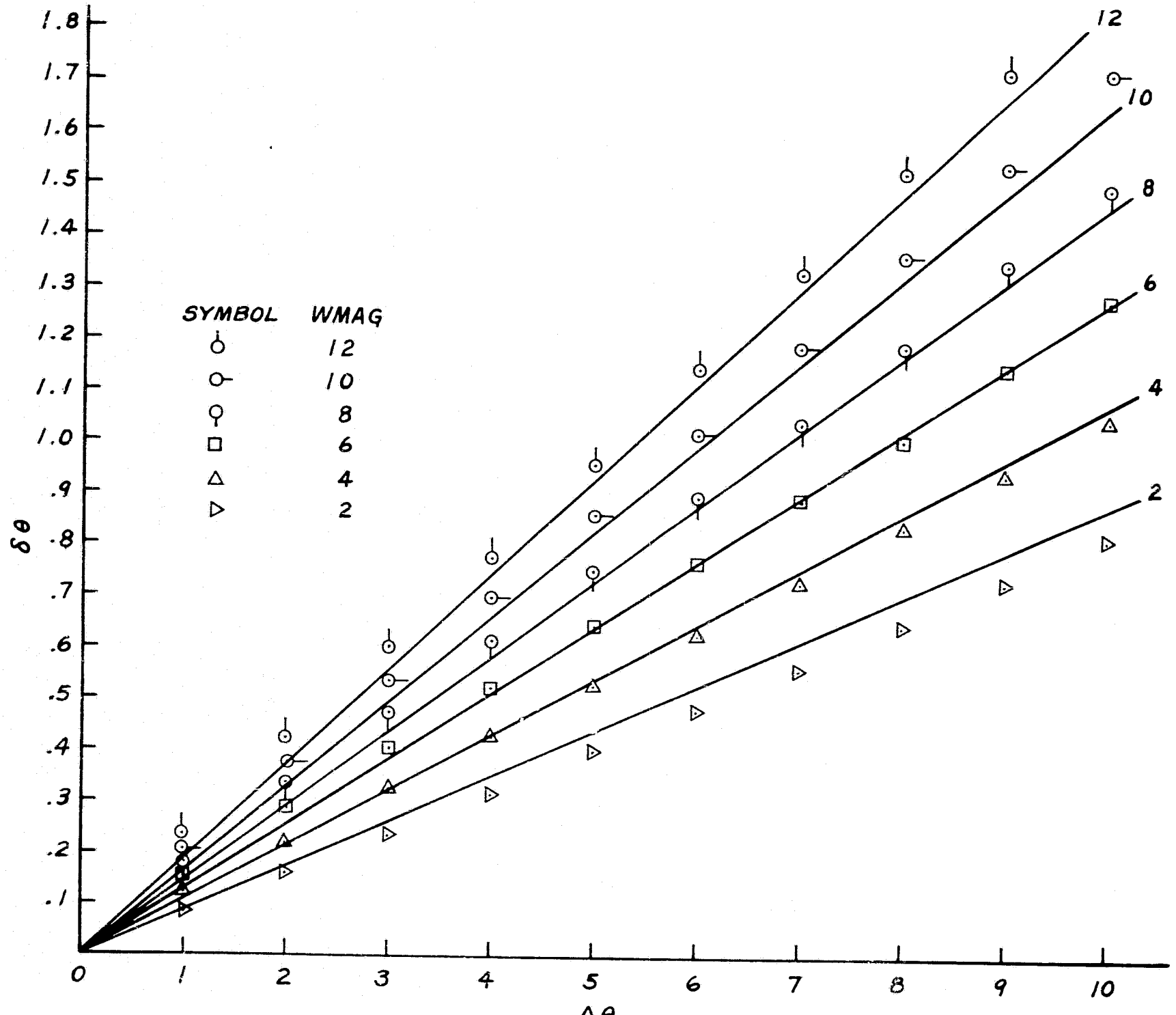

Fig. 2c. As in Fig. 2a, except C_D = 0.005 for unstable PBL.

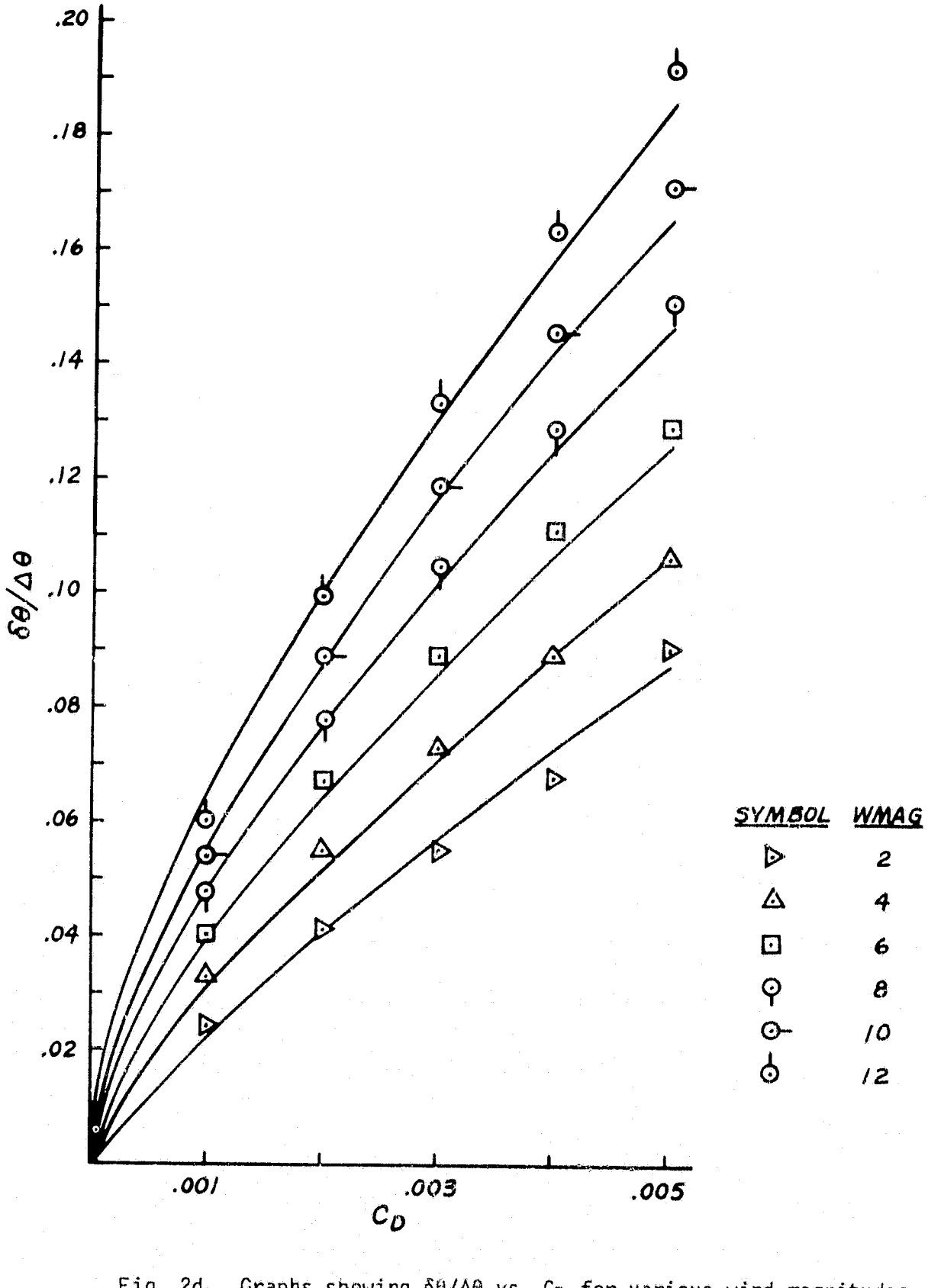

Fig. 2d. Graphs showing $\delta\theta/\Delta\theta$ vs. C_D for various wind magnitudes (for unstable PBL). Exact calculations are points shown on curve fit solutions drawn as lines.

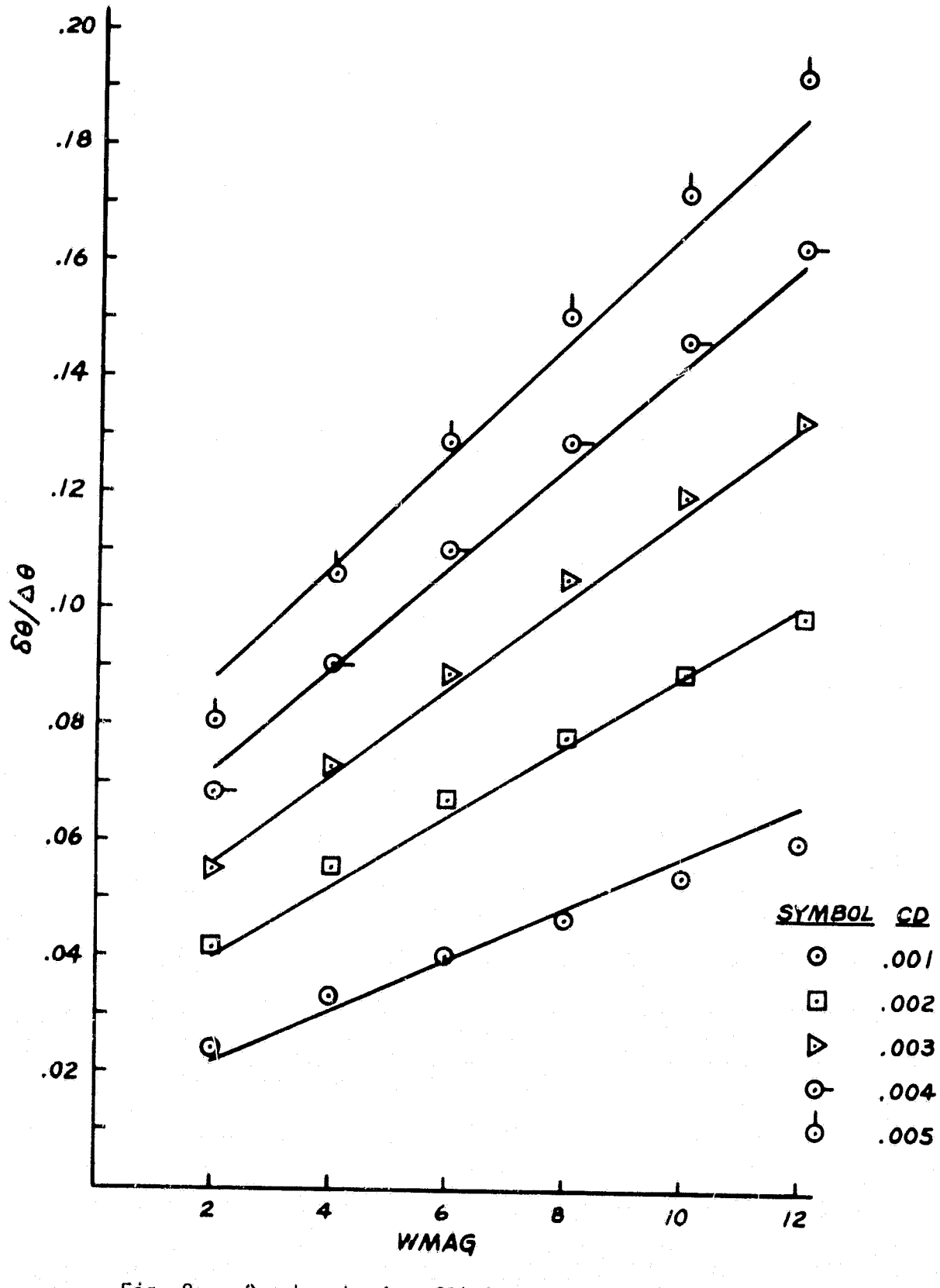

Fig. 2e. Graphs showing $\delta\theta/\Delta\theta$ vs. wind magnitude for various values of C_D (unstable PBL).

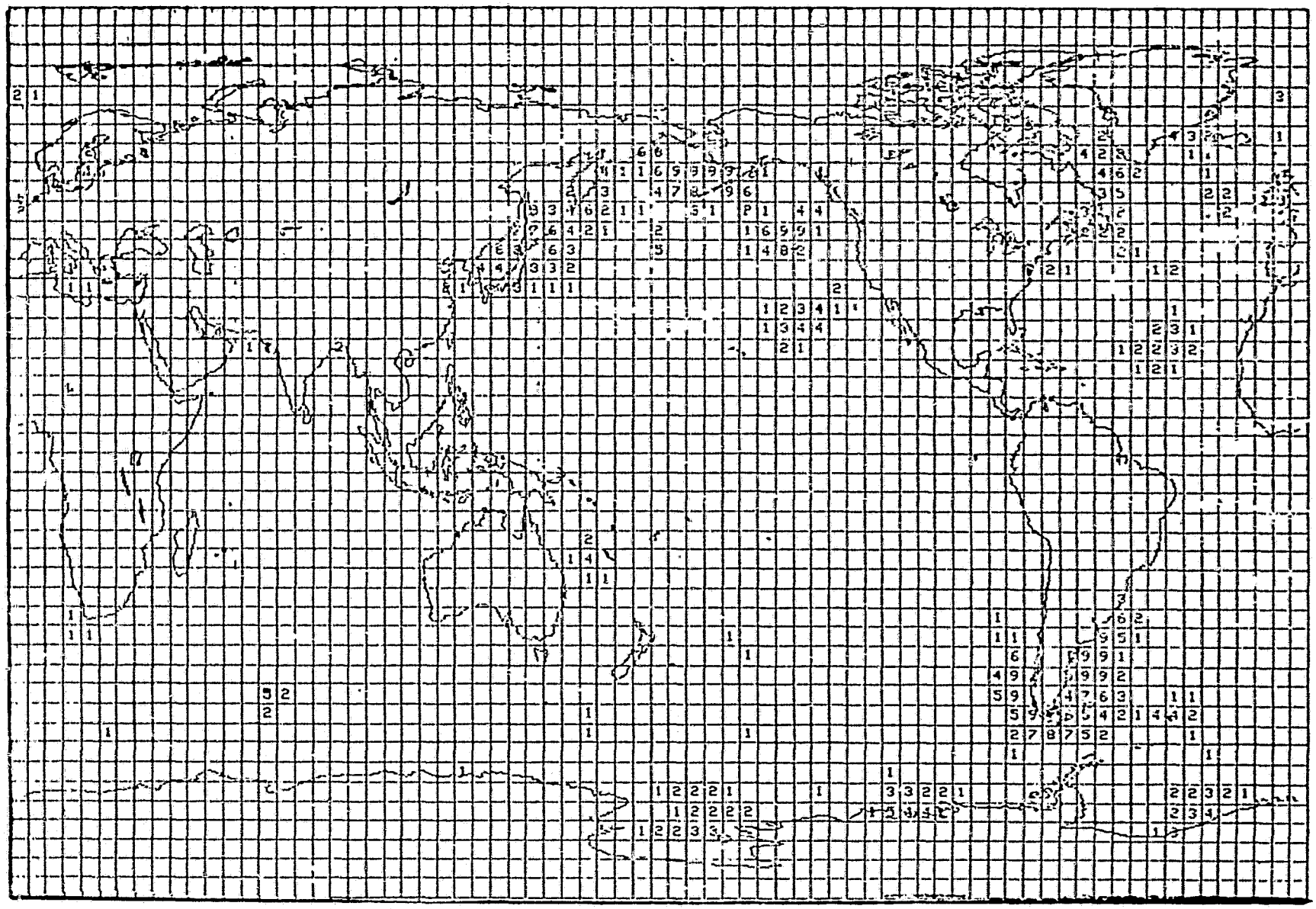

Fig. 3. Differences between surface temperature calculated at the initial time from the old and new formulation of PBL transport calculations.

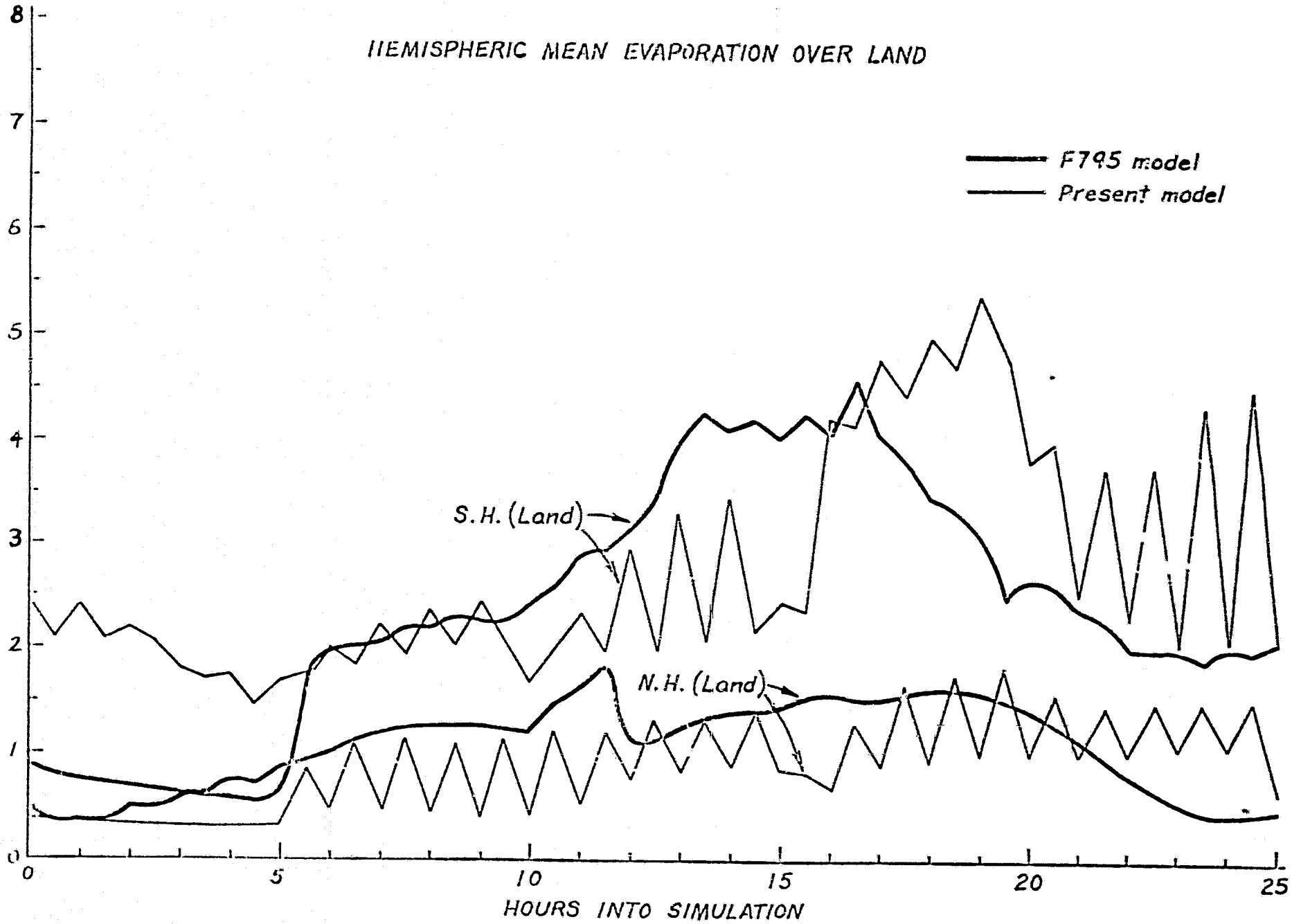

Fig. 4a. Hemispheric mean evaporation for the southern and northern hemispheres for 1 day simulation (land), old GLAS model vs. new calculation.

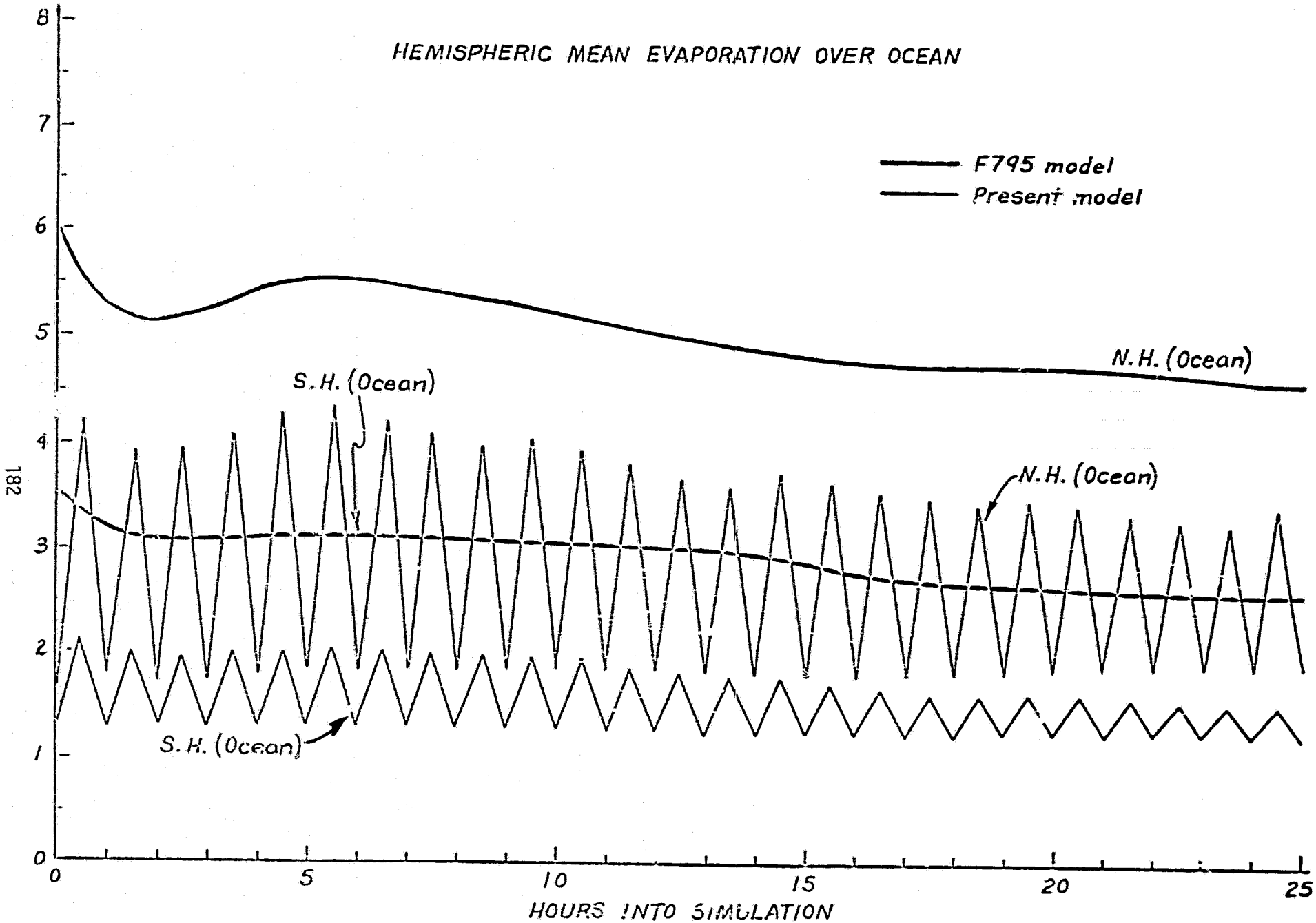

Fig. 4b. Hemispheric mean evaporation for the southern and northern hemispheres for 1 day simulation (ocean), old GLAS model vs. new calculation.

SPACE-TIME SPECTRA OF THE GLAS MODEL 500 MB GEOPOTENTIAL HEIGHT

(D. M. Straus and J. Shukla)

Space-time spectral analysis is a technique which expresses the space-time variance or covariance of meteorological fields in terms of contributions from individual zonal wavenumbers and frequency bands. Because motions of distinct space and time scales are often associated with different dynamical origins, space-time spectral analysis provides a useful diagnostic tool with which to compare model output with observations (Hayashi and Golder, 1977; Pratt, 1979).

This paper represents part of a continuing effort to document the winter space-time spectra of the GLAS general circulation model (Halem et al., 1978) and to compare them with the spectra of 14 winter seasons obtained from the NMC analyses for the years 1963-64 through 1976-77. In this paper, only the 500 mb geopotential height is considered.

The spectra can best be introduced by consideration of the quantity $G(\lambda,t)$, the 500 mb geopotential height as a function of longitude (λ), and time (t) for a fixed latitude. It must be understood that the seasonal mean and some estimate of the seasonal cycle has already been removed. If this procedure is not followed, the well known phenomenon of "leakage" will cause a gross distortion of the resulting seasonal spectra. (For a brief discussion of the phenomenon of leakage, see Bingham et al., 1967.) The space-time variance of G is defined as

$$V = \frac{1}{2\pi} \int_0^{2\pi} d\lambda \, \frac{1}{T} \int_0^{T} dt \, \left[G(\lambda,t)\right]^2 \quad , \tag{1}$$

where T is the period under consideration (here T = 90 days). V is further written as

$$V = \sum_{k=0}^{\infty} \sum_{f>0} P(k,f) \quad . \tag{2}$$

Here k is the (discrete) zonal wavenumber and is constrained to be nonnegative, while the (discrete) frequencies f are given by

$$f = \frac{m}{T} \quad , \quad 1 \leq m \leq 90 \quad , \tag{3}$$

for twice daily data. The variance P(k,f) can be further written (for $k \neq 0$) as

$$P(k,f) = PW(k,f) + PE(k,f) \quad , \tag{4}$$

where PW is the variance due to westward propagating motions and PE is due to eastward propagating motions. The meaning of PW and PE can best be appreciated

by noting that any function of longitude and time, and in particular G, can be written as

$$G(\lambda,t) = \sum_{k=0}^{\infty} \sum_{f\ 0} \{A_W(k,f)\cos(k\lambda+2\pi ft+\phi_W) + A_E(k,f)\cos(k\lambda- 2\pi ft+\phi_E)\}, \quad (5)$$

where A_W and A_E are westward and eastward propagating waves, respectively. A_W and A_E are then related to PW and PE of Eq. (4) by

$$\begin{aligned} PW(k,f) &= \tfrac{1}{4} A_W^2(k,f) \\ PE(k,f) &= \tfrac{1}{4} A_E^2(k,f) \quad . \end{aligned} \quad (6)$$

The tendency for either westward or eastward motions to dominate the total variance is given by the "net propagation tendency"

$$PR(k,f) = \frac{(PW(k,f) - PE(k,f))}{(PW(k,f) + PE(k,f))} \quad . \quad (7)$$

It is of importance to clearly delineate what kind of information is obtained from PW and PE. They do not, by themselves, indicate whether the fluctuations are due to physical standing waves, propagating waves, or neither. They only reflect the projection of the total (geopotential) field onto a complete set of basis functions which correspond to traveling waves. Thus, for instance, a value of PR close to -1.0 indicates a strong tendency for motions of a particular space-time scale to propagate eastward, but a value near 0.0 only means that no clearly dominant direction of propagation is apparent.

The model data were obtained from a winter simulation of the GLAS model which was initialized with data from 1 January 1975 and consist of twice-daily geopotential heights for the first 90 days of the simulation. The NMC analyses were obtained from NCAR (see Jenne, 1975) and consist of twice-daily fields obtained for 14 winter seasons (1963-64 through 1976-77). Each winter season was considered to start on 1 December and to be 90 days in length. In order to approximate the seasonal cycle, a parabolic was fit to each time series (whether from the model or the NMC analyses). This parabola was removed, and the remaining time series was tapered by applying a half cosine bell to the first and last 10 percent of the series. This procedure, suggested by Bingham et al. (1967), insures that those components of the annual cycle which were not accounted for by the (admittedly crude) parabolic approximation would cause minimal distortion of the calculated spectra.

The space-time variance P(k,f), obtained from the NMC analyses, is presented in Fig. 1. The function shown results from averaging the functions P calculated for each of the 14 seasons separately. Two important features of P must be noted. One is the concentration of variance in the lowest frequency, lowest wavenumber portion of the spectrum. The other is the presence of a "ridge" of high variance extending from low frequencies and wavenumbers to higher frequencies and wavenumbers. In Fig. 1, the dotted lines delineate

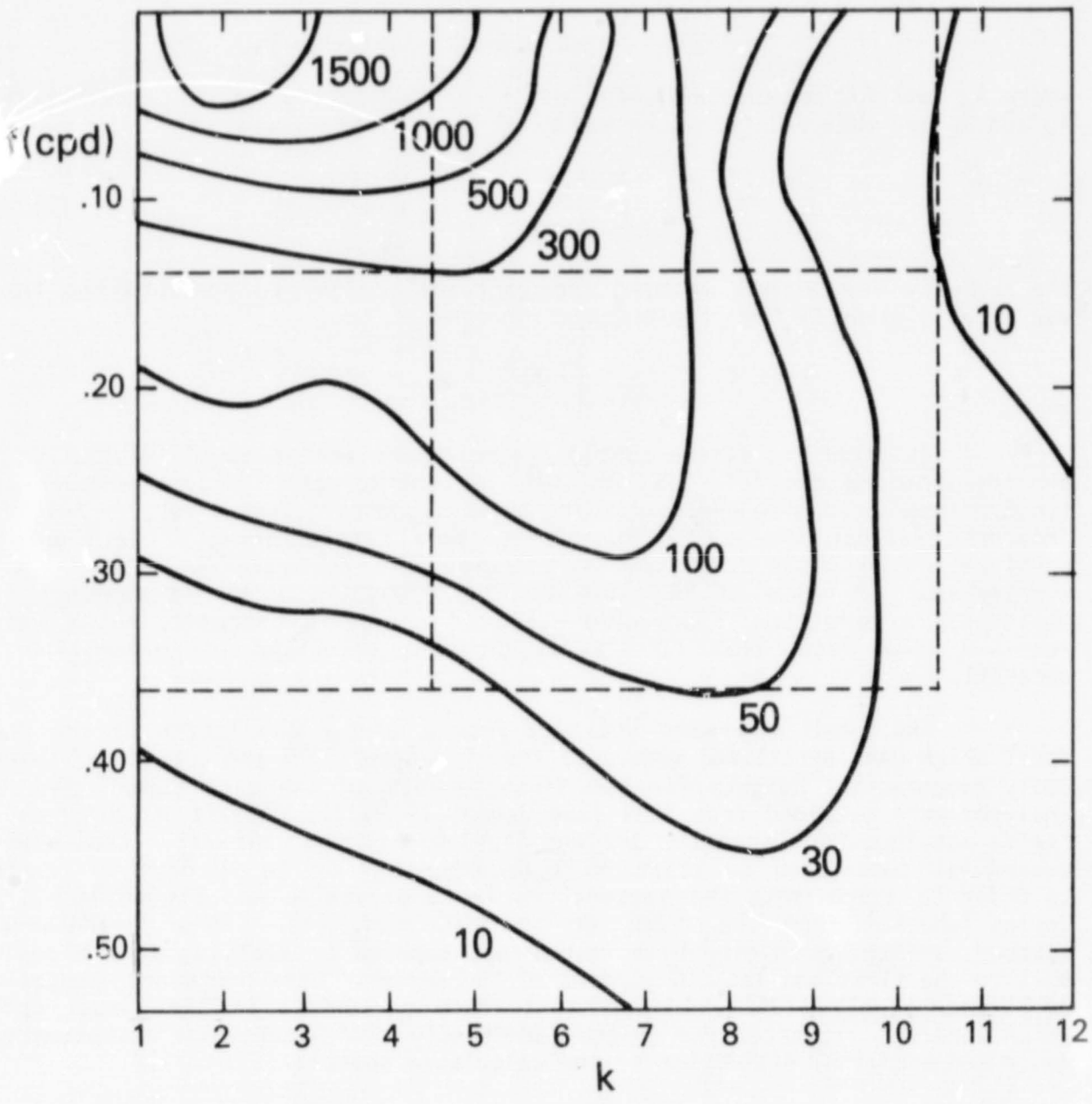

Fig. 1. Space-time variance (P(k,f), averaged over 14 winter seasons (1963-64 through 1976-77). k is the zonal wave number and f the frequency, measured in cycles per day (cpd). The dotted lines denote the four space-time regimes discussed in the text.

C - 3

four space-time regions which divide the wavenumber-frequency plane into regimes of (i) low frequency planetary waves; (ii) low frequency medium-scale waves; (iii) higher frequency planetary waves; and (iv) higher frequency medium-scale waves or baroclinic-scale waves. The precise definitions of these regions are given in Table 1. Region (i) has the bulk of the variance of the planetary waves, and region (iii) consists of space-time scales roughly corresponding to the most unstable baroclinic motions. The remainder of this paper will concentrate on these two scales.

Table 1. Definitions of spectral regions.

Region	Range of frequencies (cpd)	Range of period (days)	Range of wavenumbers
(i)	.0111 to .1333	90 to 7.5	1 to 4
(ii)	.0111 to .1333	90 to 7.5	5 to 10
(iii)	.1444 to .3556	6.9 to 2.8	1 to 4
(iv)	.1444 to .3556	6.9 to 2.8	5 to 10

The total space-time variance in region (i) is presented for the northern hemisphere in Fig. 2, both for the GLAS model and the 14-winter NMC average. The number of degrees of freedom for all of the calculations are summarized in Table 2. It is clear that the model underestimates the average low frequency planetary wave variance in midlatitudes by a considerable amount. In addition, the observed maximum between 60N and 70N is absent in the model. In Fig. 3, the model's low frequency planetary wave variance is compared to that of two individual winters. These winters were chosen to define a range of interannual variation of the variance in region (i); the winter of 1967-68 was a relatively active one in terms of low frequency planetary waves, while the winter of 1969-70 was a relatively quiet season. The model underestimate of the region (i) variance is marked, even when comparing to the latter season.

The baroclinic-scale variance (region [iii]) of the model is compared to the averaged observations in Fig. 4. The agreement is excellent, both as to the overall magnitude of the variance and its dependence on latitude. In Fig. 5, the comparison is again made between the model variance and that of two individual winter seasons chosen to define the range of interannual variability. The model variance is much more similar to that of the baroclinically active winter than it is to the quieter one. The propagation tendency PR, averaged over the baroclinic space and time scales (region [iii]) is presented in Fig. 6 for the model and the same two winter seasons. The model agrees well with both seasons in that the propagation tendency is close to -1.0, indicating a strong tendency to propagate eastward.

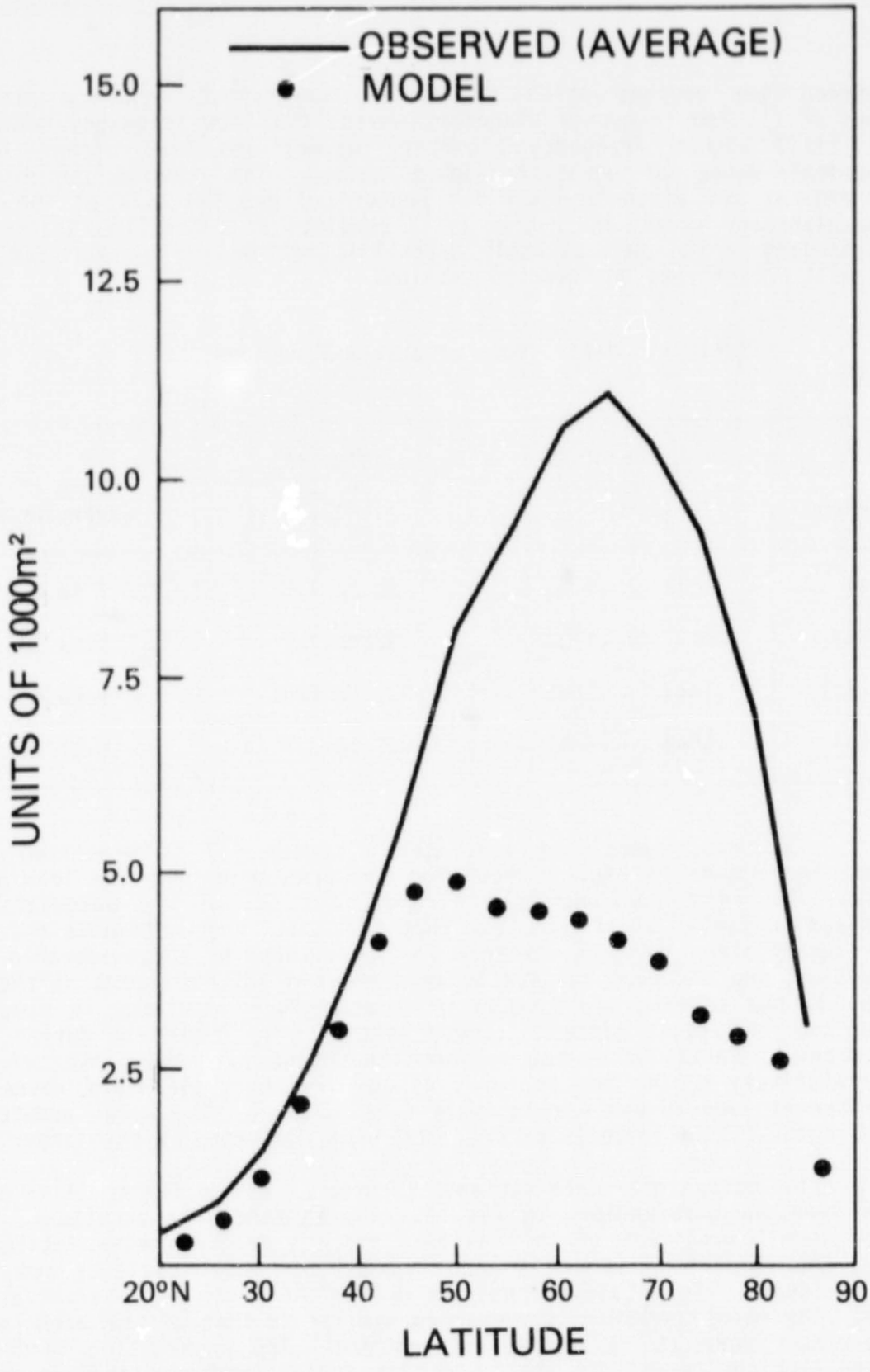

Fig. 2. Variance in regime (i) (low frequency planetary waves) for the model (dots) and for the average of 14 winter seasons (solid line).

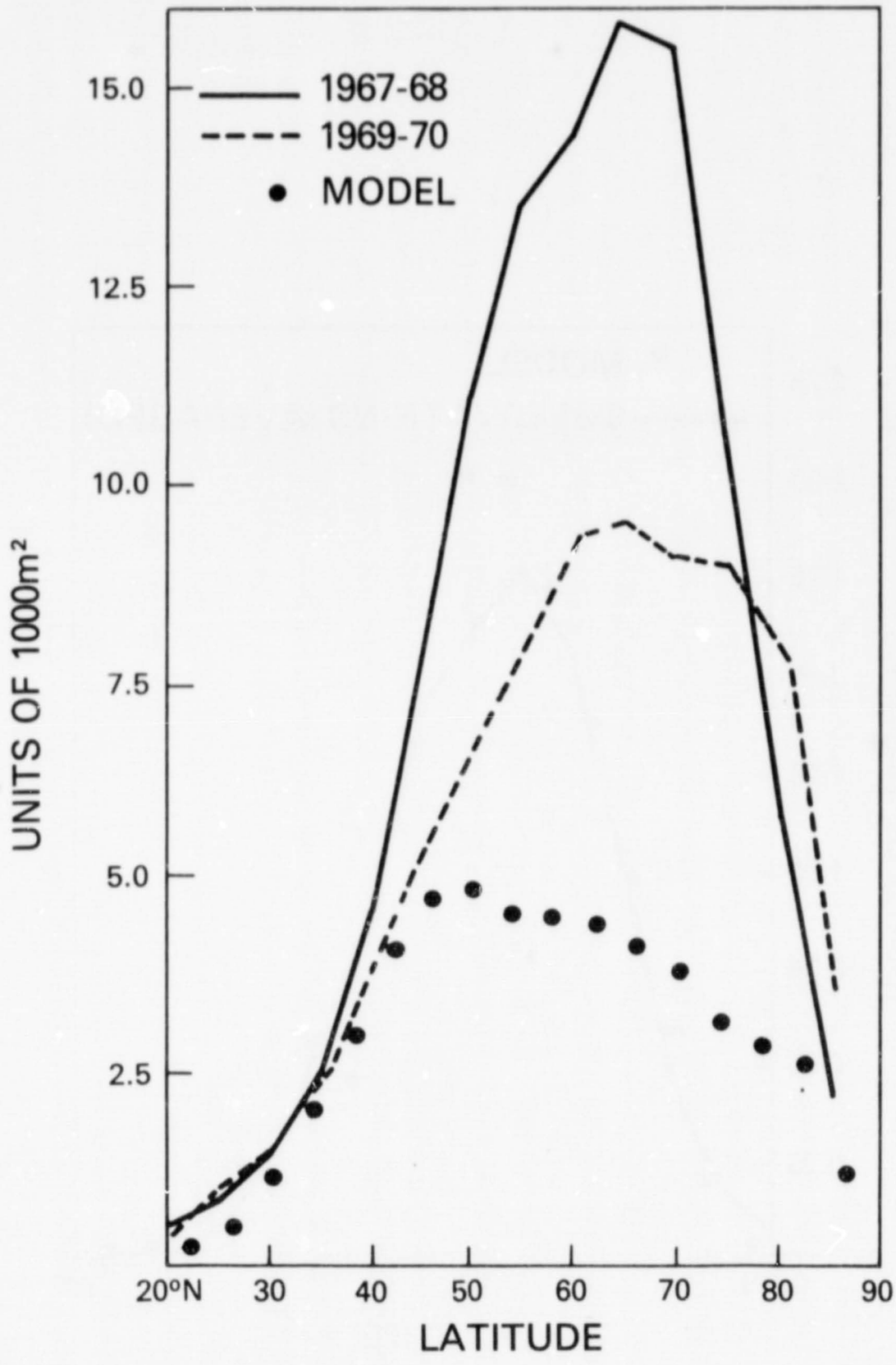

Fig. 3. Variance in regime (i) (low frequency planetary waves) for the model (dots), for observations from the winter of 1969-70 (dashed line), and for observations from the winter of 1967-68 (solid line).

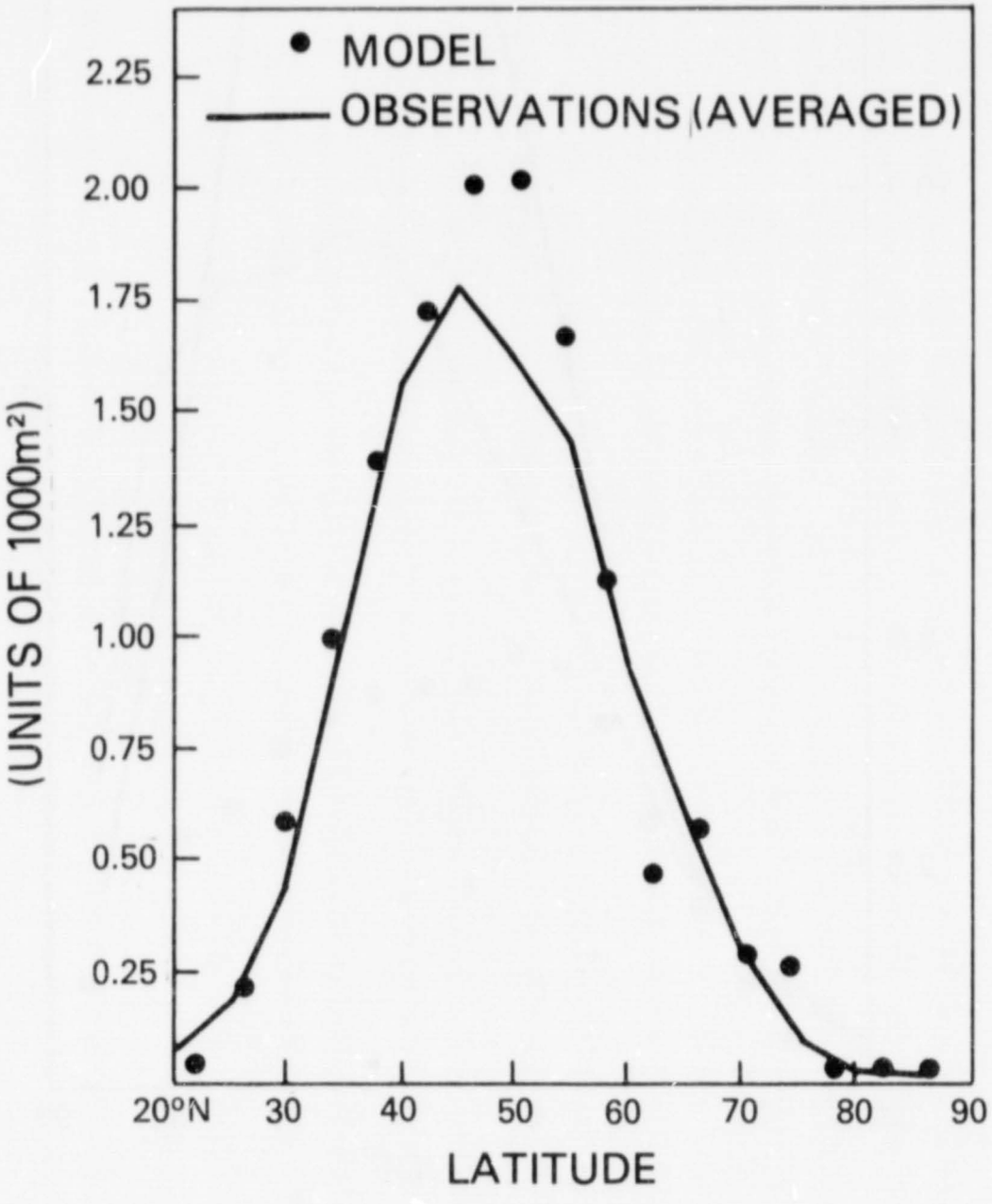

Fig. 4. Variance in regime (iv) (baroclinic-scale waves) for the model (dots) and for the average of 14 winter seasons (solid line).

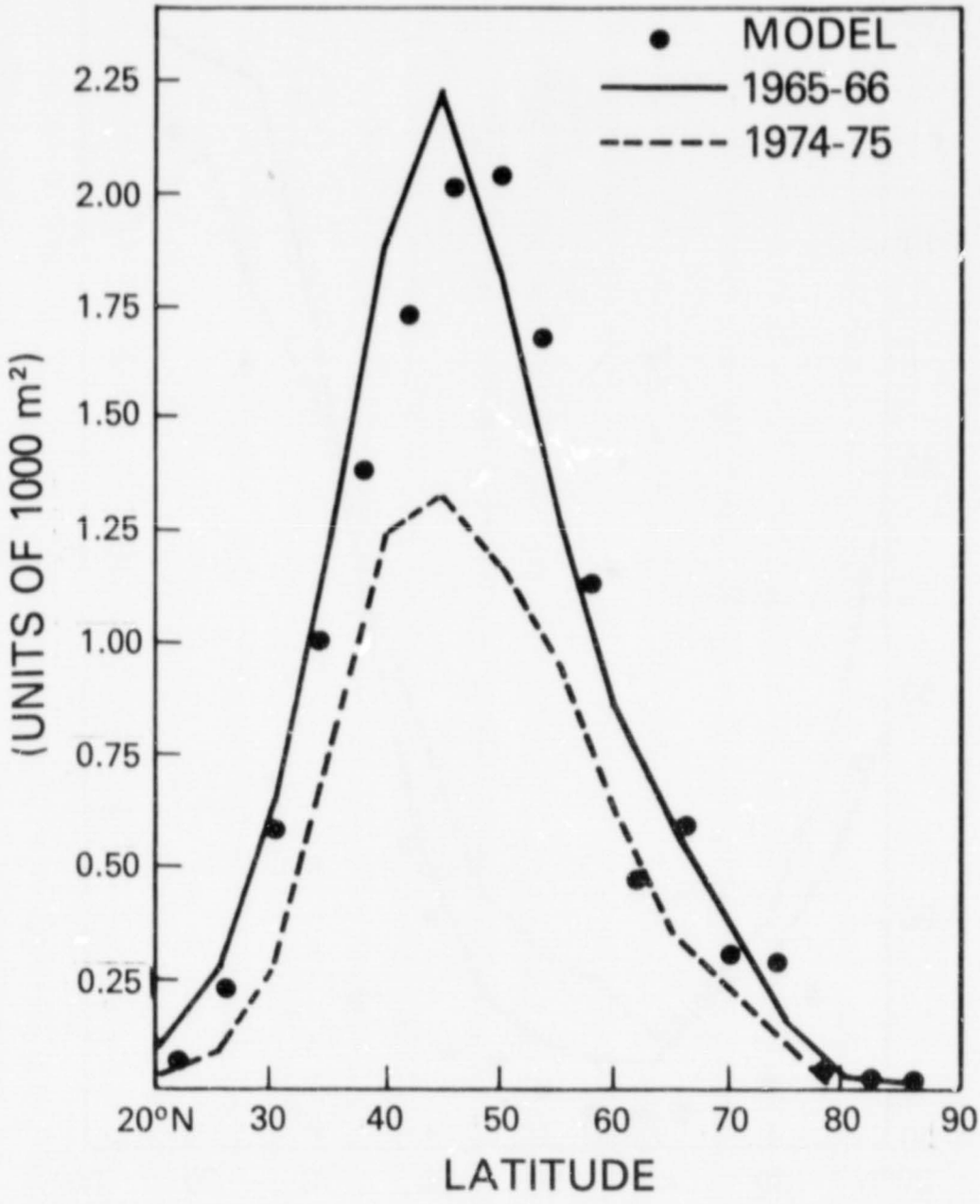

Fig. 5. Variance in regime (iv) (baroclinic-scale waves) for the model (dots), for observations from the winter of 1974-75 (dashed line), and for observations from the winter of 1965-66 (solid line).

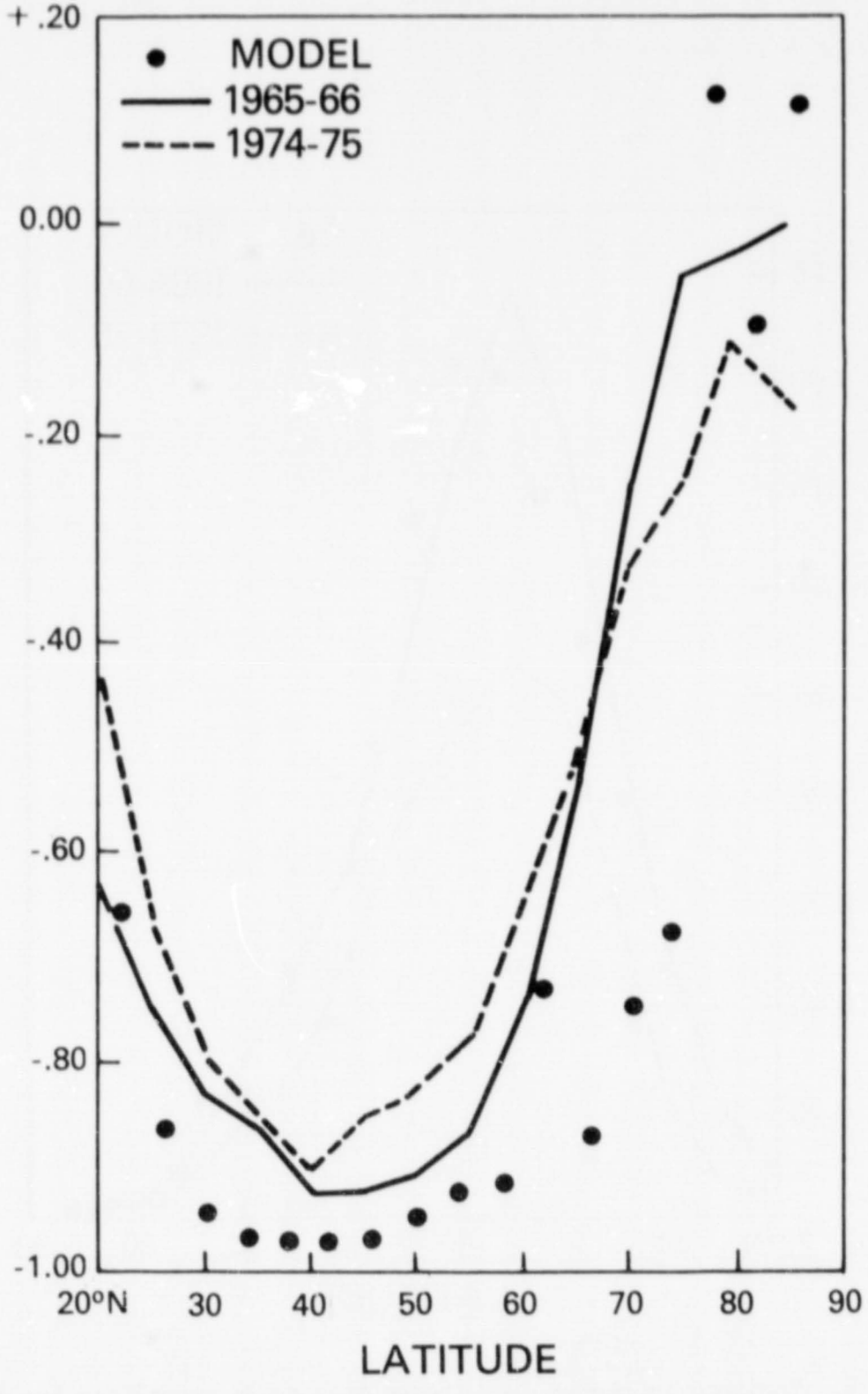

Fig. 6. Average propagation tendency in regime (iv) (baroclinic-scale waves). As in Fig. 5.

Two salient points emerge from the results that have been presented. One is that the GLAS model simulates baroclinic-scale disturbances in a very realistic manner, at least in a statistical sense. The second point is that the model seriously underestimates the amount of variance in the low frequency planetary waves. Comparisons of the GFDL and NCAR models with observations show that these models share the latter deficiency (underestimate of region [i] variance); however, they have not had the GLAS model's success in reproducing baroclinic-scale waves (Pratt, 1979).

Table 2. Degrees of freedom. For a single season, the number of degrees of freedom is 2 per wavenumber per harmonic frequency. The effect of the cosine bell taper is to reduce the number by a factor of about 0.87 (Julian, 1971).

Region	Model	Observations (single season)	Observations (14-year average)
(i)	84	84	1169
(ii)	125	125	1754
(iii)	139	139	1949
(iv)	209	209	2923

The spectra that have been presented describe the transient motions of the atmosphere and the model, exclusive of the annual cycle. It is also of some interest to study the mean fields. These were computed by averaging the (unadjusted) model or observed fields over the appropriate 90-day season. The total spatial variance of the mean field can be written as a sum of contributions from each zonal wavenumber. The sum of the variances in wavenumbers 1 through 18 (stationary waves) is presented in Figs. 7 and 8. In Fig. 7, the model is compared to the average of 14 seasons, while in Fig. 8 the model is compared to two winter seasons, one in which the stationary waves are strong (1976-77) and one in which they are weak (1970-71). The results show that the model's stationary waves are far too weak in midlatitudes. This is in contrast to the GFDL and NCAR models, whose simulated stationary waves are in better agreement with the observations (Pratt, 1979).

In conclusion, the space-time spectral analysis of the 500 mb height field has indicated some important successes and failures of the GLAS model in simulating the atmosphere. The model does simulate the baroclinic-scale waves well, both in terms of the total variance and the dominant direction of propagation. On the other hand, the model's stationary- and planetary-wave variances are much too small compared to the atmosphere.

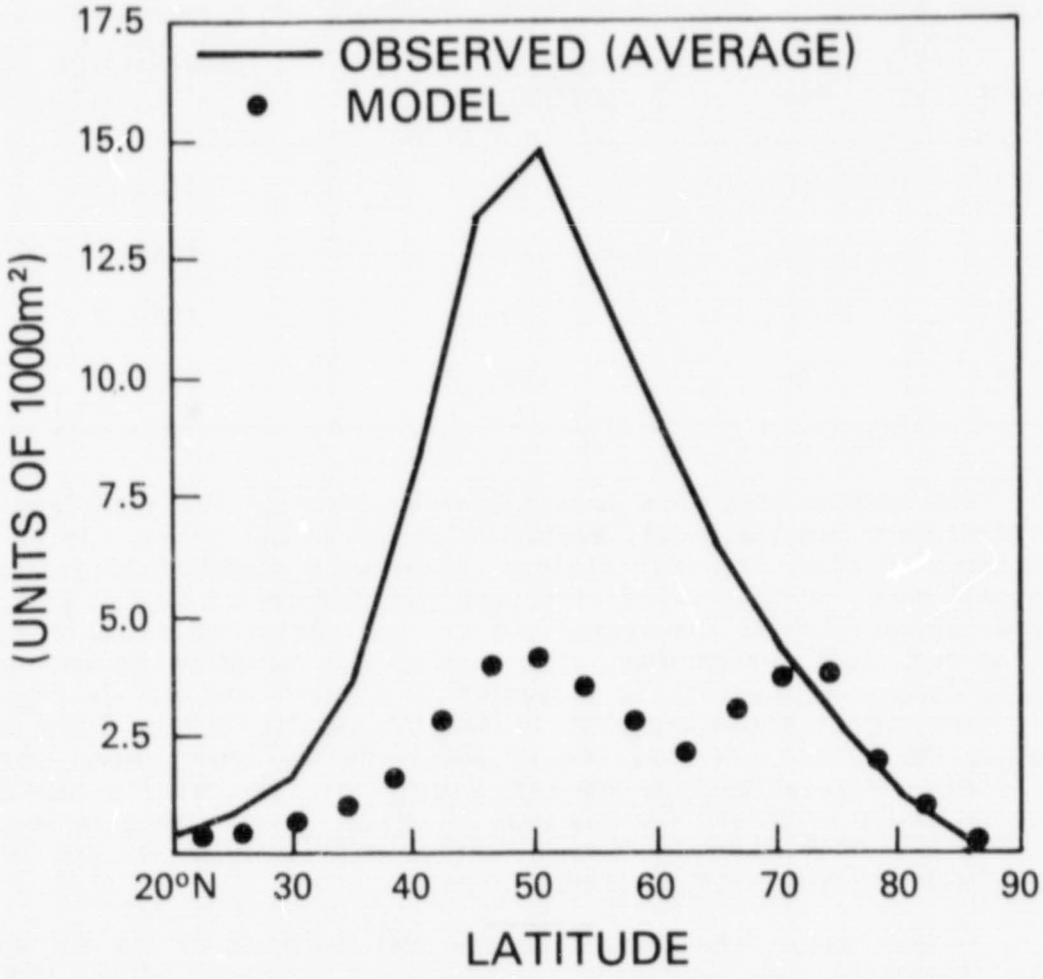

Fig. 7. Stationary-wave variance for the model (dots) and for the average of 14 winter seasons (solid line).

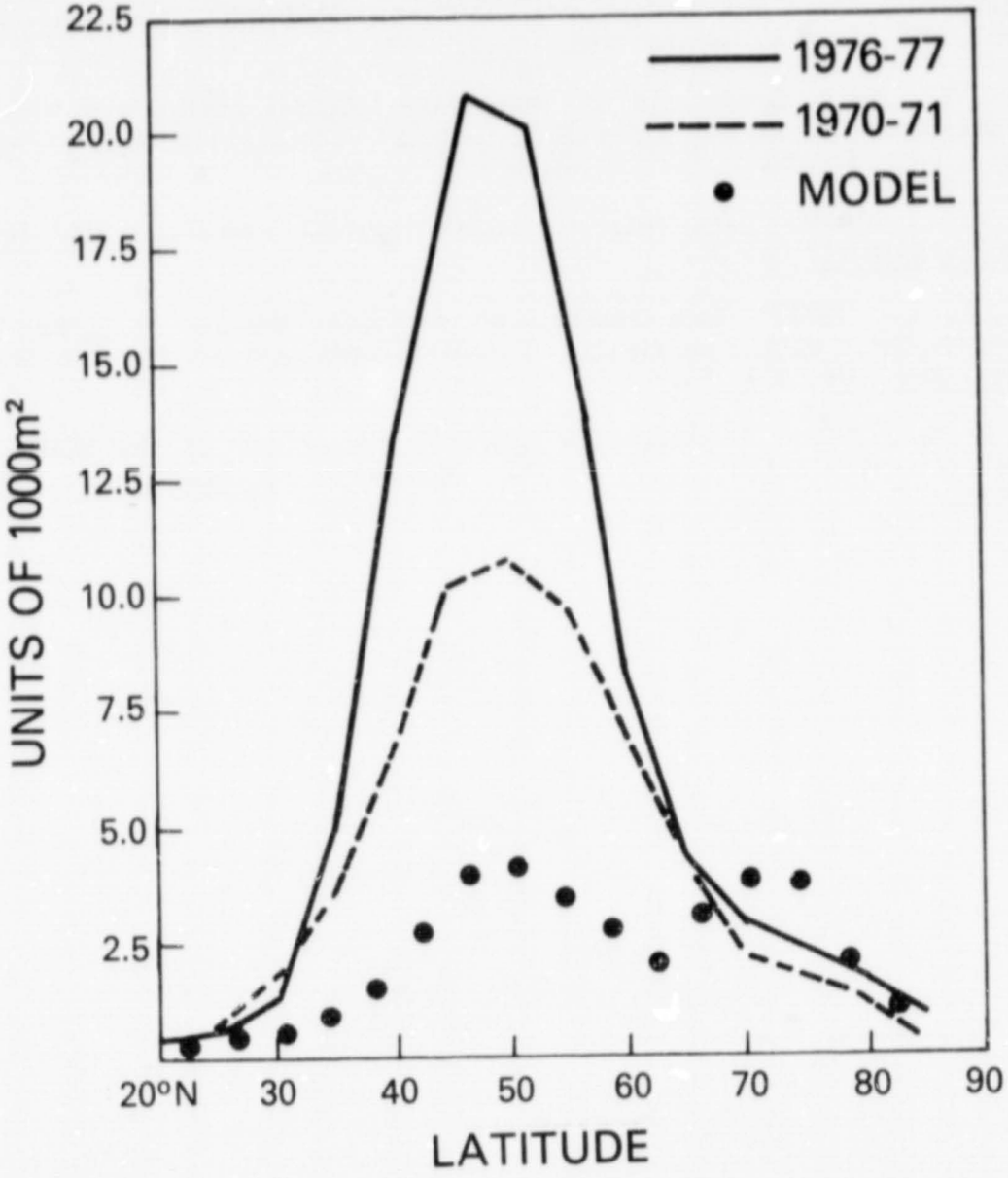

Fig. 8. Stationary-wave variance for the model (dots), for observations from the winter of 1970-71 (dashed line), and for observations from the winter of 1976-77 (solid line).

References

Bingham, C., M. D. Godfrey, and J. W. Tukey, 1967: Modern techniques of power spectrum estimation. IEEE Trans. Aud. Electr., AU-15, 56-66.

Halem, M., J. Shukla, Y. Mintz, M. L. Wu, R. Godbole, G. F. Herman, and Y. Sud, 1979: Comparisons of observed seasonal climate features with a winter and summer numerical simulation produced with the GLAS general circulation model. Report of the JOC Study Conference on Climate Models: Performance, Intercomparison and Sensitivity Studies, GARP Publ. Series No. 22, 207-253, WMO, Geneva, Switzerland.

Hayashi, Y., and D. Golder, 1977: Space-time spectral analysis of mid-latitude disturbances appearing in a GFDL general circulation model. J. Atmos. Sci., 34, 237-262.

Jenne, R. L., 1975: Data sets for meteorological research, NCAR Tech. Note NCAR-TN/1A-111, p. 20.

Julian, P. R., 1971: Some aspects of variance spectra of synoptic scale tropospheric wind components in midlatitudes and in the tropics. Mon. Wea. Rev., 99, 954-965.

Pratt, R. W., 1979: A space-time spectral comparison of the NCAR and GFDL general circulation models to the atmosphere. J. Atmos. Sci., 36, 1681-1691.

OROGRAPHICALLY INDUCED MULTIPLE EQUILIBRIA IN A HIGHLY TRUNCATED BAROCLINIC SPECTRAL MODEL

(J. G. Charney and D. M. Straus)

In a recent study, Charney and DeVore (1979) showed that the forced flow of a barotropic fluid over wavy topography in a periodic beta-plane channel may possess a multiplicity of equilibrium states of which more than one may be stable. In a certain range of forcing, there are two stable and one unstable equilibrium states. One of the stable states is a "high-index" circulation having a strong zonal flow and a relatively weak wave perturbation; the other is a low-index flow having a weak zonal flow and a relatively strong perturbation, i.e., the unstable equilibrium state has an intermediate zonal flow. It was suggested in Charney and DeVore that blocking, the presence of persistent high-pressure ridges in the Pacific, Atlantic or Central Asiatic regions is an example of an equilibrium flow of the low-index type, and that transition from it to the high-index state occurs via the instability of the intermediate state.

The discovery of multiple equilibria in a barotropic system led the present authors to investigate a corresponding baroclinic system. Are there multiple stationary equilibria, and, if so, what is their nature? Holopainen (1970) showed that the quasi-stationary planetary waves in the atmosphere are maintained by conversion of mean flow potential energy by baroclinic processes, not by conversion of mean flow kinetic energy by the action of mountain pressure torques. What then is the role of orography?

To investigate these questions, the authors studied a highly truncated, two-layer, quasi-geostrophic spectral model of the type introduced by Lorenz (1963). The model domain is a periodic channel on a mid-latitude beta plane. The spectral equations studied are precisely those of Lorenz, with the addition of topography and a variable Coriolis parameter, and the omission of an equation governing the time variation of the static stability. The parameters (such as the channel width, frictional dissipation, static stability, etc.) were taken to be representative of the real atmosphere. The modes retained correspond to a zonal flow plus only one zonal wave number, and to two modes in the north-south (y) direction. (See Charney and Straus, 1980, for further details.) The results discussed in this report are those for which the single zonal wave number was taken to be zonal wave number 3 in the real atmosphere at latitude 45N. The orography was taken to consist of a single (wave number 3) sine wave in the x-direction, and to have a projection onto only the gravest (first) y-mode.

The Hadley solution is an equilibrium state obtained by setting all time derivatives and wave amplitudes to zero. The zonal flow in the lower layer also vanishes, so that the Hadley solution remains a true equilibrium in the presence of orography.

An analysis of the stability of the Hadley solution to (wave number 3) perturbations of the first y-mode reveals the presence of two types of instability. They are distinguished by the character of the eigenvalue of the

stability matrix whose real part becomes positive, i.e., the eigenvalue corresponding to the instability. In one case, this eigenvalue is purely real, corresponding to a perturbation that grows in place. The instability is termed "orographic." In the second case, the eigenvalues occur in complex conjugate pairs, indicating a traveling disturbance. This instability is a modified form of baroclinic instability. For the set of (realistic) parameters used by Charney and Straus (1980), the Hadley solution is stable for thermal driving θ_A^* less than .131. The parameter θ_A^* is a dimensionless measure of the radiative equilibrium temperature difference between the southern and northern walls. It is related to the dimensional radiative equilibrium temperature difference (ΔT^*) and to the actual temperature difference (ΔT) that occurs in the Hadley solution, by

$$\Delta T^* = 530\theta_A^* \quad (°K),$$

$$\Delta T = 378\theta_A^* \quad (°K).$$

For $\theta_A^* > .131$ the Hadley solution becomes orographically unstable (see Table 1), and for θ_A^* above .165 it also becomes baroclinically unstable. Thus, in the range of forcing $.165 \leq \theta_A^* \leq .200$, the two types of instability coexist.

For values of θ_A^* below .131, the lower limit of topographic instability, no equilibria other than the Hadley circulation exist. At values of the driving which are slightly supercritical ($\theta_A^* = .135$), two new equilibria are found. These are referred to as "wavy equilibria" because they are steady state solutions with non-zero wave amplitudes. (For details regarding their computation, see Charney and Straus, 1980.)

Each solution is identified by a branch number. (See Tables 1 and 2.) The two new equilibria are themselves stable to further first y-mode perturbations. Characterizing the three steady states by the zonal flow in the lower layer, the (unstable) Hadley solution (zero lower layer zonal flow) lies intermediate between the (stable) branch 1 solution (weak lower layer westerlies) and the (stable) branch 2 solution (weak easterlies). Since both new solutions are stable, they divide the phase space corresponding to the first y-mode into two subdomains.

Numerical integration of the equations of motion (with only the first y-mode present), starting near either equilibrium, shows convergence to that equilibrium. Both "wavy" equilibria are, however, unstable with respect to second y-mode perturbations. Numerical integration with both y-modes present led to a variety of solutions, depending upon the initial conditions. It was possible to obtain a periodic solution (with a period of about 16 days) which consisted of a relatively weak stationary wave, upon which was superimposed transient waves. The first y-mode transient wave propagated westward whereas the second y-mode wave propagated eastward.

As the value of θ_A^* is increased, the two wavy equilibria become modified in a continuous manner. Branch 1 is characterized by lower layer zonal westerlies and branch 2 by lower layer zonal easterlies, characterizations which remain valid tnroughout the range of θ_A^* studied.

Table 1. Wavy equilibria for wave number 3, branches 1 and 2.

		Branch 1							
θ_A*	S_H	Ψ_A	Ψ_K	Ψ_L	θ_A	θ_K	θ_L	S_1	S_2
.135	Or	.0982	-.0090	.0174	.0919	-.0055	.0169	--	P
.140	Or	.1000	-.0167	.0231	.0908	-.0111	.0223	--	P
.145	Or	.1014	-.0237	.0265	.0899	-.0163	.0255	--	P
.150	Or	.1028	-.0302	.0287	.0891	-.0210	.0274	--	P
.155	Or	.1041	-.0362	.0300	.0885	-.0253	.0286	P	P
.160	Or	.1055	-.0421	.0309	.0879	-.0293	.0294	P	P
.165	Or,Bc	.1067	-.0475	.0316	.0874	-.0328	.0299	P	P
.170	Or,Bc	.1078	-.0527	.0320	.0870	-.0361	.0302	P	P
.175	Or,Bc	.1090	-.0577	.0323	.0866	-.0392	.0303	P	P
.180	Or,Bc	.1100	-.0622	.0326	.0863	-.0419	.0304	--	P
.185	Or,Bc	.1111	-.0667	.0328	.0860	-.0445	.0305	--	P
.190	Or,Bc	.1120	-.0709	.0329	.0857	-.0468	.0306	--	P
.195	Or,Bc	.1129	-.0751	.0331	.0855	-.0491	.0306	--	P
.200	Or,Bc	.1133	-.0770	.0334	.0855	-.0500	.0309	--	P
		Branch 2							
θ_A*	S_H	Ψ_A	Ψ_K	Ψ_L	θ_A	θ_K	θ_L	S_1	S_2
.135	Or	.0930	-.0001	-.0057	.0960	-.0010	-.0055	--	P
.140	Or	.0927	-.0024	-.0125	.0977	-.0046	-.0120	P	P
.145	Or	.0918	-.0055	-.0164	.0993	-.0086	-.0157	P	P
.150	Or	.0910	-.0088	-.0186	.1008	-.0126	-.0177	P	P
.155	Or	.0904	-.0120	-.0197	.1026	-.0165	-.0186	P	P
.160	Or	.0899	-.0150	-.0198	.1047	-.0201	-.0185	P	P
.165	Or,Bc	.0895	-.0177	-.0192	.1071	-.0232	-.0176	P	P
.170	Or,Bc	.0895	-.0198	-.0179	.1100	-.0257	-.0161	P	P
.175	Or,Bc	.0898	-.0214	-.0164	.1135	-.0274	-.0142	P	P
.180	Or,Bc	.0907	-.0224	-.0146	.1174	-.0283	-.0122	P	P
.185	Or,Bc	.0924	-.0229	-.0128	.1217	-.0284	-.0102	P	P
.190	Or,Bc	.0949	-.0230	-.0110	.1264	-.0277	-.0082	P	P
.195	Or,Bc	.0990	-.0225	-.0092	.1315	-.0260	-.0063	P	P
.200	Or,Bc	.1052	-.0212	-.0071	.1370	-.0229	-.0043	S,S	P

All quantities are in dimensionless form. The column headed S_H describes the stability of the Hadley circulation to perturbations of the first y-mode. The columns S_1 and S_2 describe the stability of the wavy equilibria to perturbations of the 1st and 2nd y-modes, respectively. No entry (--) denotes a stable equilibrium, Or denotes orographic instability of the Hadley circulation and Bc baroclinic instability of the Hadley circulation. P denotes a propagating instability of the wavy equilibrium (complex conjugate roots of the stability matrix), S denotes a stationary instability (purely real roots). When two types of instability are indicated, they exist simultaneously. The meaning of the variables follows: the lower layer zonal flow is $\Psi_A - \theta_A$; the upper layer zonal flow is $\Psi_A + \theta_A$. The wave in the lower layer is proportional to $(\Psi_K - \theta_K)\cos kx + (\Psi_L - \theta_L)\sin kx$, where k is the wave number. The wave in the upper layer is proportional to $(\Psi_K + \theta_K)\cos kx + (\Psi_L + \theta_L)\sin kx$.

Table 2. Wavy equilibria for wave number 3, branches 3 and 4.

		Branch 3							
θ_A*	S_H	Ψ_A	Ψ_K	Ψ_L	θ_A	θ_K	θ_L	S_1	S_2
.180	Or,Bc	.1602	.0633	.0024	.1134	.0327	-.0017	S	P
.185	Or,Bc	.1608	.0802	.0019	.1087	.0398	-.0027	S	P
.190	Or,Bc	.1606	.0902	.0016	.1064	.0441	-.0033	S	P
.195	Or,Bc	.1609	.0995	.0009	.1045	.0477	-.0040	S	P
.200	Or,Bc	.1603	.1051	.0008	.1035	.0503	-.0043	S	P
		Branch 4							
θ_A*	S_H	Ψ_A	Ψ_K	Ψ_L	θ_A	θ_K	θ_L	S_1	S_2
.180	Or,Bc	.1573	.0383	.0256	.1224	.0217	-.0006	P	P
.185	Or,Bc	.1524	.0212	.0020	.1300	.0132	-.0000	P	P
.190	Or,Bc	.1471	.0103	.0012	.1352	.0069	.0001	P	P
.195	Or,Bc	.1411	.0014	.0002	.1393	.0010	.0000	P	P
.200	Or,Bc	.1324	-.0073	-.0013	.1425	-.0059	-.0004	S,P	P

All quantities are in dimensionless form. The column headed S_H describes the stability of the Hadley circulation to perturbations of the first y-mode. The columns S_1 and S_2 describe the stability of the wavy equilibria to perturbations of the 1st and 2nd y-modes, respectively. No entry (--) denotes a stable equilibrium, Or denotes orographic instability of the Hadley circulation and Bc baroclinic instability of the Hadley circulation. P denotes a propagating instability of the wavy equilibrium (complex conjugate roots of the stability matrix), S denotes a stationary instability (purely real roots). When two types of instability are indicated, they exist simultaneously. The meaning of the variables follows: the lower layer zonal flow is $\Psi_A - \theta_A$, the upper layer zonal flow is $\Psi_A + \theta_A$. The wave in the lower layer is proportional to $(\Psi_K - \theta_K)\cos kx + (\Psi_L - \theta_L)\sin kx$, where k is the wave number. The wave in the upper layer is proportional to $(\Psi_K + \theta_K)\cos kx + (\Psi_L + \theta_L)\sin kx$.

At θ_A* = .140, the branch 2 equilibrium becomes unstable with respect to first y-mode perturbations. Since the roots of the stability matrix occur in complex conjugate pairs, the disturbance has a traveling nature, and in fact can be considered as a superposition of a westward and an eastward traveling wave. Thus, the presence of topography allows for instability of the wavy equilibrium even though the Hadley solution itself is baroclinically stable.

For still higher values of the driving ($\theta_A^* = .155$), both wavy equilibria become unstable to first y-mode perturbations. However, the branch 1 solution, which by now has acquired a larger upper layer wave, is only weakly unstable (with e-folding times of about 200 days). Numerical integration of the first y-mode equations gives rise to a periodic solution (with a period of about 17 days) in which the transient wave again propagates westward.

At $\theta_A^* = .165$, the Hadley circulation becomes both baroclinically and orographically unstable and, at $\theta_A^* = .180$, two new wavy equilibria are found, giving four branches in all. (See Table 2.) Evidence is presented in Charney and Straus (1979) which indicates that the existence of both baroclinic and orographic instability of the Hadley circulation is closely connected to the appearance of new wavy equilibria. These new equilibria can be characterized as high index, having very large upper layer zonal flows (corresponding to about 60 m/sec) and relatively much weaker wave fields. Both equilibria have zonal westerlies in the lower layer. In contrast, the branch 1 equilibrium evolves into a blocking, or low-index solution, with an upper layer wave amplitude comparable to the upper layer zonal flow.

The high-index solutions (branches 3 and 4) as well as the branch 2-solution are unstable with respect to perturbations of the first y-mode. The branch 1 solution, which is weakly unstable for $.155 < \theta_A^* < .175$, becomes stable again for $\theta_A^* > .180$. Thus, for the large value of the thermal driving corresponding to $\theta_A^* = .180$, the only realizable steady state solution of the first y-mode system is the low-index, or blocking solution. Numerical integration of the nonlinear equations, with initial conditions close to either the branch 1 or branch 2-equilibrium, converges to the stable low-index equilibrium. When the initial conditions are close to the branch 3 equilibrium, a periodic solution of 18.1 days is realized, and when they are close to the branch 4 steady state, a similar but not identical periodic solution (of period 16.6 days) is obtained. The time-averaged zonal flow in both cases is similar to that of the stable equilibrium, but the time-averaged wave amplitudes are weaker. The time-dependent flow consists of slow, westward traveling waves of variable amplitude accompanied by large oscillations in the zonal flow. All four equilibria are unstable to second y-mode perturbations, and both periodic and aperiodic solutions are possible when both y-modes are retained, depending upon the initial conditions.

In summary, orographic instability of the Hadley circulation to disturbances of wave number 3 gives rise to a wavy equilibrium which for large driving resembles blocking. However, baroclinic instability of the Hadley solution is necessary to realize high-index equilibria.

To understand better the role of the mountains in the formation of the wavy equilibria, the energetics of their maintenance has been examined. The important result is that the orographic form drag exchange between zonal and eddy kinetic energies (the only such exchange for the first y-mode) is in all cases small. For lower values of the driving, this exchange is entirely negligible, while for high driving the small orographic exchange always draws energy from the wave. Thus, the orographic interactions play an indirect role in the formation of wavy equilibria; they are a catalyst; they permit the equilibria to exist, but they do not directly support the stationary waves.

Although it is not possible to arrive at definite conclusions concerning the real atmosphere or even a continuous model from the highly truncated spectral, two-layer model examined, a number of heuristic conclusions are clearly suggested. One conclusion is that the phenomenon of blocking is a stable or quasi-stable equilibrium arising from orographic instability with strong thermal driving; and that high-index states occur also for strong driving, when the Hadley circulation becomes baroclinically as well as orographically unstable. These latter will always be unstable to large-scale perturbations, and will give rise to a wave-zonal flow mean state on which is superimposed propagating waves, drawing on the potential and kinetic energies of the mean flow and interacting with it in a periodic or at least fluctuating manner. The results further suggest that the westward propagating first y-mode waves arising from the instability of the wave-like equilibria are prototypes of low frequency, westward propagating "Rossby" waves observed in nature (Eliasen and Machenhauer, 1965, 1969, Pratt and Wallace, 1976; Blackmon, 1976; Madden, 1978). These waves, which have periods ranging from 5 to 20 days, have been previously regarded as "free" waves (Eliasen and Machenhauer, 1965, 1969; Madden, 1978), this study suggests that they arise from instabilities of the quasi-stationary topographically forced equilibria.

References

Blackmon, M. L., 1976: A climatological study of the 500 mb geopotential height of the northern hemisphere. J. Atmos. Sci., 33, 1607-1623.

Charney, J. G., and J. G. DeVore, 1979: Multiple flow equilibria in the atmosphere and blocking. J. Atmos. Sci., 36, 1205-1216.

_____, and D. M. Straus, 1980: Form-Drag Instability, Multiple Equilibria and Propagating Planetary Waves in Baroclinic, Orographically Forced Planetary Wave Systems. To be published in J. Atmos. Sci.

Eliasen, E., and B. Machenhauer, 1965: A study of the fluctuations of the atmospheric planetary flow patterns represented by spherical harmonics. Tellus, 17, 220-238.

_____, and _____, 1969: On the observed large-scale atmospheric wave motions. Tellus, 21, 149-166.

Holopainen, E. O., 1970: An observational study of the energy balance of the stationary disturbances in the atmosphere. Quart. J. Roy. Soc., 94, 626-644.

Lorenz, E. N., 1963: The mechanics of vacillation. J. Atmos. Sci., 20, 448-464.

Madden, R. A., 1978: Traveling Planetary Waves and Their Effect on the General Circulation. NCAR Cooperative Thesis No. 47, Colorado State Univ. and National Center for Atmospheric Research.

Pratt, R. W., and J. W. Wallace, 1976: Zonal propagation characteristics of large-scale fluctuations in the mid-latitude troposphere. J. Atmos. Sci., 33, 1184-1194.

A STUDY OF THE CLIMATIC NOISE OF THE GLAS GCM

(D. M. Straus and M. Halem)

The problem of distinguishing the potentially predictable component of observed monthly and seasonal atmospheric means from the unpredictable statistical fluctuations has recently received much attention (Leith, 1973, 1975; Madden, 1976; and Madden and Shea, 1978). The potentially predictable component (Leith, 1975) is defined as that element of long-term atmospheric states which is forced by influences external to the atmosphere, such as solar insolation, sea surface temperatures, ice cover, etc. The unpredictable statistical fluctuations (or "climatic noise") are due to the variability intrinsic to the atmosphere and would exist even in the presence of unchanging external conditions. That is, the statistical properties of climatic noise are defined by averaging over an ensemble of realizations, each in the presence of identical external conditions. In these definitions, the external influences may be fixed, or they may be prescribed to vary smoothly in time (as does the annual cycle).

However, this distinction is difficult to apply in practice, since the operational definition of climatic means is based on finite time averages of a single realization, namely, the atmosphere itself. The determination of the character of climatic noise from long records of real data requires that a priori assumptions be made. One such assumption is that climatic noise can be represented as a first-order autoregressive (Markov) process over a wide range of frequencies (Leith, 1973).

In this paper, stochastic forecasts were made with the GLAS GCM to test the adequacy of low-order autoregressive processes in describing the model climatic noise. Model integrations were carried out with prescribed climatological boundary conditions for differing initial states, thus providing an ensemble of simulated data which satisfies the definition of climatic noise. The fields examined were the sea level pressure and ground temperature at 54 surface stations in the continental U.S. The hypotheses tested were that these data are adequately described by white noise (H_0), by a first-order autoregressive process (H_1), or by a second-order process (H_2).

The findings show that H_0 and H_1 must be rejected at virtually all stations, but that hypothesis H_2 is consistent with the model "climatic noise" in some geographical regions. There are regions for which none of the processes considered describe the data.

The eleven integrations of the GLAS model used in this study were performed with the constant external forcings set equal to their January climatological values. The only exception is the incoming solar radiation, which was also the same in all integrations but changed in time, following the declination of the sun. The initial atmospheric conditions for the first of the integrations (run 1) were taken from an objective analysis of observed data valid for 1 January 1973; four additional sets of initial conditions (runs 2-5) were obtained from this analysis by introducing random errors with a Gaussian distribution into all fields. Similarly, the initial conditions

for three other integrations (runs 6-8) were those observed for 1 January 1974, plus two sets of similarly perturbed fields. The initial conditions for the remaining three integrations (runs 9-11) were those observed for 1 January 1975, again with two sets of similarly perturbed fields. Numerical integrations from 1 January to 31 January were carried out for each of the eleven initial states. The hourly sea level pressures and ground temperatures were interpolated to the positions of 54 selected weather stations over the U.S. (see Fig. 1) and then averaged each day. Thus, for each station and for both variables, the data consisted of eleven 31-day time series. In processing these data, it is necessary to remove the mean from each of the series separately. Further, it is necessary to remove the seasonal trend. An approximation to this trend was obtained by averaging the temperature or sea level pressure for each day across the eleven ensemble members. The resulting (average) time series was subtracted from each of the eleven original series.

The first hypothesis H_0 is that the data, consisting of $N_S = 11$ time series of $N = 31$ days each, are consistent with white noise:

$$X_{r,s} = g_{r,s}, \quad -n \leq r \leq n, \quad 1 \leq s \leq N_S, \tag{1}$$

$$\text{and} \quad N = 2n+1 \ .$$

Here $X_{r,s}$ refers to the data at day r in realization s; thus $n = 15$; $N = 31$; $N_S = 11$. The $g_{r,s}$ are random variables, uncorrelated with respect to both indices r and s, and satisfying

$$E[g_{r,s}] = 0, \qquad \text{for all } r \text{ and } s \tag{2a}$$

$$E[g_{r,s}\ g_{r',s'}] = \begin{cases} \sigma^2 \text{ if } r = r' \text{ and } s = s' \\ 0, \text{ otherwise} \ . \end{cases} \tag{2b}$$

The notation $E[\ ]$ refers to the theoretical expectation or ensemble average over all possible independent realizations; the variance σ^2 is a free parameter which can be chosen to fit the data. The precise meaning of consistency will be given in Eq. (6).

The second hypothesis H_1 is that the data are consistent with a first-order autoregressive (Markov) process (Gilman et al., 1963; Jenkins and Watts, 1968):

$$X_{r,s} = a_1 X_{r-1,s} + g_{r,s} \ , \tag{3}$$

where a_1 and the variance (σ^2) of $g_{r,s}$ are to be determined from a best fit to the data.

The hypothesis of a second-order autoregressive process (H_2) can be written as:

$$X_{r,s} = a_1 X_{r-1,s} + a_2 X_{r-2,s} + g_{r,s} \ , \tag{4}$$

where a_1, a_2, and σ^2 are to be determined.

To better understand the nature of these low-order processes, it is helpful to consider the autocovariance function at lag k

$$\gamma_k = E[X_{r,s}\, X_{r-k,s}] \ ,$$

which measures the (average) influence of X at any day on its value k days later. The hypothesis of white noise implies that the value of X on any one day is completely uncorrelated with its value on any other day. Hence $\gamma_k = 0$ if $k \neq 0$. A first-order process describes "damped persistence," with γ_k smoothly decreasing from its value at $k = 0$ to a near-zero value some days later (see Fig. 3). It can be shown that second- and third-order processes can describe a damped periodic, as well as a purely damped, component so that γ_k resembles a sine wave with amplitude decreasing in time (see Fig. 4).

The method of determining the adequacy of each of the hypotheses in describing the data is discussed in detail in Straus and Halem (1979). A few of the basic ideas are illustrated here using H_2 as an example. The "best" estimates of the parameters a_1 and a_2 in Eq. (4) are obtained by minimizing the mean-squared error V,

$$V(a_1, a_2) = \sum_{s=1}^{N_s} \sum_{r=-n}^{n} (X_{r,s} - a_1 X_{r-1,s} - a_2 X_{r-2,s})^2 \ , \qquad (5)$$

with respect to a_1 and a_2. Let the estimates so obtained be written as $\hat{a}_1$ and $\hat{a}_2$. Then, according to H_2, the residual $g_{r,s}$, given by

$$X_{r,s} - \hat{a}_1 X_{r-1,s} - \hat{a}_2 X_{r-2,s} = g_{r,s} \ , \qquad (6)$$

should behave as white noise. In this manner, a test of all the hypotheses can be accomplished by use of a single statistical test for white noise. Such a test has been described in Straus and Halem (1979). A particular hypothesis is considered consistent with the original data if the appropriate residual is consistent with white noise.

The lowest order autoregressive process that was consistent with the model data is shown in Fig. 1 (for ground temperature) and Fig. 2 (for sea level pressure). The hatching indicates stations for which none of the processes considered is consistent with the data. It is clear that white noise is not consistent with the model climatic noise, and that (except for the ground temperature at a few stations) this is also true of a first-order Markov process. There are large regions in the midwest and west for which a second-order process is consistent with both the sea level pressure and ground temperature. Note, however, that over portions of the northeast, none of the processes is consistent with the data for both variables.

The almost total failure of the first-order process to capture the data is illustrated in Fig. 3, in which is shown the autocovariance function for sea level pressure calculated from the data and that implied by the "best fit" first-order process. For lags of 0 or 1, the first-order process is in

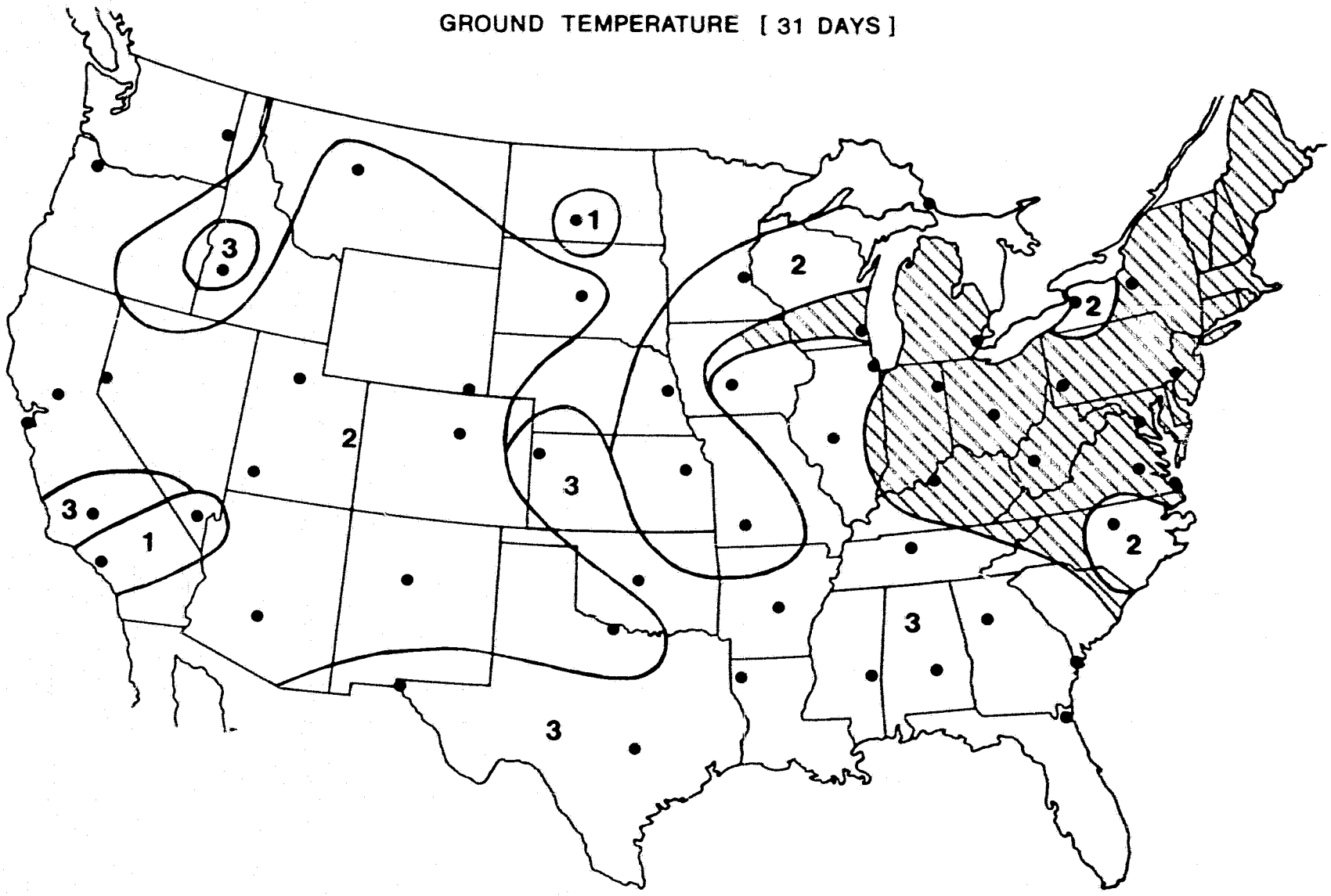

Fig. 1. Ground temperatures over the U.S. for an ensemble of eleven integrations of 31 days each. The lowest order autoregressive process that is consistent with the data is indicated. The hatching shows regions where white noise, first-, second-, and third-order processes are not consistent with the data.

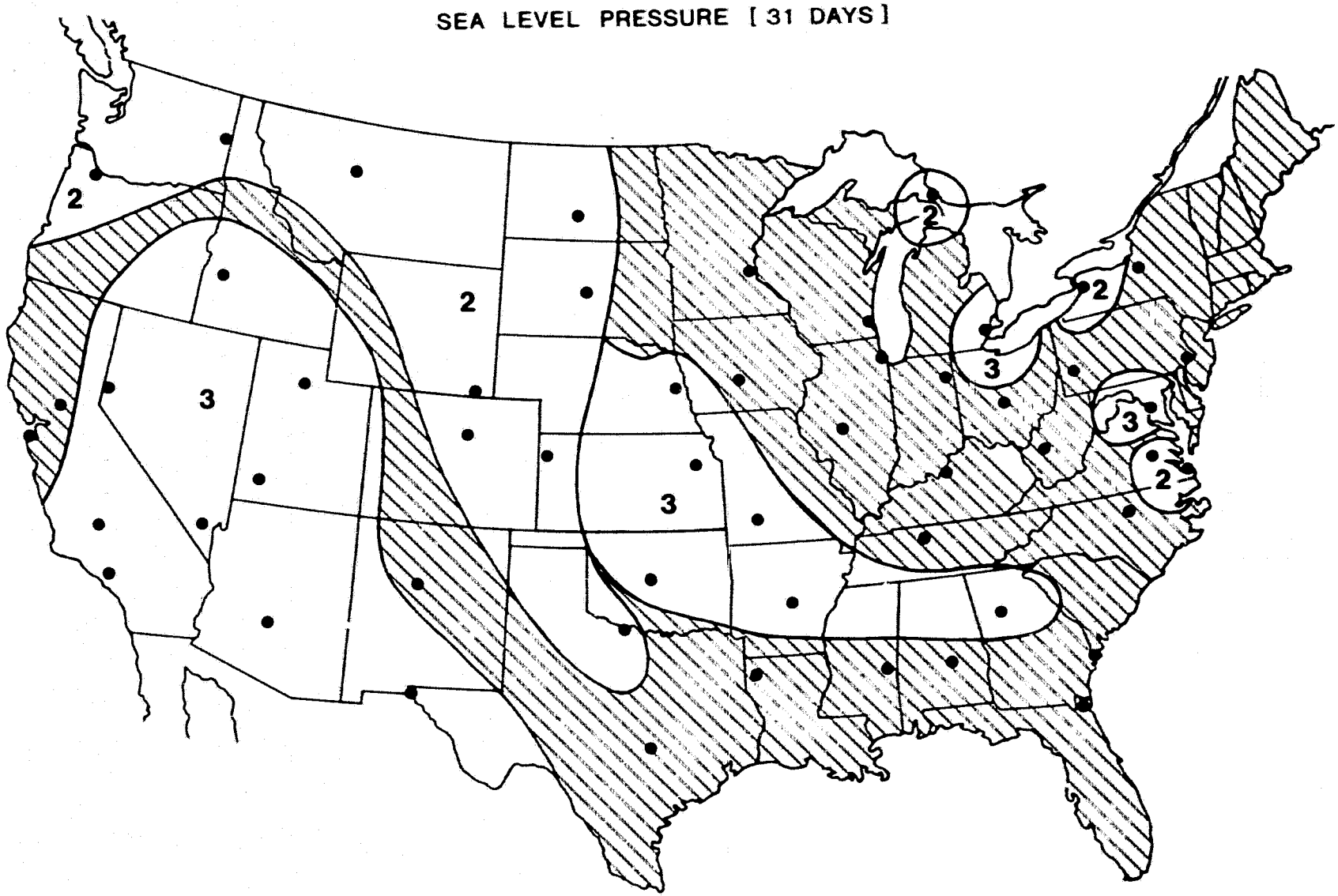

Fig. 2. Sea level pressure over the U.S. for an ensemble of eleven integrations of 31 days each. The lowest order autoregressive process that is consistent with the data is indicated. The hatching shows regions where white noise, first-, second-, and third-order processes are <u>not</u> consistent with the data.

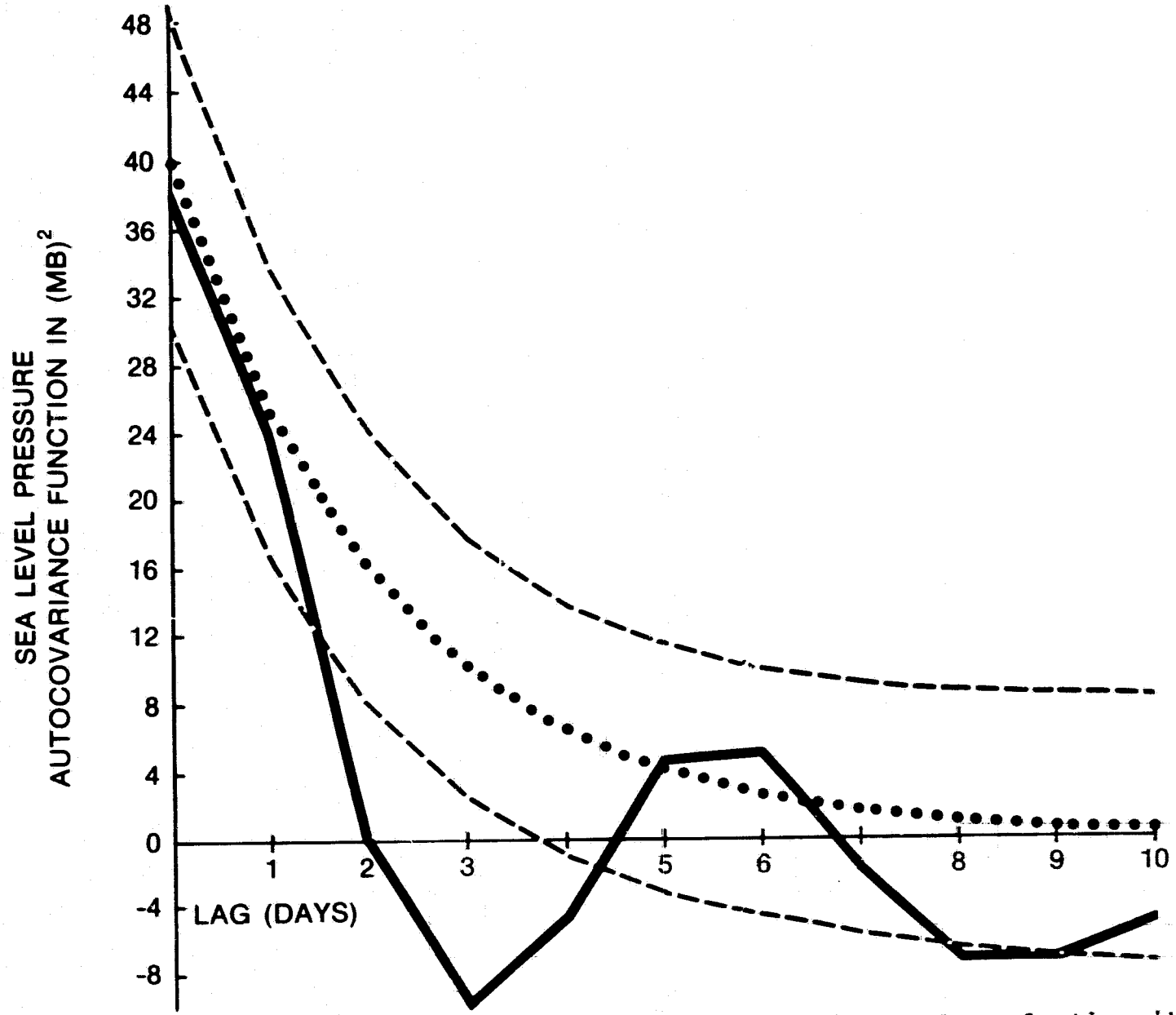

Fig. 3. Autocovariance functions. The solid line is the autocovariance function obtained directly from the data for Austin, Texas. The dotted line shows the autocovariance function of the "best fit" first-order process. The dashed lines are confidence limits on the first-order autocovariance function and depend on the sample size.

good agreement with the data. For larger lags, the sharp drop in the autocovariance function and subsequent oscillation seen in the data are not present in the first-order process. The tendency for the observed autocovariance to become negative quite rapidly is fairly general, and explains why the first-order process is not consistent with the data. Figs. 4 and 5 show the autocovariance functions of the "best fit" second- and third-order processes. Since these processes can describe damped oscillations, they are much more consistent with the data.

Two conclusions are suggested by these results. First, it may be misleading to employ simple stochastic model processes (e.g., a Markov process) in explaining meteorological data (in this case climatic noise) because of the variation in stochastic properties with geographical region. Second, a possibility arises that for some regions none of the very simple univariate processes are consistent with observational or numerically simulated data. In these cases, it may be necessary to use more sophisticated models, in which the variable in question may depend on more of its own past history than the previous two observations (high-order autoregressive processes), on its value at other locations, or even on the values of other dynamically related variables (multivariate processes).

References

Gilman, D. L., F. J. Fuglister, and J. M. Mitchell, Jr., 1963: On the power spectrum of "red noise." J. Atmos. Sci., 20, 182-184.

Jenkins, G. M., and D. G. Watts, 1968: Spectral Analysis and Its Applications, Holden-Day, publ., 525 pp.

Leith, C. E., 1973: The standard error of time-average estimates of climatic means. J. Appl. Meteor., 12, 1066-1069.

_____, 1975: The design of a statistical-dynamical climate model and statistical constraints on the predictability of climate. The Physical Basis of Climate and Climate Modelling, GARP Publication Series No. 16, Appendix 2.2.

Madden, R. A., 1976: Estimates of the natural variability of time-averaged sea level pressure. Mon. Wea. Rev., 104, 942-952.

_____, and D. J. Shea, 1978: Estimates of the natural variability of time-averaged temperatures over the United States. Mon. Wea. Rev., 106, 1695-1703.

Straus, D., and M. Halem, 1979: Autoregressive analysis of climatic noise. In preparation to be submitted to Mon. Wea. Rev.

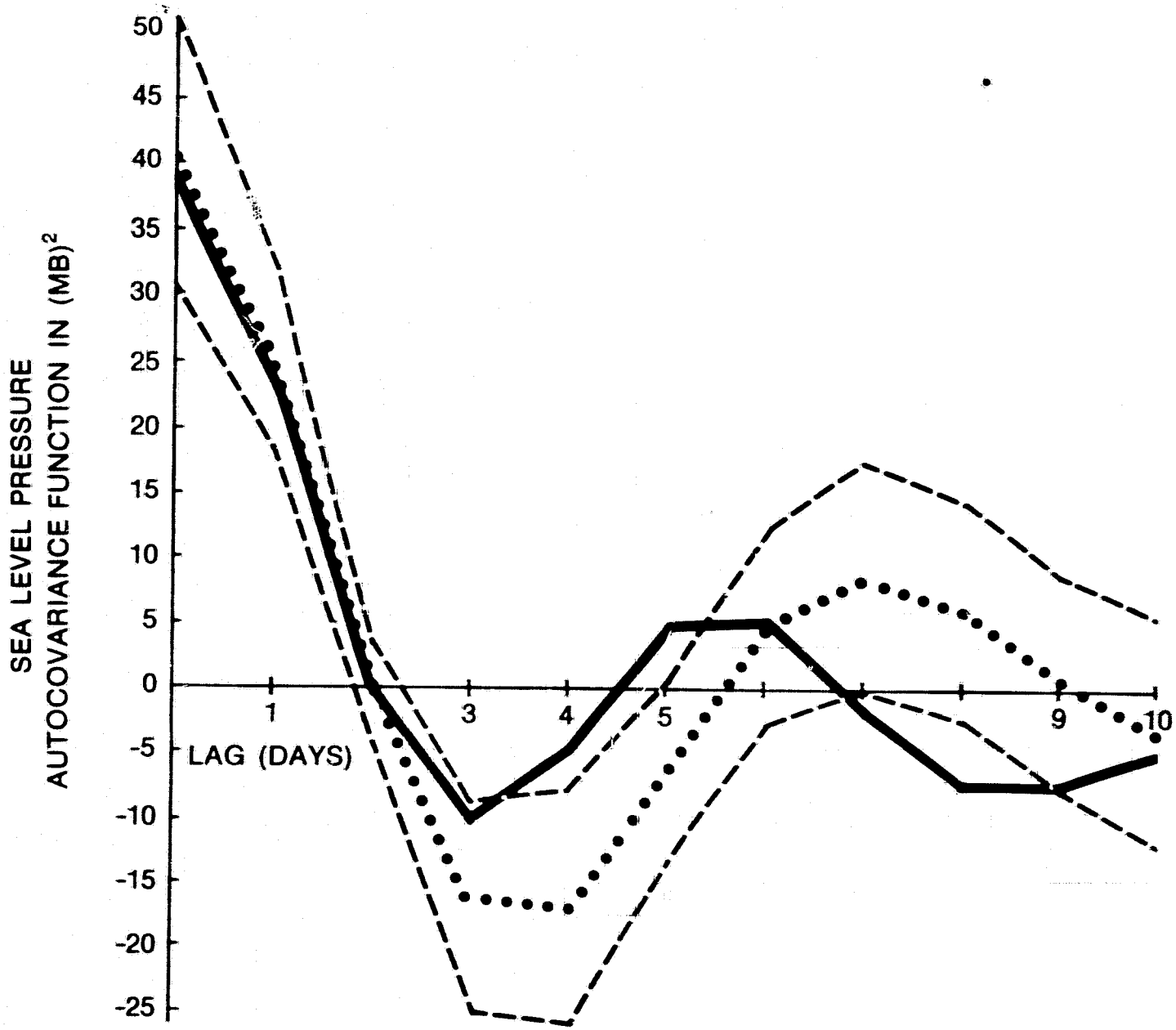

Fig. 4. Autocovariance functions. The solid line is the autocovariance function obtained directly from the data for Austin, Texas. The dotted line shows the autocovariance function of the "best fit" second-order process. The dashed lines are confidence limits on the second-order autocovariance function and depend on the sample size. (See Straus and Halem, 1979.)

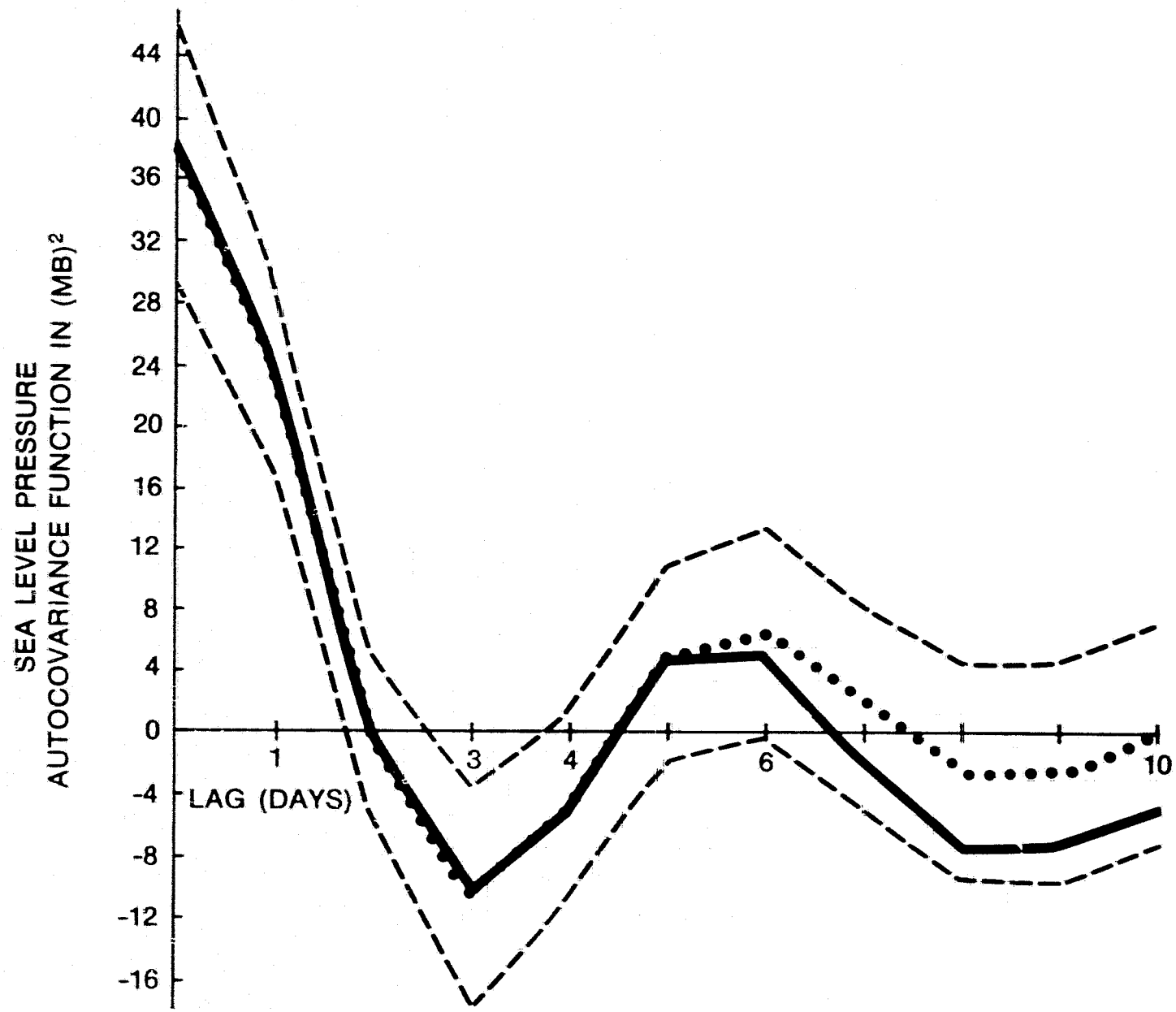

Fig. 5. Autocovariance functions. The solid line is the autocovariance function obtained directly from the data for Austin, Texas. The dotted line shows the autocovariance function of the "best fit" third-order process. The dashed lines are confidence limits on the third-order autocovariance function and depend on the sample size. (See Straus and Halem, 1979.)

SIMPLE CLIMATE MODELS OF GLACIATION CYCLES

(M. Ghil, K. Bhattacharya, C. Crafoord, E. Källén, and H. LeTreut)

An Energy-Balance Model with Time-Lagged Albedo

The long-term energy balance of the climatic system can be expressed mathematically by a nonlinear partial differential equation (PDE) of parabolic type, with latitude x as the spatial variable and temperature T as the dependent variable. The crucial nonlinearity, appearing in the source term of the equation, is related to the physical dependence of global reflectivity, called albedo, on temperature, $\alpha = \alpha(x,T)$. The function $\alpha(x,T)$ is assumed to be piecewise linear in T at constant x, leading to the existence of multiple equilibrium solutions (Ghil, 1976); some of these can be identified with possible climates of the earth. The delay τ introduced (Ghil and Bhattacharya, 1979) represents the adjustment time of α to T, $\alpha = \alpha(x,T(x,t-\tau))$.

The number of equilibria and their stability is studied as a function of the normalized average intensity of solar radiation, μ. The behavior of time-dependent solutions is studied as a function of the delay τ. Bifurcation to stable periodic solutions (Bhattacharya, 1979; Ghil and Bhattacharya, 1979) occurs with increasing τ, followed by the appearance of multi-periodic and quasi-chaotic solutions (Bhattacharya, 1979; Bhattacharya and Ghil, 1978). This behavior seems to argue for the possibility of causes internal to the climatic system playing a role in glaciation cycles: no periodic external forcing is necessary in order to obtain stable oscillations of the system on the time scales involved.

Energy-Balance Models with Ice-Sheet Dynamics and with Geodynamics

In this work, the energy-balance equation for T is simplified by eliminating spatial dependence altogether. On the other hand, the complexity of the model is increased by adding an equation for the latitudinal extent of the ice sheets, yielding a system of two coupled, nonlinear autonomous ordinary differential equations (ODEs): $c_1\dot{T} = f(T,\ell)$, $c_2\dot{\ell} = g(T,\ell)$. This system has multiple critical poin $f = 0 = g$, one of which can be identified with the present climate of the earth. This point is a stable focus for a certain range of parameter values. As the parameter c_2/c_1, corresponding to the delay in the simple partial differential equation (PDE) model, is increased, the focus becomes unstable, giving birth to a stable limit cycle (Källén et al., 1978). The amplitudes, period and phase difference between T(t) and $\ell(t)$ for the periodic trajectories are of the order of magnitude given by paleoclimatological data on glaciation cycles (Källén et al., 1979).

The model is being further refined to include the viscoelastic response of the lithosphere (crust) and asthenosphere (upper mantle) to the load of variable size ice sheets (Ghil et al., 1979). The system under study then becomes: $c_1\dot{T} = f(T,\ell)$, $c_2\dot{\ell} = g'(T,\ell,\zeta)$, $c_3\dot{\zeta} = h(\ell,\zeta)$. Its critical points correspond to those of the preceding system, but their stability properties differ (Le Treut and Ghil, 1980). It is hoped that the oscillations of the latter model will have characteristics in even better agreement with the paleoclimatological record than the ones previously discussed.

References

Bhattacharya K., 1979: A Study of Almost-Intransitivity as a Possible Cause of Terrestrial Climate Changes. Ph.D. Thesis, Physics Department, Columbia Univ., New York.

_____, and M. Ghil, 1978: An energy-balance model with multiply-periodic and quasi-chaotic free oscillations. Evolution of Planetary Atmospheres and Climatology of the Earth, Centre Nat'l. d'Etudes Spatiales, Toulouse, France, 299-310.

Ghil, M., 1976: Climate stability for a Sellers-type model. J. Atmos. Sci., 33, 3-20.

_____, and K. Bhattacharya, 1979: An energy-balance model of glaciation cycles. Report of the JOC Study Conference on Climate Models: Performance, Intercomparison and Sensitivity Studies, GARP Publ. Series No. 22, 886-916, WMO, Geneva, Switzerland.

_____, E. Källén, C. Crafoord, and H. Le Treut, 1979: Simple climate models, II: systems of nonlinear ODEs. Preprint, SIAM fall meeting, Denver, Colorado, November.

Källén, E., C. Crafoord, and M. Ghil, 1978: Free oscillations in a coupled atmosphere-hydrosphere-cryosphere system. Evolution of Planetary Atmospheres and Climatology of the Earth, 285-298, Centre Nat'l. d'Etudes Spatiales, Toulouse, France.

_____, _____, and _____, 1979: Free oscillations in a climate model with ice-sheet dynamics. J. Atmos. Sci., in press.

Le Treut, H., and M. Ghil, 1980: An energy-balance model with the dynamics of ice sheets and of isostatic sinking. Tech. Note, Laboratoire de Météorologie Dynamique, ENS, Paris, in preparation.

SIMULATION OF THE ATMOSPHERIC GENERAL CIRCULATION ON MARS AND COMPARISONS WITH SPACE-PROBE OBSERVATIONS: A STUDY IN PLANETARY CLIMATOLOGY*

(Y. Mintz)

The atmospheric general circulation on Mars is simulated with a numerical model, which differs from the one used by Leovy and Mintz (1969, paper I) in that it takes into account the planet's large-scale surface topography. The new model also has somewhat greater horizontal and vertical resolutions, improved formulations for calculating the solar and infrared radiative heating, and a better way of parameterizing the vertical convective heat transfer within the planetary boundary layer. The simulation is for the time of southern hemisphere winter, which is the time of the Viking space-probe landings.

In this simulation, the large-scale surface topography produces two kinds of forced standing waves: quasi-barotropic Rossby waves, which are kinematically forced by the topography upon the strong mid-latitude zonal flow of the winter hemisphere; and monsoon-like baroclinic circulations, which are thermally forced by strong heating over the summer hemisphere regions of high surface elevation.

As in I, transient eastward moving waves are produced in the middle and high latitudes of the winter hemisphere. The dominant period and amplitude of these waves, as shown by the surface pressure and wind variations, agree with the Viking lander observations of the winter season transient waves: a period of about 3 days, root mean square (rms) surface pressure variation of about 0.15 mb, and rms surface meridional wind variation of about 5 m s^{-1} (see Fig. 1). The dominant zonal wave number and phase speed of the transient waves also agree with what can be inferred from the Viking data: zonal wave numbers in the range 4 to 6, and phase speeds of the order 15 to 20 m s^{-1}.

The zonally and time-averaged fields of temperature and zonal wind, the mean meridional mass circulation, and the extent of the CO_2 surface ice cap, closely resemble those found in I, except for differences attributable to a southern hemisphere as against a northern hemisphere winter season. These features, therefore, do not depend on the presence or absence of surface topography, nor are they sensitive to the differences in the radiative and convective heating formulations of the two models. Both simulations show small horizontal temperature gradients and large vertical temperature gradients from the summer pole to the tropics of the winter hemisphere, a narrow zone of large horizontal temperature gradient and small vertical temperature gradient in the mid-latitudes of the winter hemisphere, and a nearly three-dimensionally isothermal state of the atmosphere over the winter polar cap. Both show a broad and intense thermally direct cell of mean meridional mass circulation centered on the winter side of the equator, and a narrow and weak thermally indirect cell on the polar side of the mid-latitude zone of large horizontal temperature gradient. In the winter hemisphere mid-latitudes, there is a very strong eastward (i.e., westerly) surface zonal wind, whose

* Abstract and figures from paper by J. B. Pollack, C. B. Leovy, P. W. Greiman, and Y. Mintz, which is being submitted to J. Atmos. Sci.

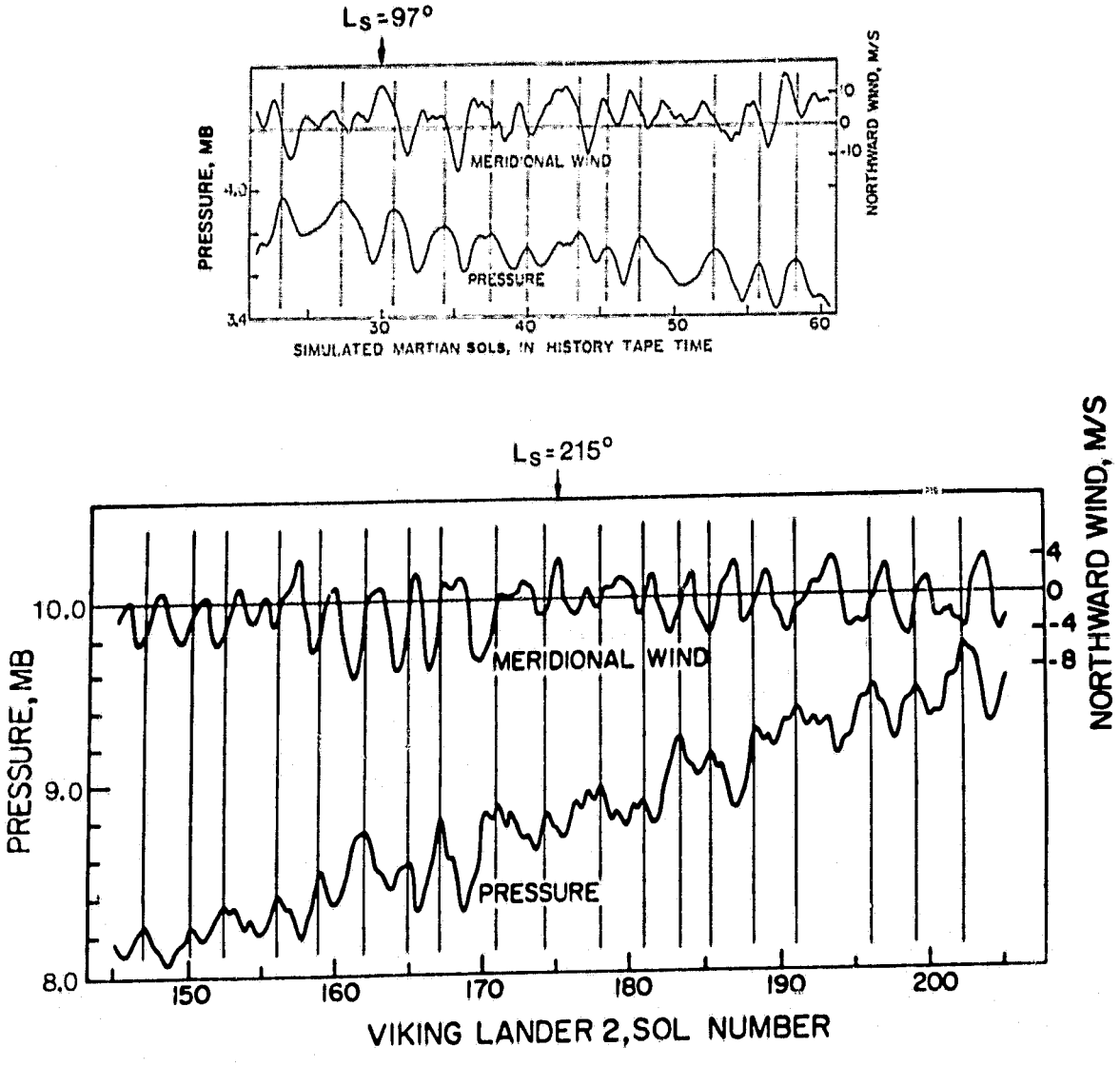

Fig. 1. Top panel: Simulated surface pressure, and simulated meridional wind component at $\sigma = 0.89$ (approximate height 0.8 km), at 120W, 50S in southern winter.

Bottom panel: Viking Lander 2 observed surface pressure, and observed meridional wind component at 1.6 m height, at 225W, 48N in northern winter.

maximum (15 m s^{-1}) is south of the latitude of the strongest thermally indirect mean meridional circulation. The vertical shear of the zonal wind, as expected, has its maximum where the poleward temperature gradient is maximum and this, together with the surface zonal wind, determines the location and intensity of the upper level mean eastward jet stream (85 m s^{-1} at 42N). Within the tropics, in both hemispheres, the surface zonal winds are westward; decreasing in intensity with height on the winter side of the equator and increasing in intensity with height on the summer side of the equator. Between the tropics and the pole of the summer hemisphere, there are several bands of alternating eastward and westward mean zonal winds, whose maximum magnitudes are about 10 m s^{-1} (see Fig. 2).

The zonally and time-averaged simulated temperatures are in good agreement with the Mariner 9 remote infrared temperature soundings and with the Viking entry temperature measurements, except that the simulated lapse rates are larger than the observed ones. This may be because the model neglects the absorption of solar radiation by the dust in the Martian atmosphere (see Fig. 3).

The simulation shows a large rate of globally averaged surface pressure fall (0.011 mb sol^{-1}) due to the condensation of atmospheric CO_2 onto the surface in the winter polar region; and this agrees very closely with the Viking Lander surface pressure measurements.

The simulated atmospheric heat transports are very large per unit atmospheric mass; but, because the mass per unit column of atmosphere is very small, the total atmospheric heat transports are small. Moreover, on the poleward side of the boundary of the condensing CO_2 polar cap, much of the poleward eddy heat transport is compensated by the equatorward heat transport of the indirect mean meridional circulation, a circulation which is mechanically forced by the transient waves. Consequently, the total poleward heat transport by the atmosphere does not balance the radiative cooling of the winter polar region and, therefore, it does not keep the temperature of that region from falling to the CO_2 frost point. The polar cap of CO_2 ice that forms on the surface, in the simulation, reaches to latitude 39S. This is within about 1° of the boundary of the observed surface ice cap.

The CO_2 surface condensation produces a net mass flux toward the condensing polar cap; and this produces a net eastward Coriolis torque, with its maximum at the edge of the condensing polar cap. It is this torque, together with the low-level eastward torque of the eddy-driven indirect mean meridional circulation, which determines the location and the great strength of the winter mid-latitude eastward surface winds.

Reference

Leovy, C. B., and Y. Mintz, 1969: Numerical simulation of the atmospheric circulation and climate of Mars. J. Atmos. Sci., 26, 1167-1190.

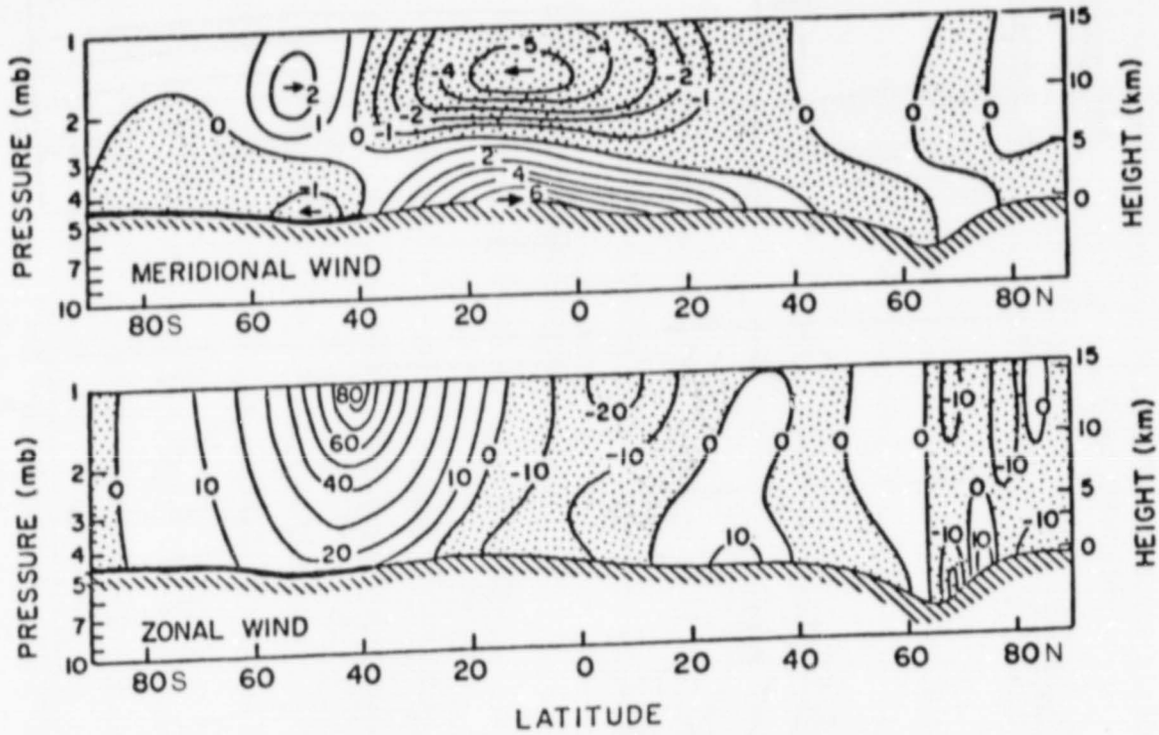

Fig. 2. Meridional cross sections of the simulated zonally and time-averaged winds (m/s). Heavy line on the surface shows the simulated surface ice cap.

Top panel: Meridional wind component (positive northward).

Bottom panel: Zonal wind component (positive eastward).

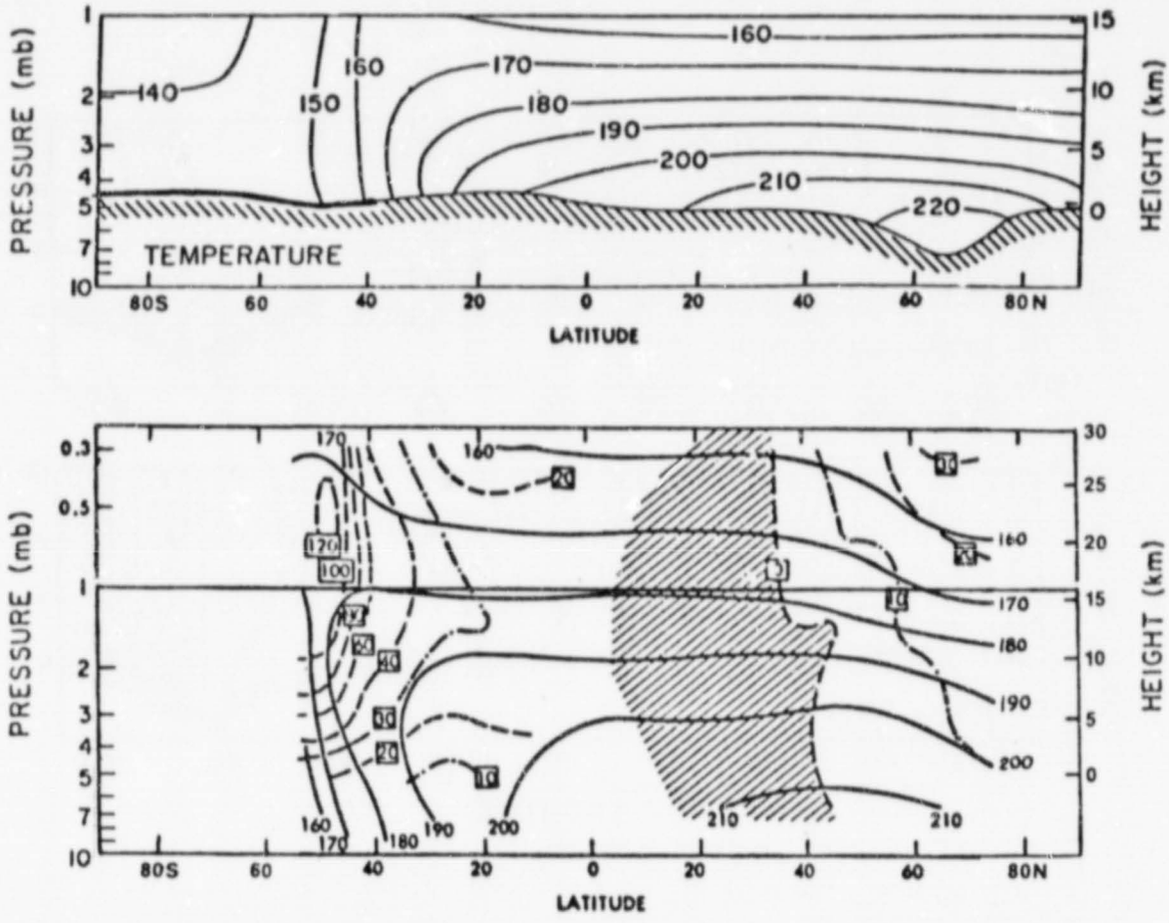

Fig. 3. Meridional cross sections of the zonally and time-averaged temperature (°K).

Top panel: Simulated temperature, in southern mid-winter.

Bottom panel: Temperature derived from Mariner 9 infrared soundings, in southern late fall-early winter.

The dashed lines and boxed-in numbers show the calculated geostrophic zonal wind (m/s) when the surface wind is neglected.

The horizontal line, at p = 1 mb, indicates where the general circulation model has its upper boundary.

IV. OCEAN/AIR INTERACTIONS

ATLANTIC OCEAN SEA SURFACE TEMPERATURE ANOMALIES

(J. Calman)

Since about three-fourths of the earth's surface is covered by water, any attempt to forecast the state of the atmosphere (or ocean) must take into account the physics of the air-sea interaction processes. The effect of this interaction is very strong in the upper hundred meters or so of the ocean where the temperature and depth of the "mixed layer" (so called because the temperature is constant from the sea surface to the bottom of the mixed layer) where the rapid fluctuations of sea surface temperature (SST) reflect the changes in the balance of turbulent fluxes of heat, mass, and momentum across the air-sea interface.

In a recent study, Bunker (1976) reported measurements by ships of sea surface temperature, wind, humidity, and cloud cover were collected from the archives of the National Climatic Center. Using bulk transfer formulas for the parameterization of turbulent fluxes, Bunker studied the annual average (from 1948-1972) components of the heat budget of the Atlantic Ocean. Subsequently, Bunker and Goldsmith (1979) have made available to other investigators their computed monthly values over the entire 25-year period of the components of the heat budget of the Atlantic Ocean. This data set has been obtained at the Laboratory for Atmospheric Sciences (GLAS) Modeling and Simulation Facility (GMSF), at NASA Goddard Space Flight Center, and is being used to study the behavior of SST anomalies in the Atlantic Ocean. It has been recognized that the usual ad hoc practice of specifying the mean monthly SST as a time-dependent boundary condition for an atmospheric general circulation model is an inadequate model of the air-sea interaction. In an effort to more correctly account for the physics of this interaction, ocean mixed-layer models, which describe changes in the mixed-layer properties (temperature, depth, velocity) as functions of the mass, momentum, heat, and turbulent energy budgets of the layer, have been developed. Several versions of the GMSF ocean mixed-layer model have been described elsewhere (Cane and Schopf, 1978; Fung and Cane, 1978a, b).

The 25 years of monthly measurements referred to above are being used to improve our understanding and modeling of the mixed layer in two ways. First, a descriptive study is underway to see how, on the basis of the measurements alone, the observed SST and wind stress, clouds, humidity, and calculated heating (from the bulk transfer calculations of Bunker) are statistically related to each other. Second, a study of the accuracy of the GMSF ocean mixed-layer model is being conducted. Previous comparisons of the predictions of the ocean mixed-layer model with observations have only been possible using the mean observed forcing and the mean observed response. It is of great interest for the purpose of constructing an interactive air-sea general circulation model to see how well the mixed-layer model predicts the observed anomalies (i.e., the departure from the mean) of SST given the observed anomalies in the forcing functions (heat, wind, stress). With the new data, such a test is possible and is now underway.

The annual and monthly means of SST, heating, and wind stress magnitude have been described (Bunker, 1976). The corresponding anomalies for January 1970 are shown in Figs. 1a-c. The time series of these anomalies at 35N, 65W are shown in Figs. 2a-c. It is surprising that correspondence between the three spatial patterns in Fig. 1 and between the three time variations in Fig. 2 is not more apparent. If the heat absorbed by the ocean is unusually large and the wind stress is unusually weak, it is expected that the SST will increase. It can be deduced from Fig. 1, however, that this relationship is not generally true. Theory suggests that it is the rate of change of SST that responds to changes in heating, rather than the SST itself, and this relationship is being investigated. Regions of expected strong currents do not appear to explain the differences. Another physical argument suggests that sea surface temperatures take some time to change and that, when the mixed layer deepens, it entrains cold water left behind the previous year. It is therefore expected that the ocean 'remembers' what happened at previous times. A look at the time series of Fig. 2 does not show an obvious time-lag correlation between the variables. The computed auto- and cross-correlation functions are shown in Fig. 3a for a point at 35N latitude, 65W longitude. The time scale of SST anomalies is several months, while those of heating and wind stress are less than 1 month and are unresolved in these data. (When linear trends are removed from the anomaly time series, the correlation functions approach zero at long lag times.) The cross-correlation of SST and heating (Fig. 3b) shows that anomalous strong heating will lead to a warmer SST for several months, while a warm SST has no correlation with future heating. Similarly, the cross-correlation of wind stress with SST shows that strong winds will cause a cooler ocean for several months while a cool SST gives no knowledge of future winds. The cross-correlation of heating and wind shows no relationship between the two quantities except at zero lag where the high correlation is an artifact due to the use of wind in the bulk transfer formula used for computing the heating. Spatial variations of these correlations are being studied to identify special regions. An important test of the heat balance equation for the mixed layer is being made by computing the correlation of the rate of change of temperature with heating and wind stress.

References

Bunker, A. F., 1976: Computations of surface energy flux and annual air-sea interaction cycles of the North Atlantic Ocean. Mon. Wea Rev., 104, 1122-1140.

_____, and R. A. Goldsmith, 1979: Archived time-series of Atlantic Ocean meteorological variables and surface fluxes. Tech. Report WHOI-79-3, Woods Hole Oceanographic Institution, Woods Hole, Massachusetts 02543.

Cane, M., and P. Schopf, 1978: A two-layer dynamic and thermodynamic model of the upper ocean. NASA Tech. Memo. 80253, Atmos. and Oceano. Res. Rev.-1978, 107-110, NASA Goddard Space Flight Center, Greenbelt, Maryland.

Fung, I., and M. Cane, 1978a: A dynamic model for the oceanic mixed layer: non-advective version. Ibid., 111-114.

_____, 1978b: A dynamic model for the oceanic mixed layer: advective version. Ibid., 115-116.

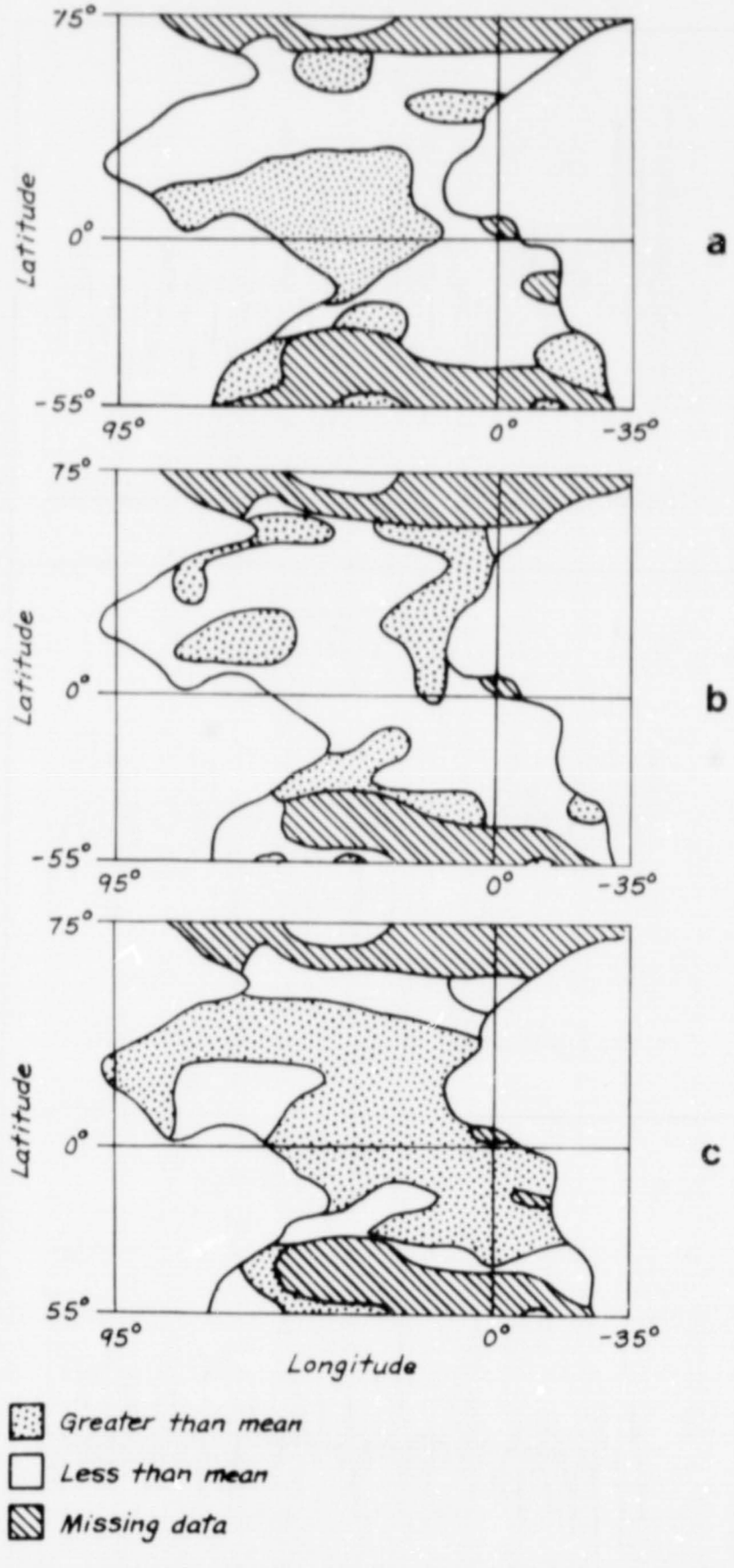

Fig. 1. Anomalies of a) SST, b) heating, and c) wind stress magnitude for January 1970.

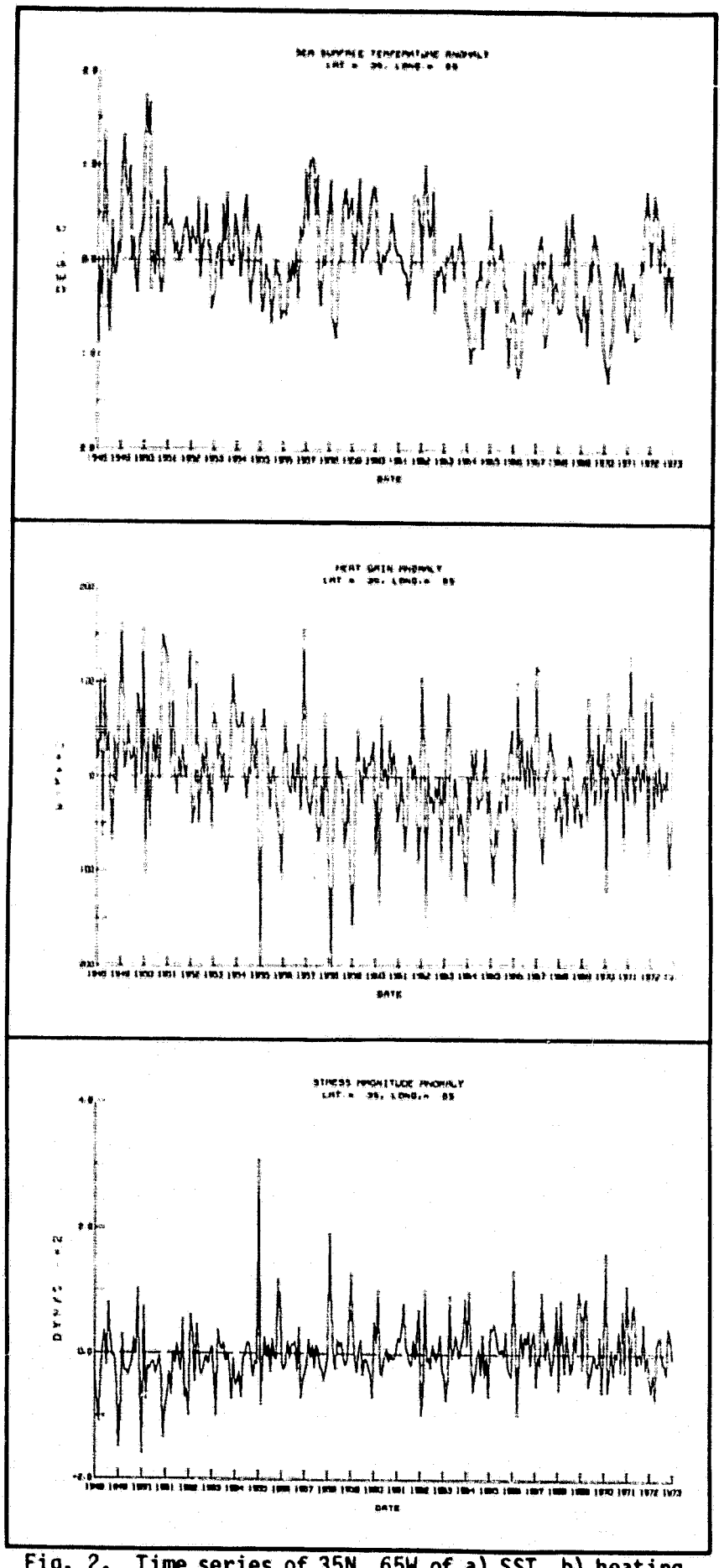

a

b

c

Fig. 2. Time series of 35N, 65W of a) SST, b) heating, and c) wind stress magnitude from 1948-1972.

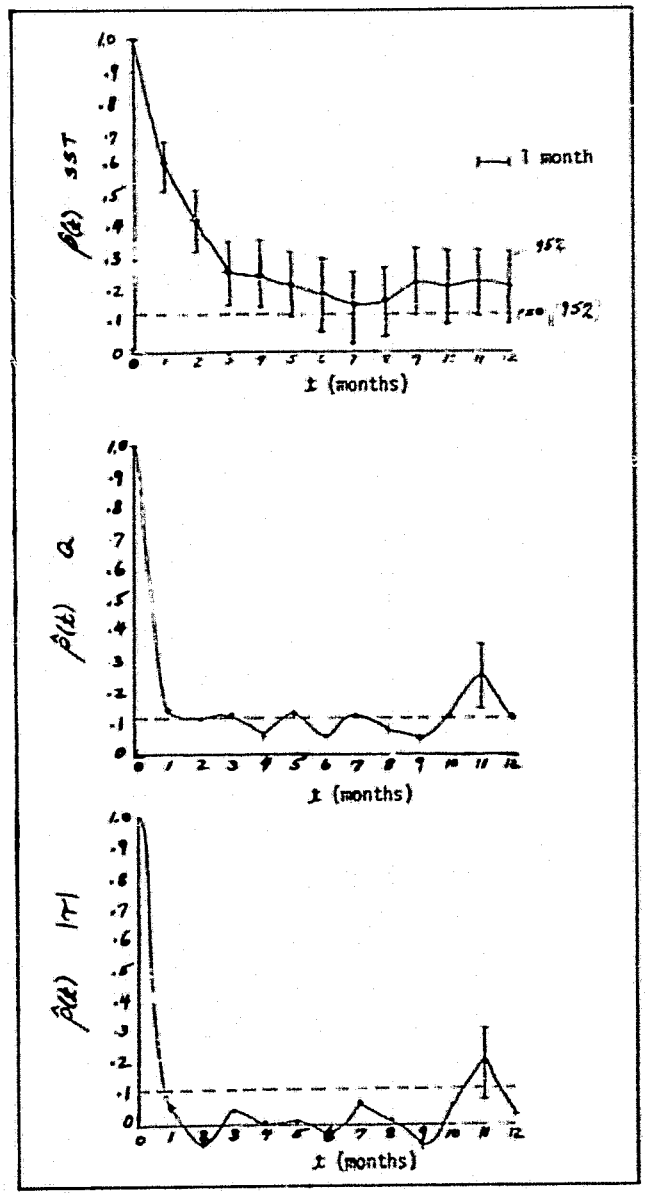

Fig. 3a. Autocorrelations of SST, heating, and wind stress at 35N, 65W.

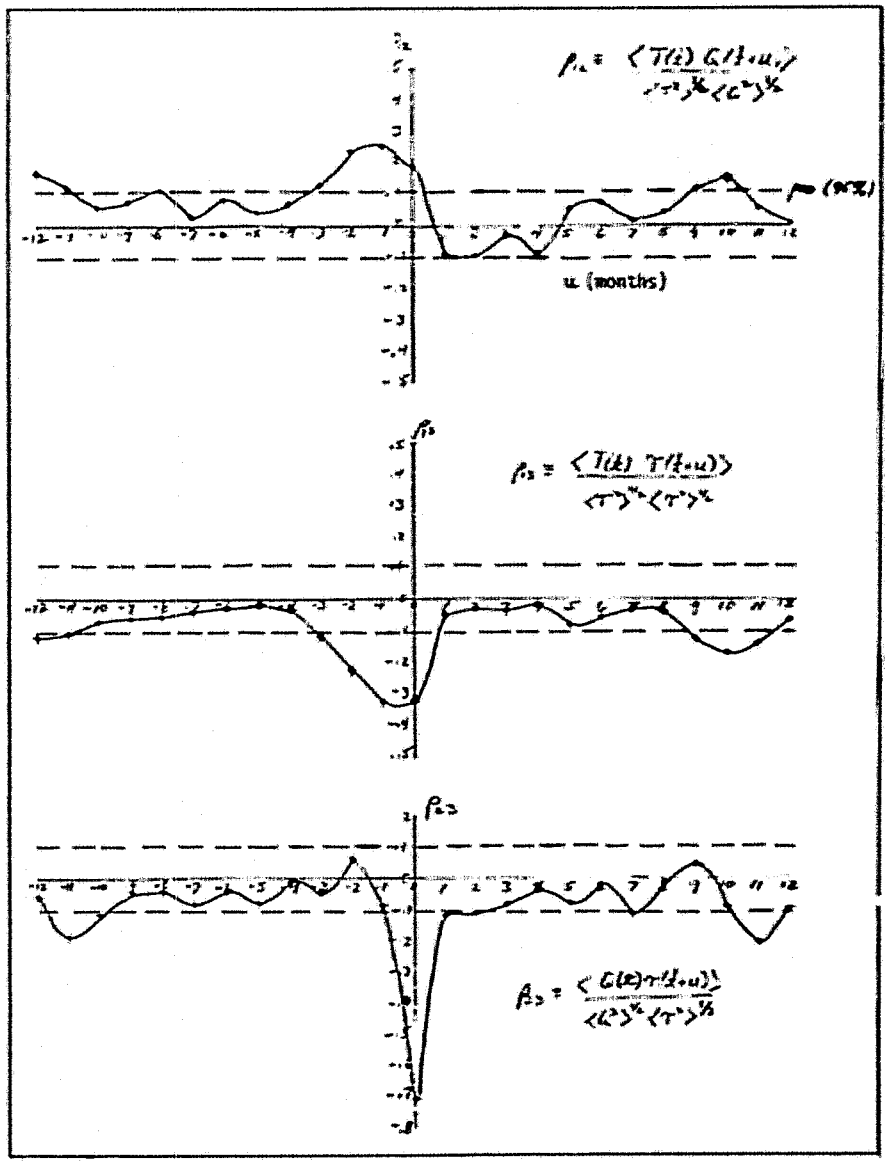

Fig. 3b. Cross-correlations of SST, heating, and wind stress at 35N, 65W.

ANALYSIS OF THE SURFACE HEAT BALANCE OVER THE WORLD OCEAN

(S. Esbensen)

During the period of the present NASA grant with Oregon State University, the major accomplishment has been the analysis of approximately 25 years of ocean weather ship data at representative locations in the North Atlantic and North Pacific Oceans (see Fig. 1). A conclusion has been reached that monthly averaged surface meteorological data can provide heat flux estimates that are within 25 percent of the monthly mean heat flux estimates calculated from each observation. The weather ship data were obtained on magnetic tapes (in TDF-11 format) from the National Climatic Center, Asheville, North Carolina, and the Scripps Institution of Oceanography, La Jolla, California.

To parameterize the heat fluxes, the bulk aerodynamic equations were used which are

$$S_o = \rho c_p C_T V_a (T_s - T_a) \qquad (1)$$

and

$$LE_o = \rho L C_E V_a (q_s - q_a) \qquad (2)$$

where S_o and LE_o are the surface sensible and latent heat fluxes, C_T and C_E are the transfer coefficients, and V, T, and q are the wind speed, temperature, and specific humidity, respectively. The subscripts "s" and "a" refer to sea level and near-surface (here assumed to be 10 m) values of atmospheric variables, respectively. The parameters ρ, c_p, and L are the near-surface air density, the specific heat of air at constant pressure, and the latent heat of condensation or evaporation. In this study, the transfer coefficients were determined from a modified version of the parameterization proposed by Benoit (1976) who used the suggestions of Deardorff (1972).

Fig. 2 summarizes the heat flux computations for January and July. S_o and LE_o are monthly averaged values of the heat fluxes produced by substituting 3-hourly observations into Equations (1) and (2), summing all of these flux estimates within a given month over the years of record, and finally dividing by the total number of observations. $\overline{S}_o$ and $\overline{LE}_o$ are the flux estimates obtained by substituting monthly averaged wind speeds, temperatures, and humidities into Equations (1) and (2). As shown in Fig. 2, the agreement between the two methods is better than 20 percent over a wide range of heat fluxes. Furthermore, this result may also hold for individual months.

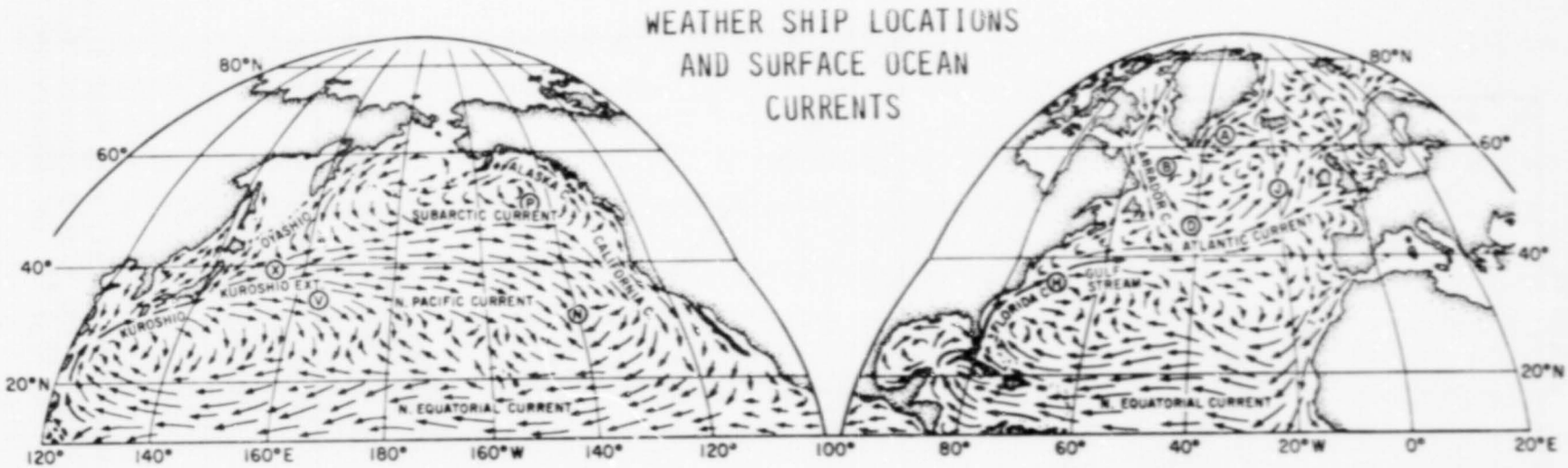

Fig. 1. Nominal ocean weather ship position.

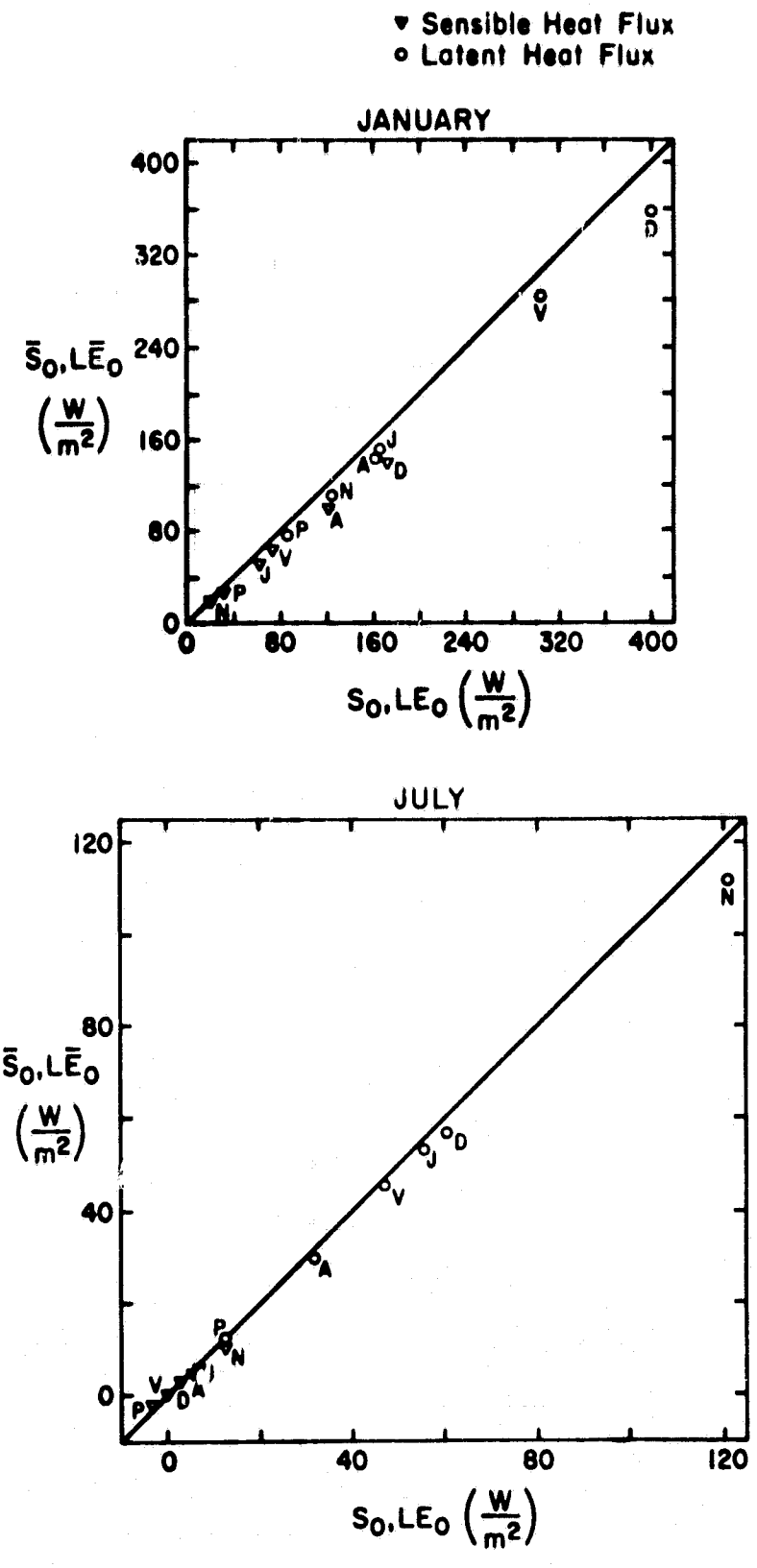

Fig. 2. A comparison of long-term monthly mean heat fluxes (S_o, LE_o) compared with heat fluxes computed from monthly mean data ($\bar{S}_o$, $L\bar{E}_o$) for (a) January and (b) July.

Fig. 3 shows the comparisons of $\overline{V_a}(\overline{T_s} - \overline{T_a})$ with $\overline{V_a(T_s - T_a)}$, and $\overline{V_a}(\overline{q_s} - \overline{q_a})$ with $\overline{V_a(q_s - q_a)}$ for twenty-three Januaries at ship D in the highly variable flux region over the North Atlantic Current. The overbars here refer to an arithmetic average of 3-hourly observations over the period of a month. Again, the agreement is remarkable. These results suggest that a combination of surface wind retrievals from satellite data and thermodynamic variables from ocean buoys may provide adequate data to monitor the monthly averaged surface heat fluxes in data sparse areas.

References

Benoit, R., 1976: A Comprehensive Parameterization of the Atmospheric Boundary Layer for General Circulation Models. NCAR Cooperative Thesis No. 39.

Deardorff, J. W., 1972: Parameterization of the planetary boundary layer for use in general circulation models. Mon. Wea. Rev., 100, 93-106.

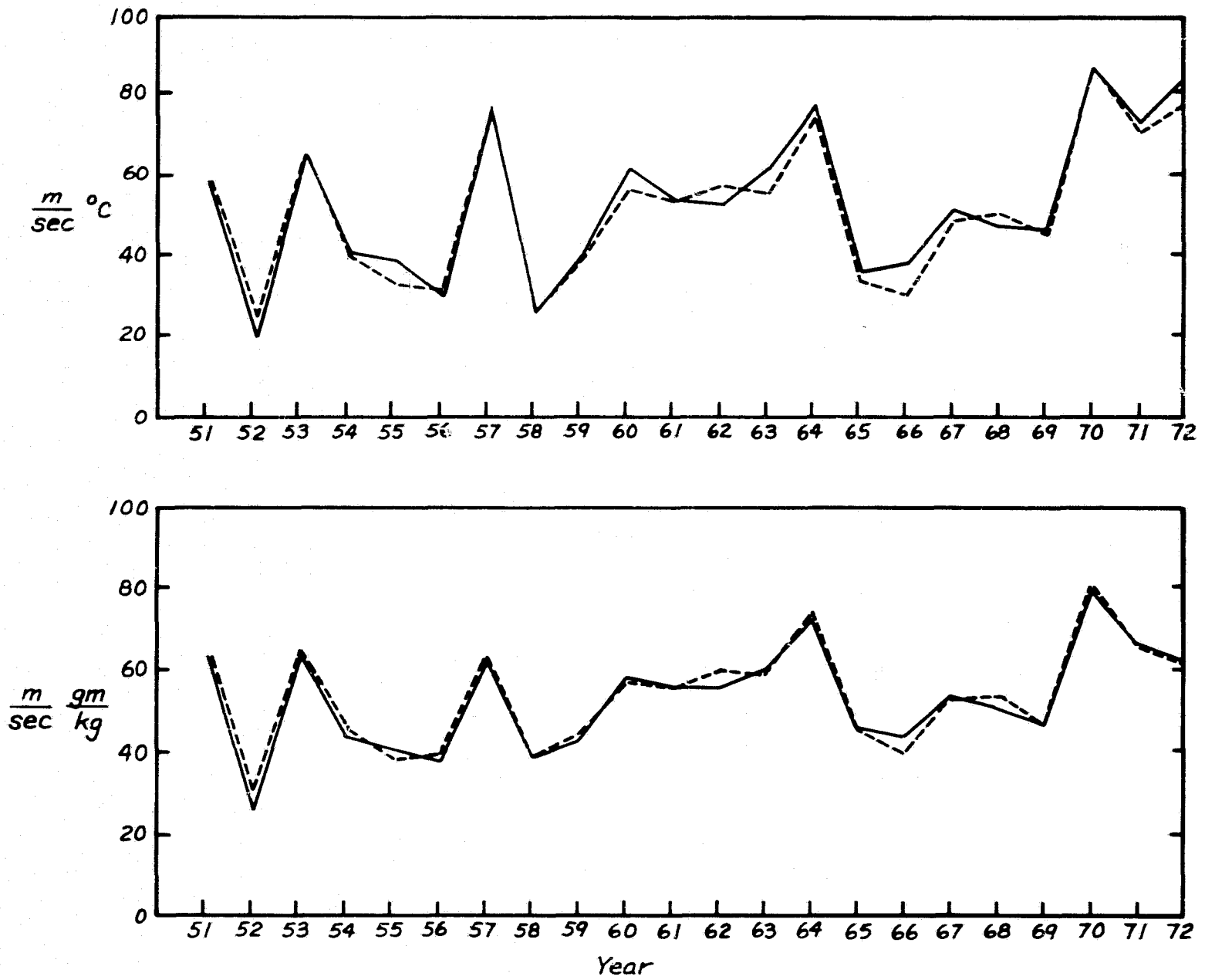

Fig. 3. Comparison of (a) $\overline{V\Delta T}$ (solid curve) with $\bar{V}\Delta\bar{T}$ (dashed curve), and (b) $\overline{V\Delta q}$ (solid curve) with $\bar{V}\Delta\bar{q}$ (dashed curve) at ship position D for successive Januaries.

RESPONSE OF A GLOBAL MIXED LAYER MODEL TO GCM FORCING

(I. Fung and M. Cane)

This study reports the continued experimentation with an ocean mixed layer model before coupling it to the atmospheric GCM.

The mixed layer model has been reported by Fung and Cane (1978). It has been shown to reasonably predict sea surface temperatures (SST) and mixed layer depths given climatological inputs of surface wind stress (τ_c) and surface heat flux (Q_c).

Climatological inputs are necessarily smooth, the value at each time step being linearly interpolated from means assumed at mid-month. Before the mixed layer model is coupled to the atmospheric GCM, it is desirable to study its response to high frequency forcing, an ideal source of which is the GCM.

The GLAS GCM has been integrated for 4 months from winter initial conditions (Halem et al., 1979). The ocean is noninteractive: SST is prescribed in time and space. From this GCM run, surface wind stress (τ) and net surface heat flux (Q) were extracted every 6 h as forcing for the mixed layer model. Due to the lack of a boundary layer in the GCM, surface winds were linearly extrapolated from levels 8 and 9 to the surface. τ was calculated from the surface winds using a drag law where the drag coefficient is a function of static stability. Q is the algebraic sum of the incident solar radiation, outgoing thermal radiation, sensible heat and latent heat of evaporation simulated by the GCM. Thus forced, the mixed layer model was integrated from climatological January initial conditions for 4 months, the duration of the GCM experiment. It is noteworthy that the mixed layer model remained stable throughout the 4 months to the high frequency atmospheric forcing.

Fig. 1 presents the zonally averaged SST departure from climatology (ΔSST) for January. A positive (negative) ΔSST means that the simulated SST is higher (lower) than the climatological value. After 1 month, ΔSST is less than 1° over most of the ocean, with the largest errors at the latitudes of the ITCZ and the roaring 40's.

The trend of SST can be deduced easily from a comparison of the GCM-derived forcing with climatology. (See Fig. 2.) The much stronger winds at all latitudes act against the excess heat flux to produce very interesting results.

North of 30N, even though $Q > Q_c$ (not enough cooling), $\tau/\tau_c \approx 3.5$. Cold water entrained from below the mixed layer dominates over the reduced heat loss from the surface. $\Delta SST < 0$, but small; the errors nearly compensate.

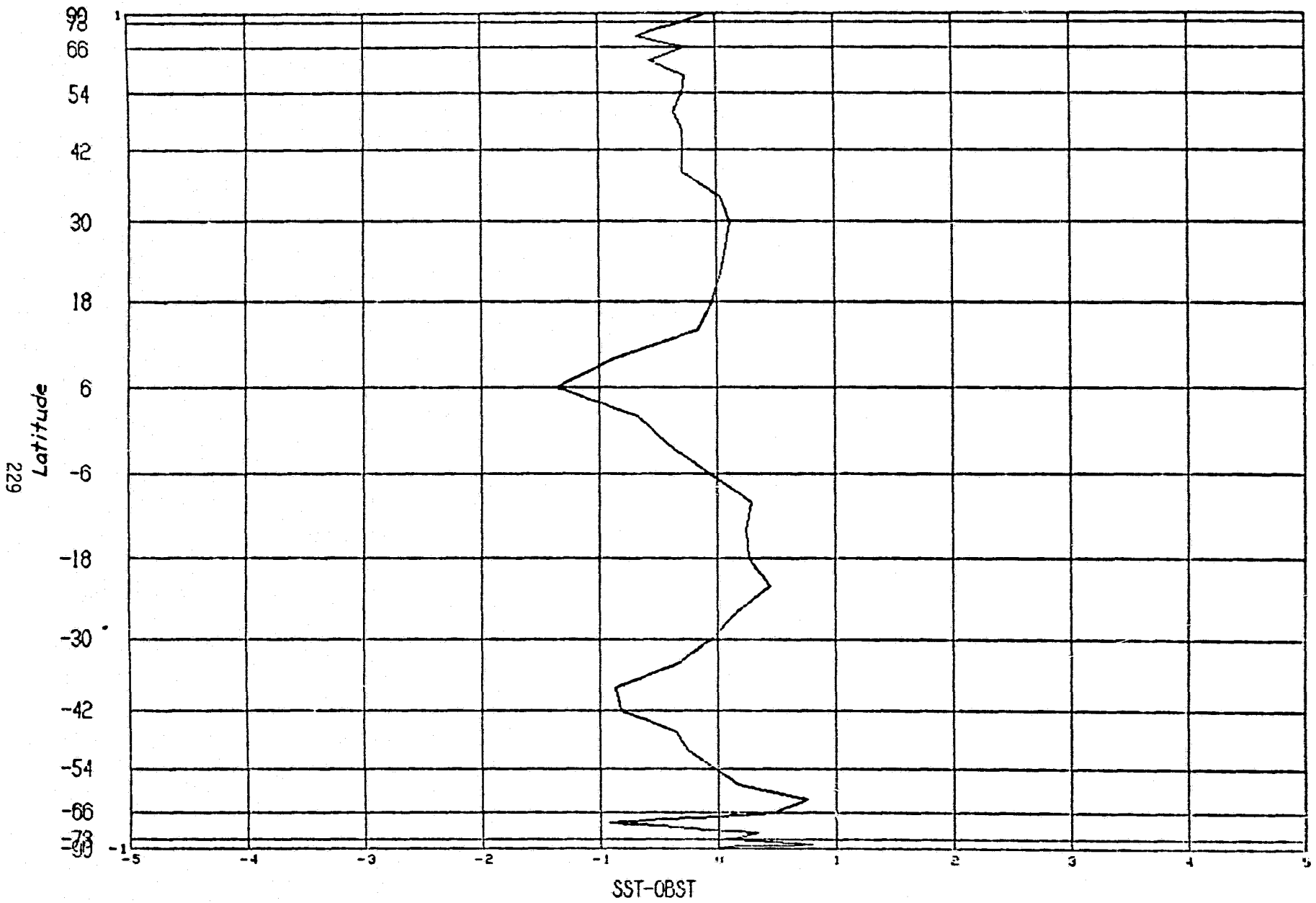

Fig. 1. Zonally averaged error in the sea surface temperature (SST) prediction after 1 month using quantities derived from a GLAS GCM winter simulation (D122), January.

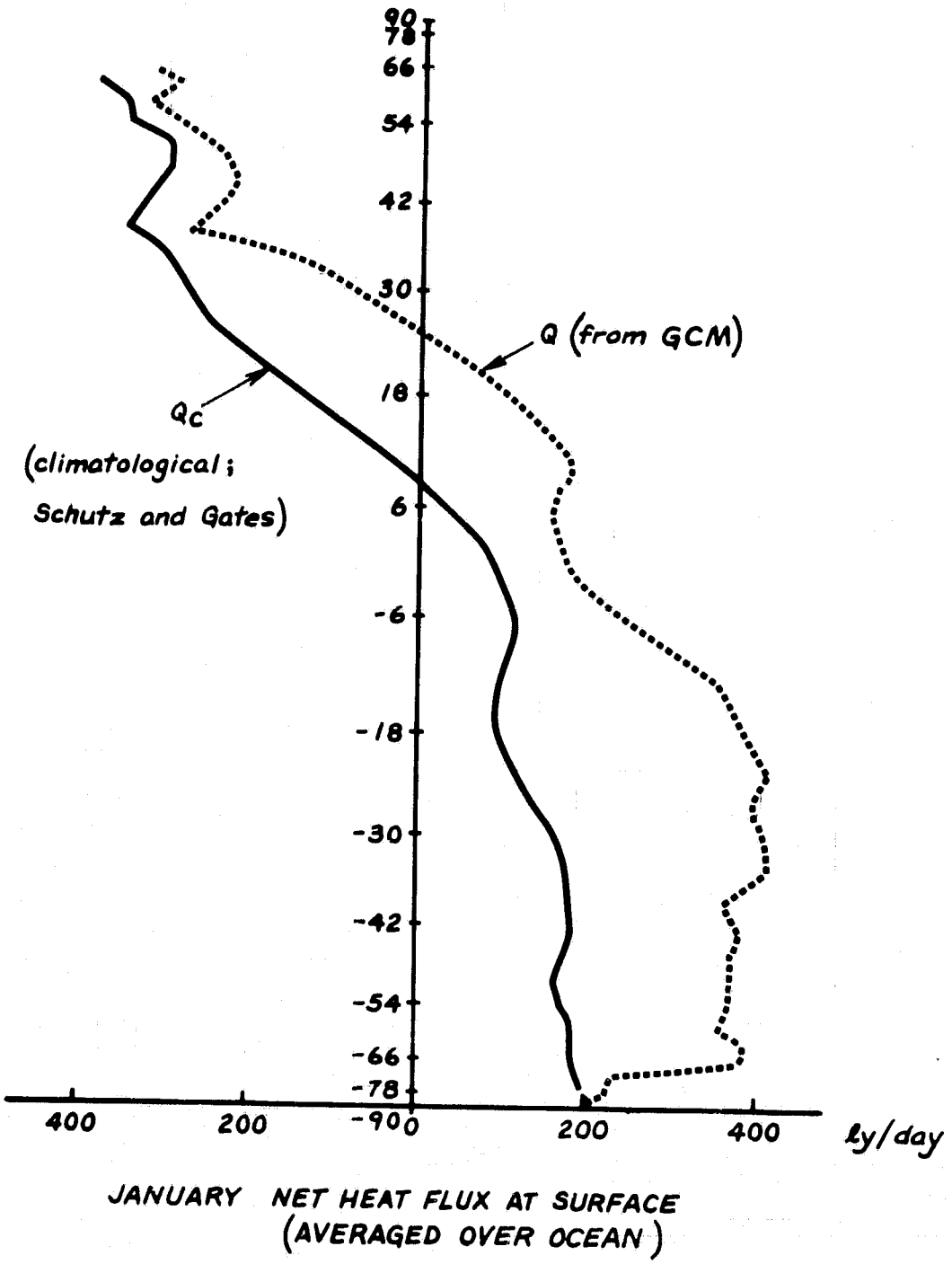

Fig. 2a. Zonally averaged (ocean points only) January heat flux from the GCM (Q) and climatology (Q_c). Climatological values from Schutz and Gates (1971).

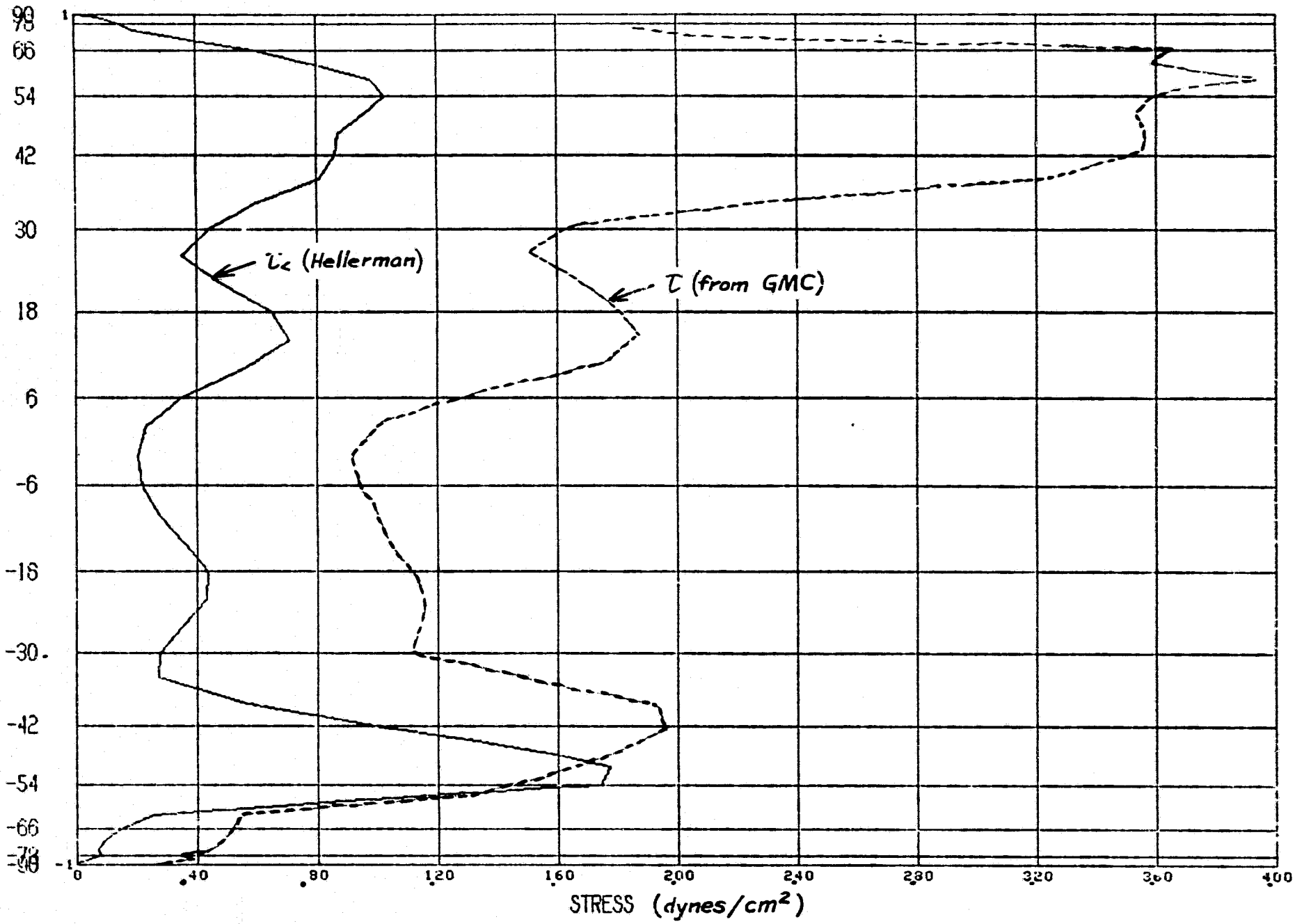

Fig. 2b. Zonally averaged January surface wind stress magnitudes over the ocean from the GCM (τ) and climatology (τ_c). Climatological values from Hellerman (private communication) based on wind roses.

Between 10N and 30N, $\tau/\tau_c \approx 2.5$., but heat is input into the ocean rather than lost from the ocean. $\Delta SST > 0$, but again the forcing errors nearly compensate.

Between 10N and 10S, $Q > Q_c$ (slight warming), $\tau / \tau_c \approx 5$. Heat is distributed into a deeper mixed layer. $\Delta SST < 0$.

Between 10S and 30S, $Q > Q_c$ (excess warming). Even though $\tau/\tau_c \approx 2.5$, the strong winds cannot overcome the very stable stratification; a shallow summer mixed layer forms. $\Delta SST > 0$, but once again the errors nearly compensate.

In the roaring 40's, the initial conditions have a deeper mixed layer than 10S to 30S. The retreating mixed layer remains deep so that, despite $Q > Q_c$, the excessive wind stirring results in cooling. This trend is continued through April where the SST departures of the order of 3°. (See Fig. 3.)

The ocean is noninteractive in the GCM experiment. With a GCM-mixed layer interactive experiment, an enhancement (reduction) of evaporation, sensible heat and thermal radiation loss from the sea surface where ΔSST is positive (negative) would be expected. The net heat flux into the oceans will be correspondingtly reduced (increased), resulting in a reduction of $|\Delta SST|$. Thus, the SST departures obtained in this study may be viewed as an upper bound for the "errors" in SST expected in an interactive run.

A further experiment has been performed where climatological wind stress and GCM heat fluxes were used as forcing for the mixed layer. The reduction in the wind stirring results in a shallower mixed layer making ΔSST more positive everywhere.

References

Fung, I., and M. Cane, 1978: A dynamic model for the oceanic mixed layer: non-advective version. NASA Tech. Memo. 80253, 111-114, Atmos. and Oceano. Res. Rev.-1978, NASA Goddard Space Flight Center, Greenbelt, Maryland.

Halem, M., J. Shukla, Y. Mintz, M. L. Wu, R. Godbole, G. Herman, and Y. Sud, 1978: Comparisons of observed seasonal climate features with a winter and summer numerical simulation produced with the GLAS general circulation model. Report of the JOC Study Conf. on Climate Models: Performance, Intercomparison and Sensitivity Studies, GARP Publ. Series No. 22, 207-253, WMO, Geneva, Switzerland.

Schutz, C., and W. L. Gates, 1971: Global climatic data for surface, 800 mb, 400 mb: January. Report R-915-ARPA, Rand, Santa Monica, California.

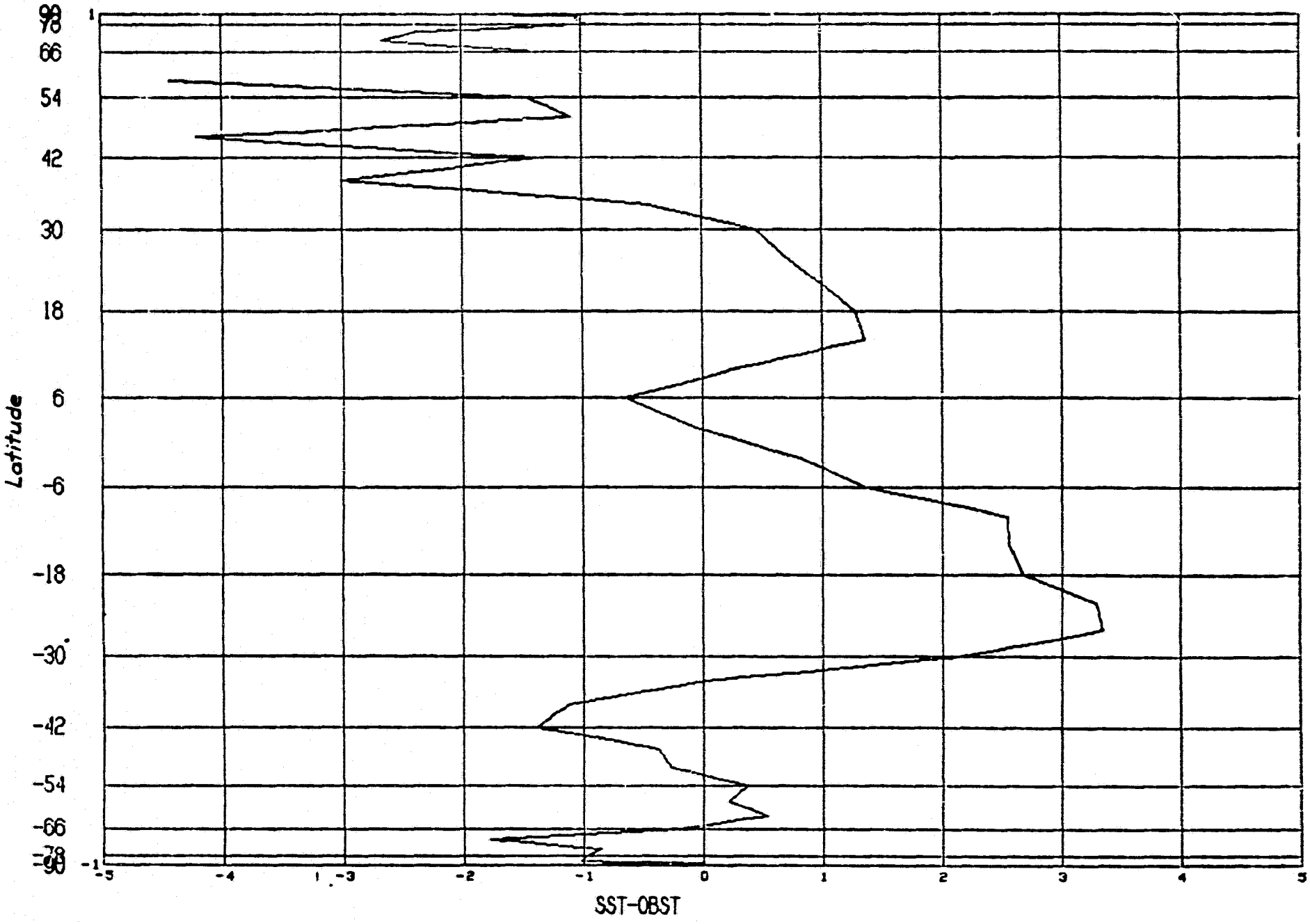

Fig. 3. Same as Fig. 1 except for April, again using January initial conditions.

A ONE-DIMENSIONAL AIR-SEA INTERACTION MODEL WITH PREDICTED CLOUDINESS

(D. A. Randall, J. Calman, C-H. Moeng, and P. Schopf)

Recent studies of the cloud-topped mixed layer have shown that stratocumulus clouds and the planetary boundary layer (PBL) both deepen as the sea surface temperature (SST) increases (for fixed divergence), but that for a sufficiently warm SST the cloud layer is abruptly destroyed as a result of penetration by the dry, warm overlying air. The influence of SST on PBL cloudiness is thus somewhat complicated.

In most studies to date, the PBL structure has been computed for prescribed values of the SST and large-scale divergence. But, of course, the SST is partially determined by local solar insolation and long wave cooling, both of which are very sensitive to cloudiness. The surface turbulent fluxes of sensible and latent heat are also influenced by PBL cloudiness.

To the extent that an increase in SST favors an increase in cloud depth, and to the extent that a deeper cloud favors a colder SST by reducing solar insolation, it can be anticipated that small fluctuations in SST and cloud depth will be damped. But if a positive fluctuation of the SST is large enough to trigger the layer cloud instability, thereby reducing the cloudiness, then the SST fluctuation may be amplified. The coupled system thus appears to be stable with respect to small perturbations but unstable with respect to large perturbations.

To study this and other aspects of local air-sea interactions, the pre-existing one-dimensional atmospheric cloud-topped mixed layer model of Randall (1980b) and the pre-existing one-dimensional oceanic mixed layer (OML) model of Fung and Cane (1978) and Cane and Schopf (1980) have been coupled. In order to provide for the radiative effects of clouds on the atmospheric turbulence and for the radiative warming and cooling of the sea surface, the model includes the radiation parameterization of Herman and Goody (1976), which includes the diurnal cycle of solar radiation. For the air, the prognostic variables of the model are the depth, wind, moist static energy, and mixing ratio of the mixed layer; for the ocean they are the depth, current, and temperature of the mixed layer. The model allows the possibility of a layer of nonprecipitating stratocumulus clouds, which promote convection and entrainment through phase changes and cloud-top radiative cooling (Randall, 1979; 1980a, b). The surface fluxes of sensible heat, moisture, and momentum are determined through the bulk aerodynamic method. The free atmosphere and deep ocean soundings are prescribed as boundary conditions. Oceanic upwelling and atmospheric subsidence are varied parametrically.

Fig. 1 shows results for the last 3 days of a 50-day test run of the coupled model. Diurnal oscillations of the SST, PBL depth, and OML depth are evident, although the SST and the PBL depth still show a linear trend with time, indicating that a longer run is needed to reach equilibrium.

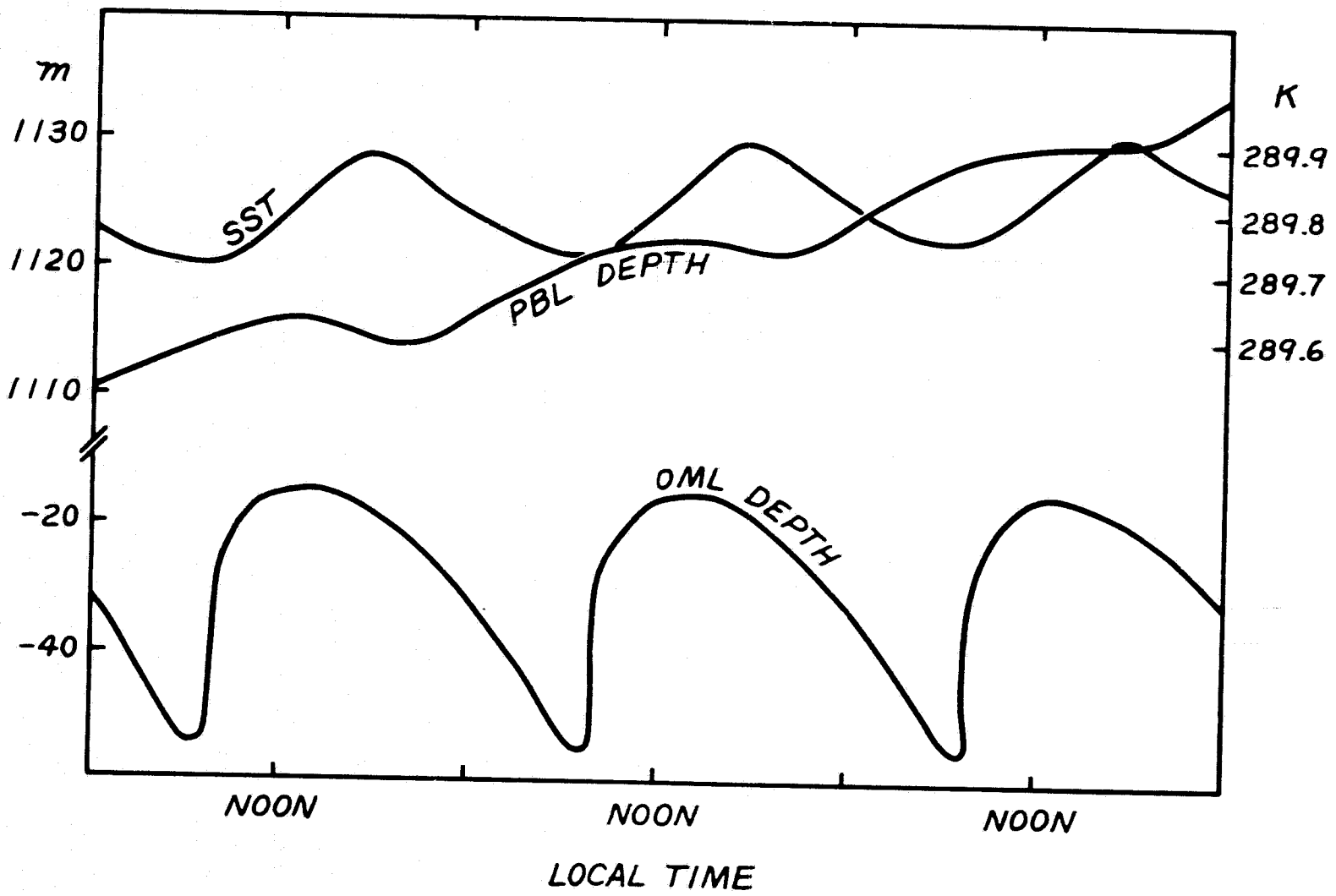

Fig. 1. Time variations of SST, PBL depth, and OML depth over the last 3 days of a 50-day test run.

The amplitude and phase of the SST and OML depth oscillations are reasonable, but the PBL depth oscillation has a smaller amplitude and different phase than anticipated on the basis of the results of Schubert (1976). This discrepancy has not yet been resolved.

In the immediate future, shakedown runs of the model will continue, so that its sensitivities and overall credibility can be evaluated. Then the model will be applied to the study of cloudiness-SST feedback mechanisms.

References

Cane, M., and P. Schopf, 1980: A two-layer dynamic and thermodynamic model of the upper ocean. NASA Tech. Memo. (herein), Atmos. and Oceano. Res. Rev.-1979, NASA Goddard Space Flight Center, Greenbelt, Maryland.

Fung, I., and M. Cane, 1978: A global dynamic model of the oceanic mixed layer. EOS, Transactions of the Am. Geophys. Union, 59, 1094.

Herman, G. F., and R. Goody, 1976: Formation and persistence of summertime Arctic stratus clouds. J. Atmos. Sci., 33, 1537-1553.

Randall, D. A., 1979: The entraining moist boundary layer. Preprint volume, Fourth Symposium on Turbulence, Diffusion, and Air Pollution of the AMS, Reno, Nevada, 467-470. (Available from the author at Laboratory for Atmospheric Sciences, NASA Goddard Space Flight Center, Greenbelt, Maryland.)

_____, 1980a: Conditional instability of the first kind, upside-down. J. Atmos. Sci., 37, 125-130.

_____, 1980b: Entrainment into a stratocumulus layer with distributed radiative cooling. J. Atmos. Sci., 37, 148-159.

Schubert, W. H., 1976: Experiments with Lilly's cloud-topped mixed layer model. J. Atmos. Sci., 33, 436-446.

ON THE DYNAMICS OF EQUATORIAL CURRENTS WITH APPLICATION TO THE INDIAN OCEAN

(M. Cane)

The dynamics of equatorial currents are considered in the light of the wind and current measurements at Gan reported by Knox (1976). For westerly and meridional winds, the response of equatorial currents is predominantly westerly, resulting in downwelling at the equator (Fig. 1). The eastward momentum generated by the wind at the surface is advected downward giving subsurface eastward flow. With persistent easterlies (as in the Atlantic and Pacific), there is an undercurrent driven by the eastward pressure gradient force, both because of the direct down gradient flow, and because of the vorticity transported by the associated meridional circulation.

It is suggested that the undercurrent that has been observed in the Indian Ocean in the early spring is similarly driven by an eastward pressure force. This pressure gradient is a nonlocal transient feature generated by the zonal readjustment of mass induced by the relaxation of the winds at the fall monsoon transition. This idea is consistent with the presence of the undercurrent in 1973 and its absence in 1974.

References

Knox, R. A., 1976: On a long series of measurements of Indian Ocean equatorial currents near Addu Atoll. Deep Sea Res., 23, 211-221.

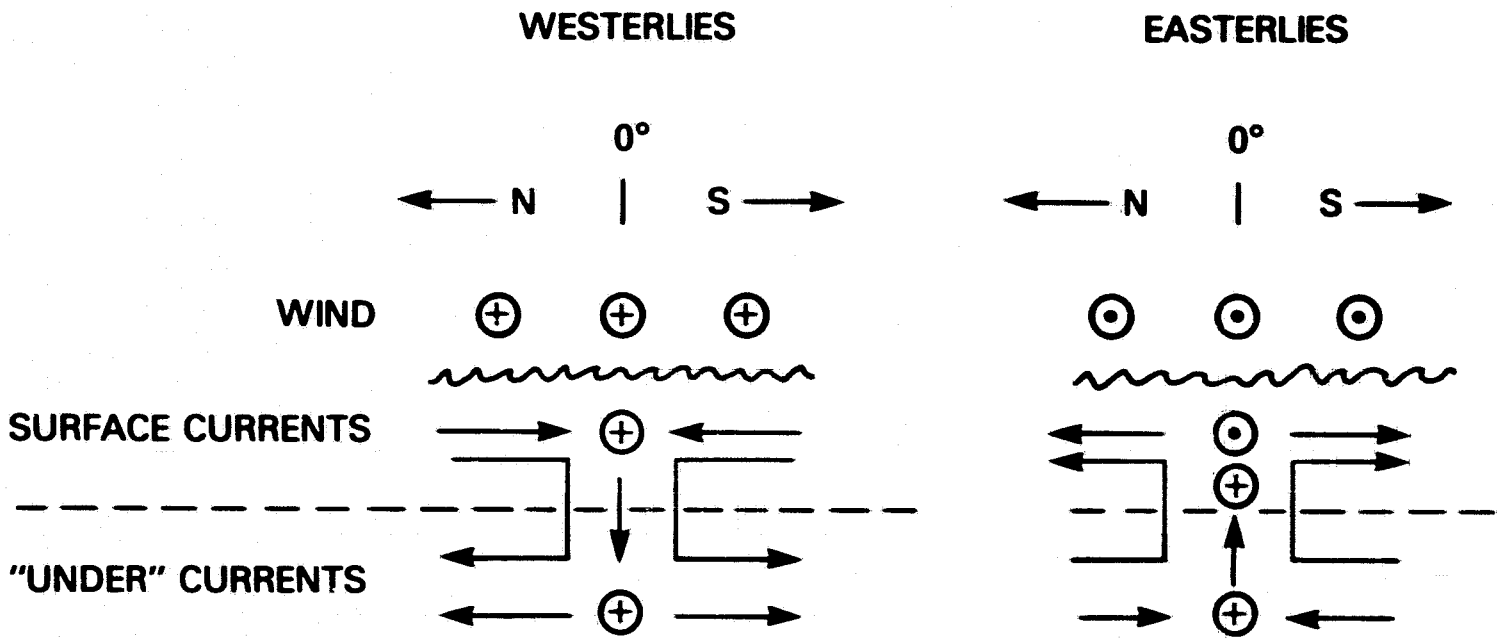

Fig. 1. Sketch of meridional section of the steady x-independent response to easterlies and westerlies, looking eastward.

A TWO-LAYER DYNAMIC AND THERMODYNAMIC MODEL OF THE UPPER OCEAN

(M. Cane and P. Schopf)

A new model has been constructed to simulate the thermodynamics and circulation of the upper ocean. The primary design goal is that the model be capable of state-of-the-art simulations of those processes that determine the sea surface temperature. The model has been kept simple so that it is inexpensive to run simulations over several years. The present fine-grid ($\Delta s \sim 24$ km) model can be used in a stand-alone mode, either as a global model or to do experiments on a regional scale, or be coupled with the GLAS atmospheric GCM.

The vertical structure of the model is depicted in Fig. 1. The upper layer, the mixed layer, is treated as a slab: Temperature and current velocities are taken as constant throughout. This is consistent with the bulk mixed-layer models now widespread (see Niiler and Kraus, 1977). The assumption that the layer is indeed well mixed is a good one for temperature (Fig. 2) but less so for currents. The depth of the mixed layer is variable and is determined by the thermodynamics, turbulent mixing, and divergence of fluid due to large-scale motions.

The layer below the mixed layer is taken to extend to the permanent thermocline with the deep ocean approximated as being at rest (cf., e.g., Charney, 1955). In this second active layer, the currents are again assumed to be uniform with depth. This is the simplest structure that allows one to model the effects of static stability on mixed layer entrainment. In both active layers, the dynamics are governed by the primitive equations. The mixed-layer depth and temperature are also affected by local mixed-layer processes. These are modeled by a bulk formulation very similar to that of Niiler and Kraus (1977). Thus, in the model, as in nature, the surface temperature is influenced by local surface heating and wind stirring, horizontal advection, and upwelling. (Cooling due to upwelling is simulated by first having surface layer divergence thin the layer, thereby bringing the cold water below nearer to the surface where turbulent mixing processes entrain it into the mixed layer.)

The model is being used to study the relationship between local thermodynamic and large-scale dynamical influences on sea surface temperature. The initial project focuses on determining the relative contributions to the seasonal heat budget of the Arabian Sea. Fig. 3 shows the sea surface temperature patterns predicted 25 days after the onset of the monsoon. This model run involves only the dynamically induced changes in surface temperature, without any surface heat flux. Eddies have begun to form and move up the coast, causing strong gradients in the sea surface temperature. For comparison, the sea surface temperature on 6 July 1966, as determined from the NIMBUS II High Resolution Infrared Radiometer (HRIR), is shown in Fig. 4 (Szekielda and LaViolette, 1970). It is apparent that the dynamically induced temperature anomalies are of the same scales and that the eddy signature observed from a satellite is similar to that produced by the model.

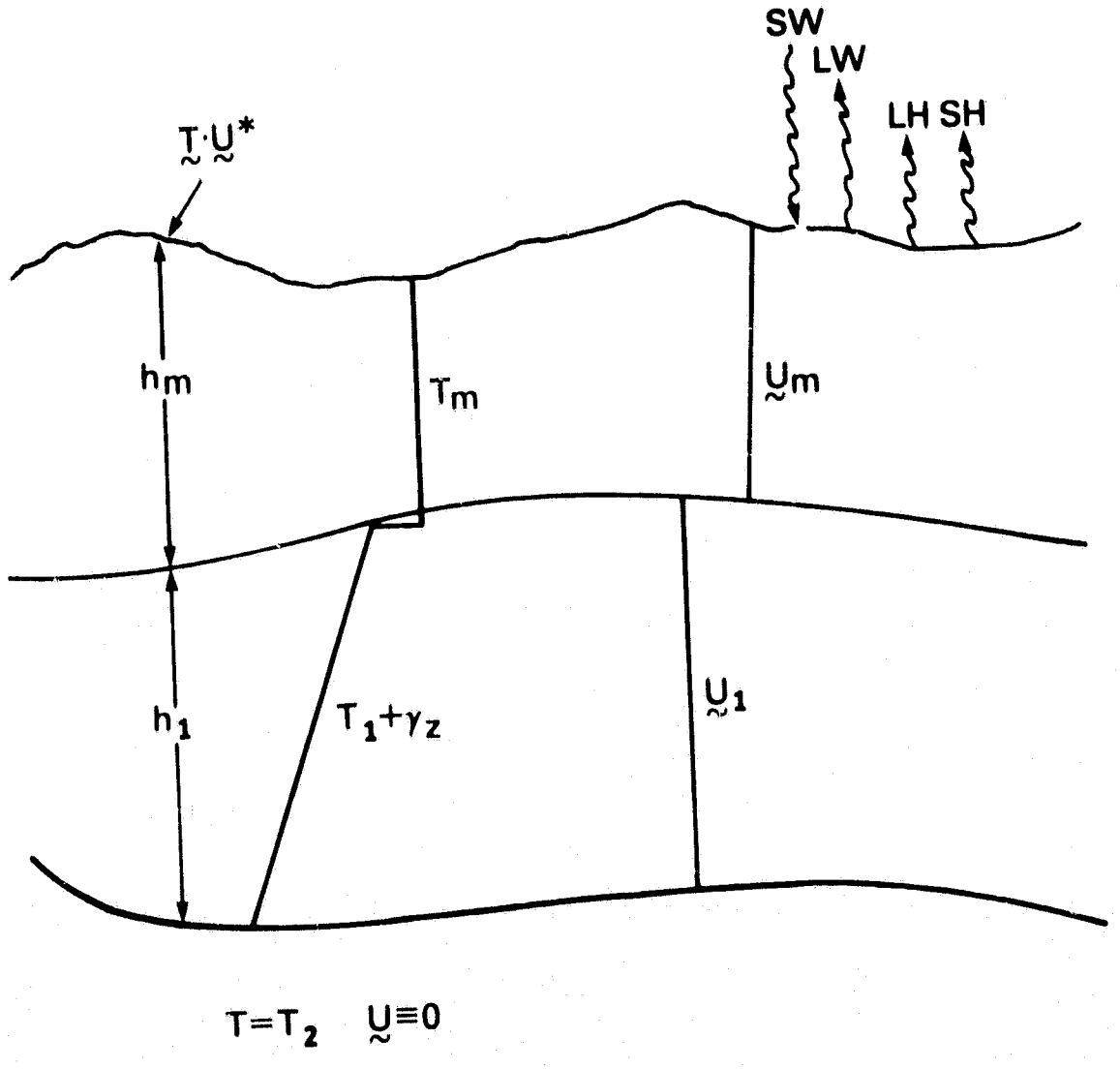

Fig. 1. Vertical structure of the model.

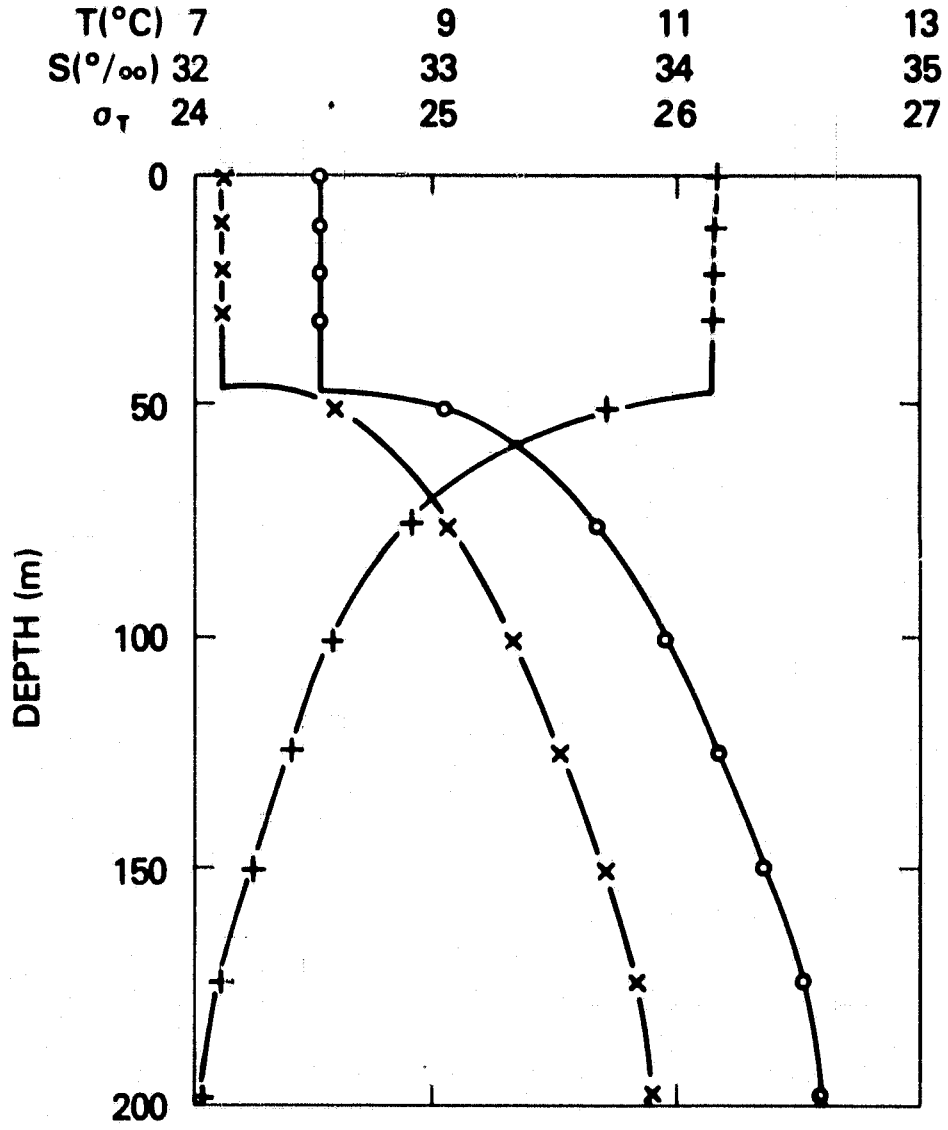

Fig. 2. Typical variation of water properties with depth, November 1962. T = temperature, S = salinity, in parts per thousand by weight σ = density anomaly. σ = 1000 (density-1) where density is in g/cm^3 and is measured at atmospheric pressure. (From H. L. Grant, A. Moilliet, and W. M. Vogel, 1968, some observations of the occurrence of turbulence in and above the thermocline, J. Fluid. Mech., 34, 443-448.)

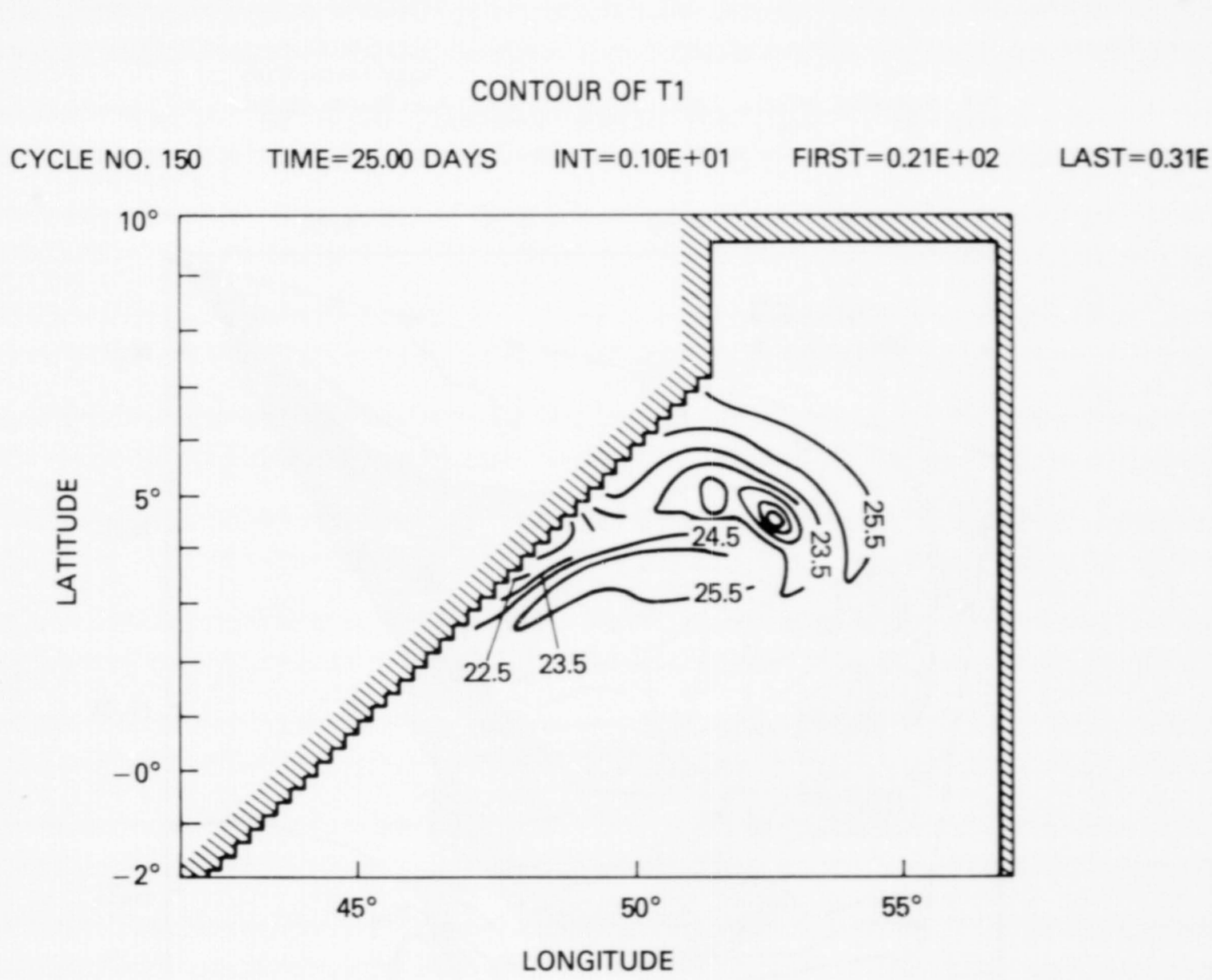

Fig. 3. Model-predicted sea surface temperature 25 days after onset of the SW-Monsoon.

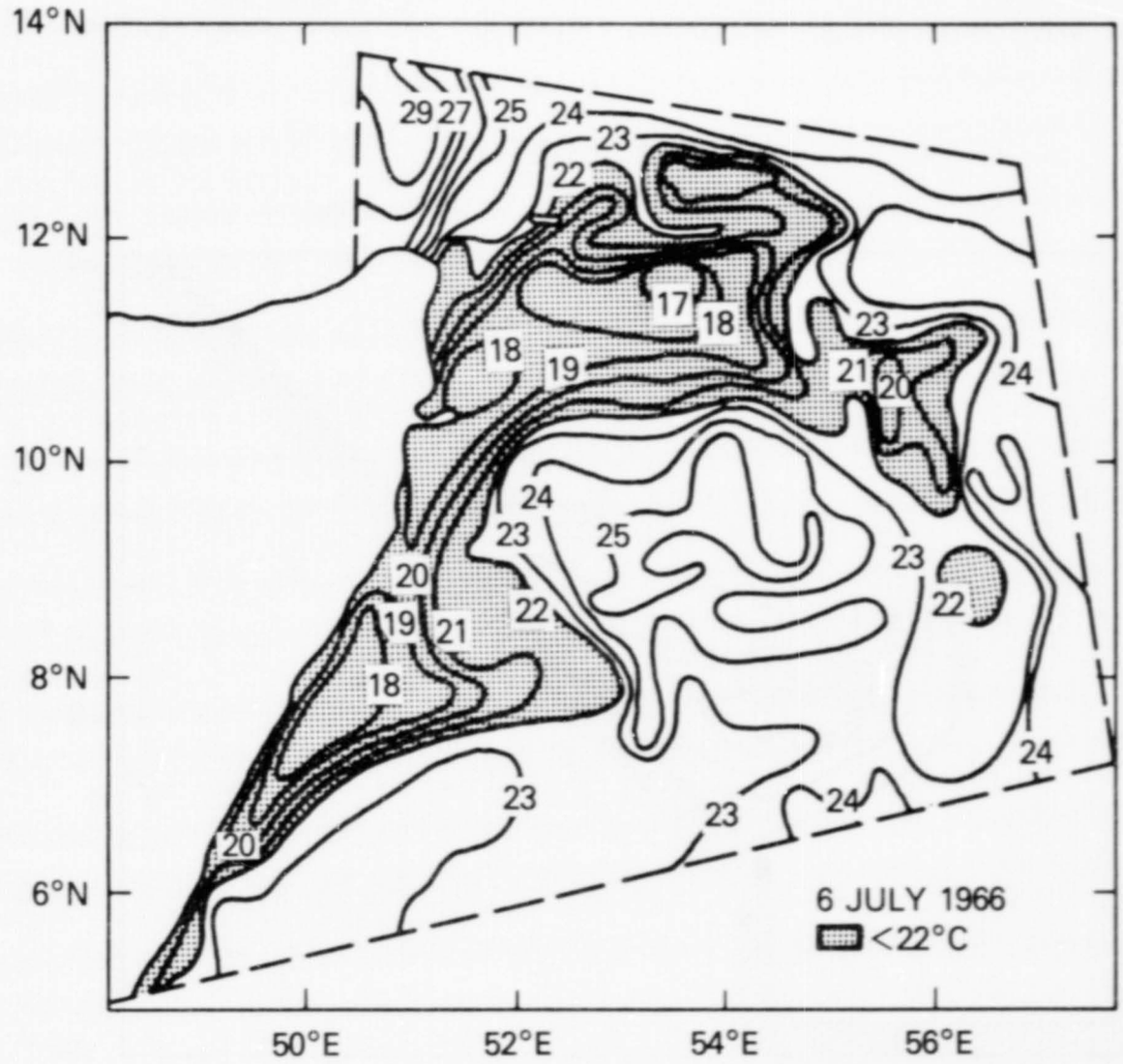

Fig. 4. Sea surface temperature observed from NIMBUS II satellite (HRIR) during the SW-Monsoon of 1966. (From Szekielda and LaViolette, 1970.)

This initial study demonstrates the importance of nonlinear dynamics and high resolution for predicting even large-scale sea surface temperature. Further work with the model in its finer-grid version is planned to examine the low-latitude heat budgets and to prepare for coupling with the GLAS GCM.

References

Charney, J. G., 1955: The generation of ocean currents by wind. J. Mar. Res., 14, 477-498.

Niiler, P. P., and E. B. Kraus, 1977: One-Dimensional Models of the Upper Ocean in Modeling and Prediction of the Upper Layers of the Ocean, E. B. Kraus, ed., Pergamon Press.

Szekielda, K. H., and P. E. LaViolette, 1970: Variations in detailed sea surface temperature structure along the Somali Coast as defined by NIMBUS II HRIR data. Unpublished manuscript.

V. SUMMER LECTURE SERIES

NATIONAL AERONAUTICS AND SPACE ADMINISTRATION

GODDARD SPACE FLIGHT CENTER

GREENBELT, MARYLAND

LABORATORY FOR ATMOSPHERIC SCIENCES

1979 SUMMER LECTURE SERIES OF THE MODELING AND SIMULATION FACILITY

June 21	J. G Charney MIT and D. M. Straus NASA/GSFC-NRC	Resonant Instability and Multiple Equilibria in Orographically Forced Baroclinic Planetary Wave Systems
June 28	D. R. Johnson Univ. of Wisc.	The Evolution of the Extratropical Cyclone and Its Interaction with Larger and Smaller Scales
July 5	R. B. Smith	Stratified Flow Over (and Around?) Isolated Topography
July 12	J. R. Bates Irish Meteorological Service	A Variational Technique for the Assimilation of Meteorological Data
July 19	J. Paegle Univ. of Utah	On the Generation of Large-Scale Divergent Winds and Related Energetics
July 26	E. Mollo-Christensen MIT	Wind Wave Development
August 2	J. Kutzbach Univ. of Wisc. CANCELLED	Nature's Monsoon Experiment Between 5,000 and 25,000 Years Ago
August 9	J. W. Deardorff Oregon State Univ.	Numerical Modeling of Stratocumulus in the Boundary Layer
August 16	S. Manabe NOAA/GFDL	Climatic Effect of an Increase of CO_2 in the Atmosphere
August 23	M. Suarez UCLA	Some Results with the UCLA General Circulation Model
August 30	S. Hastenrath Univ. of Wisc.	On Tropical Circulation and Climate Anomalies
September 6	E. Kalnay-Rivas NASA/GSFC and L.-O. Merkine Technion-Israel Inst. of Technology	A Simple Mechanism for Blocking

June 21, 1979

RESONANT INSTABILITY AND MULTIPLE EQUILIBRIA IN OROGRAPHICALLY FORCED BAROCLINIC PLANETARY WAVE SYSTEMS

J. G. Charney/MIT and D. M. Straus/National Research Council

The general circulation of the atmosphere has often been regarded as consisting of a large-scale mean circulation, on which smaller scale transient waves are superimposed. The mean circulation, thought of as a Hadley circulation modified by topographic and thermal asymmetries of the lower boundary, is the single equilibrium of the atmosphere, albeit an unstable one. The smaller scale transients consist of waves and vortices which originate as instabilities of the mean flow and which interact with it. This description does not explain the presence of persistent, large-scale flow anomalies, such as blocking, which have so much to do with the atmosphere's observed variability.

This presentation reports on research, both past and present, which suggests an explanation for the occurrence of persistent anomalies in terms of multiple equilibrium solutions. An equilibrium solution is a steady-state or periodic solution of the fundamental equations governing atmospheric dynamics. The existence of more than one solution is made possible by the asymmetries in the lower boundary, e.g. mountains. If such solutions can be found which are stable to large-scale disturbances, one has an explanation for the existence of different large-scale flow patterns. If, in addition, these equilibria are unstable to smaller scale motions (as they will be in general), the transitions between the various large-scale patterns can also be explained.

A simple model which incorporates these ideas is the spectral, quasi-geostrophic, barotropic, channel model studied by Charney and DeVore. The model is set on a mid-latitude beta plane, is severely truncated, but does include orography. Because of the truncation, there are only three degrees of freedom. One describes the zonal flow (which is forced directly), and the other two a single zonal wavenumber. Only one wavelength in the meridional direction ("first y-mode") is kept initially. The wave variables change due to advection by the mean flow, the beta-effect, friction, and an additional coupling to the zonal flow via the mountain (which has the same zonal wavenumber as the wave). The zonal flow is changed by forcing and dissipation, and also by interaction with the wave, again via the mountain. No Reynold's stresses are present. For small values of the forcing, only one steady state equilibrium exists, and it has non-zero wave components. It is also stable to perturbations of the first y-mode. However, for higher values of the forcing, three steady state equilibria exist. The two additional solutions are now stable, and the original one unstable. One of the stable states is a "high-index" circulation having a strong zonal flow and a relatively weak wave perturbation; the other is a "low-index" circulation having a weak zonal flow and a relatively strong wave perturbation. The unstable steady state has an intermediate flow.

This instability can be shown to be solely due to the interaction of the topographic wave with the zonal mean flow and is not a simple barotropic instability of the zonal flow. Numerical solutions of the three-component system, started near the unstable equilibrium, converge to either one of the stable equilibria, depending on exactly how the unstable equilibrium is perturbed. The presence and stability of these equilibria were confirmed by numerical computations on a grid model having the same geometry, driving and dissipation as the spectral model, but having many more degrees of freedom.

The interpretation can be made that blocking in the real atmosphere is an example of an equilibrium flow of the low-index type and that transition from it to the high-index state occurs via the instability of the intermediate state.

The discovery of multiple equilibria and orographic instability in a barotropic system led us to investigate a corresponding baroclinic system. The important differences between the baroclinic and barotropic models include: (i) a description of the zonal flow and wave in each of two layers (for only the first y-mode) requires 6 variables; (ii) now it is the temperature gradient (or wind shear) which is forced; and (iii) although Reynold's stresses driving the average zonal flow in both layers (barotropic component) are again absent, the waves can directly change the zonal temperature gradient (baroclinic component) by causing heat fluxes to be present.

As a consequence of (ii), the single equilibrium which exists for low values of the thermal driving is a simple Hadley solution, i.e., a zonally symmetric solution with no lower level flow. (Hence, it is the same solution with or without mountains.) If orographic waves and a lower level zonal flow are to exist, they must be produced by the unstable growth of a small initial perturbation. Such an orographic instability (corresponding to the growth of a wave in place) is indeed found. However, as a consequence of (iii), it is not the only type of instability present; baroclinic instability in the usual sense (corresponding to traveling waves) is also possible. The presence of two competing instabilities adds a great deal of richness to the behavior exhibited by the model.

The simple 6-component model was studied in detail for wavenumber 3. For low values of the thermal driving, only the Hadley solution exists. The first stability threshold to be crossed as the driving is increased is that for orographic instability. This instability of the Hadley circulation leads to the existence of two stable, steady state equilibria with finite wave amplitudes ("wavy equilibria"). As in the barotropic case, the stable equilibria are both realizable in numerical integration. However, they both correspond to relatively high-index flows, i.e., ones with wave amplitudes small compared to the zonal flow.

At higher values of the driving, the wavy equilibria themselves become baroclinically unstable, so that the system has three (including the Hadley solution) unstable steady state solutions. Numerical integration of the system leads to a periodic solution in which both the waves and the zonal flow vary in time.

One of the two wavy equilibria is, however, only very weakly unstable, and in this solution the wave amplitude increases dramatically with the external driving. At values of the forcing for which this solution begins to resemble a blocking (low-index) pattern, it becomes stable again. In this same regime, the Hadley solution becomes baroclinically (as well as orographically) unstable, and the new instability leads to two new wavy equilibria, giving four in all. The two new equilibria correspond to very high-index flows, and are unstable. The blocking solution is stable, and the fourth wavy equilibrium unstable. Numerical solutions of the system, starting from either of the latter two wavy equilibria (the first two that appeared as the driving were increased from small values), converge to the stable blocking solution. However, starting from each of the high-index equilibria, the system converges to a distinct periodic solution. Thus, there are three stable solutions for fixed driving, one steady state and two periodic.

In both the barotropic and baroclinic systems, the stability of the various steady state solutions were also studied for a second meridional wavenumber (second y-mode). Many of the solutions that were stable to first y-mode perturbations became unstable to the second y-mode, and integration of the appropriate equations with both y-modes led to the discovery of new periodic and also aperiodic solutions. Again, multiple solutions were found for fixed values of the driving.

These findings are regarded as useful primarily for their heuristic character, not for their detailed explanations of specific phenomena. They suggest that the study of steady state and periodic solutions, as well as consideration of the instabilities of these solutions, will become a useful tool for investigation of large-scale atmospheric phenomena. We believe that this approach can lead to a better understanding of large-scale variability, predictability, and climate. To know that a system is close to a stable or metastable equilibrium is to know that it will remain so for a time. To know that the system is in a state of transition is to know that it will change more rapidly and be less predictable. Climate itself becomes a question of distributions among possible equilibrium states, and climate variation a matter of how boundary changes lead to altered distributions.

June 28, 1979

THE EVOLUTION OF THE EXTRATROPICAL CYCLONE AND ITS INTERACTION WITH LARGER AND SMALLER SCALES

D. Johnson/The University of Wisconsin

The forcing of the mass circulation and angular momentum transport for two distinct types of cyclone development is summarized for the leeside development of the Alberta Cyclone of March 30-April 2, 1971. The first type of development during the initial 48 hours of the cyclone's lifetime was characterized by an inward branch of a mass circulation in the upper isentropic layers and an outward branch in lower isentropic layers. The upward branch of the mass circulation was forced by the combination of negative pressure and inertial torques while the outward branch was forced by the combination of positive pressure and inertial torques. The transfer of storm absolute angular momentum was downward through the action of the torques with the result that the "spin-up" of the relative circulation of the extratropical cyclone occurs in the lower troposphere. Figure 1 from Johnson, Wash and Petersen (1976) shows that the tendency of specific storm angular momentum is positive in the lower layers, while it is negative in upper layers. During this type of development, precipitation is light and the flow is nearly adiabatic. Through a decomposition of the lateral transport processes into geostrophic and ageostrophic modes, the results indicate that development occurs primarily through the modes identified with baroclinic amplification of waves and that the cyclone develops in the low troposphere through larger scale forcing in the presence of topography.

The second type of development occurring during the last 48 hours of the cyclone's lifetime was characterized by an inward mass transport in the lower isentropic layers and outward transport in the upper isentropic layers. The inward branch of the mass circulation was forced by an excess of the negative pressure and frictional torques over the positive inertial torque while the outward branch was forced by the excess of the positive pressure torque and eddy angular momentum convergence over the negative inertial torque. During the transition stage between the two types of development, the precipitation within the cyclone's circulation intensifies, and angular momentum is transferred upwards in association with ascending diabatic trajectories and the release of latent heat along with the action of pressure torques. The qualitative contrast of the areal extent of the precipitation processes during the lifetime of the cyclone is portrayed in the three satellite pictures on three successive days (Figure 2). The first of the three geosynchronous images is taken during the second day of the cyclone's lifetime and displays little convection, while the last two taken during the third and fourth day show the extensive convection that developed within the cyclone circulation. The excess of the inward transport of angular momentum towards the cyclone's axis of rotation over the outward transport and the transfer of angular momentum upwards serves to "spin-up" the relative circulation at all levels and rapid occlusion follows. Note in Figure 1 that the tendency of specific storm angular momentum is positive at all levels. The partitioning of the lateral transport processes reveals that this type of cyclone development primarily occurs through the ageostrophic component of the mass circulation and that the mass circulation is forced

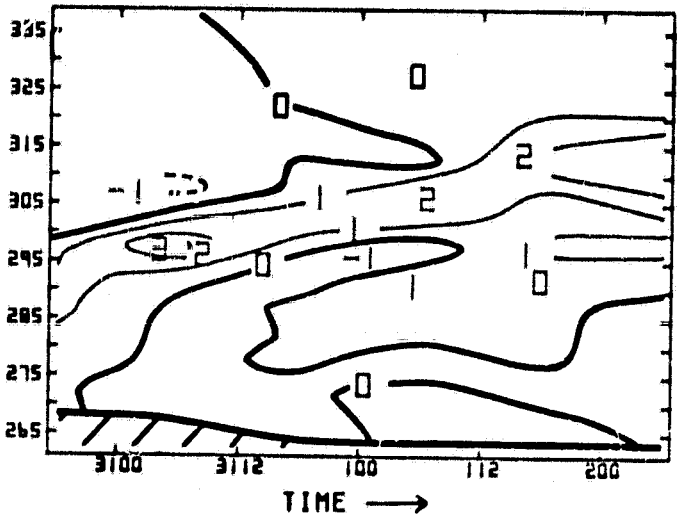

Figure 1. Tendency of specific storm angular momentum for Alberta Cyclone of 30 March - 2 April 1971.

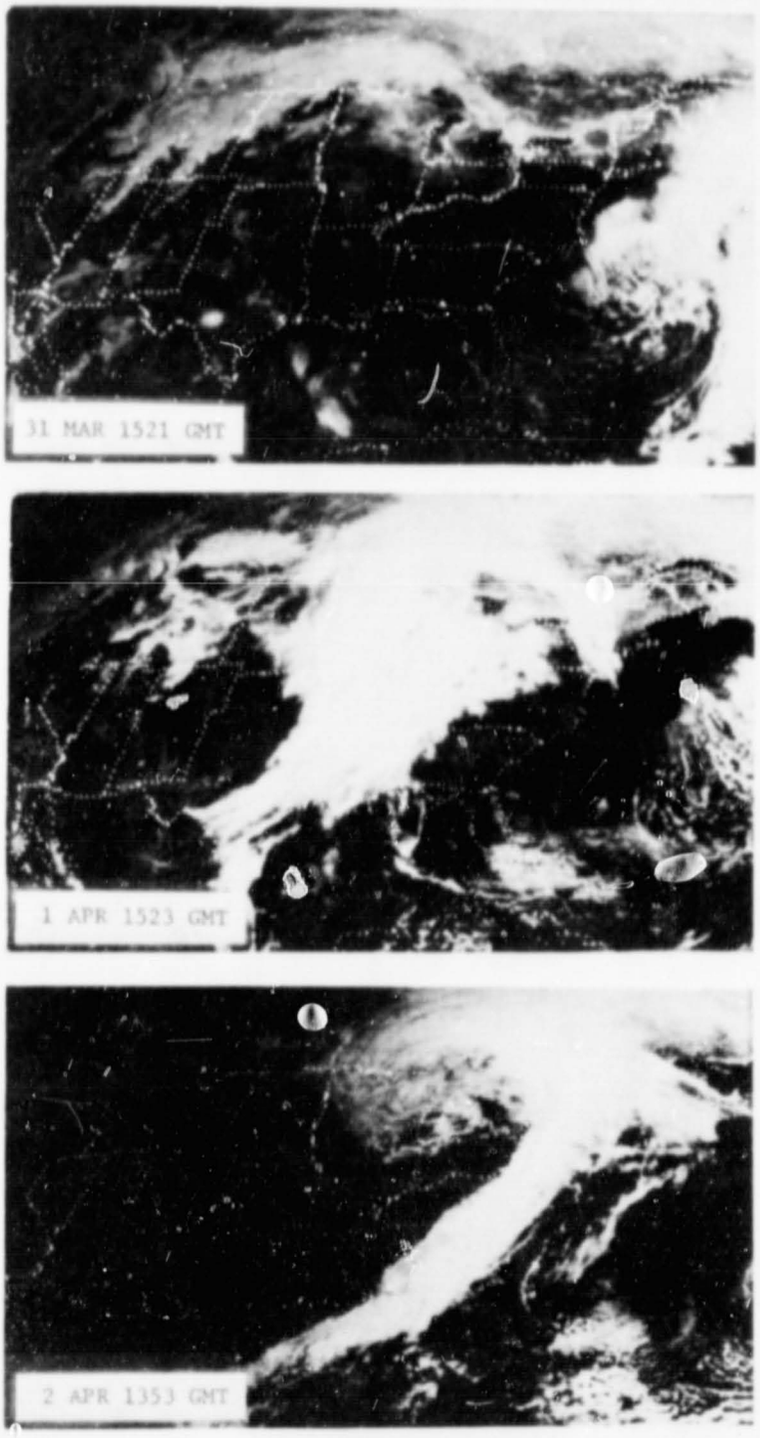

Figure 2. Three successive ATS-III satellite photos of Alberta Cyclone of 31 March - 2 April 1971.

by physical processes identified either with the cyclone vortex or smaller scales embedded within the cyclone. This period of growth of the small-scale cyclone from a secondary vortex embedded within an amplifying baroclinic wave to a large-scale occluded vortex within a large-amplitude wave is one where small-scale processes associated with the boundary layer and latent heat release through convection and frontal circulations force larger scale development.

Reference

Johnson, D. R., C. H. Wash, and R. A. Petersen, 1976: The mass and absolute angular momentum budgets of the Alberta cyclone of 30 March-2 April 1971. Preprint Volume, Sixth Conf. on Weather Forecasting and Analysis of the AMS, May 10-13, Albany, NY, 350-356.

July 5, 1979

STRATIFIED FLOW OVER (AND AROUND?) ISOLATED TOPOGRAPHY

R. B. Smith/Yale University

The theoretical study of the airflow over mountains began with Lyra (1943) and Queney (1947). Since then, the subject has received a great deal of attention, in part, because the mathematical problem is well posed and, in part, because the flow can be considered steady. Still, in spite of these simplifications, the mountain flow problem has the basic elements of all problems in dynamical meteorology, namely the importance of the degree to which the flow is hydrostatic and/or geostrophic. The equations used by Lyra and Queney illustrate this point (also see Smith, 1979a).

$$\rho U\frac{\partial u'}{\partial x} - \rho f v' = -\frac{\partial P'}{\partial x} \tag{1}$$

$$\rho U\frac{\partial v'}{\partial x} + \rho f u' = -\frac{\partial P'}{\partial y} \tag{2}$$

$$\rho U\frac{\partial w'}{\partial x} = -\frac{\partial P'}{\partial z} - g\rho' \tag{3}$$

$$\frac{\partial u'}{\partial x} + \frac{\partial v'}{\partial y} + \frac{\partial w'}{\partial z} = 0 \tag{4}$$

$$\frac{U}{\rho}\frac{\partial \rho'}{\partial x} = \frac{1}{g} N^2 w'. \tag{5}$$

Noting the importance of the horizontal scale L on the advective terms in 1, 2, and 3, we can reason (with benefit of hindsight) as follows. For flow over narrow mountains, the vertical force balance will involve only the first two terms in (3) but, as L increases, the buoyancy force becomes relatively more important and eventually the terms on the right-hand side of (3) will dominate and hydrostatic balance is achieved.

As the horizontal scale continues to increase, equations (1) and (2) change from a balance between advective acceleration and pressure gradient force to a balance between Coriolis force and pressure gradient force, i.e., geostrophic balance.

For fixed: U, N, f, as the mountain width (L) increases

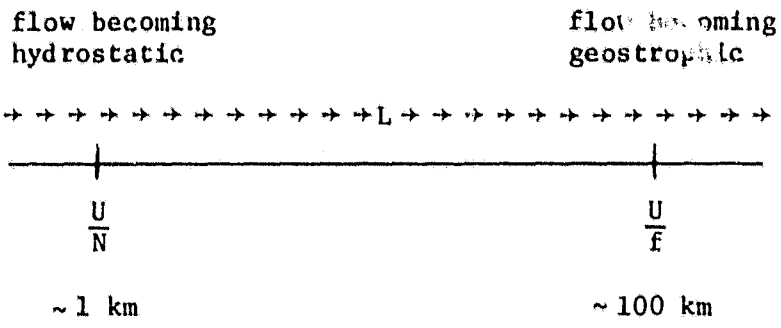

Generally speaking, as the buoyancy forces increase in importance and the flow becomes more nearly hydrostatic, the fluid becomes able to support internal gravity waves and the disturbance produced by the mountain can extend to great heights (Figure 1). [Several GOES film loops are shown indicating the high level cirrus formed in vertically propagating mountain waves over the Appalachians and the Front Range.] The theory of mountain waves also predicts the existence of a pressure difference across a mountain caused by mountain wave generation. Recently, this pressure difference has been directly measured using sensitive microbarographs placed on each side of a narrow mountain ridge (Smith, 1978).

Most of the theoretical work on mountain flows has been restricted to two-dimensional flow over an infinite ridge but recently solutions have been obtained for flow past an isolated mountain (Smith, 1980). These solutions show, for the first time, the tendency for the low-level flow to be deflected to each side of the mountain and for the laterally displaced air to be replaced by the descent of potentially warmer air from aloft. This pattern of surface flow is associated with the generation of a 3-D wave pattern aloft.

As we proceed to larger (i.e., synoptic) scales of motion, the Coriolis force becomes important. Eventually, when the Rossby number (U/fL) is small, the Coriolis force will dominate, quasi-geostrophic theory becomes valid, and the ability of the fluid to support internal gravity waves is destroyed by the Coriolis resistance to horizontal divergence. Recent theoretical and observational work (Smith, 1979b) has shown, however, that even for mountain ranges as wide as 300 km or so, mountain waves continue to play an important role (see Figure 2). It seems then that the quasi-geostrophic approximation should not be used in the analysis of flow over moderate-scale orography as the mountain waves are thereby lost; and with them go several important qualitative features--the propagation of the disturbance to great heights, the pressure difference across the mountain, and preference for flow to go around, rather than over, the mountain.

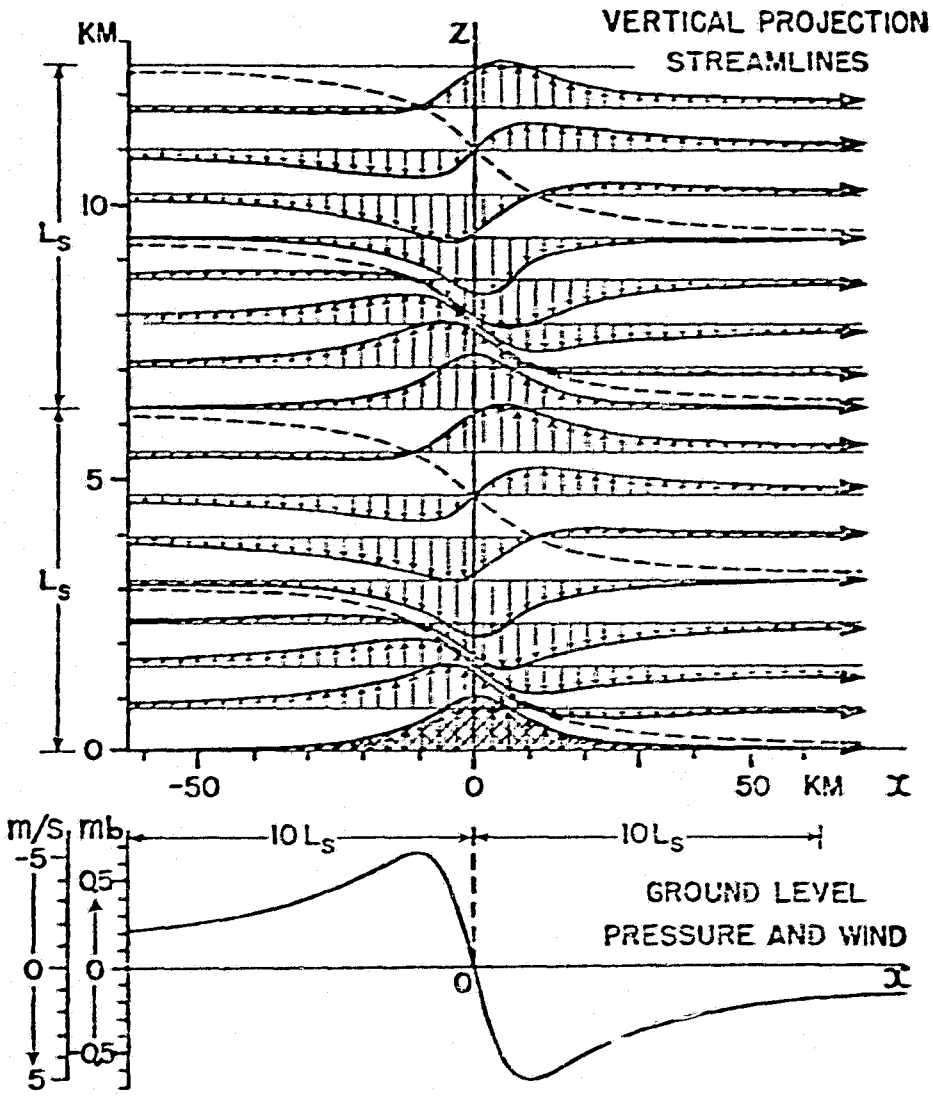

Figure 1. The vertical displacement of the streamlines by a 1 km high ridge, computed by neglecting the Coriolis force. The incoming wind speed is 10 m/s and the buoyancy frequency is .01 sec^{-1}. The flow over a ridge of this width is hydrostatic and is dominated by the generation of mountain waves. The lower part of the figure shows the perturbation wind speed and pressure at ground level (from Queney, 1948).

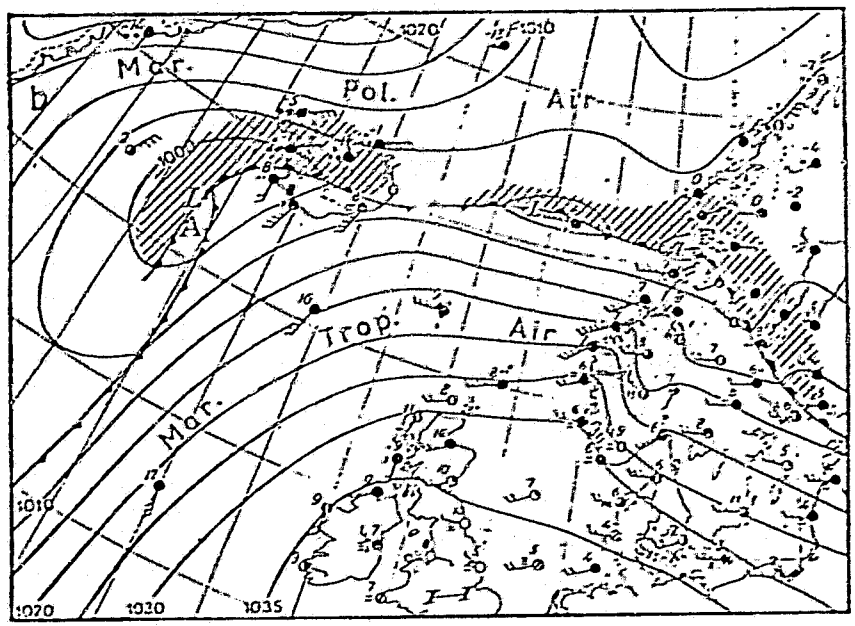

(a)

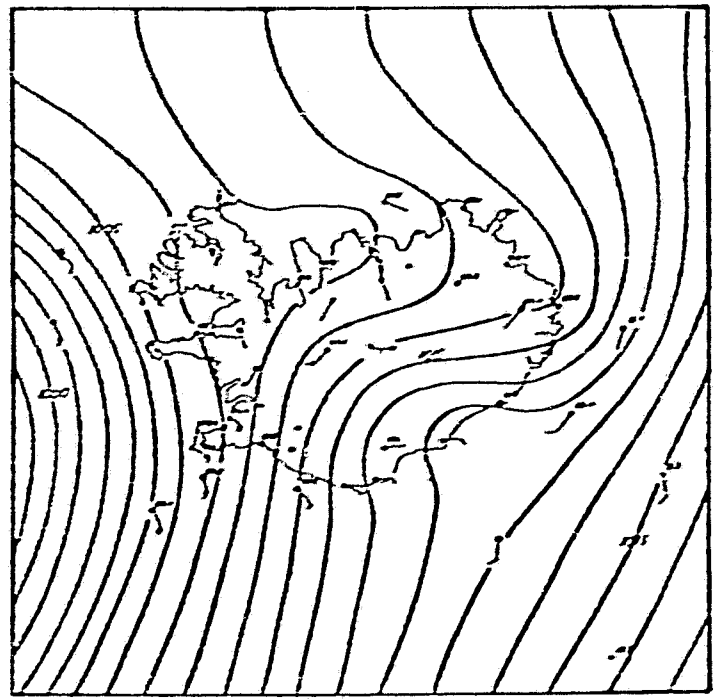

(b)

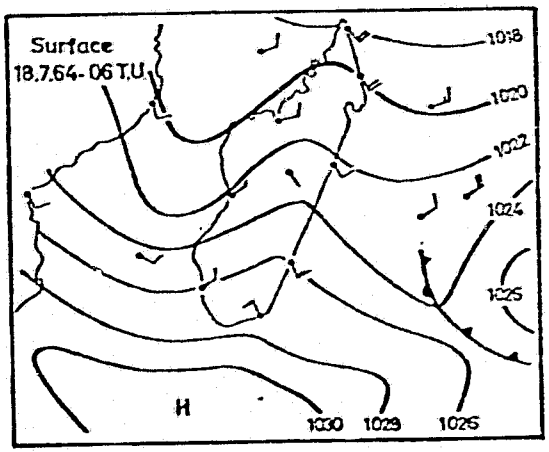

(c)

Figure 2. Three examples of the perturbation to the surface wind and pressure fields caused by orography (a) The Scandinavian mountains, March 24, 1953 0900z (from Spinnangr and Johansen, 1954), (b) Iceland (from Bergthorsson and Sigurdsson, 1976) and (c) Madagascar, July 18, 1964 (from Donque, 1975). The length scale of these flows (a few hundred km) is large enough so that the Coriolis force is important but the pressure asymmetry - high pressure upstream and low pressure downstream - seen in the figure is evidence that the Coriolis force is not so dominant that it prevents the generation of mountain waves.

References

Bergthorsson, P., and S. Sigurdsson, Anomalous sea level pressure due to mountains, unpublished manuscript from the Icelandic Wea. Bureau, 1976.

Donque, G., Contribution Geographique a l'etude du Climate de Madagascar, Nouvelle Imprimerie des Arts Graphiques, 478 p., 1975.

Lyra, G., Z. Angew. Math. Mech., 23, 1-28, 1943.

Queney, P., Dept. of Met., Univ. of Chicago, Misc. Report No. 23, 81 p., 1947.

Queney, P., Bull. Am. Met. Soc., 29, 16-26, 1948.

Smith, R. B., J. Atmos. Sci., 9, 1644-1654, 1978.

Smith, R. B., Adv. in Geophys., 21, B. Saltzman, ed., 87-230, 1979a.

Smith, R. B., J. Atmos. Sci., 36, 177-180, 1979b.

Smith, R. B., Linear theory of stratified hydrostatic flow past an isolated mountain, submitted to Tellus, 1980.

Spinnangr, F., and H. Johansen, Meteorologiske Annaler, 3, No. 14, 351-424, 1954.

July 12, 1979

A VARIATIONAL TECHNIQUE FOR THE ASSIMILATION OF METEOROLOGICAL DATA

J. R. Bates/Irish Meteorological Service

A variational method is proposed for global assimilation of meteorological data in which information from the previous forecast is used more fully than in existing methods. In most existing data assimilation schemes, the previous forecast is used only in providing a first guess for the analysis, while the initialization takes no further account of forecast information. Included in that category is the method based on nonlinear normal mode initialization.

In the scheme proposed here, the forecast tendencies of vorticity and divergence, together with the forecast vertical motion and diabatic heating (all smoothed over the final three hours of the forecast), are used to modify the analyzed mass and wind fields, with the aim of preserving the maximum amount of useful historical information and of ensuring a smooth evolution of the computed atmospheric flow.

Let (ψ°, ϕ°) be the analyzed stream function and geopotential and let χ° be the velocity potential derived (at the first iteration) from the forecast vertical motion. Let $(\alpha_1, \alpha_2, \alpha_3)$ be precision moduli associated with $(\psi^\circ, \chi^\circ, \phi^\circ)$. We minimize the functional

$$I = F\, a^2 \cos\theta d\theta d\lambda$$

$$I = \alpha_1 \left(\psi_x-\psi_x^\circ\right)^2 + \left(\psi_y-\psi_y^\circ\right)^2 + \alpha_2 \left(\chi_x-\chi_x^\circ\right)^2 + \left(\chi_y-\chi_y^\circ\right)^2 + \alpha_3(\phi-\phi^\circ)^2 \; a^2\cos\theta d\theta d\lambda \qquad (1)$$

over the globe, where (ψ, χ, ϕ) are functions to be determined. As constraints on the functional (1), we choose forms of the vorticity and divergence equations in which the tendencies and the nonlinear terms are prescribed:

$$G_1 = f\nabla^2\chi + \beta(\psi_x+\chi_y) + a_1 = 0 \qquad (2)$$

$$G_2 = \nabla^2\phi - f\nabla^2\psi - \beta(\psi_y-\chi_x) + a_2 = 0 \qquad (3)$$

where

$$a_1 = \frac{\partial}{\partial t}\nabla^2\psi^F + \nabla\cdot\rho\underset{\sim}{v} + \omega\frac{\partial\underset{\sim}{v}}{\partial p} \times\underset{\sim}{k}$$

$$a_2 = \frac{\partial}{\partial t}\nabla^2\chi^F + \nabla\cdot\rho\underset{\sim}{k}\times\underset{\sim}{v} + \omega\frac{\partial\underset{\sim}{v}}{\partial p} - \nabla\left(\frac{v^2}{2}\right)$$

The superscripts "F" denote forecast values. The nonlinear terms in a_1 and a_2 are derived from the observed (analyzed) values at the first iteration, but are updated using the new values (ψ, χ, ϕ) at succeeding iterations.

After the first iteration χ° is derived from a vertical motion given by the thermodynamic equation

$$\omega = \frac{\partial T}{\partial t}^F + \underset{\sim}{v}\cdot\nabla T + Q^F / Cp \quad \frac{\alpha}{Cp} - \frac{\partial T}{\partial p} \qquad (4)$$

where T is derived from the hydrostatic equation

$$T = -\frac{P}{R}\frac{\partial\phi}{\partial p}$$

In this way, all the equations of motion enter the iterative procedure.

To minimize the functional (1) subject to the constraints (2) and (3), we define

$$\tilde{F} = F + \lambda, G_1 + \lambda_2 G_2 \qquad (5)$$

where λ_1, λ_2 are undetermined Lagrange multipliers. The Euler-Lagrange equations for this system are found to be

$$\frac{\partial\tilde{F}}{\partial\psi} - \frac{\partial}{\partial\lambda}\frac{\partial\tilde{F}}{\partial\psi_\lambda} - \frac{1}{\cos\theta}\frac{\partial}{\partial\theta}\frac{\partial\tilde{F}}{\partial\psi_\theta}\cos\theta + \frac{\partial^2}{\partial\lambda^2}\frac{\partial\tilde{F}}{\partial\psi_{\lambda\lambda}} + \frac{1}{\cos\theta}\frac{\partial^2}{\partial\theta^2}\frac{\partial\tilde{F}}{\partial\psi_{\theta\theta}}\cos\theta = 0$$

with similar equations where χ, ϕ replace ψ. Applied to (5), these equations become

$$2\alpha_1 \nabla^2(\psi-\psi^\circ) + \frac{\partial}{\partial n}(\lambda_1\beta) + L(\lambda_2) = 0 \tag{6}$$

$$2\alpha_2 \nabla^2(\chi-\chi^\circ) + \frac{\partial}{\partial n}(\lambda_2\beta) - L(\lambda_1) = 0 \tag{7}$$

$$2\alpha_3 (\phi-\phi^\circ) + \nabla^2\lambda_2 = 0 \tag{8}$$

where we have assumed $(\alpha_1, \alpha_2, \alpha_3)$ are constants and

$$L = f\nabla^2 + \frac{\beta}{a}\frac{\partial}{\partial\Theta} \tag{9}$$

The equations (2), (3), (6), (7), (8) in $(\psi, \chi, \phi, \lambda_1, \lambda_2)$ can be solved by expanding in spherical harmonics. Letting

$$\begin{matrix}\chi\\ \psi\\ \lambda_1\\ \lambda_2\\ \phi\end{matrix} = \mathrm{Re} \sum_{m=0}^{J} \sum_{n=m}^{m+J} \begin{matrix}-i\tilde{\chi}_n^m\\ \tilde{\psi}_n^m\\ i(\tilde{\lambda}_1)_n^m\\ (\tilde{\lambda}_2)_n^m\\ 2R\phi_n^m\end{matrix} \overline{P}_n^m(\mu)\, e^{im\lambda} \tag{10}$$

$$
\begin{array}{lll}
a_1 & & i\left(\frac{2\Omega}{a^2}\right)(\tilde{a}_1)^m_n \\
a_2 & J \quad m+J & \left(\frac{2\Omega}{a^2}\right)(\tilde{a}_2)^m_n \\
\rho^\circ = \mathrm{Re} & & \left(\frac{1}{a^2}\right)(\tilde{\rho}^\circ)^m_n \quad \bar{p}^m_n(\mu)\, e^{im\lambda} \\
\delta^\circ & & i\left(\frac{1}{a^2}\right)(\tilde{\delta}^\circ)^m_n \\
\phi^\circ & m=0 \quad n=m & 2\Omega(\tilde{\phi}^\circ)^m_n
\end{array}
\tag{11}
$$

where $\mu=\sin\theta$ and $\bar{p}^m_n(\mu)$ are the normalized Lagrange functions, we find, after eliminating ϕ from (3) by means of (8) and using some standard recurrence relationships,

$$\epsilon^m_{n+1}\,\tilde{\chi}^m_{n+1} + \epsilon^m_n\,\tilde{\chi}^m_{n-1} + m\tilde{\psi}^m_n = (\tilde{a}_1)^m_n \tag{12}$$

$$-c_n(\tilde{\lambda}_2)^m_n + \epsilon^m_{n+1}\,\tilde{\psi}^m_{n+1} + \epsilon^m_n\,\tilde{\psi}^m_{n-1} + m\tilde{\chi}^m_n = (\tilde{a}_2)^m_n + n(n+1)(\tilde{\phi}^\circ)^m_n \tag{13}$$

$$2\tilde{\alpha}_1\, n\,(n+1)\tilde{\psi}^m_n + m(\tilde{\lambda}_1)^m_n + \epsilon^m_{n+1}(\tilde{\lambda}_2)^m_{n+1} + \epsilon^m_n(\tilde{\lambda}_2)^m_{n-1} = -2\tilde{\alpha}_1(\tilde{\rho}^\circ)^m_n \tag{14}$$

$$2\tilde{\alpha}_2\, n(n+1)\tilde{\chi}^m_n + m(\tilde{\lambda}_2)^m_n + \epsilon^m_{n+1}\,(\tilde{\lambda}_1)^m_{n+1} + \epsilon^m_n(\tilde{\lambda}_1)^m_{n-1} = 2\tilde{\alpha}_2(\delta^\circ)^m_n \tag{15}$$

where

$$\varepsilon_n^m = (n^2-1) \quad \frac{n^2-m^2}{4n^2-1} \quad , \quad \tilde{\alpha}_1 = \frac{1}{2\Omega}\,\alpha_1$$

$$C_n = \frac{[n(n+1)]^2}{2\tilde{\alpha}_3} \quad , \quad \tilde{\alpha}_2 = \frac{1}{2\Omega}\,\alpha_2$$

$$, \quad \tilde{\alpha}_3 = 2\Omega a^2 \alpha_3$$

These equations can be written

$$AX = B$$

where A is a real square matrix and B is a complex column vector of order 4(J+1). The solution X, when iterated over all levels until convergence occurs, gives the adjusted motion field which is consistent with the tendencies of the previous forecast.

ON THE GENERATION OF LARGE-SCALE DIVERGENT WINDS AND RELATED ENERGETICS

J. Paegle/The University of Utah

Burger (1958) demonstrated that the ultra-long waves of the atmosphere should obey a simplified vorticity equation of the form

$$f \frac{\partial \omega}{\partial p} = \beta v \tag{1}$$

where f and β are the Coriolis parameter and its meridional gradient, respectively, ω is the vertical motion and v is the meridional wind.

Integration of (1) over pressure gives

$$\omega(p) = \int_{o}^{p} \frac{\beta v}{f} dp \tag{2}$$

In mid-latitudes, the integrand of (2) has a magnitude on the order of 10^{-2} day^{-1}, for v on the order of 10 m/s. Thus, for essentially barotropic ultra-long waves, (2) suggests

$$\omega(\text{surface}) = 0 \ (100 \text{ mb/day})$$

while for ultra-long waves for which v changes sign with height

$$\omega(\text{surface}) << 100 \text{ mb/day}$$

Therefore, for the barotropic case, parcels of air that follow ultra-long wave trajectories on the surface of the earth would have pressure variations that greatly exceed observed values, except in the vicinity of high mountains. It may be concluded that barotropic planetary scale waves are possible only in the presence of high mountains that have a significant projection upon ultra-long wave components.

Figure 1 presents 200 mb and 850 mb meridional flows summed over longitudinal wavenumbers 0-3 at various latitudes. The data is from the DST period February 1, 1976-March 5, 1976, and is described in more detail by Paegle, et al. (1979). The fundamental conclusion is that from about 28N, southward into most of the Southern Hemisphere, the ultra-long waves are more similar to vertically reversing monsoonal circulations than to nearly barotropic wind systems shaped by topography. In the mid-latitudes of the Northern Hemisphere, the present results support the important role of topography found in many other studies.

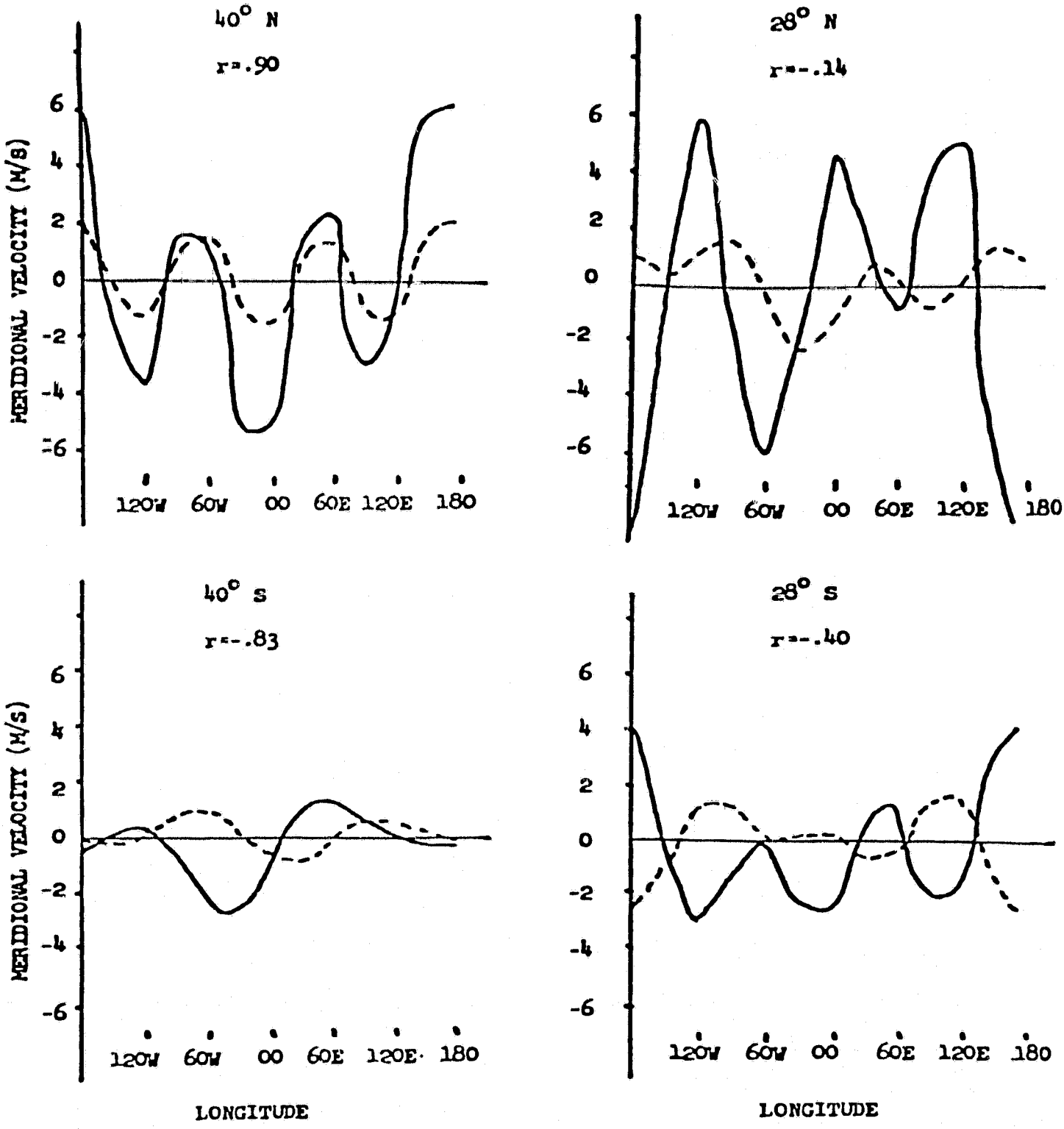

Figure 1. Long wave contribution to the meridional flow component at indicated latitudes at 200 mb (solid curves), and 850 mb (dashed curves) for the time average of the winter 1976 DST data. The correlation coefficients between the two levels are indicated by r values.

Figure 2 displays the 200 mb divergent meridional wind for the same data set. It shows strong upper level outflow from the heavily precipitating regions over the Amazon basin, equatorial Africa, and the tropical Western Pacific. There is some similarity of these areas to the 200 mb ageostrophic meridional flow from high to low pressure shown in Figure 3. These poleward divergent and ageostrophic flows appear to emanate from strong convective heating zones calculated by Herman and Schubert (1979) for this data set and are associated with accelerations of the subtropical jet stream displayed in Figure 4.

The meridional energy flux of the time-averaged fields is shown in Figure 5. It indicates poleward energy fluxes from about 40S to about 20N, at 200 mb, indicating that the stationary features of the subtropical jet stream may be influenced by the distribution of tropical latent heating.

These results suggest that longitudinal gradients of tropical heating play a more direct role in the forcing of long tropospheric waves than is usually indicated. Further study should be done with forthcoming FGGE data analyses to test the generality of the conclusions. This could be particularly important if the short-term predictability of energy fluxes and divergent and ageostrophic flows is as sensitive to tropical, and even cross-equatorial, effects as suggested in modeling studies presented by Paegle, et al. (1979) and by Lewis (1979).

References

Burger, A., Tellus, 10, 195-205, 1958.

Herman, G. F., and S. D. Schubert, Fourth NASA Weather and Climate Program Science Review, Jan. 24-25, NASA Conf. Publ. 2076, 177-181, 1979.

Lewis, F. P., Latent heat-induced divergence and the ultra-long waves of the subtropics and mid-latitudes, Doctoral Dissertation, Department of Meteorology, The University of Utah, 1979.

Paegle, J., J. N. Paegle, F. P. Lewis, and A. J. McGlasson, Description and interpretation of planetary flow structure of the winter 1976 DST data, submitted to Mon. Wea. Rev., 1979.

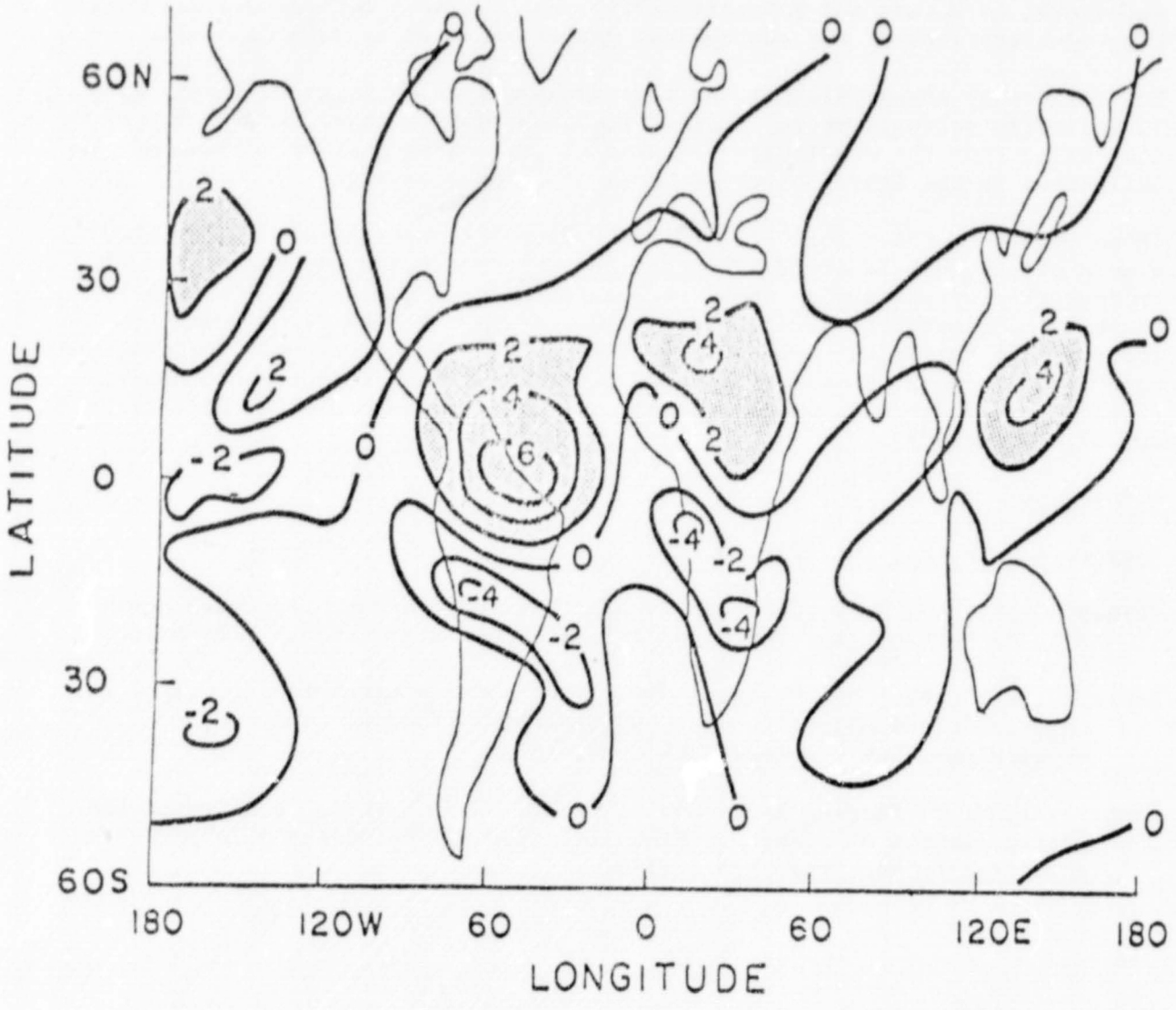

Figure 2. Divergent meridional wind component at 200 mb, averaged over the winter 1976 DST period. Shaded regions indicate southerlies > 2m/s

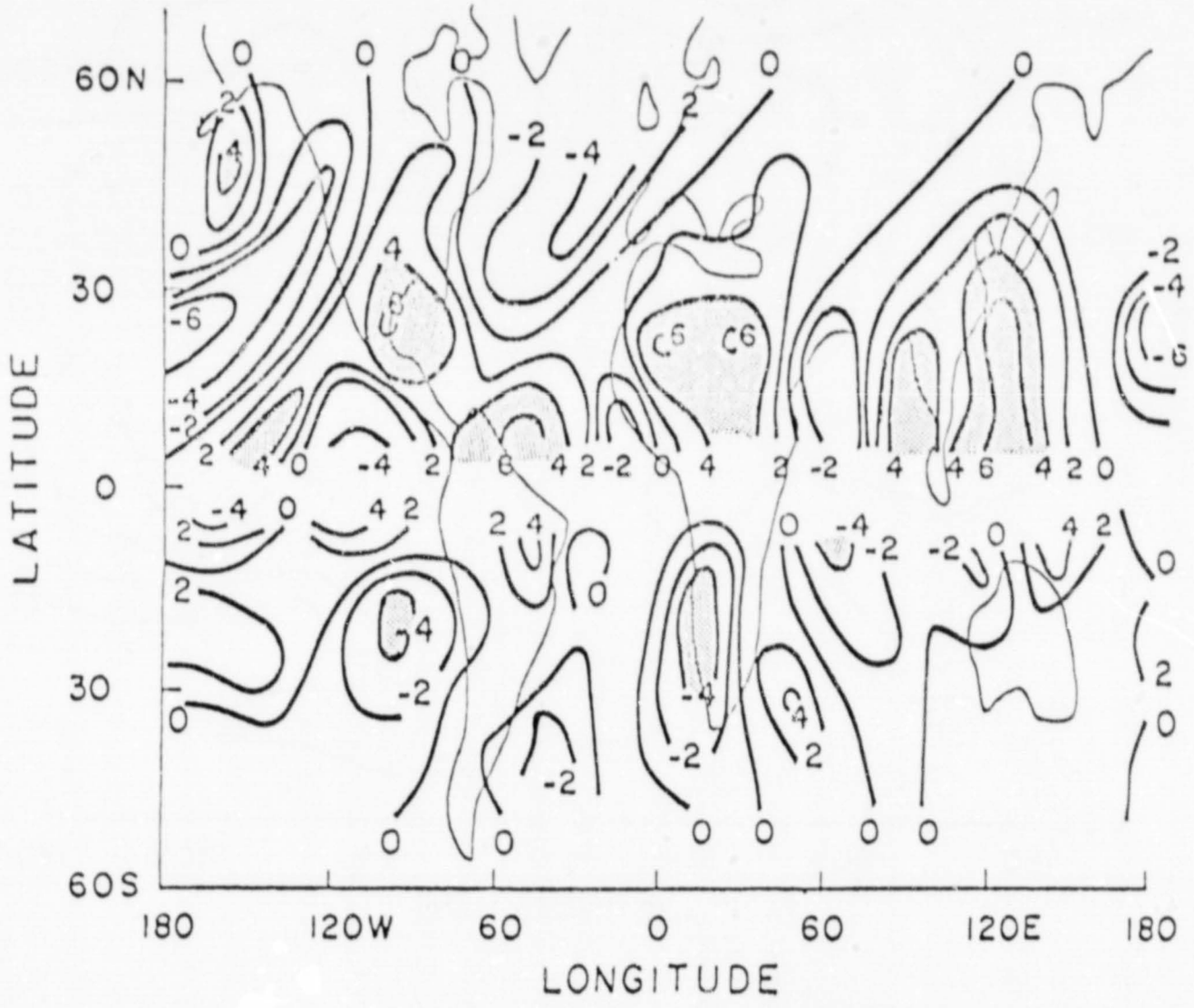

Figure 3. Cross-isobaric meridional wind component at 200 mb, averaged over the winter 1976 DST period. Shading indicates regions where the poleward ageostrophic values exceed 4 m/s. The region between 8°N and 8°S is not analyzed because of the poorly determined geostrophic wind at these latitudes.

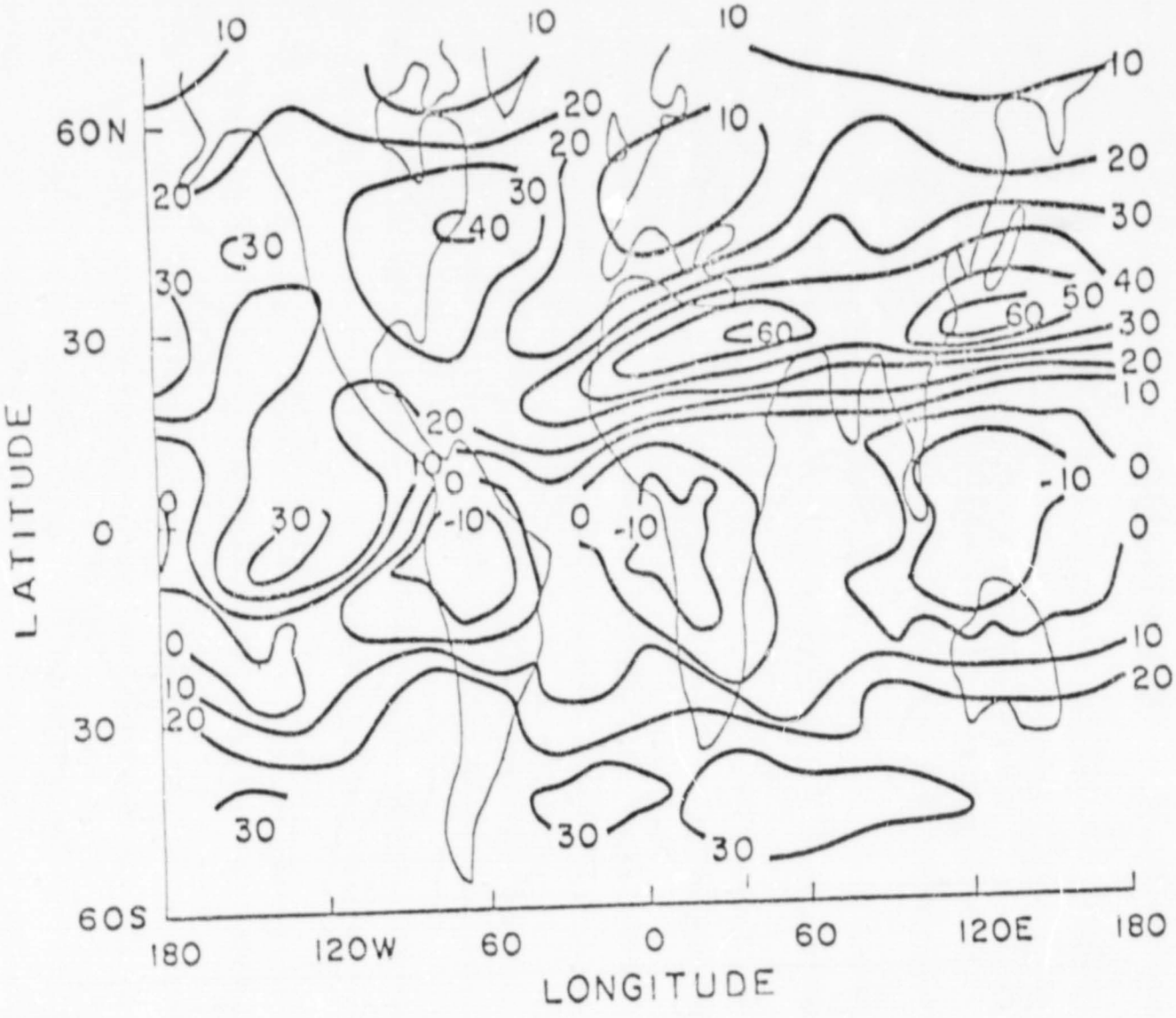

Figure 4. Time-averaged zonal wind component at 200 mb for the winter 1976 DST data (m/s).

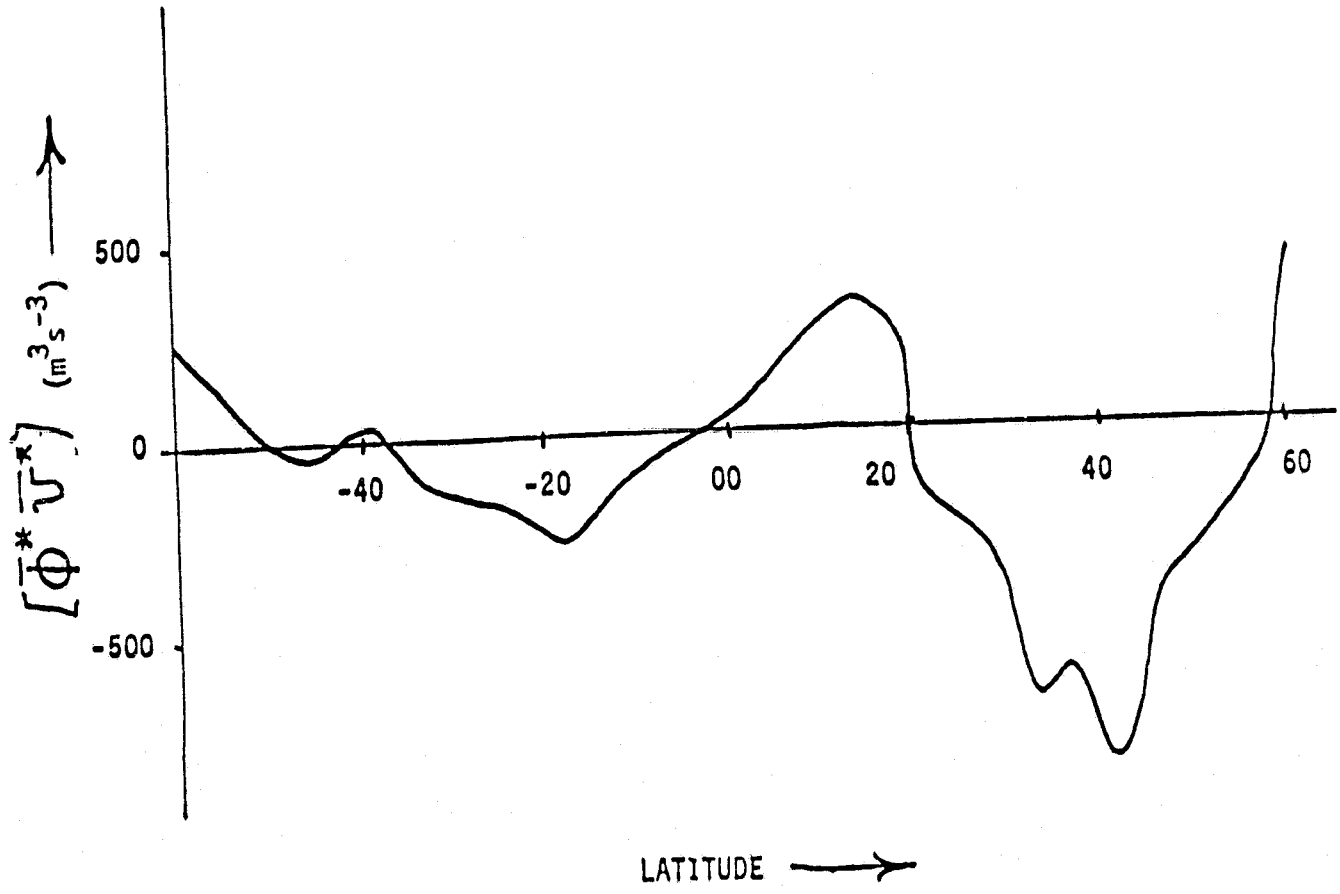

Figure 5. Meridional energy flux as estimated from the correlation of geopotential and meridional flow for the average 200 mb DST data.

July 26, 1979

WIND WAVE DEVELOPMENT

E. Mollo-Christensen/MIT

A presentation is made of observations of wind waves on the ocean and as observed in the laboratory during a recent experiment performed jointly with A. Ramaonjiarisoa at l'Institute Mecanique Statistique de la Turbulence at the University of Aix-Marseille II.

The new information shows the existence of subharmonic transitions in the wave field, as predicted by the analysis of Longuet-Higgins (1978). This subharmonic instability is followed by crest-pairing, a process by which one crest simply overtakes the previous crest and disappears (Figure 1). Through this process, the wave loses momentum, and this momentum has to be transferred either to the mean flow as drift current or to waves of larger scale. If the momentum transfer takes place at a favorable phase of the larger scale waves, the larger scale waves will grow by absorbing momentum and thus also some wave energy.

This process is demonstrated in experiments on group collision in the absence of wind, in experiments with group collision in the presence of wind and naturally occurring wind waves, and also by observation of naturally occurring field.

The process of wind group formation is also discussed. First, group formation by crest-pairing, then group merger because group of different length formed through crest-pairing and merger tend to have slightly different group velocity. The group lengths, measured in terms of wavelengths, tend to cluster around the Fibonacci numbers (Figure 2). When the groups become very long, through merger, they tend to split again; the result is a recurrence process, similar to the Fermi-Pasta-Ulam recurrence.

In conclusion, while nonlinear waves tend to propagate and form groups according to the predictions of third-order theory, including following the nonlinear Schroedinger equation for modulations, the presence of crest-pairing violates the conservation of crests criterion, so that, to the modulation equations one will have to add transition rules, yet to be defined. It also appears that internal wave packets, as observed on the seasonal thermocline, will tend to cluster in lengths around the Fibonacci multiples of the wavelength, as suggested by satellite observation. Crest-pairing may also be a process of importance in other kinds of wave fields, possibly including topographic Rossby waves.

Yet another observation is that the sudden occurrence of subharmonic fluctuations also takes place in the air boundary layer over the wave field. This could well be caused by vortex pairing, as observed in free shear layers by Winant and Browand (1974). While the results are preliminary, they suggest that strongly nonlinear processes that occur very rapidly, and thus will tend to appear negligible in a scaling analysis, may still be of crucial importance.

References

Longuet-Higgins, M. S., Proc. Roy. Soc. A, 360, 489-505, 1978.

Winant, C. D., and F. K. Browand, J. Fluid Mech., 63, 237-256, 1974.

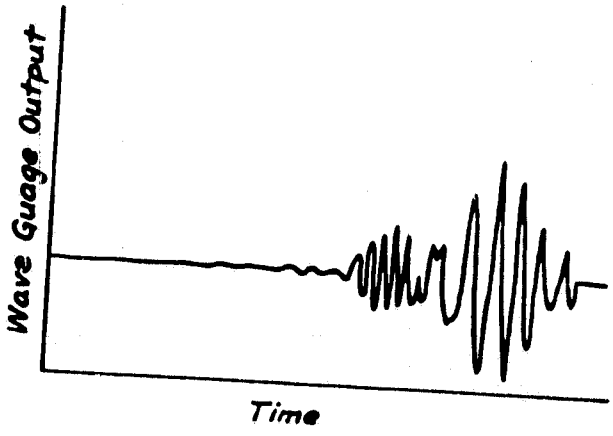

Figure 1. Crest Pairing Induced when Low Frequency Group of Gravity Waves Overtakes High Frequency Group

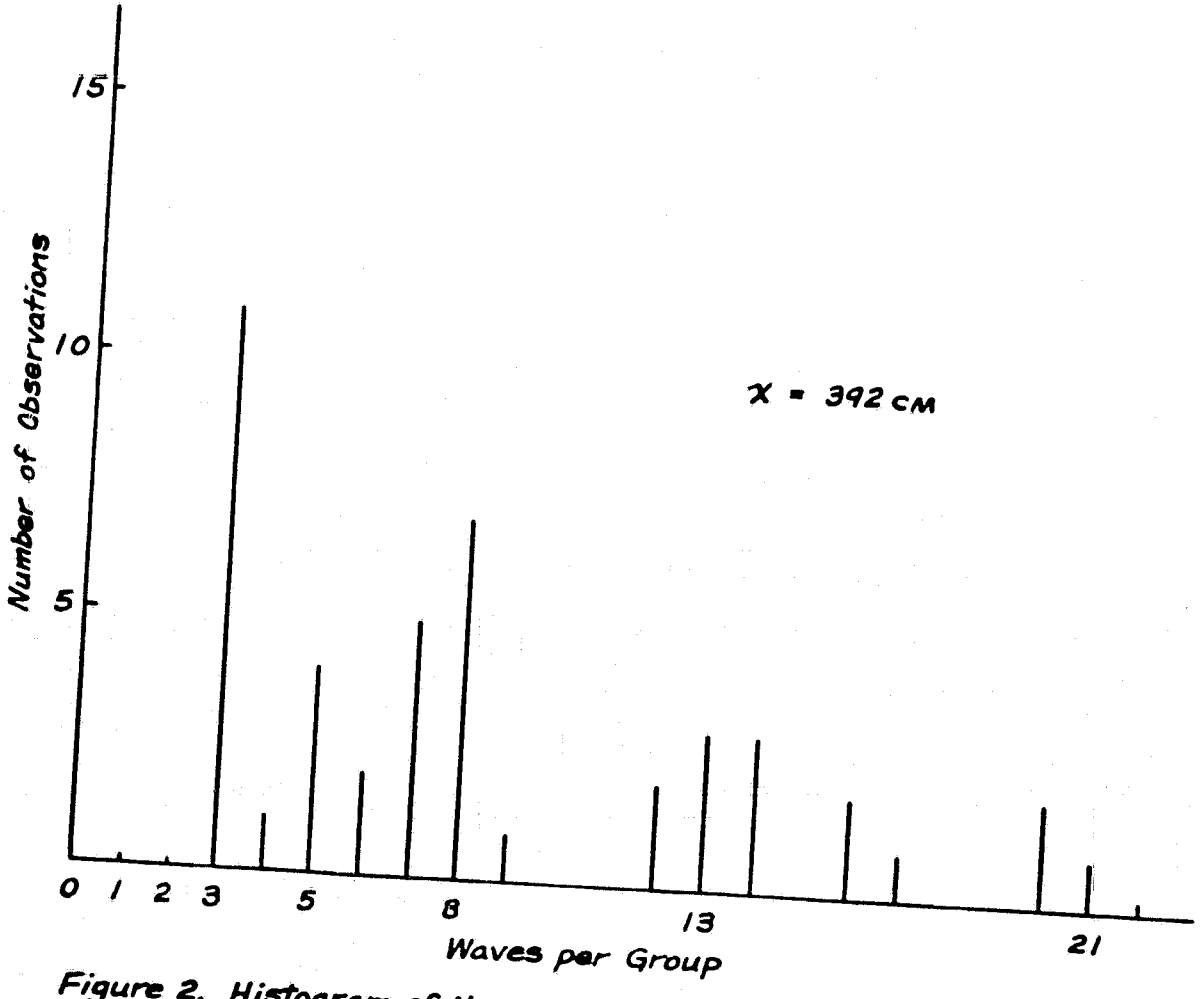

Figure 2. Histogram of Number of Waves per Group. Note Clustering about Fibonacci Numbers, which are 0, 1, 2, 3, 5, 8, 13, 21, etc.

August 9, 1979

NUMERICAL MODELING OF STRATOCUMULUS IN THE BOUNDARY LAYER

J. W. Deardorff/Oregon State University

Much of the motivation for studying the turbulence in a boundary layer which contains stratocumulus in its upper portion lies in predicting the entrainment rate. The mixed-layer growth rate is the difference between the entrainment rate and the large-scale vertical velocity at the mixed-layer top. The boundary layer height is then an integral of the growth rate over time. The stratocumulus-capped marine layer often situated just off the west coast of the US, for example, may, because of subsidence, frequently be too shallow to cross the coast range of western Oregon in a sea-breeze situation in summer. The interior valleys may swelter in a heat wave until the marine layer can grow another 100μm deeper and flow through the passes in the coast range. Satellite photographs clearly illustrate the problem.

The three-dimensional numerical model of the clear boundary layer developed by Deardorff (Boundary-Layer Meteor., 1974) was modified and applied to a boundary layer that could be saturated in its upper portion. Recently, the results have been analyzed for the case of the "dry cloud" with or without strong surface heating but with radiative cooling at its top, for a real cloud occupying the upper half of the boundary layer with or without radiative cooling at the top, and for a cloud-filled boundary layer with radiative cooling at its top.

In the dry-cloud cases, the cloudtop cooling was inserted at a fixed height within the upper mixed layer but below the mean capping inversion or stable layer. The enhancement of buoyancy flux in the upper mixed layer was very noticeable, and it was clearly seen how the mechanism alone, in the absence of any surface heat flux, could generate the turbulence that would keep a mixed layer well mixed.

In the numerical simulations of real stratocumulus, the influences of cloud water were very important in enhancing the buoyancy flux in the cloud layer. This was due to two reasons: (1) the upward moisture flux in the cloud layer caused a positive buoyancy flux there because of the Clausius-Clapeyron relationship, and (2) evaporation of cloud droplets into air entraining down into the cloud top caused this entrainment to proceed more quickly and easily. Thus, the negative buoyancy flux of entrainment that was observed to occur in the cloudtop region rapidly switched over to a positive buoyancy flux at slightly smaller heights. A strong positive moisture flux was also observed in this region, due to the entrainment of dry air. Consequently, the mean moisture content of the mixed layer tended to decrease with time in the deep mixed layers studied, and cloud base tended to rise with time, even when the evaporation rate from the surface was appreciable.

In the real cloud simulations, the addition of radiative flux divergence (longwave) to the upper 50μm of cloud within each grid column produced no appreciable change in shape of the buoyancy-flux profile and turbulence energy. This was apparently due to the fact that the cloudtop hummocks were

located within the horizontal mean capping inversion, and the radiative extinction scale utilized (less than 50μm) was smaller than the depth of this mean capping inversion. However, the opposite result probably would have been obtained if the cases studied had been for shallow mixed layers and if the radiative extinction length scale had been considerably larger (100-150μm).

With or without radiative flux divergence at cloud top, the entrainment rates obtained from the numerical simulations with cloud-water present, even after normalization by the mixed-layer convective velocity scale, were found to be about an order of magnitude greater than for a clear mixed layer with comparable capping-inversion strength . This result is ascribed to the powerful influence of evaporative cooling acting on air which entrains down into the mixed layer.

Unfortunately, due to model truncation error at and above simulated cloud top, many of the conclusions on the entrainment rate and entrainment buoyancy flux were more qualitative than quantitative. Future numerical simulations of this nature could benefit substantially by using a much finer vertical grid than 50μm, at least in the vicinity of the mixed-layer top.

August 16, 1979

CLIMATIC EFFECT OF AN INCREASE OF CO_2 IN THE ATMOSPHERE

S. Manabe/Geophysical Fluid Dynamics Laboratory, NOAA

A recent study of the climatic impact of future anthropogenic increase in the atmospheric CO_2-concentration is described. For this study, a global model of climate with realistic geography and with seasonal variation of insolation was constructed. The model consists of: (1) a spectral model of the atmospheric general circulation, (2) a simple mixed-layer ocean model with a uniform thickness, and (3) a heat- and water-balance model of the continents. It is encouraging that this climate model successfully reproduces many of the basic characteristics of the seasonal variation in the geographical distribution of atmospheric temperature. The climatic effects of a CO_2-increase are evaluated by comparing two model climates, with the normal and four-times-the-normal concentration of carbon dioxide.

In conclusion, the warming of the model atmosphere in response to a quadrupling of CO_2-concentration is most pronounced in the lower troposphere of high latitudes due to the poleward retreat of the highly reflective snow cover and sea ice. The warming over the Arctic Ocean and the surrounding regions is at a maximum in early winter and is at a minimum in summer. Thus, the amplitude of the seasonal temperature variation reduces markedly. The reduction of sea ice thickness is responsible for the aforementioned seasonal asymmetries in warming.

August 23, 1979

SOME RESULTS WITH THE UCLA GENERAL CIRCULATION MODEL

M. Suarez/UCLA

The latest version of the UCLA general circulation model (GCM) was discussed. Simulations made with earlier versions of the model showed that, although the model compares favorably with the state of the art, it had several deficiencies. Some deficiencies were particular to the UCLA GCM; others were common to most GCM's. In an effort to improve the model, both for general circulation studies and for numerical weather prediction, two major design changes have been made:

(1) A potential enstrophy-conserving advection scheme in the equation of motion has replaced the previous scheme, which only conserved enstrophy for non-divergent flow. It is hoped that this scheme will improve the simulation of topographically forced motions.

(2) The treatment of the planetary boundary layer (PBL) has been dramatically modified by making the predicted PBL-top a coordinate surface. These and other more minor changes were discussed.

August 30, 1979

ON TROPICAL CIRCULATION AND CLIMATE ANOMALIES

S. Hastenrath/The University of Wisconsin

Variations of circulation and climate have been studied for a portion of the tropical belt extending from the Americas across the Atlantic to Africa and the Indian Ocean. Ship observations during 1911-1972 compiled as individual monthly means for one and five degree square areas provided the major data basis. This ensemble of observations is supplemented by conventional surface climatological and upper-air records at land stations and series of lake levels and river discharge.

A background climatology has been established for reference and has included the publication of atlases of the climate and circulation, and the oceanic heat budget, of the tropical Atlantic and Eastern Pacific (Hastenrath, 1977a,b,c,d; 1979; Lamb, 1977; Hastenrath and Lamb, 1977a,b; 1978a,b; Hastenrath and Guetter, 1978). A two-volume climatic atlas of the Indian Ocean is in press (Hastenrath and Lamb, 1979).

Mechanisms of climatic hazards have been studied with emphasis on the Central American-Caribbean region, the Ecuador-Peru coast, Northeast Brazil, Subsaharan Africa, and the Indian Subcontinent (Hastenrath, 1976; 1978; Hastenrath and Heller, 1977; Covey and Hastenrath, 1978; Kaczmarczyk and Hastenrath, 1979; Lamb, 1978a,b; Hastenrath and Wendland, 1979). Even during extremely deficient or abundant rainy seasons in a given region, departures in the large-scale circulation are small, albeit distinct. Statistical significance of departures can be tested against the climatic variability for the 60-year base period. It has further become apparent that patterns must be viewed in context over very large areas. With this provision, characteristic departure patterns can be identified in the large-scale circulation.

For example, during deficient rainy seasons in the Central American-Caribbean region (Hastenrath, 1976), the equatorward flank of the North Atlantic high is strengthened, the Northeast trade winds speed up, albeit in a band further South, and marked negative sea surface temperature anomalies extend from the realm of the cold Canary current across the North Atlantic in a broad zonal band between 10-20N; a tendency for opposite sea surface temperature departures is observed over much of the tropical South Atlantic; and the Eastern Pacific is anomalously warm in similarity to El Nino events which have a tendency to coincide with Central American-Caribbean droughts. Stratification with respect to droughts in Subsaharan Africa yields similar departure configurations (Lamb, 1978a,b). Abundant rainy seasons are concomitant with approximately inverse circulation anomaly patterns.

Rainfall in Northeast Brazil (Hastenrath and Heller, 1977; Covey and Hastenrath, 1978) is related to the southernmost seasonal migration of the near-equatorial confluence axis and convergence band over the Western Atlantic. During drought years, these quasi-permanent circulation features stay comparatively far North, concomitant with an equatorward expansion of the South Atlantic and a poleward retraction of the North Atlantic subtropical highs. This is accompanied by

positive sea surface temperature departures over much of the tropical North Atlantic and negative anomalies in the South Atlantic and the adjacent equatorial waters. Again, abundant rainy seasons in Northeast Brazil are characterized by broadly inverse atmospheric-hydrospheric departure patterns.

A signficant negative correlation between Northeast Brazil rainfall and Eastern Pacific sea surface temperature (Covey and Hastenrath, 1978), as well as an apparent linkage between events on the Indian Subcontinent and the Americas, seems to be related to a large-scale mass exchange of the Southern Oscillation type, but requires further study. On the whole, there is a strong spatial correlation in annual rainfall totals in the zonal direction over thousands of kilometers whereas, in the meridional direction, correlations rapidly fade out and reverse sign.

Map analyses, based on stratification with respect to extreme hydrometeorological events in key regions, are complemented by principal component analysis and spectral techniques (Hastenrath, 1978; Hastenrath and Wendland, 1979; Kaczmarczyk and Hastenrath, 1979). Principal component analysis (Hastenrath, 1978) identifies preferred modes of departure patterns in the pressure and sea surface temperature fields. These corroborate the various regional stratification studies, in that similar spatial patterns are obtained and the time series of principal components are significantly correlated with hydrometeorological index series in key regions. Spectral techniques (Hastenrath and Wendland, 1979; Kaczmarczyk and Hastenrath, 1979) were used in an attempt at a preliminary inventory of the preferred time scales of variability in the regional climates and of the large-scale spatial linkages of regional extreme events.

Major departure characteristics of anomalous rainy seasons are already apparent at the height of the preceding winter circulation, the inertia of the atmosphere-ocean system, thus offering the potential of seasonal foreshadowing. Our work so far has been essentially diagnostic. Prospects for prognosis have emerged particularly from departure fields and time series of pressure, wind, and sea surface temperature in sensitive ocean areas. Timely availability of predictors will be crucial in operational prediction schemes. Remote sensing by satellites could become highly useful in such endeavors, as satellite data banks geared at the needs of climate diagnostics and prognosis come into being.

References

Covey, D. L., and S. Hastenrath, Mon. Wea. Rev., 106, 1280-1287, 1978.

Hastenrath, S., J. Atmos. Sci., 33, 202-215, 1976.

Hastenrath, S., Quart. J. Roy. Meteor. Soc., 103, 519-526, 1977a.

Hastenrath, S., Tellus, 29, 523-529, 1977b.

Hastenrath, S., J. Meteor. Soc. Japan, 55, 494-497, 1977c.

Hastenrath, S., Archiv. Meteor. Geophys. Bioklim., Ser. A, 25, 309-321, 1977d.

Hastenrath, S., J. Atmos. Sci., 35, 2222-2231, 1978.

Hastenrath, S., Proceedings of Third Annual NOAA Climate Diagnostics Workshop, Oct. 31-Nov. 2, Miami, Fla., 1978.

Hastenrath, S., and P. Guetter, Archiv. Meteor. Geophys. Bioklim., Ser. B, 26, 97-103, 1978.

Hastenrath, S., and L. Heller, Quart. J. Roy. Meteor. Soc., 103, 77-92, 1977.

Hastenrath, S., and P. Lamb, Climatic Atlas of the Tropical Atlantic and Eastern Pacific Oceans, Univ. of Wisc. Press, 1977a.

Hastenrath, S., and P. Lamb, Mon. Wea. Rev., 105, 1019-1029, 1977b.

Hastenrath, S., and P. Lamb, Heat Budget Atlas of the Tropical Atlantic and Eastern Pacific Oceans, Univ. of Wisc. Press, 1978a.

Hastenrath, S., and P. Lamb, Tellus, 30, 436-448, 1978b.

Hastenrath, S., and P. Lamb, Climatic Atlas of the Indian Ocean, Part 1. The Surface Climate and Atmospheric Circulation and Part II. The Oceanic Heat Budget, Univ. of Wisc. Press, 1979.

Hastenrath, S., and W. Wendland, Tellus, 31, 28-38, 1979.

Kaczmarczyk, E., and S. Hastenrath, On spectra and coherence of tropical climate anomalies, unpublished manuscript, 1979.

Lamb, P., Archiv. Meteor. Beophys. Bioklim, Ser. B, 25, 21-31, 1977.

Lamb, P., Tellus, 30, 240-251, 1978a.

Lamb, P., Mon. Wea. Rev., 106, 482-491, 1978b.

September 6, 1979

A SIMPLE MECHANISM FOR BLOCKING

E. Kalnay-Rivas/NASA GSFC and

L.-O. Merkine/Technion-Israel Institute of Technology

In this study, we show that atmospheric blocking can occur as a result of local resonant interaction between forced Rossby lee waves. In order to study the simplest possible model of local generation of blocking, we use the barotropic vorticity equation on a β-plane open channel. Unperturbed zonal flow entering the channel infringes on an isolated mountain (Figure 1)* and produces steady state Rossby lee waves (Figure 3a). We then allow interaction between this basic solution and Rossby waves produced by another source of localized forcing.

In the first part of the paper, we find by means of an analytical study of the far field solution, that friction plays a singular role in the dynamics of Rossby waves. In the presence of friction, Rossby lee waves generate a rectified current downstream of the orography, which does not vanish if we let friction go to zero. The generation of Rossby lee waves, and the orientation of the rectified current depends on the width of the channel Ly, through the ratio between the minimum meridional wave number (π^2/L_y^2) and β/U. Figure 2 shows a schematic representation of the steady state solution as determined from the far field analysis. The characteristics of the near field (dashed in Figure 2) are inferred from the perturbation energy equation.

Multiplying the potential vorticity equation

$$\left(\frac{\partial}{\partial t} + U_1 + \psi'\nabla\right)\left(\nabla^2\psi' + \beta y + f_o \frac{hm}{H}\right) = -\frac{\nabla^2\psi'}{\tau} \quad , \tag{1}$$

by $-\psi'$ and integrating over the open channel, a perturbation kinetic energy is obtained:

$$\frac{\partial KE'}{\partial t} = G' - D' + B' \quad , \tag{2}$$

where G', D' and B' are generation, dissipation and lateral boundary transports of perturbation kinetic energy, respectively. The generation term, due to the interaction of the zonal flow, the perturbation flow and the topography, is

$$G' = -U \frac{f_o}{H} \int v' h_m \, dx \, dy \quad , \tag{3}$$

$$h_m \neq 0$$

* A sponge layer was introduced to dissipate waves with negative group velocity generated during the transient stage. Like the rigid top boundary condition of atmospheric models, the upstream boundary condition of unperturbed flow is well posed, but produces spurious reflection of transient long waves which propagate upstream.

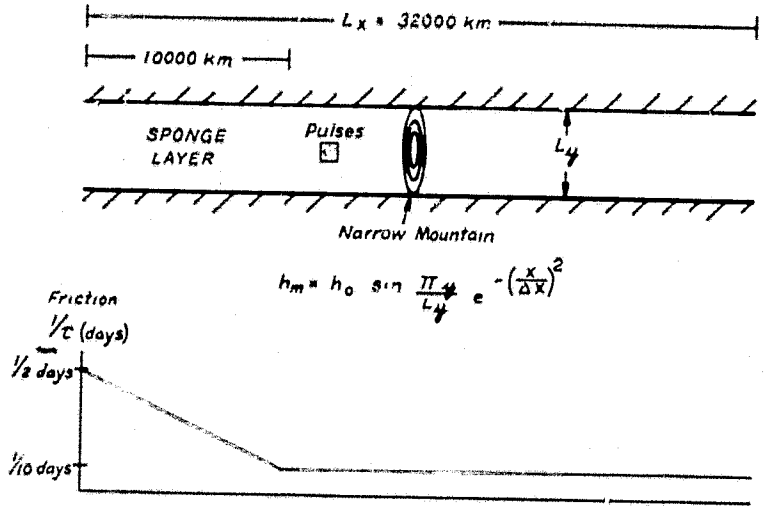

Figure 1. Open channel on a β-plane geometry. The small squad domain represents the region where pulsating lows are generated.

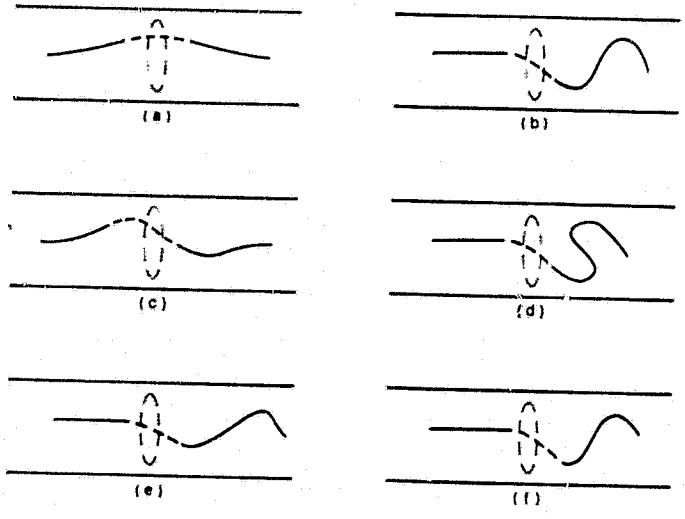

Figure 2. Schematic representation of the steady state streamfunction solution when zonal flow impinges on a narrow mountain. Cases a and b: Frictionless flow; Cases e to f: Flow with Ekman friction.
a: $\beta/U < (\pi/L_y)^2$; b: $\beta/U > (\pi/L_y)^2$; c: $\beta/U < (\pi/L_y)^2$; d: $\beta/U > 2(\pi/L_y)^2$;
e: $(\pi/L_y)^2 < \beta/U < 2(\pi/L_y)^2$; f: $\beta/U = 2(\pi/L_y)^2$.

and is proportional to the intensity of the northerly flow ($v'<0$) over the orography h_m. This indicates the existence of a positive feedback mechanism. Perturbation kinetic energy is realized, as Rossby lee waves, downstream of the mountain, whereas the upstream flow is largely undisturbed. Strong generation of perturbation kinetic energy will intensify the low in the lee of the mountain. This, in turn, increases the zonal pressure gradient, increasing at the same time the northerly flow and the generation of perturbation energy. The positive feedback mechanism allows a simple interpretation of the multiple flow equilibria solutions found by Charney and DeVore (1979) for nonlinear flow over topography. Under initial conditions corresponding to high index, the generation of perturbation kinetic energy is inefficient, and the flow will remain in the "attractor basin" of the high index solution. If the initial flow has a large amplitude perturbation flow (low index) with a favorable phase, there will be strong generation, and the flow will remain low index. If the phase is unfavorable perturbation kinetic energy will decay and the flow will evolve towards high index.

The analysis of the generation term can be generalized to any type of stationary forcing (orography, heating or even locally enhanced baroclinic instability). If we represent the effect of localized forcing by a term $\frac{\nabla^2\Psi_o(x,y)}{T}$ in the vorticity equation (1), the generation term becomes

$$G' = 1/T\iint_{\Psi_o \neq 0} \nabla\Psi'_o\nabla\Psi/dx\,dy \qquad (4)$$

Again, the generation of perturbation energy depends on the phase relationship between the perturbation flow and the streamlines associated with the vorticity source. In the case of surface heating, there are also possible feedback mechanisms, since the intensity of the heat fluxes depends on the characteristics of the flow itself (speed, temperature, moisture content, etc.).

In most of our experiments, we studied the interaction between stationary Rossby waves induced by orography (Figure 3a) and the flow induced by the periodic generation of pulses or "lows" upstream of the mountain. Every 3 days we increased the instantaneous value of the potential vorticity by an amount equal to 30 percent of the Coriolis parameter. This was done in a square domain of 1500 km side indicated by darker shading in Figure 1. These "lows" can be interpreted as a crude simulation of the effect of periodic cyclogenesis in a region of enhanced baroclinicity.

Since the pulses are always of the same sign, the net effect of the generation of lows in the absence of a mountain is to produce a small amplitude time-averaged flow (Figure 3b) superimposed with an even smaller amplitude time varying solution. It is the time-averaged solution that can interact resonantly with the orography, so that our results are approximately independent of the frequency of generation of the pulses.

When the pulses are generated upstream of the mountain, the results depend crucially on the position of the region of generation. If the pulses are generated at a region 6000 km upstream of the mountain, their induced flow is

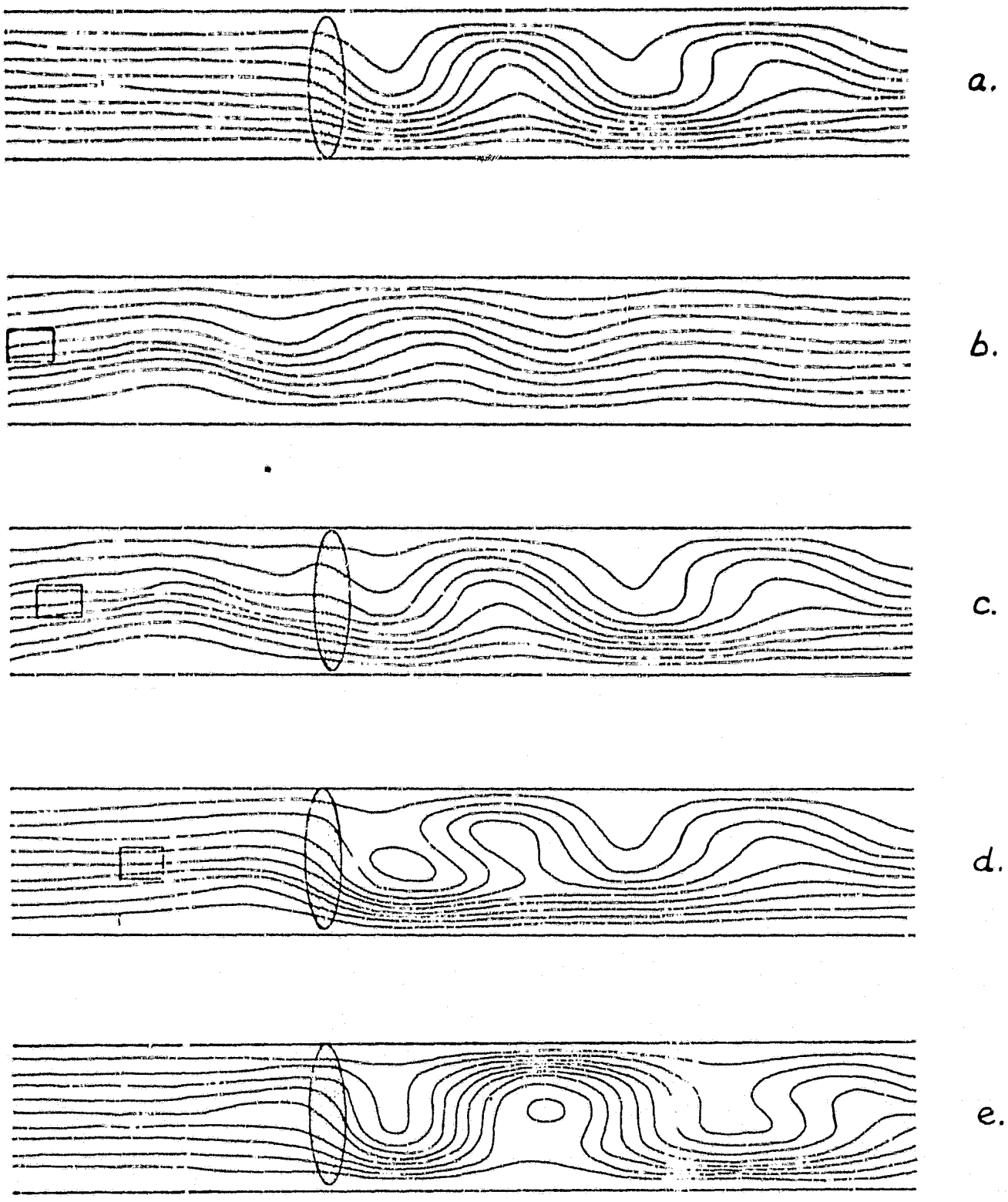

Figure 3. Streamfunction field obtained with $U = 10 m\ sec^{-1}$, $Ly = 5000$ km, $\tau = 20$ days, maximum mountain height of 2000 m. a) No pulses, b) Pulses (lows) every 3 days, no orography (time-averaged solution); c and d) Lows generated every 3 days from the indicated square domain; e) As in 3b, but with maximum mountain height of 3000 m.

unfavorable for the generation of perturbation kinetic energy over the orography the resulting flow (Figure 3c) is not very different from the unperturbed flow (Figure 3a). However, when the lows are generated at a region 4000 km upstream of the mountain, there is strong blocking development downstream of the orography (Figure 3d). Somewhat similar blocking patterns can be obtained by increasing the orographic forcing itself, from a maximum height of 2000 m to 3000 m (Figure 3e) in the absence of pulses.

The orographic generation of perturbation kinetic energy corresponding to the three cases of Figure 3a, c and d is plotted in Figure 4. Note the very rapid response in the enhancement of the generation of KE' after the signal from the pulses first reach the orography. As indicated before, the generation is quite insensitive to the frequency of generation of individual pulses (except for its influence in the amplitude of the time-averaged flow). The observed overshooting in the generation is typical of the numerical experiments. The positive feedback mechanism increases the generation of KE' by deepening the low downstream of the mountain until the generation is compensated by advection and dissipation of KE'. This results, for smaller values of the dissipation constant (20 days in Figure 4), in a vacillating flow, even in the case of no pulses. Higher values of the friction (τ = 10 days) produce a steady state solution.

The realistic blocking development presented in Figure 3d is a nonlinear resonance phenomenon. We repeated experiments 3a, 3c and 3d with a linear model (Figures 5a, 5b, and 5c). Even though there is, as expected, resonant enhancement, the pattern in Figure 5c does not resemble blocking. The effect of a rectified current downstream, referred to in Figure 2 and clearly observable as a tilt in Figure 3 is absent in Figure 5.

In Figure 6, we have increased the width of the channel from 5000 km, used in Figure 3 to 8000 km, so that stationary Rossby waves with meridional wavenumber 2 and 3 can also be excited. The results are similar to those previously presented, except that we observe a strong excitation of the meridional wavenumber 2 component downstream of the region of pulse generation but immediately upstream of the mountain. Other integrations show an even stronger wavenumber 2 response, resembling the observed blocking upstream of the Rockies with low pressure in the coast of California and an intense ridge in northern latitudes.

The simple model presented here may be relevant to blocking in the real atmosphere. In particular, persistent blocking in the Atlantic seems associated with a favorable circulation over the Rockies, with enhanced northerly flow over orography and perhaps enhanced heating over the Gulf Stream. This can be seen to be the case in the persistent anomalous circulation observed in December 1976 (Taubensee, 1977) and January 1977 (Wagner, 1977). Indeed, enhanced orographic forcing seems to have been associated with a favorable distribution of anomalous sea surface temperatures in the Pacific. Following a suggestion of Namias (1978), Shukla and Bangaru (1979) have recently performed a sensitivity experiment with a GLAS GCM in which they introduced observed sea surface temperature anomalies in the Pacific multiplied by a

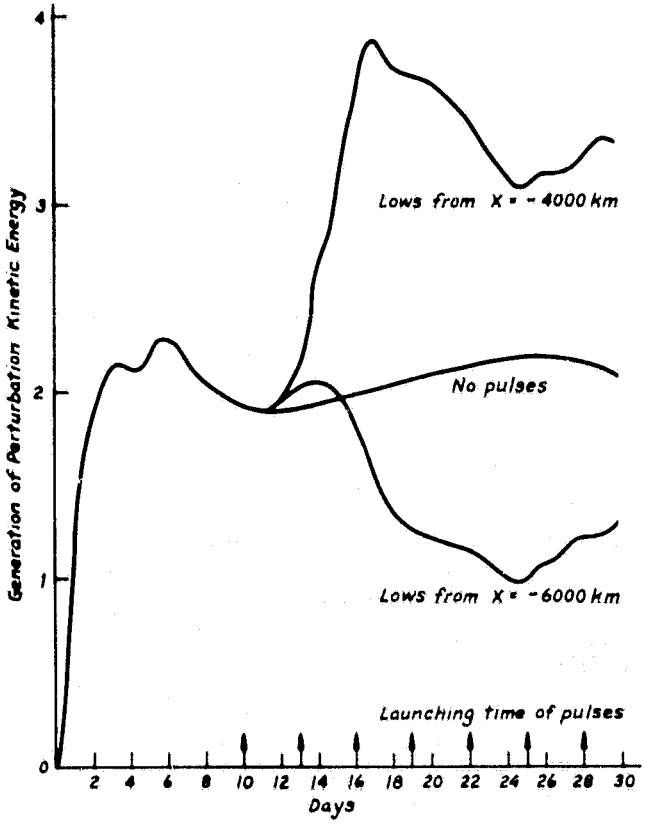

Figure 4. Generation of perturbation kinetic energy corresponding to the cases 3a, 3c and 3d.

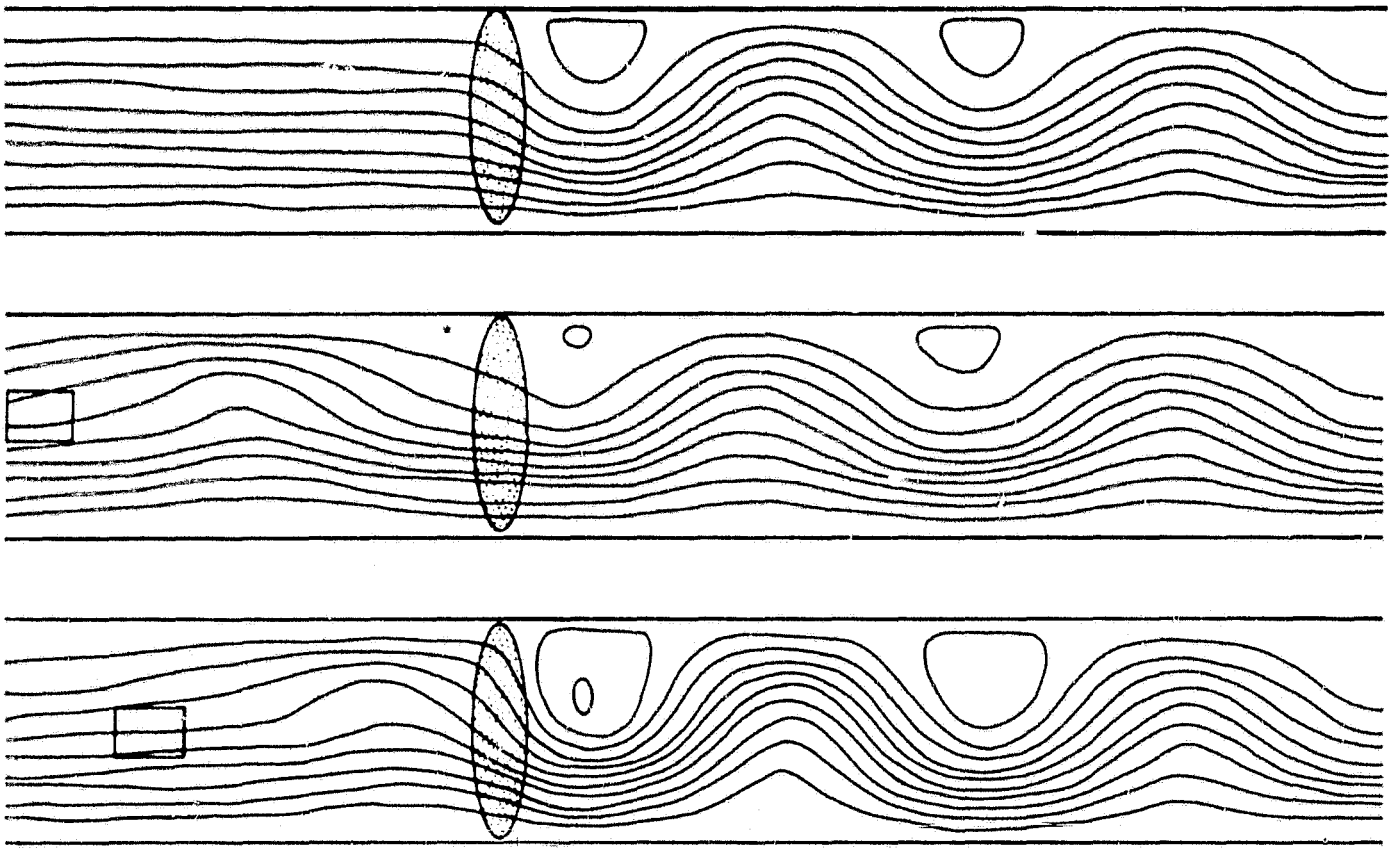

Figure 5. As in Figures 3a, 3c and 3d, but with a linear model.

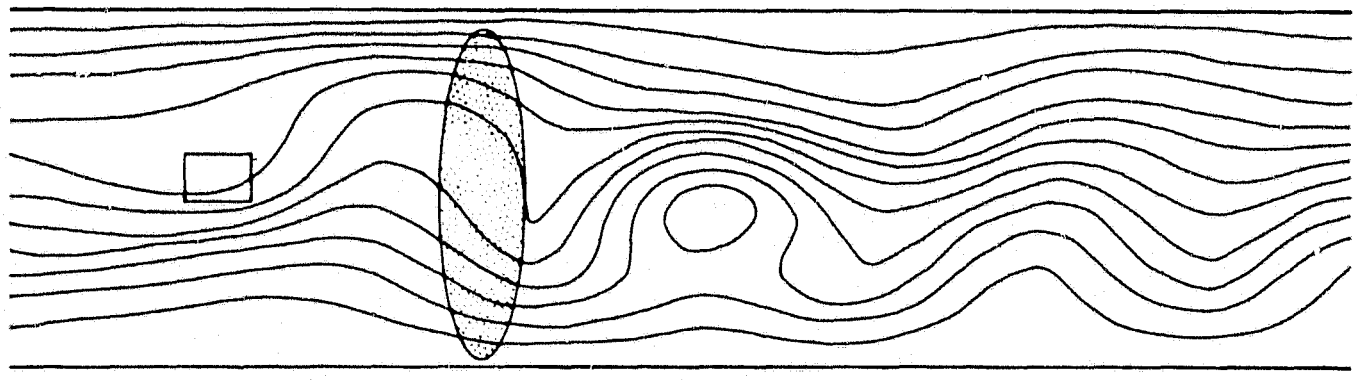

Figure 6. As in Figure 3d, but with Ly = 8000 km.

factor of 9/5 (Figure 7a). The SST anomalies enhanced the generation term over the Rockies (Figure 7b) and, as in the simple barotropic model, produced a maximum response downstream of the regions of orographic and thermal forcing.

We are presently conducting a systematic study of observed Atlantic blocking situations, and the relationship between the generation of perturbation energy over the Rockies and the duration of blocking.

Acknowledgments

The authors have benefited from discussions with J. G. Charney, J. M. Wallace, J. Paegle, M. Ghil, and M. Halem. J. Shukla has kindly provided us with Figure 7. The other figures were drafted by L. Rumburg.

References

Charney, J. G., and J. G. DeVore, 1979: Multiple flow equilibria in the atmosphere and blocking. J. Atmos. Sci., 36, 1205-1216.

Namias, J., 1978: Multiple causes of the North American abnormal winter 1976-1977. Mon. Wea. Rev., 106, 279-295.

Shukla, J., and B. Bangaru, 1979: Effect of Pacific sea surface temperature anomaly over North America: a numerical experiment with the GLAS model. Report of the JOC Study Conf. on Climate Models: Performance, Intercomparison and Sensitivity Studies. GARP Publ. Series No. 22, 501-518, WMO, Geneva, Switzerland.

Taubensee, R. E., 1977: Weather and circulation of December 1976. Mon. Wea. Rev., 105, 368-371.

Wagner, A. J., 1977: Weather and circulation of January 1977. Mon. Wea. Rev., 105, 553-557.

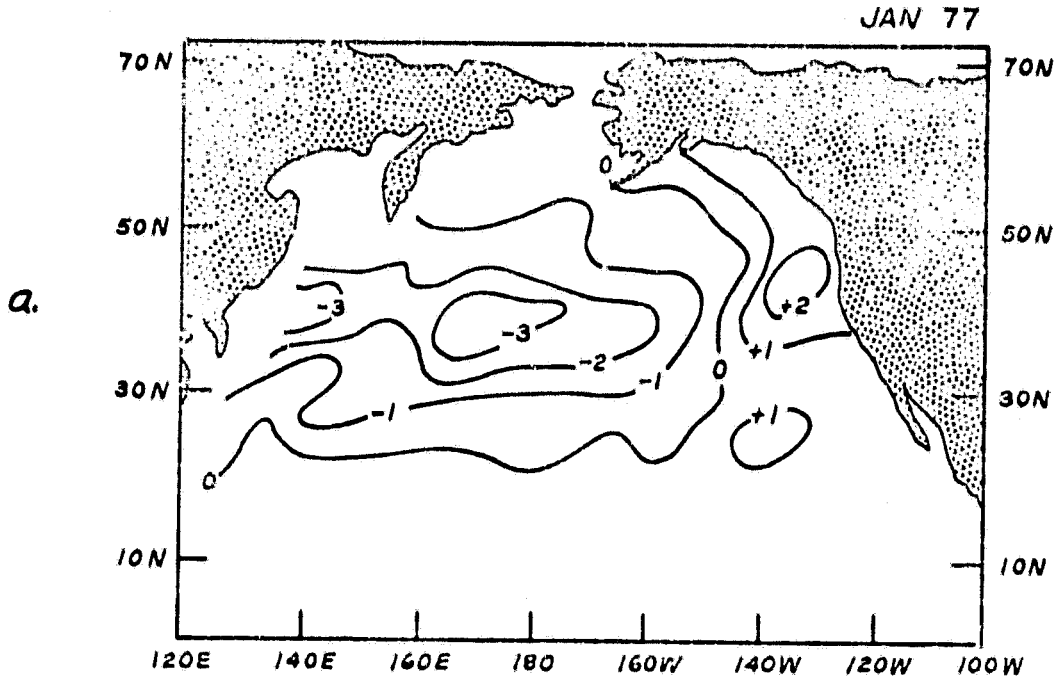

a.

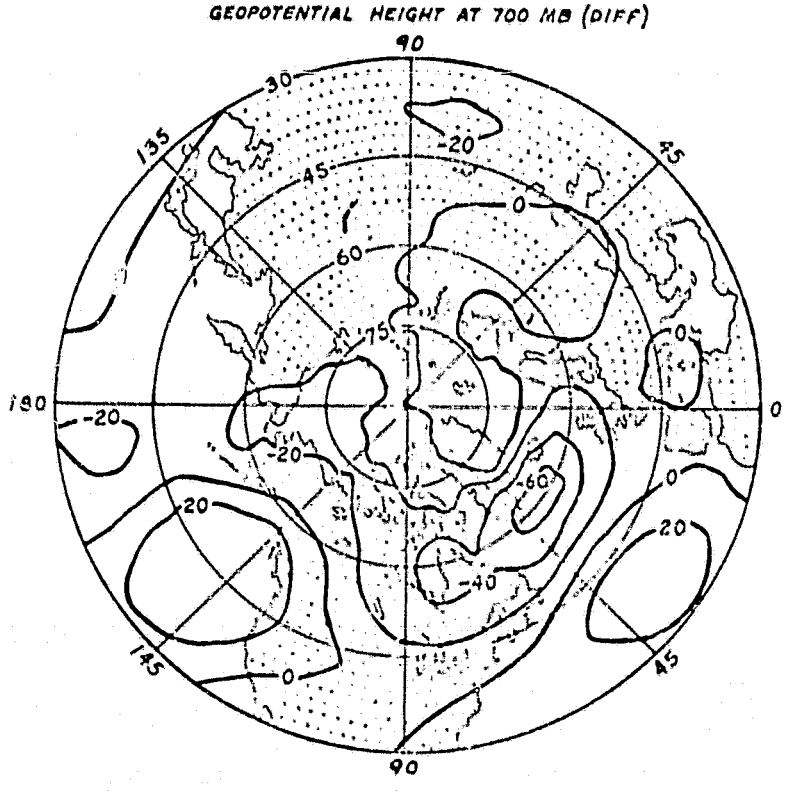

b.

Figure 7. a. Observed Pacific Sea Surface Temperature Anomalies (°F) during the Winter of 1976-1977.
b. Computed 700 mb Geopotential Height Anomalies (Reproduced from Shukla and Bangaru, 1979).

VI. RECENT PUBLICATIONS

RECENT PUBLICATIONS

Atlas, R., 1979: Case studies of major DST-6 sounding impacts with the GLAS model. NASA Conf. Publ. 2076,

_____, 1979: A comparison of GLAS SAT and NMC high resolution NOSAT forecasts from 19 and 11 February 1976. NASA Tech. Memo. 80591.

_____, M. Halem, and M. Ghil, 1979: The influence of satellite temperature sounding data and increased model resolution on forecasting. Research Activities in Atmospheric and Oceanic Modeling, Report No. 19, JOC, GARP WMO Working Group on Numerical Experimentation.

_____, _____, and _____, 1979: Subjective evaluation of the combined influence of satellite temperature sounding data and increased model resolution on numerical weather forecasting, Fourth Conf. on Numerical Weather Prediction, Preprint Volume, 319-328, AMS, Silver Spring, MD, October 29-November 1.

_____, and R. Rosenberg, 1980: A case study of the impact of satellite-derived temperature soundings on the prediction of an intense winter storm. In preparation.

Cane, M. A., 1979: The response of an equatorial ocean to simple wind stress patterns I: model formulation and analytic results. J. Mar. Res., 37, 233-252.

_____, 1979: The response of an equatorial ocean to simple wind stress patterns II: numerical results. J. Mar. Res., 37, 253-299.

_____, 1980: On the dynamics of equatorial currents with application to the Indian Ocean. Accepted by Deep Sea Res.

_____, V. Cardone, M. Halem, and J. Ulrich, 1980: A simulation study of the impact of Seasat-A on weather prediction. Submitted to Mon. Wea. Rev.

_____, and E. S. Sarachik, 1979: Forced baroclinic ocean motion III: an enclosed ocean. J. Mar. Res., 37, 355-398.

Charney, E., C. Lee, J. Rosenfield, 1979: Calculations of rotatory strengths in chiral chromophores, sensitivity to structural parameters in diewes. J. Amer. Chem. Soc., 101, 6802-6804.

Charney, J. G., and D. M. Straus, 1980: Form-drag instability, multiple equilibria and propagating planetary waves in baroclinic, orographically forced planetary wave systems. To appear in J. Atmos. Sci.

Ghil, M., 1980: The compatible balancing approach to initialization, and four-dimensional data assimilation. Submitted to Tellus.

_____, 1980: Successive bifurcations and the Ice-Age problem. To appear in Bifurcation Phenomena in Mathematical Physics and Related Topics, C. Bardos, ed., D. Reidel Publ. Co., Dordrecht, Holland.

_____, and R. Balgovind, 1979: A fast Cauchy-Riemann solver. Math. Comp., 33, 585-635.

_____ and _____, 1980: A Langevin equation for large-scale atmospheric flow. NASA Tech Memo. (herein), Atmos. and Ocean. Res. Rev.-1979, NASA Goddard Space Flight Center, Greenbelt, Maryland.

_____, and K. Bhattacharya, 1979: An energy-balance model of glaciation cycles. Report of the JOC Study Conf. on Climate Models: Performance, Intercomparison and Sensitivity Studies, GARP Publ. Series No. 22, 886-916, WMO, Geneva, Switzerland.

_____, M. Halem, and R. Atlas, 1979: Time-continuous assimilation of remote-sounding data and its effect on weather forecasting. Mon. Wea. Rev., 107, 140-171.

_____, _____, and _____, 1979: Effects of sounding temperature assimilation on weather forecasting: model dependence studies. Remote Sounding of the Atmosphere from Space, H-J. Bolle, ed., Pergamon Press, 21-25.

_____, E. Kallen, and C. Crafoord, 1979: Free oscillations in a climate model with ice-sheet dynamics. To appear in J. Atmos. Sci.

Halem, M., J. Shukla, Y. Mintz, M. L. Wu, R. Godbole, G. Herman, and Y. Sud, 1979: Comparisons of observed seasonal climate features with a winter and summer numerical simulation produced with the GLAS general circulation model. Report of the JOC Study Conf. on Climate Models: Performance, Intercomparison and Sensitivity Studies, GARP Publ. Series No. 22, 207-253, WMO, Geneva, Switzerland.

Helfand, H. M., 1979: The effect of cumulus friction on the simulation of the January Hadley circulation by the GLAS model of the general circulation. J. Atmos. Sci., 36, 1827-1841.

_____, 1980: Dependence of the atmospheric heat budget on the parameterization of cumulus convection in the GLAS model of the general circulation. Submitted to Mon. Wea. Rev.

Herman, G. F., 1979: Thermal radiation in Arctic stratus clouds. Submitted to Quart. J. R. Meteor. Soc.

_____, and W. T. Johnson, 1979: The response of the Goddard GCM to sea ice boundary conditions. Report of the JOC Study Conf. on Climate Models: Performance, Intercomparison and Sensitivity Studies, GARP Publ. Series No. 22, 538-562, WMO, Geneva, Switzerland.

_____, and _____, 1980: Arctic and Antarctic climatology of the GLAS GCM. Submitted to Mon. Wea. Rev.

_____, and _____, 1980: The effect of extreme sea ice boundaries on the climatology of the GLAS GCM. Sea Ice Processes and Models, N. Washington Press, publ.

_____, M. L. Wu, and W. T. Johnson, 1979: The effect of clouds on the earth's solar and infrared radiation budgets. Submitted to J. Atmos. Sci.

Kalnay-Rivas, E., and D. Hoitsma, 1979: Documentation of the Fourth-Order Model. NASA Tech. Memo. 80608.

_____, and _____, 1979: The effect of accuracy, conservation and filtering on numerical weather forecasting. Fourth Conf. on Numerical Weather Prediction, Preprint Volume, 302-312, AMS, Silver Spring, MD, October 29-November 1.

_____, and L.-O. Merkine, 1980: A simple mechanism for blocking. Accepted by J. Atmos. Sci.

_____, W. Baker, M. Halem, R. Atlas, and D. Edelmann, 1980: GLAS experiments with FGGE II-b data. In preparation.

Lin, J. D., 1980: On the force-restore method for prediction of ground surface temperature. J. Geophys. Res., in press.

_____, 1980: Evaporation from bare soils. To be presented at IAHR/APD Int'l. Conf. on Water Resources Development, Taipei, Taiwan, 12-14 May.

_____, J. J. Alfano, and P. Bock, 1979: Modeling and terrestrial hydrology for the global atmosphere: the future role of satellite data. Satellite Hydrology/Proc. Fifth Pecora Mem. Sympo., Sioux Falls, South Dakota, 11-15 June, in press.

_____, J. J. Alfano, and P. Bock, 1979: A large-scale ground hydrology model which interacts with the atmosphere. Proc. 18th Cong. of Int'l. Assoc. for Hydraulic Res., 3, 375-382, Cagliari, Italy, 10-14 September.

_____, _____, and _____, 1980: Modeling the terrestrial hydrology for the global atmosphere. I. The ground hydrology model; II. Tests of the ground hydrology model; III. Interactive experiments of the ground hydrology model with the NASA GLAS general circulation model. In preparation.

Mintz, Y., 1979: On the simulation of oceanic general circulation. Report of the JOC Study Conf. on Climate Models: Performance, Intercomparison and Sensitivity Studies, GARP Publ. Series No. 22, 607-687, WMO, Geneva, Switzerland.

Parkinson, C. L., and G. F. Herman, 1980: Sea ice simulations based on GLAS GCM model output. Submitted to Mon. Wea. Rev.

Pollack, J. B., C. B. Leovy, P. W. Grieman, and Y. Mintz, 1980: Simulation of the atmospheric circulation on Mars, and comparisons with Space-Probe observations. Submitted to J. Atmos. Sci.

Rambaldi, S., and D. A. Randall, 1979: A Lagrangian model of a nascent slab-symmetric thermal. Submitted to Mon. Wea. Rev.

Randall, D. A., 1979: The entraining moist boundary layer. Fourth Sympo. Air Pollution and Turbulence Diffusion, Preprint Volume, AMS, Reno, Nevada, 467-470. (Available from the author at NASA Goddard Space Flight Center, Greenbelt, Maryland 20771.)

_____, 1980: Conditional instability of the first kind, upside-down. J. Atmos. Sci., 37, 125-130.

_____, 1980: Entrainment into a stratocumulus layer with distributed radiative cooling. J. Atmos. Sci., 37, 148-159.

_____, and G. J. Huffman, 1979: A stochastic model of cumulus clumping. Submitted to J. Atmos. Sci.

_____, and _____, 1979: A stochastic model of cumulus clumping. Presented at the GATE seminar, The Impact of GATE on Numerical Modeling of the Atmosphere and Ocean, Woods Hole, Massachusetts, August.

Rosenberg, A., and J. Susskind, 1979: Theory of pure rotational transitions in doubly degenerate torsional states of ethane. Phys. Rev. Letters, 42, 1613-1620.

_____, and _____, 1979: On nuclear spin statistics in rotational transition intensities in tetrahedral AB_4 molecules. Can. J. Phys., 57, 1081-1089.

Schlesinger, M. E., and Y. Mintz, 1979: Numerical simulation of ozone production, transport and distribution with a global atmospheric general circulation model. J. Atmos. Sci., 36, 1325-1361.

Straus, D. M., 1980: Long-wave baroclinic instability in the troposphere and stratosphere with spherical geometry. Submitted to J. Atmos. Sci.

_____, and M. Halem, 1980: Autoregressive analysis of climatic noise. To be submitted to Mon. Wea. Rev.

Susskind, J., and A. Rosenberg, 1980: Temperature retrievals from TIROS N. Submitted to Remote Sensing of Oceans and Atmos., Academic Press, publ.